University of Sussex

# Using clusters of galaxies as novel and standard probes of dark matter

**Sunayana Bhargava**

Submitted for the degree of Doctor of Philosophy

Department of Physics & Astronomy

University of Sussex

April 2020

# Declaration

I hereby declare that this thesis has not been and will not be submitted in whole or in part to another University for the award of any other degree.

Signature:

Sunayana Bhargava

UNIVERSITY OF SUSSEX

Sunayana Bhargava, Doctor of Philosophy

# Clusters of galaxies as novel and standard probes of dark matter

## Summary

In this thesis, we apply samples of red-sequence selected galaxy clusters with archival X-ray observations as novel and standard probes of dark matter. We detail the construction of samples consisting of clusters in the Sloan Digital Sky Survey and Dark Energy Survey areas selected using the redMaPPer cluster finder, with X-ray confirmation provided by the *XMM* Cluster Survey (XCS). We apply one of these samples to the investigation of an unmodelled X-ray line at $\simeq 3.5$ keV in the spectra of clusters of galaxies. Using the largest cluster sample to date for such a study, we analyse the spectra of 118 galaxy clusters to search for evidence of a flux excess at $\simeq 3.5$ keV, which has a suggested origin in the decay of resonantly produced sterile neutrino dark matter with mass $m_s \simeq 7$ keV. Our results find evidence against a dark matter interpretation of the 3.5 keV feature. We then apply all three samples to calibrating the centering performance of redMaPPer. Central galaxies selected by redMaPPer do not always robustly trace the centre of the cluster's underlying dark matter distribution, while X-ray emission is seen to be a more reliable tracer of the cluster potential. We therefore model the offset between optical and X-ray determinations of the cluster centre using the redMaPPer catalogues and public data from *XMM-Newton*. The centering performance of the cluster finder is a key component in the accurate measurement of cluster masses and derived estimates of cosmological parameters. Although we find cluster miscentering to be a subdominant source of systematic error in optical datasets ($\sim 2\%$), it is likely to constitute a more significant contribution to cluster cosmology in future, larger datasets such as LSST.

# Acknowledgements

I would like to begin by thanking my supervisor Kathy Romer for her unfaltering guidance and support over the past four years. I have learnt a great deal working with you and will always be grateful for the faith you maintained in my work. I would also like to thank Paul Giles who I was lucky enough to gain as both a collaborator as well as a mentor during my PhD. Thank you for your patience, knowledge, and the enormous amount of time spent shaping my projects into precise answers to scientific questions.

A huge thank you to Tesla Jeltema for welcoming me into her research group during my time at UC Santa Cruz. You have provided me with constant encouragement and support that is well beyond what I could have hoped for. I am grateful to have had the opportunity to work with you and eagerly look forward to collaborating on future projects!

Thank you to the Dark Energy Survey collaboration for allowing me to do exciting research, introducing me to many excellent scientists, as well as supplying the funds for me to travel widely. Observing trips and collaboration meetings have been one of the highlights of my PhD, not only for their locations but also for the reminder that, no matter how abstract, science remains a fundamentally human endeavour.

I would also like to thank the XCS research group, especially Philip Rooney, Alberto Bermeo, and Julian Mayers for training me up with all the necessary X-ray astronomy skills to complete this PhD. I also acknowledge funding support from the UK Science and Technology Facilities Council via Research Training Grant ST/N504452/1.

My doctoral years in Brighton have been deeply memorable and exciting, in part thanks to all the wonderful people I met along the way.

Thank you Dániel, Ridwan, Alex, Hannah, Lucía, Zé, Steven, Scott, Mateja and so many others for making me feel welcome when I first arrived at the Astronomy Centre. A special

thanks to Benoît Fournier for many spirited discussions. Thank you to my incomparable 4C13 officemates, Carlos, Azizah, Rosemary, Michele and Edward for endless support and entertainment. To Giulio Fabbian for hosting multiple soirées and keeping me well-fed during my last year at Sussex, as well as being a fantastic housemate. To the astronomers who were always keen for Friday evening beers at Falmer (and tolerating my lateness) - Lucas, Dan, Aswin, Edward, Dimitrios, Jussi, Luke, Kareem, Maria, David, Reese, Ian, Andrew (and many more!) Thank you also to my friends on the west coast, Katie, Katinka, Lena, Devon and Roy for keeping my evenings lively. I'd especially like to thank Spencer Everett for making my time in Santa Cruz so memorable.

To Jessica Hislop for being my first conference companion and becoming a dear friend ever since. Chris Lovell, for keeping me dancing through the highs and lows. Jadesola Orekoya, for always looking out for me, and Ciaran Fairhurst, for being my rock. Finally, to Pippa Cole for being the most generous, loving friend and housemate over the last four years.

Thank you to my friends outside of Brighton; the wonderful poets in Octavia who dutifully reminded me to stay tender and continue writing poetry alongside science (to the benefit of both pursuits). To my dear friends Michelle, Shruti, and Radha for keeping me motivated throughout this journey. I would also like to thank David Hooper for believing in me as I nervously embarked on this PhD.

I would finally like to thank my family for their unwavering love and support. I am incredibly fortunate to have such caring parents who, despite many hardships, always believed in my ability to persevere and succeed in research. Thank you for always encouraging me to follow my passions. This thesis is dedicated to my mother, whose own PhD remained unfinished after moving overseas to start a family. I am only able to finish this thesis today because of everything you started.

*"A woman in the shape of a monster*
*a monster in the shape of a woman*
*the skies are full of them."*

— **Adrienne Rich, *Planetarium***

# Contents

# List of Tables

# List of Figures

# Chapter 1

# Introduction

Astronomers have grappled with the immensity of the cosmos for millennia. Over the course of 14 billion years, a largely homogeneous universe gradually ceded to the formation of complex structures, allowing the night sky to become the familiar canvas of nebulae, stars, and galaxies we observe today. Understanding how these objects evolved and contribute to the overall mass in the Universe has been a central project for astronomers and cosmologists alike, and, despite great leaps in scientific knowledge, remains unresolved.

Galaxy clusters are the largest gravitationally collapsed objects in the Universe. With typical masses between $10^{13}$ and $10^{15} M_{\odot}$, these entities are both the largest virialised structures, and the smallest to contain a representative sample of all the matter in the universe (Bahcall, 1999). The spatial distribution of clusters across cosmic time can be used to discriminate between multiple cosmological models (Press and Schechter, 1974), while the ratio of baryons to total matter in a collapsed cluster can be treated as paradigmatic of the cosmic average. More recently, galaxy clusters have found another use in the indirect detection of dark matter - the invisible, dominant mass component in our cosmos. One example of this use claims that unmodelled X-ray signatures appearing in the spectrum of the cluster plasma may arise from theoretically well-motivated dark matter candidates. As such, clusters are poised as exciting cosmological tracers as well as ideal laboratories for testing new physics. To enable these uses, one requires the availability of large, well-understood and statistically complete cluster samples. To provide context to what follows, we begin with an overview of the most salient concepts in cosmology required for cluster studies.

## 1.1 Cosmology primer

### 1.1.1 Density contributions

When considering the simplest models of an expanding universe, only the gravitational force of matter influences the dynamics of expansion. This leads to three possible scenarios: a flat, open or closed universe. A flat universe, as its name suggests, has no curvature. It contains just enough matter to eventually stop cosmic expansion, but does not have enough gravitational force to recollapse back to a singularity. An open universe has negative curvature (e.g. saddle-shaped) and insufficient mass to halt expansion, thereby growing indefinitely. Finally, a closed universe has positive curvature (e.g. spherical) and enough matter to stop expansion and eventually recollapse on itself.

To produce a flat universe, the mass-energy density required is referred to as the critical density, denoted by $\rho_c$. One can write the density of a universal component as a ratio to the critical density, such as

$$\Omega_i = \frac{\rho_i}{\rho_c} \tag{1.1}$$

where $i$ denotes the component of interest. The symbol $\Omega_M$ describes the contribution from non-relativistic (including baryonic and dark) matter. $\Omega_R$ describes the contribution from radiation, referring to relativistic particles (photons and neutrinos). This radiation component dominated in the early universe, prior to the epoch of recombination – during which charged electrons and protons first became bound to form electrically neutral hydrogen atoms – but is negligible today. Recent evidence from the cosmic microwave background (hereafter CMB), strongly suggests a flat, homogeneous universe (Planck Collaboration et al., 2018), which agrees with our understanding of inflation theory and implies an overall energy density of $\Omega_{tot} = 1$. Prior to the discovery of cosmic expansion in 1927 by Edwin Hubble, a cosmological constant ($\Lambda$) was included in Einstein's field equations to satisfy a static, flat, matter-dominated universe. More recently, observations of type Ia supernovae determined the universe favours a non-zero, positive cosmological constant, and measured a density of matter, $\Omega_M \simeq 0.3$ (e.g. Perlmutter et al., 1999; Riess et al., 1998). The combination of evidence for a flat Universe and insufficient amount of observed matter support a need for a cosmological constant to provide an additional energy density contribution. We therefore obtain an expression for the total energy density which is

$$\Omega_{\rm tot} = \Omega_M + \Omega_\Lambda. \tag{1.2}$$

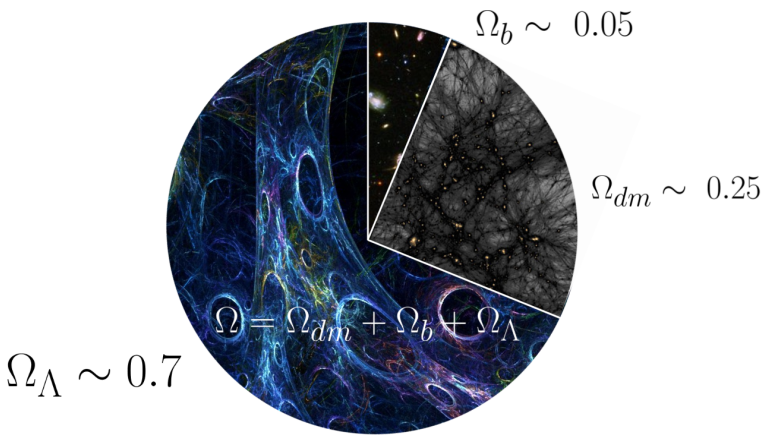


Figure 1.1: The composition of our observable universe, in which approximately 70% of the energy density in the universe is in the form of dark energy ($\Omega_\Lambda$), while the remaining 30% is in the form of mass, ($\Omega_M$), which is itself 25% dark matter ($\Omega_{dm}$) and 5% baryonic matter, ($\Omega_b$). Image by S. Everett.

The general term for this additional component is 'dark energy,' which originates as a term in Einstein's theory of general relativity. A cosmological constant is the simplest form of dark energy, as it has an energy density which is constant in space and time. Nevertheless, other models are possible, which, for example, feature a time-varying component of dark energy. In general, dark energy can be thought of as a fluid with an equation of state

$$p_\Lambda = w\rho_\Lambda \tag{1.3}$$

where $w$ is the equation of state parameter for $\Lambda$. If dark energy is a cosmological constant, $w = -1$ (resulting in a negative pressure). Solving for a more general class of dark energy models, any value of $w < -1/3$ will produce a universe with accelerated expansion.

Our current and most widely accepted cosmological model is the ΛCDM (Lambda cold dark matter) model. In this model, the universe consists of three major components: dark energy, which behaves like a cosmological constant ($\Lambda$), 'cold' (non-relativistic) dark matter (abbreviated CDM); and ordinary matter. It is considered the most simple model, which accurately explains key properties of the universe such as the uniformity of the CMB, large scale structure, big bang nucleosynthesis and accelerated expansion.

The model can be defined entirely by six independent parameters: the physical baryon density, $\Omega_b h^2$, physical dark matter density, $\Omega_c h^2$, and age of the universe ($t_0$). It also constrains the scalar spectral index $n_s$, reionization optical depth $\tau$ (measures of the scale-dependence and amplitude of CMB fluctuations), and degree of curvature ($A_s$). The most

precise constraints available obtained on these parameters are from Planck Collaboration et al. (2018). Throughout this thesis, we assume a flat ΛCDM cosmology with $\Omega_M = 0.3$ and $\Omega_\Lambda = 0.7$, which is a reasonable approximation for these measured densities.

### 1.1.2 Distance measures

#### Proper and comoving distance

The proper distance $d(t)$ between two objects increases over time in an expanding universe as the objects move farther apart from each other. It is therefore useful to define a comoving distance $\chi$, which takes cosmic expansion into account, such that objects moving apart only due to expansion have a constant $\chi$. The proper and comoving distance are related by

$$d(t) = a(t)\chi \tag{1.4}$$

in which $a(t)$ refers to the dimensionless scale factor of the Universe, with $t$ counted from the birth of the universe and $t_0$ set to the current age. By definition, $a(t_0) = 1$.

#### Hubble parameter

The Hubble parameter relates the rate of expansion to the proper distance between two objects. It is easily obtained by differentiating Equation 1.4 with respect to time,

$$v(t) = \dot{a}(t)\chi \tag{1.5}$$

and can be rewritten as

$$v(t) = \frac{\dot{a}(t)}{a(t)} d(t) \tag{1.6}$$

The quantity $\dot{a}/a$ defines the Hubble parameter, and is written as $H(z)$ or $H(t)$. We can relate this to its present day value, the Hubble constant ($H_0 \simeq 70$ km s$^{-1}$ Mpc$^{-1}$) via

$$H(z) = H_0 E(z) \tag{1.7}$$

where $E(z)$ is describes the evolution of $H$ with redshift $z$ (described below), depending on the underlying cosmology. For a flat universe with a cosmological constant, one can write

$$E^2(z) = \Omega_M (1+z)^3 + \Omega_\Lambda \tag{1.8}$$

Using this cosmology, the present value of the critical density, $\rho_{c,0}$ can be determined using Equation 1.1 via

$$\rho_{c,0} = \frac{3H_0^2}{8\pi G} \tag{1.9}$$

**Cosmological redshift**

To define cosmological redshift, consider a photon that has been emitted at time $t_e$ and received at $t_0$. During this time, the universe has expanded by a factor $a(t_0)/a(t_e)$, hence the wavelength of the photon has also been stretched by

$$a(t_0)/a(t_e) = \lambda_0/\lambda_e = 1 + z \tag{1.10}$$

We can relate the scale factor directly to the redshift by writing $a(t) = \frac{1}{1+z}$.

**Distance-redshift relation**

It is possible to write the comoving distance in terms of redshift and the underlying cosmology contained in $E(z)$, according to

$$\chi = \frac{c}{a_0 H_0} \int_0^z \frac{dz}{E(z)} \tag{1.11}$$

Using this, it is possible that if the cosmological parameters in Equation 1.8 are known, one can calculate the distance to an object with a measured redshift. The converse is true as well, i.e. if the distance and redshift are known, one can derive the underlying cosmological parameters.

**Luminosity and angular diameter distance**

Proper distance is not directly measurable but distances can be determined if the physical size or intrinsic luminosity of an object is known. Then, we can define a luminosity distance $d_L$, in terms of the measured flux $F$, such that

$$F = \frac{L}{4\pi d_L^2} \tag{1.12}$$

The angular diameter distance is derived by measuring the angle $\theta$ subtended by an object with a physical diameter $D$. It can be written in terms of $d_L$, as per

$$d_A = d_L/(1 + z)^2 \tag{1.13}$$

### 1.1.3 Comoving volume

If there is a known number density of objects based on theory, it is possible to count objects in a given redshift range and determine the comoving volume. This is useful because the volume depends on the expansion history similar to distance measures. It is also possible

to directly constrain cosmology from the comoving volume. Considering a proper volume element, $dV$, with a proper area $dA$ and proper depth $dr$, we can write

$$dV = dAdr = d_A^2 d\Omega dr \tag{1.14}$$

where $d\Omega$ is the solid angle (not to be confused with the cosmological $\Omega$) and $d_A$ is the angular diameter distance to the element.

As described above, the angular diameter distance relates an object's physical size to its angular size. In a static universe, this distance is defined as

$$d_A = \frac{D}{\theta} \tag{1.15}$$

where $D$ is the proper distance and $\theta$ is the angle subtended by the object in the sky. However, an expanding universe grows by a factor $1+z$ in the time taken for the photons to travel from the source to the observer. Hence, the distance in Equation 1.15 is underestimated by a factor $1+z$, leading to

$$d_A = \frac{\chi}{1+z} \tag{1.16}$$

Replacing $\chi$ with Equation 1.11, we can rewrite Equation 1.14 as

$$dV_\chi(z) = \frac{c}{a_0 H_0} \frac{(1+z)^2 d_A^2}{E(z)} d\Omega dz \tag{1.17}$$

### 1.1.4 Growth of structure

It is possible to constrain cosmology using the growth of structure rather than distances and volumes, given that initial density perturbations grew to form large scale structure in a cosmology-dependent way. Firstly, we define the variation in initial density perturbations in terms of the density contrast $\delta$,

$$\delta = \frac{\rho - \bar{\rho}}{\bar{\rho}} \tag{1.18}$$

where $\rho$ is the density in a given region and $\bar{\rho}$ is the mean matter density. Therefore, regions where the density $\delta > 0$ are considered overdense and collapse to form structures, and those with $\delta < 0$ are underdense, forming voids. In an expanding Universe, only regions denser than a critical value collapse ($\sim 178$ times the background density). This number is determined by assuming an idealised model in which the collapse of overdensities occurs via single, top-hat spherical perturbations in an otherwise homogeneous universe.

Since galaxy clusters are the largest collapsed structures, they are sensitive to the amplitude of the $\delta$ distribution. They can constrain the linear growth of structure via

Figure 1.2: Figure from Allen et al. (2011). Observations of Abell 1835 ($z = 0.25$) at X-ray (left), optical (centre) and millimetre (right) wavelengths, illustrating the multi-wavelength morphology and processes within a massive, dynamically relaxed cluster. All three images are centered on the X-ray peak position and have the same spatial scale (5.2 arcmin or $\sim 1.2$ Mpc).

measurements of the $\sigma_8$ parameter, which defines the standard deviation of $\delta$ values measured in a sphere with an $8h^{-1}$ Mpc radius. A larger measured value for $\sigma_8$ corresponds to a less uniform initial density distribution, which implies more structure in the Universe. Since clusters grow from the high tail of the density distribution, measurements of the number of clusters can be used to constrain $\sigma_8$.

## 1.2 Cluster observations

A typical galaxy cluster is approximately 15% baryonic matter and 85% dark matter (Rosati et al., 2002). One third of the baryonic matter comprises stars inside the cluster member galaxies. The remainder fills the space between member galaxies in the form of hot, ionised gas, known as the intracluster medium (ICM). Clusters are observable in multiple wavelengths, with the advantage that each waveband traces different components and processes within the cluster (see Figure 1.2). Galaxies are visible in the optical range, X-rays trace the diffuse intracluster gas, radio observations can determine the presence of active galactic nuclei (AGN) and magnetic field activity, and millimetre frequencies highlight the interplay of the CMB with the ICM via inverse Compton scattering. In the sections below, we summarise the physics underlying multi-wavelength observations of galaxy clusters.

### 1.2.1 Optical observations

Optically selected clusters were first catalogued by George O. Abell in 1958 (Abell, 1958a). Using only visual inspection, over 4000 clusters were detected based on overdensities of galaxies, under the requirement that at least 50 galaxies were contained within a counting radius $R = 1.5h^{-1}$ Mpc and a predefined magnitude range. All clusters were assumed to have a nominal redshift in the range 0.02 - 0.2, though later measurements have confirmed some of these clusters are as distant as $z = 0.4$. The catalogue, initially consisting of 2712 clusters in the Northern Survey, was later expanded to include clusters in the southern sky in 1989 (Abell et al., 1989). An additional 1,361 clusters were found in the Southern Sky Survey (SSS) (Schuster, 1980) giving a total catalogue size of 4,703 clusters. Another cluster catalogue was later compiled by Zwicky and others (Zwicky et al., 1961), who extended the analysis using a less strict criteria in the definition of galaxy overdensities.

A key observable in the optical range is the cluster richness, which is measured according to the number of observed galaxies associated with a cluster. For large cluster samples, the richness is generally well-correlated with the number of cluster member galaxies (Dressler, 1980), however, in individual cases, it can be less accurate due to projection effects. Cluster richness measurements can utilise the fact that galaxy populations in cluster environments are dominated by elliptical and lenticular galaxies. These are passive, 'red and dead' galaxies which contain little or no ongoing star formation. Hence, they form a tight locus on the colour-magnitude relation, known as the red sequence (see Bower et al., 1992; Stott et al., 2009). Optical cluster finders can exploit this property by assigning cluster richness based on the abundance of red-sequence galaxies in a cluster (Gladders and Yee, 2000). In this thesis, we extensively utilise redMaPPer, a red-sequence based cluster finder (Rykoff et al., 2014), to optically confirm the clusters in the samples used.

Other optical measurements for clusters include the velocity dispersion of member galaxies in the cluster, assuming virial equilibrium (described in Equation 1.24), a property which correlates strongly with cluster richness (Girardi et al., 1993). Using the virial theorem, the velocity dispersion of galaxies can be used to derive the total cluster mass (Section 1.3.1). Finally, it is possible to measure the spatial distribution of red sequence galaxies of a given luminosity at various redshifts via the luminosity function (e.g. Zhang et al., 2017). Results from these studies have been contentious, with some reporting a deficit of faint red sequence galaxies at high redshifts (e.g. De Lucia and Blaizot, 2007), implying that these galaxies formed later than brighter ones, while others have found

little evidence of evolution in the red sequence luminosity function up to redshift 1.5 (e.g. Andreon, 2008).

### 1.2.2 Millimetre observations

The Sunyaev-Zel'dovich effect (hereafter the SZ effect) refers to the distortion of CMB radiation through inverse Compton scattering by electrons in the intracluster medium (ICM) (Sunyaev and Zeldovich, 1970). During these interactions, low-energy CMB photons are scattered to higher energies. As a result, the intensity of the CMB spectrum peaks at a slightly higher frequency (Birkinshaw, 1999) relative to the uniform CMB background. While the observed intensity of the SZ effect is dependent on the temperature and density of the ICM (due to the effects on the electron energies and rate of interactions), it is notably redshift-independent. This is because the attenuation of CMB energy density in an expanding universe decreases by a factor of $(1+z)^4$, but is exactly cancelled by the increased energy of the CMB photons at the time of scattering. This gives the SZ effect a clear advantage over other observables, due to the ability of millimetre telescopes to see this effect in all clusters – so long as they retain an ICM component– back to the epoch of their formation (Grainge et al., 2014). The SZ effect in clusters can be probed via measurements of the Comptonisation parameter $y$, which is defined as the integral of electron pressure along the line of sight,

$$y = \int \sigma_T n_e \frac{k_B T_e}{m_e c^2} dl \tag{1.19}$$

where $\sigma_T$ is the Thomson cross-section, $n_e$ is the electron gas density and $T_e$ is the electron temperature.

The total or integrated SZ flux in some solid angle defined by $d\Omega$ can hence be written

$$Y_{SZ} = \int_\Omega y d\Omega \tag{1.20}$$

Under the assumption that the electron gas density is in equilibrium with the cluster potential well, the integrated Comptonisation parameter $Y$ traces the cluster mass (described in Section 1.4.5). We note an additional kinematic SZ effect is due to the interactions between electrons and CMB photons due to the bulk motion of the cluster (see e.g. Haehnelt and Tegmark, 1996), although this is a considerably weaker effect than the thermal SZ effect discussed here. There are various examples of SZ cluster catalogues, such as from *Planck* (Ade et al., 2016). SZ catalogues from the South Pole Telescope (SPT) can be found in Vanderlinde et al. (2010), and the Atacama Cosmology Telescope (ACT) in Hilton et al. (2018).

### 1.2.3 X-ray observations

The X-ray emission within a galaxy cluster directly traces the hot gas between member galaxies. X-rays were first detected from the Virgo cluster in 1966 using rocket-based detectors (Felten et al., 1966). A list of X-ray surveys and associated cluster catalogues are provided in Section 2.1.1.

X-ray emission originates from the ICM, an energetic plasma comprising hydrogen and helium ions (formed during baryogenesis), and additionally enriched with heavier elements processed during stellar fusion. Typically the heavy (heavier than helium) element abundance in clusters is one third of that found in the Sun ($0.3Z_{\odot}$). The two dominant X-ray emission mechanisms within the ICM are thermal bremmstrahlung and line emission.

#### Thermal bremsstrahlung

Thermal bremsstrahlung (also known as free-free emission) occurs as a result of electrons being accelerated around ions in the cluster plasma. It is the principal emission mechanism from very high temperature ($T > 10^6$ K) ion plasmas (e.g. galaxy halos; clusters of galaxies). The cluster plasma is referred to as 'thermal' because the electrons and ions are in thermal equilibrium. The frequency of the thermal radiation is also strongly dependent on the plasma temperature. The equation for thermal bremsstrahlung can be written as

$$\epsilon_{\nu}^{ff} \propto Z^2 n_e n_i g_{ff} T^{-1/2} e^{-h\nu/kT_g} \tag{1.21}$$

where $n_e$ and $n_i$ are the number density of electrons and ions, respectively. The emissivity due to bremsstrahlung emission is defined as the emitted energy per unit time, frequency and volume. The Gaunt factor $g_{ff}$ corrects for quantum mechanical and distant collisional effects. It is stated that for an intracluster gas in thermal equilibrium, there is only a single temperature for the plasma. Hence, Equation 1.21 can be written simply as the exponential of the frequency $\nu$, implying that cluster emission falls off sharply at higher frequencies.

#### Line emission

The second mechanism is termed line emission and occurs from elemental transitions in the cluster plasma, as a result of collisions between ions and electrons. Processes that contribute to the X-ray line emission from a diffuse plasma include collisional excitation of electrons, radiative and dielectronic recombination and others. The emissivity due to a

collisionally excited line is usually written (Osterbrock, 1974),

$$\int \epsilon_{\nu}^{line} d\nu = n(X^i) n_e \frac{h^3 \nu \Omega(T) B}{4\omega_{gs}(X_i)} \left[\frac{2}{\pi^3 m_e^3 kT}\right]^{1/2} e^{-\Delta E/kT} \tag{1.22}$$

where $h\nu$ is the energy of transition, $\Delta E$ is the difference in excitation energy between the excited state and the ground state. $B$ is the branching ratio of the line and $\Omega(T)$ is the collisional strength, which weakly depends on temperature. Finally, $\omega_{gs}$ is the statistical weight of the energy levels of the ion.

Although the emissivities of line emission and bremsstrahlung are dependent on the gas density, their ratio is density independent. If one of these equations is used to fit a temperature for the plasma, the ratio can be used as a density-independent diagnostic of the cluster abundance of heavier ions and ionisation states (Bahcall and Sarazin, 1978).

The presence of a 7 keV Fe line in the X-ray spectra of galaxy clusters, first discovered in the Perseus cluster (Mitchell et al., 1976), provided strong evidence against any non-thermal model for the origin of the X-ray emission. Specifically, any non-thermal processes would not produce line emission. The fact that the iron abundance in clusters–despite the variation in cluster properties–is roughly constant, implies that the line and continuum emission are both thermal. It further implies that the ICM has a similiar origin in all clusters, regardless of the cluster's dynamical state.

### X-ray luminosity

We can see from both Equations 1.21 and 1.22, all X-ray emission is proportional to the density of ions and elections. The bolometric luminosity $L_{\rm X}$ of the ICM is therefore given by the integral of $\epsilon$ over all frequencies, and then over the volume of the cluster

$$L_{\rm X} \propto \int n_e n_i T^{-1/2} dV \tag{1.23}$$

The luminosity is strongly dependent on the overall density, exhibiting a weaker dependence on the gas temperature (Sarazin, 1986). Additionally, the density squared dependence of the X-ray emission means that luminosity measurements are sensitive to gas physics in the cluster core. Mechanisms such as rapid radiative cooling or merging can change the thermodynamic state of this core gas, subsequently affecting luminosity scaling relations in clusters (Pratt et al., 2009). These are defined in Section 1.4.

### X-ray temperature

The X-ray spectrum of a cluster shows both the continuum emission from bremsstrahlung and line emission from prominent (e.g. Fe and Si) ions (refer to Böhringer and Werner,

2010, for a review on abundances in clusters). By fitting a model to the observed spectrum, it is possible to measure the temperature of the ICM. The temperature is typically in the range $\sim 1 - 15$ keV. The intracluster gas is heated to these temperatures during cluster formation, as gas atoms produce thermal energy while entering the gravitational potential well of the cluster. Heating continues until the cluster is in thermal equilibrium, i.e. once it reaches the virial temperature. Since the temperature gives the mean kinetic energy of gas particles, one can apply the virial theorem

$$2K + U = 0 \tag{1.24}$$

to obtain

$$3k_B T \simeq -\frac{GM_\Delta^2}{R_\Delta} \tag{1.25}$$

Since we are considering the potential energy between gas particles and the cluster potential, we can rewrite Equation 1.25 as

$$T \propto \frac{GM_\Delta \mu m_p}{3k_B R_\Delta} \tag{1.26}$$

where $\mu m_p$ is the mean gas mass per particle, $M$ and $R$ are the total cluster mass and radius, measured with respect to some overdensity $_\Delta$, $k_B$ is the Boltzmann constant, and $G$ is the gravitational constant. A radial temperature profile for clusters can be obtained by measuring the temperature in several annular regions. With good data quality, such profiles are typically resolvable up to $R_{500}$, the radius within which the density of the cluster is 500 times the critical value at the cluster redshift (see Vikhlinin et al., 2005).

### X-ray surface brightness

The simplest spatial distribution of gas is according to an isothermal or $\beta$-profile with a constant temperature. One can express the distribution of the ionised gas density in a cluster relative to the overall density (Cavaliere and Fusco-Femiano, 1976),

$$\rho_{gas} = \rho_0 (1 + r/r_c^2)^{-3\beta/2} \tag{1.27}$$

where $\rho_0$ is the central density and $r_c$ is the core radius of the cluster. The $\beta$ value is given by $\mu m_p \sigma_r^2 / kT$, where $\sigma_r$ is the velocity dispersion. In this model, the analytic King approximation, which describes the distribution of galaxies in the central cluster region, is used (King, 1972).

Observationally, it is typical to measure a surface brightness profile rather than the gas density. Using the $\beta$-profile model, the X-ray surface brightness for clusters follows

(Neumann and Arnaud, 1999)

$$I(r) \propto \left[1 + \left(\frac{r}{r_c}\right)^2\right]^{-3\beta+1/2} \tag{1.28}$$

The surface brightness can be written as

$$I_\nu = \int_{b^2}^{\infty} \frac{\epsilon_\nu dr^2}{\sqrt{r^2 - b^2}} \tag{1.29}$$

where $\epsilon_\nu$ is the X-ray emissivity (which scales with the gas density), and $b$ is the projected distance from the centre of the cluster. Therefore, by measuring the value of $I(r)$, followed by deprojecting, it is possible to measure the gas density distribution.

## 1.3 Cluster mass estimates

In order to constrain fundamental cosmological parameters using clusters, reliable estimates of the cluster mass are required (Sadat, 1997). However, estimating the total mass inside a galaxy cluster is nontrivial, since the majority of its mass consists of dark matter (Zwicky, 1933). Clusters contain between $10^{13} - 10^{15} M_\odot$ dark matter and ionised gas with a temperature $\sim 10^7$ K. A typical cluster also contain 100s of galaxies ($\sim 10^{13} M_\odot$). Although the cluster observations stated above inform us about baryonic processes, they do not form the whole picture. Nevertheless, cluster mass determinations are possible typically based on assumptions of dynamic equilibrium and spherical symmetry. The key mass determinations are outlined below.

### 1.3.1 Virial mass

The simplest way to determine the total cluster mass is by using the virial theorem (Equation 1.24), under the assumption the cluster is both in dynamical eqilibrium and spherically symmetric. The virial mass can be computed if the number of cluster galaxy redshifts is minimal. We equate the kinetic energy of the test particle (e.g. a galaxy) falling into the cluster potential, in terms of the mass, $m$ and velocity dispersion $\sigma_r$, such that

$$\frac{m\sigma_r^2}{2} \simeq \frac{3GMm}{5R} \tag{1.30}$$

which can be rearranged in terms of the cluster mass $M$ and radius $R$, yielding

$$M \simeq \frac{\sigma_r^2 R}{G} \tag{1.31}$$

More accurate measurements using the virial mass require a surface pressure term correction. This is because the cluster halo is embedded in a cosmological density field, with

ongoing infall (see Shapiro et al., 2004, for a detailed review of this effect). This non-zero pressure term can decrease the estimated mass by a maximum of $\sim 20\%$ (see Diaferio, 2009, and references therein). These uncertainties become an order of magnitude larger if the galaxies are not fair tracers of the cluster's overall mass distribution.

When the number of galaxy spectra is large enough to produce a velocity dispersion profile, the Jeans equations for a steady-state spherical system can be applied. The cumulative mass is then

$$M(r) = \frac{\sigma_r^2 R}{G}\left[\frac{d\ln\sigma_r^2}{d\ln r} + \frac{d\ln\rho}{d\ln r} + 2\beta\right] \tag{1.32}$$

where $\rho(r)$ is the density profile of the galaxy, $\sigma_r(r)$ is the 3-dimensional velocity dispersion, and $\beta$ is the velocity anisotropy parameter (not to be confused with the $\beta$ used in Equation 1.28). These quantities can be determined under model assumptions of mass density and velocity dispersion profiles.

The mass density profile is not directly measurable, however, numerical simulations by Navarro, Frenk and White (hereafter simply NFW, Navarro et al., 1996) indicate that CDM halos with masses spanning several orders of magnitudes follow a universal density profile, whose shape is independent of mass or cosmology. This profile can be written as

$$\rho(r) = \frac{\rho_0}{\frac{r}{R_s}\left(1+\frac{r}{R_s}\right)^2} \tag{1.33}$$

which is a function of the characteristic density, $\rho_0$, and scale radius, $R_s$, both of which are specific to the halo. While this is an effective choice for a mass profile, an alternative model termed the Einasto profile (Einasto, 1965), is considered to be a better fit to halos with steeper density profiles than those predicted by NFW (e.g. Dutton and Macci, 2014), with the advantage of having a finite (zero) central slope, unlike the NFW profile which has a divergent (infinite) central density.

An advantage of the dynamical mass estimate in Equation 1.32 over the X-ray method (stated below) is that it is insensitive to several forms of non-thermal pressure support that affect X-ray mass measurements such as bulk motions, turbulence or core physics.

### 1.3.2 Hydrostatic mass

If the pressure force from the intracluster gas is balanced by the gravitational force from the total cluster mass, the cluster is said to be in hydrostatic equilibrium and obeys the following

$$\Delta P = -\rho_g \Delta\phi(r) \tag{1.34}$$

where $P = \rho_g k T_g / \mu m_p$ is the gas pressure (using the ideal gas law), $\rho_g$ is the gas density, and $\phi(r)$ is the gravitational potential of the cluster.

Under the assumption of spherical symmetry, the pressure and the gravitational potential vary only with respect to the distance $r$. Hence, we can simplify Equation 1.34 as

$$\frac{1}{\rho_g}\frac{dP}{dr} = -\frac{d\phi}{dr} = \frac{-GM(r)}{r^2} \tag{1.35}$$

where $r$ is the radius from the cluster centre and $M(r)$ is the total cluster mass within the radius. By replacing the left-hand side of Equation 1.35 with the expression for gas pressure, we obtain

$$\frac{dP}{dr} = \frac{k}{\mu m_p}\frac{d}{dr}(\rho T) = \frac{k}{\mu m_p}\left[\rho\frac{dT}{dr} + T\frac{d\rho}{dr}\right] \tag{1.36}$$

Combining Equations 1.35 and 1.36, rearranging in terms of the cluster mass $M(r)$, we find

$$M(r) = \frac{-r^2 k}{G\mu m_p \rho(r)}\left[\rho\frac{dT}{dr} + T\frac{d\rho}{dr}\right] \tag{1.37}$$

Finally, Equation 1.37 can equivalently be written

$$M(r) = \frac{-r^2 kT}{G\mu m_p}\left[\frac{d\ln\rho}{d\ln r} + \frac{d\ln T}{d\ln r}\right] \tag{1.38}$$

A key property of the hydrostatic mass is its strong dependence the gas temperature, and comparatively weak dependence on the density. Assuming hydrostatic equilibrium, the total mass (within $R$) can be determined from measurements of the gradients of cluster temperature and gas density profiles. The use of hydrostatic equilibrium is a well-established method of deriving X-ray cluster masses, first applied by Bahcall (1977), followed by Mathews (1978). Typically, the surface brightness and temperature profiles are measured separately, after which both need to be deprojected into 3D space to reproduce the correct physical profile for the cluster.

Although this is a reliable method to determine cluster masses, neglecting the impact of non-thermal pressure mechanisms such as bulk motions, turbulence or core physics can lead to underestimates of the true cluster mass. Hydrodynamical cluster simulations predict that the hydrostatic bias is between 5% to 35% (e.g. Rasia et al., 2006; Jeltema et al., 2008). Previous studies such as those done by (Lau et al., 2013) have included the contribution of gas acceleration to correct the mass bias, finding it to be a small contribution though significant in the outskirts of massive clusters. Comparisons between different mass estimators, namely weak lensing (detailed in Section 1.3.3) and the hydrostatic method, have also quantified the extent of the hydrostatic mass bias. In general, it is considered that the agreement between X-ray and lensing mass estimates depend on

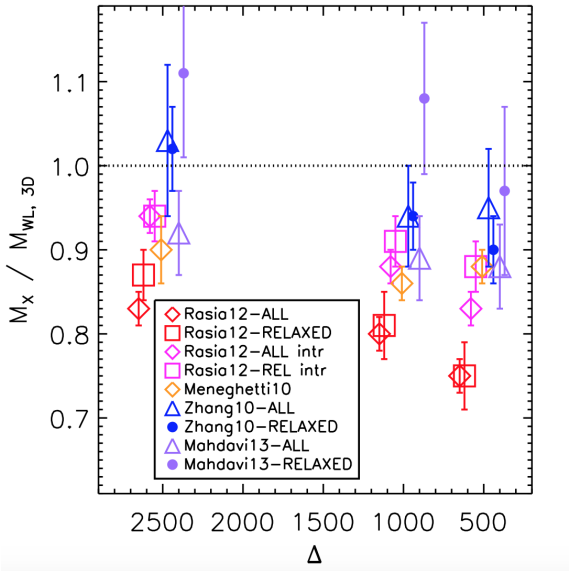


Figure 1.3: Figure from Ettori et al. (2013) showing a comparison between X-ray and weak lensing mass estimates from observed (Zhang10, Mahdavi13) and simulated (Meneghetti10, Rasia12) datasets. This figure is adapted from Table 5 in Rasia et al. (2012). Relaxed refers to systems with either a not-disturbed X-ray morphological appearance or a relatively low level of the gas entropy in their cores.

the radius considered and dynamical state of the cluster (i.e. whether it is relaxed or dynamically active), as shown in Figure 1.3. Recent work in Mahdavi et al. (2013) has shown that in a study of 50 clusters, the hydrostatic masses underestimate weak lensing masses by 10% on average, while relaxed clusters produce no bias. However, disturbed clusters show a large and constant bias between 15-20% at all radii ($\Delta = 2500, 1000, 500$).

For a comprehensive review of the role of hydrostatic mass estimates using X-ray observations, the reader is referred to Ettori et al. (2013).

### 1.3.3 Lensing mass

#### Strong gravitational lensing

Due to the large mass of clusters, they contain deep gravitational potential wells at their centres. One of the predictions of Einstein's general theory of relativity states that massive objects curve space-time, and hence, the path of photons passing these objects will bend. Gravitational lensing refers to the distortion of light from background galaxies due to an intervening structure, such as a galaxy cluster, in the foreground. If these distortions are easily visible, e.g. in the form of arc-like structures, Einstein rings or multiple images, the phenomenon is referred to as strong lensing (as shown in Figure 1.4). Strong lensing

Figure 1.4: Abell 370, one of the first galaxy clusters where astronomers observed the phenomenon of gravitational lensing, taken by the NASA/ESA Hubble Space Telescope's newly repaired Advanced Camera for Surveys (ACS). The arcs and streaks in the image signify stretched images of background galaxies. Credit: NASA, ESA, the Hubble SM4 ERO Team and ST-ECF.

dominates at the core of the cluster, where the density is highest. By measuring the deflection between multiple lensed images and the true source image, a projected cluster mass can be derived. These projected masses are only accurate within the extent of the gravitational arcs (Meneghetti et al., 2010) and can be biased if extrapolated beyond this radius. Deprojected masses derived from strong lensing are also particularly sensitive to triaxiality, given that shape of a cluster is not exactly spherical, potentially leading to cluster mass biases at the $\sim 10\%$ level. Nevertheless, studies of small samples of highly relaxed clusters have found strong lensing mass measurements to be in good agreement with X-ray studies (e.g. Newman et al., 2011).

### Weak gravitational lensing

A more subtle effect impacts background galaxies on a larger, statistical scale due to a foreground object. This manifests in small elliptical distortions to background galaxy shapes and is known as weak gravitational lensing. It is not possible to measure this effect for individual galaxies, but using multiple background galaxies, one can find a statistical way to quantify these distortions (first detected by Bacon et al., 2000). A key advantage of weak gravitational lensing is that one can probe the cluster mass out to larger radii (unlike strong lensing, which only probes the central region). Furthermore, similar to

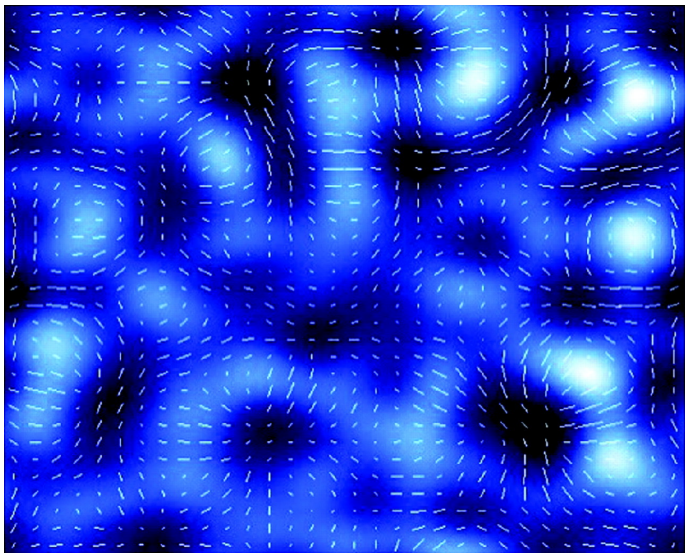

Figure 1.5: Figure from Richard S. Ellis (2010). An idealised image of weak lensing. The blue background shows a projected mass distribution, where white areas are high mass density peaks. The white ticks indicate the average shapes and orientations of a population of background galaxies (assumed statistically to be round in shape), viewed through the dark matter. In the white areas, the background galaxies are tangentially aligned around the structure, which can be distinguished from the other galaxies in the field.

strong lensing, the weak lensing measurement is insensitive to the dynamical state of the cluster.

In effect, weak lensing behaves as a coordinate transformation that distorts the images of background galaxies around a cluster. The transformation can be described with two terms - the convergence and shear. The convergence term magnifies the background galaxies by increasing their size, and the shear term stretches them tangentially around the foreground lens. To measure the tangential shear ($\gamma_T$), one must measure the ellipticities of the background galaxies, and then estimate the systematic alignment caused by lensing. Unfortunately, galaxies are not intrinsically circular, so their measured ellipticity is a combination of their intrinsic ellipticity and tangential shear effect. Furthermore, the intrinsic ellipticity can contribute more than the shear signal, depending on the foreground mass. Therefore, multiple background galaxy measurements need to be combined to decrease this effect, termed 'shape noise.' This is possible because the orientation of intrinsic ellipticities of galaxies should be effectively random, and subtracted easily. Any remaining systematic alignment between multiple galaxies can then be attributed to lensing (see Figure 1.5).

To measure a cluster mass, it is typical to fit an observed and azimuthally-averaged

tangential shear $\langle\gamma_T\rangle$ profile with a simple parameterised mass model, such as the NFW profile (Hoekstra, 2003, 2007). The value of $\langle\gamma_T\rangle$ is measured as a function of distance to the cluster centre, $r$, via

$$\langle\gamma_T\rangle(r) = \frac{\bar{\Sigma}(<r) - \bar{\Sigma}(r)}{\Sigma_{crit}} = \bar{\kappa}(<r) - \bar{\kappa}(r) \tag{1.39}$$

where $\bar{\Sigma}(<r)$ is the mean surface density measured within a circular aperture with radius $r$. The convergence, denoted by $\kappa$ is defined as the ratio of $\Sigma/\Sigma_{crit}$ where $\Sigma_{crit}$ is defined by

$$\Sigma_{crit} = \frac{c^2}{4\pi G}\frac{D_s}{D_l D_{ls}} \tag{1.40}$$

and $D_l$, $D_s$ and $D_{ls}$ refer to the angular distance to the lens, source and between the source and lens, respectively. The measured lensing signal therefore requires knowledge of the redshift of the lens and background (or source) galaxies. It is worth nothing that within the literature, it has become increasingly common to present the lensing signal as $\Delta\Sigma(r) = \Sigma_{crit}\gamma_T(r)$, which absorbs the redshift dependence, and is more convenient for comparing the lensing profiles between cluster samples (Hoekstra, 2003).

These profiles can then be fit using e.g. a single, isothermal sphere (SIS) or compared with simulated NFW profiles with minimal free parameters to derive cluster mass estimates. Nevertheless, there are numerous sources of systematics which need to be taken into account such as projection effects, cluster member contamination (termed 'boost factors') and miscentering. The impact of miscentering on cluster mass estimates forms the basis of Chapter 4.

Weak lensing mass analyses are able to precisely control systematic errors to within 4% (see e.g. Smith et al., 2015). Nevertheless, the intrinsic scatter in weak lensing mass reconstructions is comparable to hydrostatic masses, which are reported to have an intrinsic scatter of 20% (Becker and Kravtsov, 2011) and 15% (Ettori et al., 2019) respectively. Examples of clusters with weak lensing mass estimates can be found in LoCuSS (Okabe et al., 2010), CLASH (Umetsu et al., 2014) and Weighing the Giants (Applegate et al., 2014) samples. Weak lensing analyses now span a wide range in the mass-redshift plane of clusters, including low mass clusters (Kettula et al., 2015) and high redshift systems (Schrabback et al., 2017).

### 1.3.4 Caustic mass

Returning to assumptions of Newtonian dynamics (see Section 1.3.1 for a recap), the velocity required to escape a spherical gravitational potential can be written as

$$v_{esc}^2 = -2\phi(r) \tag{1.41}$$

This already informs us that a measurement of the escape velocity probes the underlying mass distribution of the system (in this case, a cluster). However, the $v_{esc}$ in Equation 1.41 is a three-dimensional quantity. In reality, observations of clusters provides only the component of $v$ along the line-of-sight (l.o.s.) at projected distances $r_\perp$. Taking into account the anistropy parameter $\beta$, it is possible to measure the tangential velocity $v_\perp$, as

$$< v_{esc}(r_\perp)^2 > = < v_{l.o.s.}^2(r_\perp) > \frac{3 - 2\beta(r_\perp)}{1 - \beta(r_\perp)} \tag{1.42}$$

This can then then be used to infer a mass using

$$GM(< r_{200}) = \mathcal{F}_\beta \int_0^{r_{200}} v_{l.o.s}^2(r) dr \tag{1.43}$$

where $\mathcal{F}_\beta$ is a function that depends on the density, potential and anistropy profile. It is usually approximated as a constant and calibrated through simulations (Gifford et al., 2017). Because the caustic mass method relies on the escape velocity (and hence the underlying gravitational potential), it is able to probe the mass profile of the cluster to well beyond the virial radius (unlike hydrostatic mass methods which are most precise at $R_{500}$, where X-ray emission is constrained). Like lensing estimates, caustic masses are independent of the dynamical state of the cluster, and are insensitive to the physical processes that might contribute to the hydrostatic bias. Comparisons between caustic mass methods and others have been done by e.g. Maughan et al. (2016). They conclude that in their caustic mass methods, the assumption of a constant value of $\mathcal{F}_\beta$ may overestimate the true mass, stating the overall caustic measurement has an intrinsic scatter with the respect to the true mass of $\sim 30\%$. Nevertheless, it is a valuable independent test of the mass, given it is affected by entirely different systematics. Caustic masses generally shows agreement within 20% with hydrostatic masses across a radial range $[0.2 - 1.25]R_{500}$, with an over/underestimation no more than 10%, favouring a small value of the hydrostatic bias (Maughan et al., 2016). Comparisons between the caustic technique and lensing measurements have been carried out by e.g. Geller et al. (2013), finding similar levels of agreement at the virial radius ($\sim$ 30%), consistent with the expected errors in the individual techniques.

## 1.4 Cluster scaling relations - 'mass proxies'

It is possible to derive an estimate for the total cluster mass without directly reconstructing it by one of more of the methods described in Section 1.3, via the use of cluster mass-observable relations (MORs). These relations rely on straightforward 'mass proxies,' which correlate tightly with mass, ideally with minimal scatter across the specified mass or redshift range. Some scaling relations can be predicted from cluster physics or fitted from empirical data. Mass-observable relations are an effective way to measure the total mass, but their reliability depends on the degree of scatter and bias, as well as survey completeness. Scaling relations which arise from theory assume a self-similar model for galaxy clusters, which we describe below, before discussing the most relevant scaling relations for this thesis.

### 1.4.1 Self-similarity

The self-similar model for galaxy clusters was first proposed in Kaiser (1986), and makes three key assumptions: *i)* initial density fluctuations in an Einstein-de Sitter universe ($\Omega_m = 1$) are scale-free, therefore galaxy clusters can form from the gravitational collapse of dark matter halos at any mass and length scale, *ii)* the amplitude of those fluctuations (on different mass and length scales) decrease according to a power law in redshift *iii)* Clusters contain only two components: collisionless matter (including galaxies and dark matter), and adiabatic gas (i.e. the ICM is governed only by gravitational processes).

Using these simplifying assumptions, we can predict simple power law relationships between the different properties of galaxy clusters. In the relations below, the cluster properties such as mass, radius, and temperature are valid for any chosen overdensity $_{\Delta}$.

### 1.4.2 The mass-temperature relation

For a gas in equilibrium, we write the average kinetic energy per particle of a monatomic gas with temperature $T$ as

$$\langle K_i \rangle = \frac{3}{2} kT \tag{1.44}$$

which, for $N$ particles can be written

$$K \propto N \langle K_i \rangle \propto M_{gas} kT \tag{1.45}$$

Under assumptions of self-similarity, $M_{gas}$ should trace the overall cluster mass $M$, hence

$$K \propto M_{gas} kT \propto MkT \tag{1.46}$$

We then use the cluster potential energy in Equation 1.25 with the virial theorem once more to obtain

$$MkT \propto \frac{M^2}{R} \tag{1.47}$$

Assuming spherical symmetry, we can rewrite the total mass in terms of its radius $R$ and mean density $\rho$, to obtain

$$R \propto M^{1/3}\rho^{-1/3} \tag{1.48}$$

Substituting Equation 1.48 into Equation 1.47 and rearranging, we obtain

$$M \propto (kT)^{3/2}\rho^{-1/2} \tag{1.49}$$

Finally, recalling the critical density (Equation 1.9) and the Hubble evolution parameter (Equation 1.7), we find that $\rho \propto E(z)^2$ and therefore

$$M \propto T^{3/2}E(z)^{-1} \tag{1.50}$$

The mass-temperature relation implies that clusters of the same mass are hotter at higher redshift, since the evolution parameter $E(z) \propto z$. Additionally, within a sufficiently small redshift range, the hottest clusters also have the highest mass. Measurements of the $M-T$ scaling relation from e.g. Arnaud et al. (2005) and Lieu et al. (2016) (see Figure 1.6) have found that fitting a relation $M \propto T^b$ for clusters across a range of density constrasts ($\Delta = 2500, 1000, 500, 200$) results in values for the slope $b \sim 1.5$, which is consistent with self-similar predictions. However, Arnaud et al. (2005) find the normalisation of the relation is discrepant by $\sim 30\%$ with the prediction from purely gravitation based models. This implies there are some non-gravitational processes such as galaxy feedback and cooling which can produce offsets in the observed scaling relation.

### 1.4.3 The luminosity-mass relation

To derive the relationship between X-ray luminosity and cluster mass, we first recall the expression for the bolometric X-ray luminosity in Equation 1.23. We assume, under self-similarity, that $n_e$, $n_i \propto \rho$, therefore

$$L_X \propto \rho^2(kT)^{1/2}R^3 \tag{1.51}$$

We replace the radius $R$ in terms of $M$ and $\rho$ using Equation 1.48 to get

$$L_X \propto \rho(kT)^{1/2}M \tag{1.52}$$

Replacing $\rho$ in terms of $E(z)$, we find

$$L_X \propto E(z)^2(kT)^{1/2}M \tag{1.53}$$

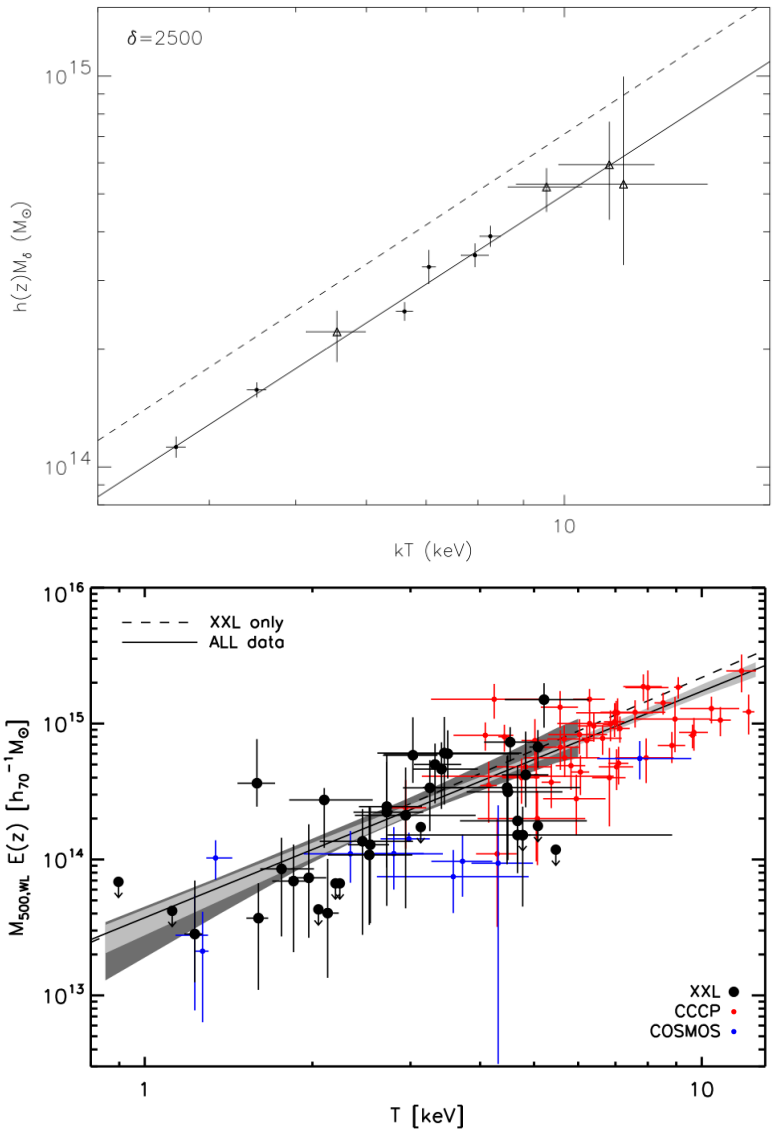


Figure 1.6: Measurements of the $M-T$ relation in galaxy cluster samples. Top: $M-T$ relation from Arnaud et al. (2005), showing 6 relaxed clusters observed by *XMM-Newton*. The black dashed line shows the self-similar prediction. Bottom: $M-T$ relation from Lieu et al. (2016), showing 96 clusters from the XXL, CCCP and COSMOS samples with corresponding best fit lines for all and XXL-selected clusters.

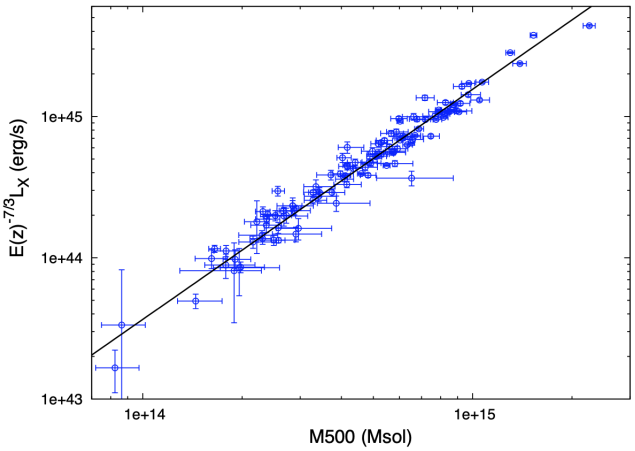


Figure 1.7: Example of a $L - M$ relation from Maughan (2007) with masses estimated from the $Y_{\rm X}M_{500}$ relation and bolometric luminosities measured from spectral fits in the $(0.15 < r < 1)R_{500}$ aperture, and scaled by the predicted self-similar evolution.

Finally, substituting the expression for $T$ from Equation 1.50, we obtain

$$L_X \propto E(z)^{4/3} M^{4/3} \tag{1.54}$$

The luminosity-mass relationship states that clusters of the same mass are correspondingly more luminous at higher redshift, and for two clusters at the same redshift, the more luminous cluster will also have the highest mass. Examples of measurements of the luminosity-mass relation can be found in Reiprich and Böhringer (2002), Maughan et al. (2006), Maughan (2007) and Stanek et al. (2006). An example of a measured relation can be seen in Figure 1.7. The luminosity-mass relation is an easily obtainable scaling relation because it requires only a few tens of counts to be measured. Unfortunately, it also shows the largest scatter among the scaling relations derived using a sample of galaxy clusters (Lovisari et al., 2015), due to the impact of central excess emission, that is, the surface brightness in the centre of the cluster exceeding the single $\beta$-profile model (Reiprich and Böhringer, 2002). Some have argued the scatter can be reduced by using the core-excluded luminosity as a mass proxy (Mantz et al., 2018).

### 1.4.4 The luminosity-temperature relation

We can finally infer the relationship between the X-ray luminosity and temperature by combining Equations 1.50 and 1.54 to find

$$L_X \propto E(z) T^2 \tag{1.55}$$

The luminosity-temperature relation is the longest studied and arguably the most robust X-ray scaling relation (see Edge and Stewart, 1991; Arnaud and Evrard, 1999; Maughan et al., 2006; Pratt et al., 2009; Hilton et al., 2012). However, many of these studies have noticeably found deviations from the self-similar prediction stated in Equation 1.55. Namely, a steeper slope has been observed in all, such that $L_X \propto T^{2-3}$. It is suggested that this discrepancy is due to an additional source of energy heating the ICM preferentially in low mass systems. This is likely due to either supernovae in cluster member galaxies or from the AGN in the centre of the cluster (Hilton et al., 2012).

### 1.4.5 The $Y_{\rm X}$-mass relation

The integrated Comptonisation parameter, $Y_{SZ}$ is proportional to the product of the gas mass and temperature. An X-ray analogue, $Y_X$ can similarly be defined using only X-ray observables (Kravtsov et al., 2006)

$$Y_{\rm X} = M_{gas} T_{\rm X}. \tag{1.56}$$

Substituting in Equation 1.50, we can recover a scaling relation, encompassing an overdensity $\Delta$ times the critical density at the cluster redshift, $\rho_c(z)$,

$$Y_\Delta \propto E(z)^{2/3} M^{5/3} \tag{1.57}$$

The parameter $Y_{\rm X}$ is considered a robust mass proxy due to low scatter and weak dependence on the physics of the ICM and cluster morphology (Arnaud et al., 2007).

### 1.4.6 Other relations

Examples of other relations, which are not theoretically motivated, include the K-band luminosity-mass relation, in which the K-band luminosity is seen as a good tracer of stellar mass (Ziparo et al., 2016). A probabalistic measurement of the overall stellar mass, $\mu_*$ is also an effective proxy for cluster mass (Palmese et al., 2020). Another relation used extensively in this thesis is the optical-richness-mass relation. This is well-motivated based on the assumption that the number of galaxies traces the underlying cluster potential, i.e. the clusters with the most member galaxies also have the largest overall mass. This relation has been measured for various optically selected cluster samples (e.g. Rozo and Rykoff, 2014; Simet et al., 2016; Chiu et al., 2019). The richness is considered a fairly low-scatter mass proxy (Rykoff et al., 2012). Nevertheless, it is possible to calibrate the scatter in the mass-richness relation by checking its agreement with other observable properties such as

the X-ray luminosity and temperature (e.g. Hollowood et al., 2019; Farahi et al., 2019). The calibration of richness scaling relations using X-ray observables is discussed in Chapter 4.

### 1.4.7 Deviations from self-similarity

Deviations from self-similarity in cluster scaling relations are attributed to non-gravitational processes which take place in the central region or core of the cluster. Typically, this is due to baryonic physics such as stellar feedback, AGN feedback and cooling (McDonald et al., 2017). Clusters with cool cores deviate from self-similar predictions and are described by a cooling flow model (Fabian, 1994), detailed below.

Plasma in regions of the cluster, with a cooling time shorter than the age of the system, should be cooling due to strong X-ray radiation where emission is proportional to the density $(n_e, n_i)$ squared. Since the density of the ICM is highest towards the center of the cluster, the radiative cooling time drops a significant amount farther from the centre. As a result, the central cooled gas can no longer support the weight of the external hot gas, and contracts. The resulting pressure gradient between the cold and hot gas drives what is known as a cooling flow, where the hot gas from the external regions flows slowly towards the center of the cluster BCG. However, star formation rates in the central galaxies within clusters have consistently been lower than expected (Johnstone et al., 1987), leading to what is known as the 'cooling flow problem.' Later work by Peterson et al. (2003) has shown there is little evidence of cool X-ray emitting gas in clusters, thereby resolving the observed deficit of star-forming BCGs.

Disturbed or merging clusters also deviate from self-similar predictions, due to the fact they are not exclusively dominated by gravitational processes.

While there is no clear distinguishing feature between a cool-core (CC) and non cool-core (NCC) cluster, there are a number of ways to quantify the difference such as a sharp drop in the temperature at the centre of the cluster, and a corresponding "peaked" brightness in the central region (e.g. Rossetti and Molendi, 2010), as shown in Figure 1.8. In order to use scaling relations for cosmological studies, it is important to quantify the fraction and impact of CC clusters in samples to ensure minimal scatter and bias in cluster mass determinations.

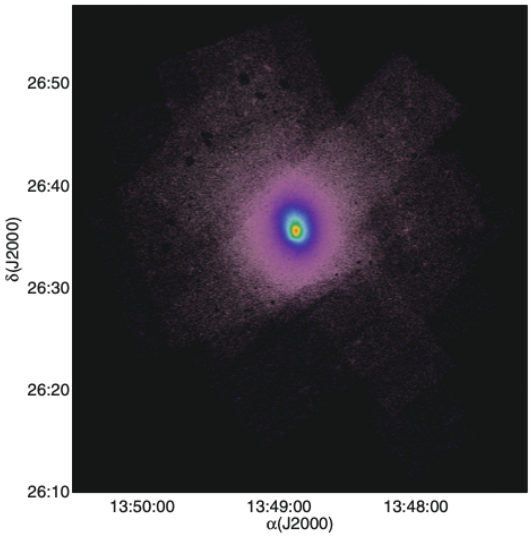


Figure 1.8: Figure from Hudson et al. (2010) showing an example of a background subtracted, exposure corrected mosaic image created from the 12 Chandra exposures of strongly cool-cored cluster A1795. A sharply peaked bright central region is visible in the cluster.

## 1.5 Cosmology with clusters

Now we have described various methods to determine the cluster mass, it is possible to use clusters for cosmological studies. The cosmological constraining power of clusters arises from two measurements – the baryon fraction $f_b$, and the cluster mass function.

### 1.5.1 Baryon fraction

Assuming that galaxy clusters are large enough to enclose a representative volume of the universe, the ratio of baryonic mass to total cluster mass is expected to match the cosmic baryon fraction.

$$f_b = \frac{M_b}{M_{tot}} = \frac{\Omega_b}{\Omega_M} \tag{1.58}$$

Knowing that the baryon content of clusters can be described by a gas and stellar component, Equation 1.58 can be written as

$$f_b = \frac{M_b}{M_{tot}} = \frac{M_{gas} + M_{stars}}{M_{tot}} \tag{1.59}$$

First measurements of the baryon fraction found a value of $f_b \sim 0.1$ (White et al., 1993), which provided early evidence that $\Omega_M$ was considerably less than 1 and therefore an Einstein-de Sitter cosmology was incorrect. Another assumption about the baryon fraction is that it is expected to be the same at all redshifts, since after cluster formation, all clusters can be treated as representative "standard buckets" for the universal baryon

fraction. Therefore, $f_b$ depends only on the distance to the cluster, which is sensitive to the underlying cosmology via $E(z)$. To determine the distance to the cluster, we consider a cluster with an angular size on the sky defined by $\theta$. We can find the proper radius of the cluster via

$$R = \theta d_A \tag{1.60}$$

The proper volume of the cluster is then,

$$V = \frac{4}{3}\pi(\theta d_A)^3 \tag{1.61}$$

We can then rewrite $M_{gas}$ as a product of density and volume, using Equation 1.61,

$$M_{gas} \propto \rho_{gas}(\theta d_A)^3 \tag{1.62}$$

Recalling Equation 1.23, we note that the gas density is related to the X-ray luminosity, which, in turn, is related to the observed flux via Equation 1.12. Therefore we can write the gas density in the following terms,

$$\rho_{gas} \propto (L/V)^{1/2} \tag{1.63}$$

which, using Equations 1.61 and 1.12, we obtain

$$\rho_{gas} \propto \left(\frac{F d_L^2}{\theta^3 d_A^3}\right)^{1/2} \tag{1.64}$$

which, rewritten in terms of $M_{gas}$ from Equation 1.62, becomes,

$$M_{gas} \propto d_L d_A^{3/2} \tag{1.65}$$

When evaluating the total cluster mass $M_{tot}$, we can use the fact that $M_{tot} \propto d_A$ via the cluster radius, so the estimated value of $f_b$ scales with distance according to

$$f_b = \frac{M_{gas}}{M_{tot}} \propto d_L d_A^{1/2} \tag{1.66}$$

Hence, cosmology via the baryon fraction measurement requires knowledge of $d_A, d_L$ to the cluster redshift $z$. However, if we know the predicted value of $f_b$ from theory, we can infer values of $d_A, d_L$ and see how well it fits the observed data for a given underlying cosmology (Allen et al., 2002, 2008). The resulting constraints for the $f_b$ test are comparable to those from independent probes such as the CMB and type-Ia supernovae (see Figure 1.9).

Some caveats to note for this cosmological application is that the value of $M_{tot}$ might be unreliable due to assumptions such as hydrostatic equilibrium. The baryon fraction is

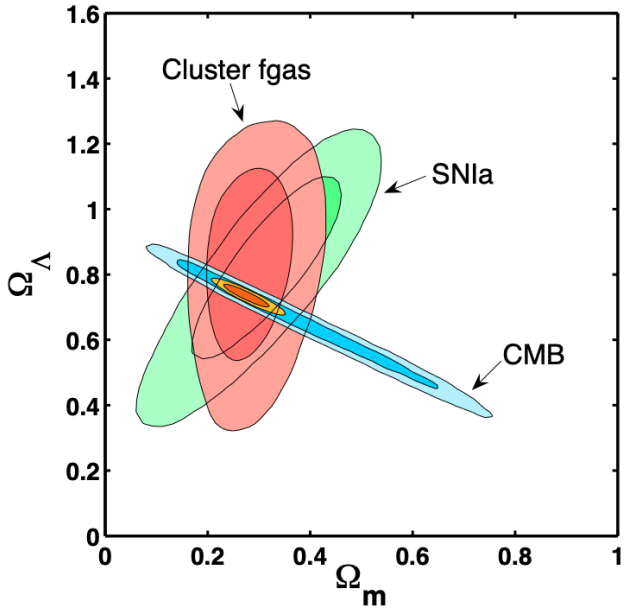


Figure 1.9: Constraints on parameters $\Omega_M$ and $\Omega_\Lambda$ from the cluster baryon fraction measurement from Allen et al. (2008). The best fit cosmological values are $\Omega_M \simeq 0.27$, $\Omega_\Lambda \simeq 0.86$ with $1\sigma$ and $2\sigma$ confidence regions shown. The CMB and type-Ia supernovae constraints are shown in blue and green, respectively.

therefore most reliable when used on a sample of large, relaxed clusters. The value of the baryon fraction might also not be constant if evaluated at smaller radii (e.g. $R_{2500}$) due to the 'missing baryon problem' thereby deviating from the assumption that the baryonic mass in clusters is representative of the universal baryon fraction (e.g. Ettori, 2003).

### 1.5.2 Cluster mass function

Clusters arise from the gravitational collapse of rare high peaks of primordial density perturbations in the early universe (Peebles, 1993). Because they probe the high end of the cosmic density field, the observed abundance of galaxy clusters is sensitive to particular cosmological scenarios (Press and Schechter, 1974). The evolution of galaxy clusters is driven by the growth rate of density fluctuations, which essentially depends on the value of the matter density parameter $\Omega_M$ and $\sigma_8$ (see Oukbir and Blanchard, 1992, 1997; Eke et al., 1998). Depending on a whether the universe has a high or low density, the cluster population evolves differently, with each case producing a distinct spatial distribution of clusters as a function of mass and redshift in a comoving volume. This is known as the cluster mass function. Various cosmological models are able to predict the number density, which allow for the determination of the best-fit cosmology based on the agreement of the

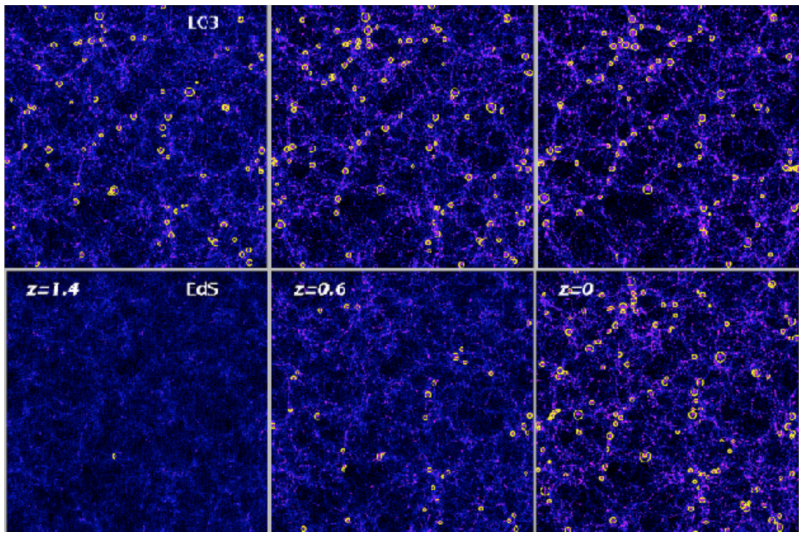


Figure 1.10: N-body simulation from Borgani and Guzzo (2001) illustrating cluster evolution in two cosmological models. The top panel shows a dark matter distribution in a flat, low density model with $\Omega_M = 0.3$. The bottom panel describes an Einstein-de-Sitter case with $\Omega_M = 1$. Each panel consists of three redshift snapshots. The yellow circles mark the positions of galaxy clusters selected based on their predicted X-ray properties.

model with the data.

The mass function for different cosmologies can be derived analytically, however they are most commonly measured from large volume, N-body simulations (see Figure 1.10). Note that the late time structure is a poor discriminator for the two different cosmologies (right panels in Figure 1.10), and thus requires the leverage of redshift evolution to illustrate the growth of clusters over time.

To measure the mass function observationally, three steps are required. Firstly, cluster surveys are required to detect and count galaxy clusters. Next, the survey selection function determines the volume in which clusters have been detected and counted. Finally, the masses of clusters in a given volume must be calculated, typically through use of scaling relations discussed in Section 1.4.

As discussed in Section 1.2, various multi-wavelength signatures for clusters have facilitated their detection. Among these are red sequence based cluster surveys, SZ surveys and X-ray surveys. Each of these detection methods have their benefits and caveats, which are folded into the selection function of the chosen survey. A key property of each survey is the limit at which it can no longer detect clusters, known as the detection limit. To determine the survey volume, we start with the survey area, defined by the solid angle $\Omega$ on the sky, in which we expect to detect $n$ clusters in some mass bin $(M \pm \Delta M)$.

The comoving volume element can be written as a product of the comoving area element multiplied by a redshift range according to

$$dV_\chi(z) = \frac{c}{a_0 H_0} \frac{(1+z)^2 d_A^2}{E(z) d\Omega dz} \tag{1.67}$$

This volume be integrated over the solid angle and redshift range of the survey to determine the full survey volume. The redshift range is defined between $z = 0$ and $z_{max}$, at which the detectability of a cluster drops below the survey limit. Non-trivially, the value of $z_{max}$ also depends on the mass of the cluster considered since more massive (e.g. X-ray bright or optically rich) clusters are detectable to higher redshifts. Therefore, the redshift limit can be seen as a function of the cluster mass, $z_{max}(M)$. The survey area $\Omega$ is also dependent on the cluster mass, due to its dependence on source flux. To estimate the total survey volume or the 'selection function,' the volume element is integrated

$$V(M) \sim \int_0^{z_{max}(M)} \Omega(M, z) dz \tag{1.68}$$

From Equation 1.68, it is clear that the survey volume scales with the mass of detected clusters. In other words, large survey volumes correspond to massive clusters, which are brighter and easier to detect. For example, in X-ray surveys, the computed value of $V(M)$ arises from the luminosity-mass relation (see Equation 1.54), since the flux limit of the survey corresponds to some mass on that relation.

Examples of measurements of the cluster mass function can be found in Reiprich and Böhringer (2002) and Vikhlinin et al. (2009). Figure 1.11 shows two illustrations of a measured cluster mass function, fitted to two underlying cosmologies. The cluster sample is also split into two redshift ranges ($0.025 < z < 0.25$ and $0.55 < z < 0.9$). It is clear that the cosmological model on the left-hand side is a better fit to the data, thereby ruling out an Einstein-de Sitter model. Another key point is that the both the theoretical and observed cluster mass function are redshift-sensitive, as shown by the fact that the blue and black lines (high and low redshift, respectively) scale differently as a function of cluster mass. Although this is a powerful measurement, it is subject to numerous systematics. The dominant source of error in mass function estimates arises from the choice of mass-observable relation used by a given survey, which has some quantifiable scatter.

Using the earlier example of an X-ray survey, the selection of clusters based on the luminosity-mass scaling relation may not reflect the 'true' population of clusters, as clusters with an anomalously high flux for their chosen mass may be over-represented. This is known as Eddington bias, described in Figure 1.12). This bias can be minimised with improved knowledge of the scatter in the luminosity-mass (or indeed any mass-observable)

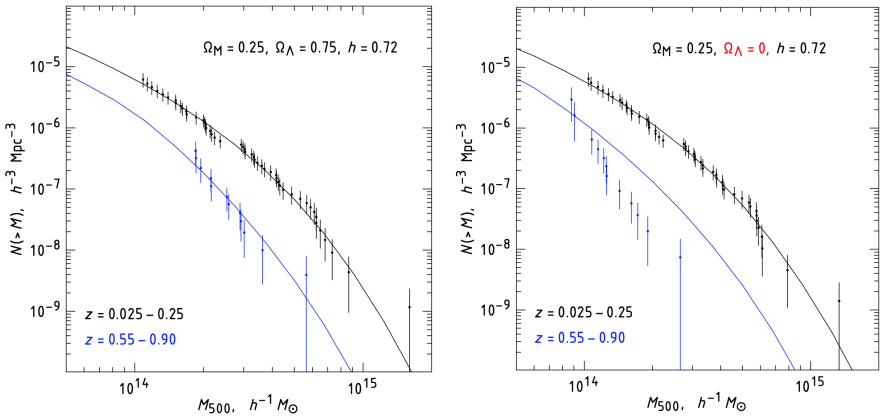


Figure 1.11: Illustration of sensitivity of the cluster mass function to the cosmological model from Vikhlinin et al. (2009). The left panel shows the measured number density and in a low (black line) and high (blue line) redshift ranges computed for a low density cosmological model. The right panel shows both the data and the model for a cosmology with no dark energy.

relation, and has been implemented in various studies. The motivation for Chapter 4 is to produce precise stacked weak lensing mass estimates for a sample of clusters, which can be used to measure a cluster mass function and relevant cosmological parameters.

## 1.6 Thesis Overview

The thesis is presented as follows. In Chapter 2, we introduce the *XMM* Cluster Survey (XCS) and redMaPPer (RM) cluster catalogues from which X-ray and optical information is obtained. A description of the cluster finding methodology using both XCS and RM is presented, followed by the matching process and measurement of key X-ray properties. In Chapter 3, we investigate the use of an X-ray and optically selected sample of galaxy clusters as an indirect probe of a novel dark matter candidate. Given that this topic is fairly recent in cluster studies – in addition to covering both topics in X-ray astrophysics and particle physics – we have enclosed a specialised introduction for this chapter. In Chapter 4, we revert to a more traditional application of galaxy clusters by using the samples constructed in Chapter 2 to model the impact of cluster miscentering by the RM cluster finder using publicly available X-ray data. This systematic effect is known to bias richness measurements and possibly drive offsets in cluster mass estimates and cosmological parameters in optical datasets. We present our conclusions in Chapter 5.

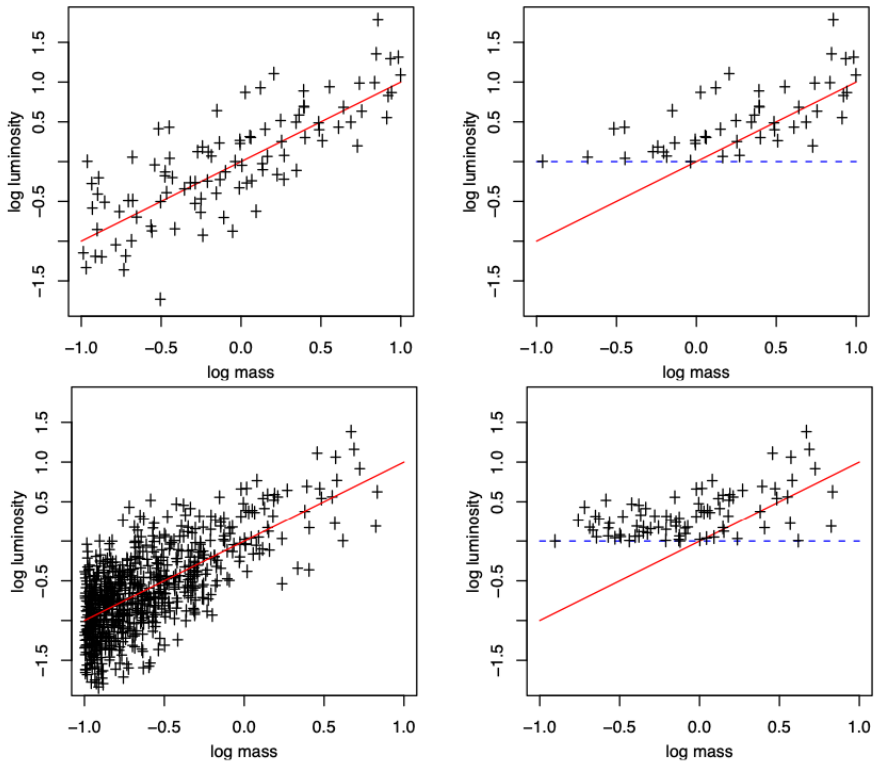


Figure 1.12: Figure and caption taken from Mantz et al. (2010). Illustration of Malmquist and Eddington biases in fictitious luminosity-mass relations (red lines), with simulated data (crosses). In the top panels, clusters are distributed uniformly in log-mass, whereas in the bottom panels the distribution of log-masses is exponential. The left-hand panels reflect the true distribution of all clusters in mass and luminosity, while the right-hand panels show only the simulated clusters with luminosities greater than a threshold value, indicated by the dashed, blue lines. The figure illustrates that both the sample selection function and the underlying mass function must be taken into account when fitting the scaling relations.

# Chapter 2

# Construction of redMaPPer cluster samples using archival *XMM-Newton* observations

In this Chapter, we detail the construction of a catalogue consisting of cross-matched clusters detected from the 8th data release of the Sloan Digital Sky Survey (hereafter SDSS DR8) and the *XMM* Cluster Survey (hereafter XCS). We begin with a review of salient X-ray and optical surveys used within this thesis, followed by a detailed description of the XCS methodology and redMaPPer cluster finding algorithm (Rykoff et al., 2014). The XCS methodology is derived from the work presented in Lloyd-Davies et al. (2011), with more recent incremental updates detailed in Section 2.3.1 and 2.6. The most up-to-date version of the XCS pipeline is described in Giles et al. (in prep). The redMaPPer analysis on the photometric datasets has been run externally; we only use the data products for the samples. Next. the matching procedure between X-ray and optical data is described. An X-ray analysis is performed on all confirmed clusters in the SDSS footprint for use in Chapter 3. We go on to develop two additional samples which consist of clusters detected in the Year 1 and Year 3 (hereafter Y1 and Y3) footprints of the Dark Energy Survey (hereafter DES). All three samples are used in Chapter 4. All three samples constitute original work produced in collaboration with P. A. Giles (on the X-ray analysis and measurements), and R. Wilkinson, C. Vergara-Cervantes and D. Turner (on the visual inspection of cluster candidates). For brevity, throughout the rest of the thesis, we will denote the X-ray and redMaPPer SDSS sample as XCS-SDSS, and the X-ray and redMaPPer DES Y1 and Y3 samples as XCS-DESY1 and XCS-DESY3, respectively.

## 2.1 X-ray surveys

All X-ray observations in this thesis have been performed using the *XMM-Newton* space observatory (described in Section 2.1.1). Where stated, ancillary X-ray observations relevant for Chapters 3 and 4 were performed by the *Chandra* X-ray observatory (Section 2.1.2). We also provide brief descriptions of other prescient X-ray telescopes for historical context, and describe key cluster catalogues derived from these surveys where applicable.

### 2.1.1 *XMM-Newton*

The X-ray Multi Mirror (XMM) Newton Observatory was launched by the European Space Agency (ESA) in 1999. While it was nominally scheduled for a two-year mission, the spacecraft has continued for almost 19 years beyond its expected lifetime, with the goal of investigating X-ray sources, performing narrow and broad range spectroscopy, as well as the first simultaneous imaging of objects in both X-ray and UV wavelengths. *XMM-Newton* sits at an inclination of 40° with a highly eccentric 48-hour elliptical orbit around the Earth. Since the Earth's atmosphere absorbs the vast majority of X-rays, they are not detectable from Earth-based telescopes; therefore space-based telescopes are required to make these observations. This orbit was chosen for two main reasons - to avoid the radiation belts surrounding the Earth, which can damage the instruments and generate false readings, and to allow for longest possible observation periods. It has three main scientific instruments - the European Photon Imaging Camera (EPIC), the Reflection Grating Spectrometer (RGS) and the Optical Monitor (OM). The EPIC instrument is of primary importance for *XMM-Newton* observations. The EPIC cameras offer the possibility to perform sensitive imaging observations over the telescope's roughly circular field of view (FOV) of 30 arcmin in diameter, in the energy range from 0.15 to 15 keV with moderate spectral ($\sim$ 80 eV) and angular resolution (PSF of 6 arcsec FWHM). It is actually a composite of three cameras in one, which use three different detectors to resolve X-ray emission. The detectors, are termed "charge-coupled devices" or CCDS for short. Two of the detectors are metal oxide semiconductors and hence referred to as 'MOS1' and 'MOS2.' The other is called the PN detector. Benefits of the detectors vary according to their properties. Notably, the time resolution of the PN detector is considerably better than the MOS, however the MOS detectors have higher spatial resolution and can distinguish smaller X-ray objects. The resolution of both cameras is nevertheless limited by the PSF. The PN camera is considerably more sensitive than the MOS over the 0.1 to 10 keV energy range, allowing it to detect fainter objects (see Turner et al., 2001; Strüder et al.,

| Camera | FOV | Effective area (at 1 keV) | Time resolution | Spatial resolution (1 pixel) |
|---|---|---|---|---|
| EPIC PN | $27.5' \times 27.5'$ | 1227 $cm^2$ | 73.4 ms | $4.1'$ |
| EPIC MOS | $33' \times 33'$ | 922 $cm^2$ | 2.6 s | $1.1'$ |

Table 2.1: Comparison of key properties of the PN and MOS CCDs.

2001, for reviews). This is due to its large effective area, which determines the ability of the mirrors to collect radiation at different photon energies. A table of key properties of both the PN and MOS detectors is displayed in Table 2.1.

In addition to the *XMM* Cluster Survey (described below), numerous other surveys have exploited the *XMM* public archive for cluster studies. Many of these surveys are have been motivated by the detection of clusters in previously unexplored areas of the mass-redshift plane. Examples include (XCLASS, Clerc et al., 2012) and (2XMMi/SDSS, Takey et al., 2011). There are additional *X*MM survey volumes built to overlap with wide-area surveys such as COSMOS (Finoguenov et al., 2007), or ones with contiguous areas to obtain cosmological parameter estimates (XMM-LSS, XXL, Pierre et al., 2004; Pierre et al., 2016).

### 2.1.2 *Chandra*

Launched by NASA in July 1999 (only a few months before *XMM-Newton*), the *Chandra* X-ray Observatory (CXO) is another pivotal X-ray instrument used for a variety of studies. Chandra is sensitive to X-ray sources 100 times fainter than any previous X-ray telescope, enabled by the high angular resolution of its mirrors (0.5 arcseconds), which are superior to *XMM-Newton* (6 arcseconds). The Science Instrument Module (SIM) holds the two focal plane instruments, the Advanced CCD Imaging Spectrometer (ACIS) and the High Resolution Camera (HRC), moving whichever is called for into position during an observation. The ACIS instrument is principally used in the *Chandra* analysis of X-ray clusters, making it analogous to the EPIC instrument for *XMM-Newton*. Overlapping X-ray observations from both *Chandra* and *XMM-Newton* can be used to independently measure X-ray properties for clusters, as well as determining instrumental differences between both surveys. Examples of Chandra catalogues include the Chandra Cluster Cosmology Project (CCCP, Vikhlinin et al., 2009), in which a sample of *Chandra* observations of clusters originally detected by ROSAT are used for cosmological studies.

### 2.1.3 The *Einstein* Observatory

The Einstein Observatory, launched into orbit in 1978, was the first NASA X-ray imaging telescope designed to observe objects outside of our solar system. Its 40 arcsecond angular resolution, field-of-view of tens of arcminutes, and a sensitivity several 100 times greater than any mission before it enabled the capability to image extended objects, diffuse emission, and detect faint sources. The Einstein-Observatory Extended Medium Sensitivity Survey (EMSS) was the first to demonstrate the ability to serendipitously detect clusters in large numbers in X-ray surveys. A total of 93 clusters were found in 778 square degrees of sky, and EMSS made a preliminary detection of evolution in the X-ray properties of clusters (Gioia et al., 1990).

### 2.1.4 ROSAT

ROSAT, the ROentgen SATellite, was an all-sky X-ray observatory launched by the United States on June 1st, 1990, operating until February 1999. The ROSAT imager had a 38 arcminute sq. FOV with 2 arcsecond spatial resolution. Though sensitive in a narrow energy range (0.1-2.5 keV), the satellite was used extensively in the creation of X-ray cluster catalogues. Catalogues have included the MAssive Cluster Survey (MACS, Ebeling et al., 2000a), which aimed to compile a sample of more than 200 X-ray luminous clusters at $z > 0.3$. Another catalogue was created using the ROSAT-ESO Flux Limited X-ray (REFLEX, Böhringer et al., 2004) catalogue, consisting of 447 galaxy clusters. Others include 400d (Burenin et al., 2007), the ROSAT Brightest Cluster Survey (BCS, Ebeling et al., 1997), the Bright Serendipitous High-redshift Archival ROSAT Galaxy Cluster Survey (Bright SHARC, Romer et al., 2000) and the SPIDERS catalogue (Clerc et al., 2016). More recently, the MARD-Y catalogue has assembled between 1086 and 2171 galaxy clusters (52% and 65% new) produced using multi-component matched filter (MCMF) follow-up with the full 5000 deg$^2$ of DESY3 optical data and $\sim$ 20000 overlapping 2RXS X-ray sources (Klein et al., 2019).

### 2.1.5 *Hitomi*

The *Hitomi* X-ray astronomy satellite (Takahashi et al., 2018) was commissioned by the Japan Aerospace Exploration Agency (JAXA) for studying extremely energetic processes in the Universe. The spacecraft was launched on 17 February 2016 and contact was lost on 26 March 2016, due to multiple incidents with the attitude control system leading to an uncontrolled spin rate and breakup of structurally weak elements. During its short dura-

tion, it nevertheless contributed significantly to the field of X-ray astronomy. The Perseus cluster was the first-light target for *Hitomi*, observed with the Soft X-ray Spectrometer (SXS). The SXS was an array of 35 calorimeter pixels - a device used to detect X-rays by converting the absorbed energy from an X-ray photon into heat. *Hitomi* had a spectral resolution of 4.9 eV FWHM, with its Soft X-ray Telescope (SXT) covering a $3' \times 3'$ FOV. Among its key advances was taking a 275 ks exposure of the Perseus cluster, during which it measured the highest resolution spectrum available for this system (Aharonian et al., 2018). This has since been a cornerstone in interpreting the elusive '3.5 keV line' which forms the motivation of Chapter 3.

## 2.2 Optical surveys

Optical observations used in this thesis were performed using two ground-based surveys, SDSS and DES (Sections 2.2.1 and 2.2.2).

### 2.2.1 Sloan Digital Sky Survey

The Sloan Digital Sky Survey is a major imaging and spectroscopic redshift survey which operates using the wide-angle 2.5m optical telescope at Apache Point Observatory in New Mexico, United States. The telescope uses a multiband large format mosaic CCD camera to image the sky in five optical bands $(u, g, r, i, z)$, though not simultaneously as each filter is separated by 71.72 seconds of drift scan time. The filter curves for SDSS are shown in Figure 2.1. SDSS also has two digital spectrographs to obtain the spectra of about 1 million galaxies and 100,000 quasars (York et al., 2000). The imaging survey covers approximately 10,000 contiguous square degrees (sq. deg) in the Northern Galactic Cap. In addition, there is an equatorial stripe known as Stripe 82 in the Southern Galactic Cap, which has been observed repeatedly. This is both to find variable objects and, when co-added, to reach a magnitude limit which is considerably lower than the Northern imaging survey. This region is also important as it is the one area of overlap between DES and SDSS (see Figure 2.18), and hence can be used to calibrate optical properties between surveys. Since operations started in 2000, there have been sixteen public data releases (Abazajian et al., 2003; Ahumada et al., 2019), all of which are cumulative (i.e. each data release includes essentially all data from the previous releases).

The SDSS DR8 data release (Aihara et al., 2011) is used extensively throughout this thesis. The coverage of DR8 is increased by 2500 deg$^2$ with respect to DR7, covering a total area of 14,555 deg$^2$. The DR8 coverage is shown in Figure 2.2

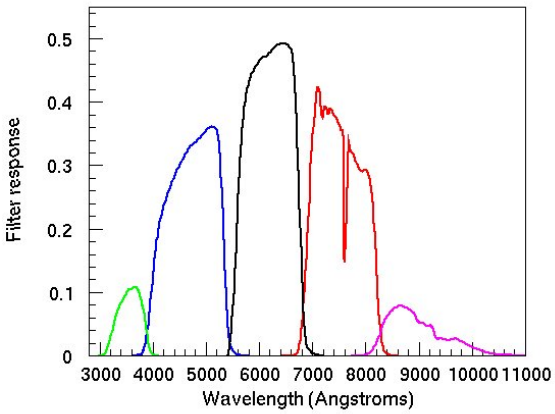


Figure 2.1: The response curves for each of SDSS's five optical bands, showing the throughput defining the survey's photometric system, which includes extinction through an airmass of 1.3 at Apache Point Observatory.

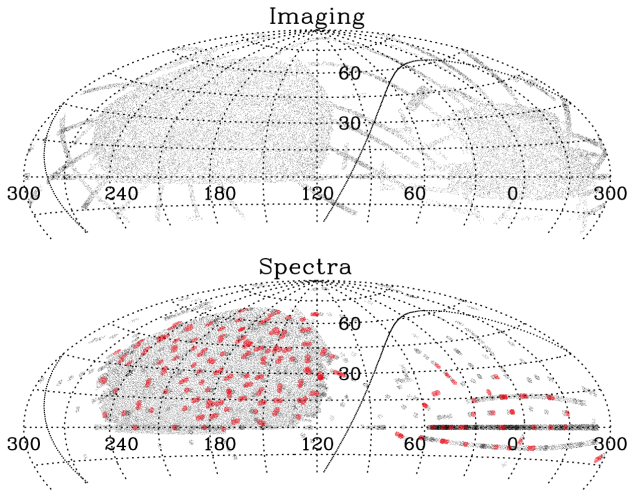


Figure 2.2: Figure from Aihara et al. (2011). The sky coverage of DR8 in J2000 Equatorial coordinates, showing the imaging (upper) and spectroscopy (lower) footprints. The coverage is centred on a RA=120°, with the Galactic plane shown by the solid curve. The red regions in the spectroscopy footprint designate the coverage of the SEGUE-2 plates, providing spectroscopy of approximately 118,000 stars at both high and low Galactic latitudes.

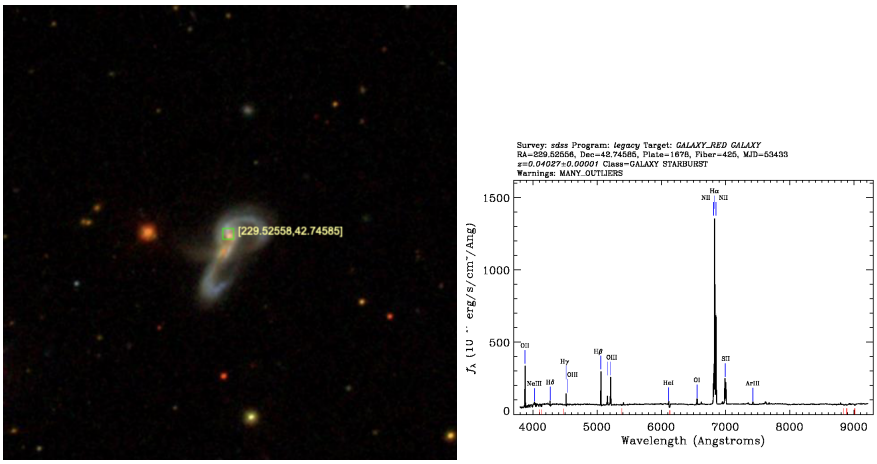


Figure 2.3: Example of SDSS *ugriz* image (left) and spectrum (right) of galaxy SDSS J151806.13+424445.0, at $z = 0.04$. Image and spectrum obtained using `https://skyserver.sdss.org/dr16/`

Numerous dedicated surveys exist in the SDSS footprint, developed over the course of its various data releases. Such surveys aim to understand stellar evolution in our Milky Way (e.g. APOGEE, Prieto et al., 2008), measure the scale of baryon acoustic oscillations, (BOSS, Dawson et al., 2012), study galaxy evolution (MaNGA, Bundy et al., 2014). More recently, the SPIDERS survey has aimed to perform a homogeneous and complete spectroscopic follow-up of X-ray AGN and galaxy clusters using SDSS and X-ray data (Clerc et al., 2016).

### 2.2.2 Dark Energy Survey

The Dark Energy Survey is a 5000 deg$^2$ contiguous optical and near-infrared imaging survey scanning the southern sky. Its primary instrument, the Dark Energy Camera (DECam), is a 3 square degree mosaic camera mounted at the prime focus of the Blanco 4-metre telescope at the Cerro-Tololo Inter-American Observatory (CTIO) in Chile (Honscheid and DePoy, 2008). DECam has one of the widest fields of view (2.2 degrees in diameter) available for ground-based optical and infrared imaging surveys, with a resolution of 0.263″/pixel. DECam is optimized for the wavelength range, 400-1000 nm with four filters with nominal wavelength ranges: $g$ band (400-550 nm), $r$ band (560-710 nm), $i$ band (700-850 nm), and $z$ band (830-1000 nm). All DES images used in this thesis have been made using the *gri* bands.

The DES footprint was designed to have significant overlaps with the South Pole Telescope and Stripe 82 (in large part avoiding the Milky Way). It additionally has

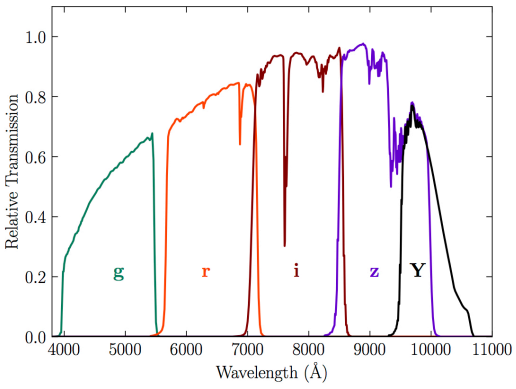


Figure 2.4: Standard bandpasses for DECam $g, r, i, z$ and $Y$ filters. The bandpasses represent the total system throughput, including atmospheric transmission (airmass = 1.2) and the average instrumental response across the science CCDs.

overlaps with other optical imaging surveys such as the Kilo-Degree Survey[1] (KiDS, de Jong et al., 2013) and Hyper Suprime-Cam[2] (HSC, Aihara et al., 2018). The survey took 758 observing nights spread over six years to complete, covering the survey footprint ten times in five photometric bands $(g, r, i, z, Y)$. DES officially began in August 2013 and completed its last observing night on 9th January 2019 (see Figure 2.5 for the DES footprint). The response of the individual band filters is displayed in Figure 2.4. An illustration of the multi-band imaging quality can be seen in Figure 2.6.

The survey's principal aim has been in constraining the dark energy equation-of-state parameter $w$, in addition to other cosmological parameters. The four key probes employed to achieve this goal have included galaxy clusters (Abbott et al., 2020). weak lensing and galaxy clustering (Abbott et al., 2018), cosmic shear (Troxel et al., 2018), and type Ia supernovae (Abbott et al., 2019). It nevertheless has various other applications, from searching for gravitational wave counterparts, Milky Way studies and searches for trans-Neptunian objects (see Dark Energy Survey Collaboration et al., 2016, for a review).

According to Dark Energy Survey Collaboration et al. (2016), "As of December 2015, the number of galaxies with confirmed photometric redshifts was 100M, and the number of galaxy clusters was 150K." At the time of writing, the number of confirmed galaxy clusters with photometric redshifts in the range $z \in [0.1, 0.95]$ is approximately 25,000 (E. Rykoff, private comms).

[1] http://kids.strw.leidenuniv.nl
[2] https://www.naoj.org/Projects/HSC/

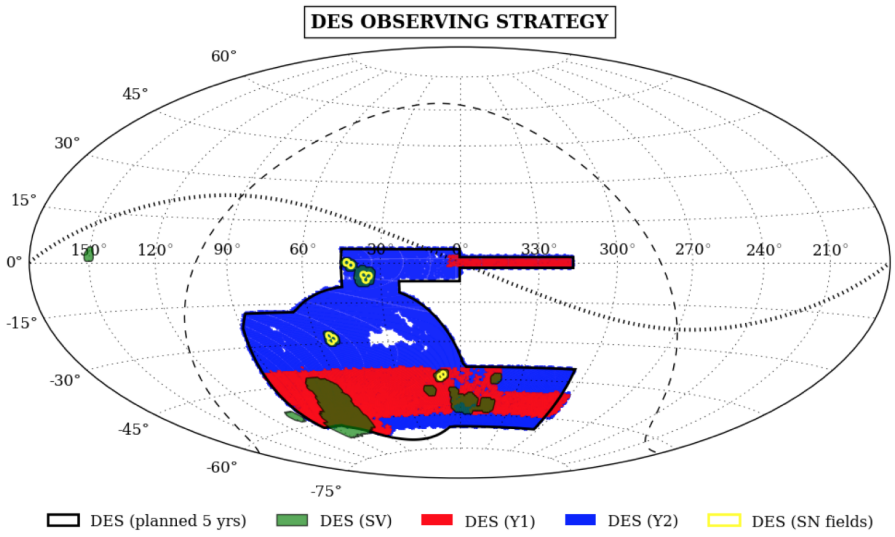


Figure 2.5: Figure from Dark Energy Survey Collaboration et al. (2016) showing a Hammer projection in equatorial coordinates, with the dashed and dotted lines indicating the Galactic plane and the ecliptic plane, respectively. The DES survey footprint for the Science Verification (SV), Year 1 (Y1), Year 2 (Y2) and the final 5-year survey. The 10 supernova fields which form approximately 27 deg$^2$ of the survey footprint are shown in yellow.

Figure 2.6: Example of a DES *gri* colour image of a spiral galaxy (NGC 300), showing distinct, diffuse star forming regions in the spiral arms. The multiband imaging highlights the stellar histories in the system, given by the different colours.

## 2.3 Data reduction

The processing of X-ray observations from *XMM-Newton* were handled via the *XMM* Cluster Survey's data reduction pipelines. The corresponding optical catalogues from SDSS, DES Y1 and DES Y3 were produced using the red sequence based cluster finder, redMaPPer. We describe the key steps in the X-ray data reduction pipeline, followed by the methodology used by the redMaPPer algorithm in the sections below.

### 2.3.1 The *XMM* Cluster Survey

The *XMM* Cluster Survey (hereafter XCS, Romer et al., 2001) aims to catalogue all clusters of galaxies that have been detected by the *XMM-Newton* satellite. This includes both clusters that have been specifically targeted by *XMM* and those detected serendipitously. The primary science goal of XCS is to constrain cosmological parameters using the evolution of abundance of clusters. Other goals include the determination of scaling relations, understanding astrophysical processes such as AGN variability, and studies of galaxy evolution. The first XCS data release (XCS-DR1) was made in 2012 (Mehrtens et al., 2012), and included 503 optically confirmed clusters, of which 402 had reliable X-ray temperature measurements. Details of the X-ray analysis on this sample were published in a companion paper, Lloyd-Davies et al. (2011).

Since then, many improvements have been made to both the XCS data reduction pipelines and in the creation of new cluster samples, largely by Rooney (2016), Bermeo (2017), Mayers (2017) and Vergara-Cervantes (2019). We outline the main steps involved in reducing and processing the XCS data below.

#### Cleaned events lists

Each *XMM* observation has its own ObsID, a unique ten-digit identification number. Each raw observation contains information such as the pointing location, timing, camera mode and record of all detected events. The *XMM* data reduction from XCS begins with the *XMM* observation data files (ODFs), where there is exactly one ODF per observation. Constructing *XMM* images from ODFs requires the use of an Interactive Data Language (IDL) based pipeline called Xip (XCS Events List Cleaning and Image Making Pipeline). The Xip creates calibration files for each of the ODFs. These are subsequently combined to create a 'cleaned events list.' There are two key aspects to note when producing the cleaned events list. Firstly, since *XMM* does not have a shutter, the CCDs are taking data all the time, even while data is being read out. So if an 'out-of-time' photon arrives

at the detector during the readout period, it will be assigned to an incorrect position and energy. The PN detector is impacted most significantly by this. An out-of-time events list is thus created for the PN detector and then subtracted from the cleaned PN events list. Secondly, the impact of flaring needs to be taken into account. This is caused by high energy particles funnelled towards the detectors by the X-ray mirrors. The effect from these events is mitigated by producing light curves in 50 second time bins in a high ($\sim 10-15$ keV) and soft ($\sim 0.1-1$ keV) energy band. The high energy band accounts for the quiescent particle background (QPB), while the soft band accounts for the aforementioned flaring. Each of these light curves have a mean and standard deviation. These light curves are clipped by removing time bins where the count rate is $3\sigma$ away from the mean, as these are likely affected by high background levels. Then a new mean and standard deviation are calculated. This process is repeated up to 50 times to ensure almost all contaminated time bins are removed. Once this process is complete, a good time interval (gti) is defined for the creation of a cleaned events list. This list is the starting point used to detect sources, make images and spectra. The cleaned events files are in Flexible Image Transport System (`FITS`) format.

### Image generation

Using the cleaned events files, XIP generates single camera images by extracting data in two energy bands ($0.5-2$ keV and $2-10$ keV) to create a two-dimensional image, spatially binned with a pixel size of $4.35''$, via the XMM Science Analysis Software (SAS) command `evselect`. A corresponding exposure map is also produced. Although the entire field of view of the EPIC is exposed at the same time, the exposure map is not homogeneous due to the impact of chip gaps and vignetting. An example of an XCS image and exposure map generated from a cleaned events list, showing these features, is shown in Figure 2.7.

As well as producing images from each individual camera, it is possible to combine PN, MOS1 and MOS2 images. To do this, the MOS1 and MOS2 images and exposures must be appropriately scaled to having the same sensitivity as the PN detector. This requires knowledge of the energy conversion factor (ECF) which measures the energy flux associated with a given count rate. The energy fluxes are determined by assuming a absorbed power law model common for extragalactic X-ray point sources. The absorption in the power law accounts for the fact X-ray photons are absorbed by material along the line of sight, and can be quantified by measuring the galactic hydrogen column density for a given source position.

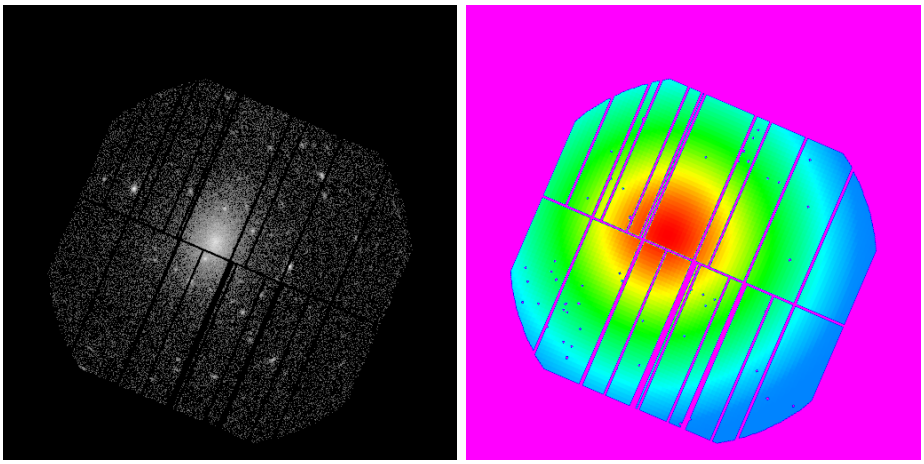

Figure 2.7: An example of a XIP reduced PN image and exposure map taken for *XMM* observation ID 0201900101 in the 0.5 - 2 keV energy band. On the left is the XCS image, where the white areas represent flux from X-ray bright sources. On the right is the generated exposure map, displaying that the effective area is highest in the centre (red), falling off non-uniformly at larger distances (vignetting). The lines across both the image and exposure map represent chip gaps in the EPIC PN instrument.

### Source detection

Once the images for each observation are produced in the relevant energy bands described above, it is possible to identify sources in the image. This is done using the X-ray Automated Pipeline Algorithm (XAPA), which is based on the WAVDETECT package (Freeman et al., 2002). A wavelet analysis is performed on the convolved XIP images at nine different pixel scales ($\sqrt{2}$, 2, $2\sqrt{2}$, 4, $4\sqrt{2}$, 8, $8\sqrt{2}$, 16 and 32). At each scale, pixel values which are significantly above the background (significant pixels) are considered to be associated with astronomical sources. Due to the presence of faint extended sources in X-ray images, the wavelet analysis has two runs. In Run 1 (pixel scales ranging from 1-2), bright compact sources are found. These are subsequently masked out before Run 2 (pixel scales ranging from 3-9). This method is necessary because bright point sources can pollute the wavelet signal on large scales, mimicking extended sources. However, it is possible that genuine extended sources detected in Run 1 are excluded from Run 2, thereby underestimating their size and misclassifying them as point sources. Clusters with sharply peaked or 'cuspy' brightness profiles e.g. those with cool-cores are likely to be more affected by this selection effect. To resolve this, XAPA invokes a 'cuspiness test,' carried out between Runs 1 and 2. A $5 \times 5$ pixel grid, $Q$ is centred around each detected source in Run 1. The cuspiness

of the central region, $C$ is evaluated according to

$$C = \frac{Q_{max} - Q_{min}}{Q_{max}} \tag{2.1}$$

where $Q_{max}$ and $Q_{min}$ are the maximum and minimum pixel values within the grid, respectively.

Applying this to multiple X-ray sources, it is found that genuine point sources have a $C \geq 0.85$. Therefore, any source with $C < 0.85$ have a flatter brightness profile–which are potentially extended sources–can therefore be detected again in Run 2.

Following the wavelet analysis, a source list is generated for each image based on the grouping of significant pixels. The exact size of each source depends on the point spread function (PSF) of the *XMM* instrument. The PSF is a strong function of the off-axis angle (defined as the angle between the centre of the field of view and source location). As sources are detected at large distances from the centre, the shape of the PSF distorts from being circularly symmetric to ellipsoidal and finally bow-tie shaped. Characterising the *XMM* PSF is nontrivial, requiring simulations based on measurements of the mirror shapes, or ground-based X-ray experiments on the mirror modules, or fitting 1-dimensional profiles. Currently for the XCS analysis, the PSF is determined using the Extended Accuracy Model (EAM). Objects which are detected at high off-axis angles or otherwise have a low photon count might be classified as 'PSF-sized' rather than explicitly extended or point-like. These are usually cool-core clusters or instrument artefacts and hence visually inspected to ensure robust classifications.

The final XCS catalogue therefore contains a candidate list of extended, point-like and PSF-sized sources, of which the subset of extended Xapa sources are treated as cluster candidates. See Figure 2.8 for an example of an *XMM* observation with associated source classifications.

### 2.3.2 RedMaPPer

The **red**-sequence **Ma**tched-filter **P**robabilistic **Per**colation (redMaPPer) cluster finding algorithm (Rykoff et al., 2014) is used to find clusters inside optical photometric surveys such as SDSS and DES.

The redMaPPer (hereafter RM) algorithm iteratively self-trains the red sequence model to any available spectroscopic redshifts to measure photometric redshifts.

Its first step is in training its red sequence model. This is achieved by finding galaxies with known spectroscopic redshifts and using them as a seed to find overdensities of galaxies of similar colours. Next, this empirical red-sequence model is used to group

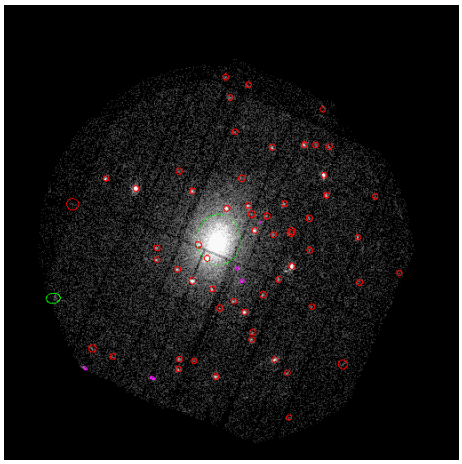

Figure 2.8: An example of a XIP reduced image after running the XAPA routine to identify sources. All detected sources are highlighted in green (extended), red (point-like) or magenta (PSF-sized). This is a targeted observation of cluster RXC J0003.8+0203, hence there is a clear extended source in the centre of the FOV.

galaxies into clusters, and assign a photometric redshift to the clusters. These photometric estimates are used to retrain the red-sequence, until the photometric and spectroscopic properties reach convergence.

After the red-sequence model has converged, RM uses this model to calculate the number of nearby red-sequence galaxies centered on every galaxy in the photometric catalog (i.e. from SDSS DR8). Galaxies that show an excess of nearby galaxies are ranked according to the likelihood that there is a potential cluster centered on that galaxy. The richness of the highest ranked cluster is measured, and its members probabilistically removed from the other candidate clusters (to avoid double counting). The algorithm then moves on to the next highest ranked candidate central galaxy, and the procedure is iterated. This process is called percolation (we describe errors in this step, termed 'mispercolations,' in Section 2.5). This reduces the photometric catalogue to a list of independent, red-sequence confirmed clusters. The RM-defined richness ($\lambda$) of each cluster is defined as the sum of membership probabilities over all galaxies within a scale radius $R_\lambda$, where $R_\lambda = 1.0h^{-1}\mathrm{Mpc}(\lambda/100)^{0.2}$. A luminosity cut is also applied whereby $L_{cut} = 0.2L_*$, selected based on where the scatter in the resulting mass-richness relation is lowest.

In the first stage of catalogue production, central galaxies are selected as the brightest members. The statistical properties of these candidate centrals are then used to define a set of filters that can be used to recenter clusters in a more probabilistic way. This procedure is iterated until the brightest and most probable central galaxy are in agreement. This technique, however, means that in the final catalogue, the chosen central galaxies are

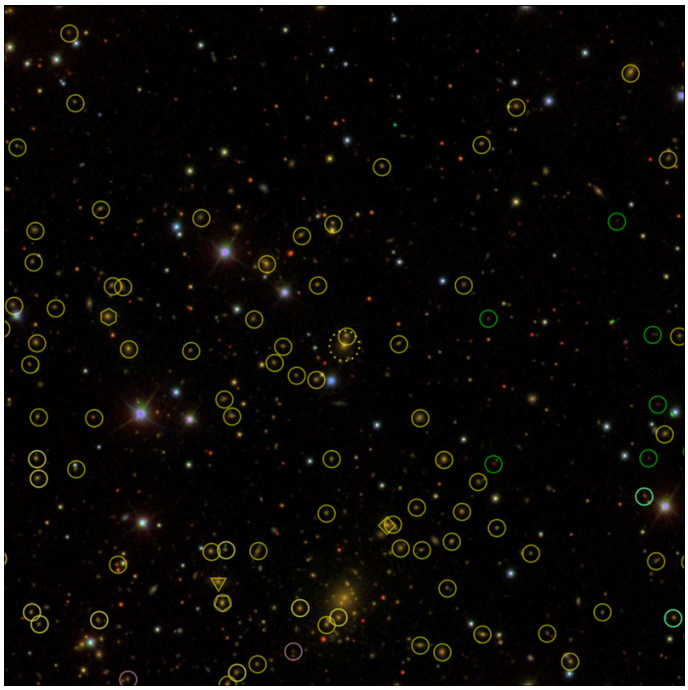

Figure 2.9: Example of a galaxy cluster in the RM SDSS DR8 catalogue with RM ID 22, showing the placement of RM assigned five most likely central galaxies. In order from most likely to least likely central, the shapes are: dotted circle, triangle, diamond, pentagon and hexagon.

not always the brightest cluster members, but also take into consideration the local galaxy density in the immediate neighborhood of the galaxy. The final RM catalogue contains a list of galaxy clusters and associated data, including positions, redshifts, richnesses, membership probabilities, and the top-five most-likely centres (and corresponding centering probabilities, see Figure 2.9).

The RM catalogue used to develop the XCS-SDSS cluster sample is derived from SDSS DR8 (Aihara et al., 2011). For more information on the magnitude and colour cuts applied to the input catalogue, the reader is referred to the seminal paper describing the RM application to the SDSS DR8 catalogue (Rykoff et al., 2014) and companion paper (Rozo et al., 2015). The RM algorithm is applied to approximately 10,000 sq. degrees of SDSS DR8 data, generating a catalogue of clusters over the redshift range $z \in [0.08, 0.55]$. The photometric redshift errors for the clusters are almost Gaussian, with a measured scatter $\sigma_z \simeq 0.006$ at $z \simeq 0.1$, increasing to $\sigma_z \simeq 0.02$ at $z \simeq 0.5$ due to increased photometric noise near the survey limit. The median value for $z_{red} - z_{spec}/(1+z)$ for the full sample is 0.006 (See Figure 2.10). The impact of projection effects is stated to be low ($\leq 5\%$), implying that the number of detected clusters, their associated redshifts and

richnesses, are robust. The RM-SDSS catalogue contains a total of 396,047 clusters, of which 66,028 have a richness of $\lambda > 20$. This forms the starting point of the RM sample prior to crossmatching clusters with those in the *XMM-Newton* archive. A volume-limited version of the RM SDSS DR8 catalogue is used in Chapter 4, and spans a redshift range $z \in [0.1, 0.35]$.

## 2.4 Crossmatching clusters between RM and XCS

The crossmatching begins with RM-SDSS clusters with a richness greater than or equal to 20. This cut is applied to ensure a match exists between a RM detected cluster and a DM halo. The RM-SDSS sample is then matched to all *XMM* observations[3] with usable EPIC science data, under the requirement that the RM position falls within $13'$ of the aimpoint. Next, all *XMM* observations are filtered based upon the total exposure time, where the total exposure time is defined as the sum of $0.5\times$PN$+0.5\times$(MOS1+MOS2), which accounts for the fact that the MOS1 and MOS2 cameras are approximately half as sensitive as the PN camera. Usable observations are those in which the vignetting-corrected exposure within a 5 pixel radius centered on the RM position is greater than 3 kiloseconds (ks), and the median exposure is greater than 1.5ks. The cut applied to the mean exposure is to ensure the X-ray source does not appear too faint in the image. The cut on the median exposure excludes any RM clusters whose associated X-ray observation might be affected by chip gaps (see Figure 2.7 for appearance of chip gaps). These exposure cuts are repeated at a position $0.8\mathrm{R}_\lambda$ away from the RM position (in the direction away from the centre of the *XMM* observation) to encapsulate the mis-centering measured between the RM central galaxy and the X-ray peak position. The impact and calibration of miscentering in the XCS-SDSS sample is discussed in Chapter 4. In Figure 2.11, we demonstrate the key steps in associating RM clusters to *XMM* observations, prior to running Xapa (Section 2.3.1) to identify X-ray extended sources in the observations. Based on the requirements listed above, there are 1249 SDSS-DR8 RM clusters with $\lambda >$20 that fall upon an *XMM* observation.

All *XMM* observations which contain a RM cluster are subject to the data reduction process described in Section 2.3.1. The Xapa routine is run on each observation, generating a list of point and extended sources. At the position of the RM defined central position, we search for all Xapa extended sources within a comoving radial distance of $2h^{-1}$ Mpc, calculated based on the RM cluster redshift.

[3] collected from http://nxsa.esac.esa.int/nxsa-web/

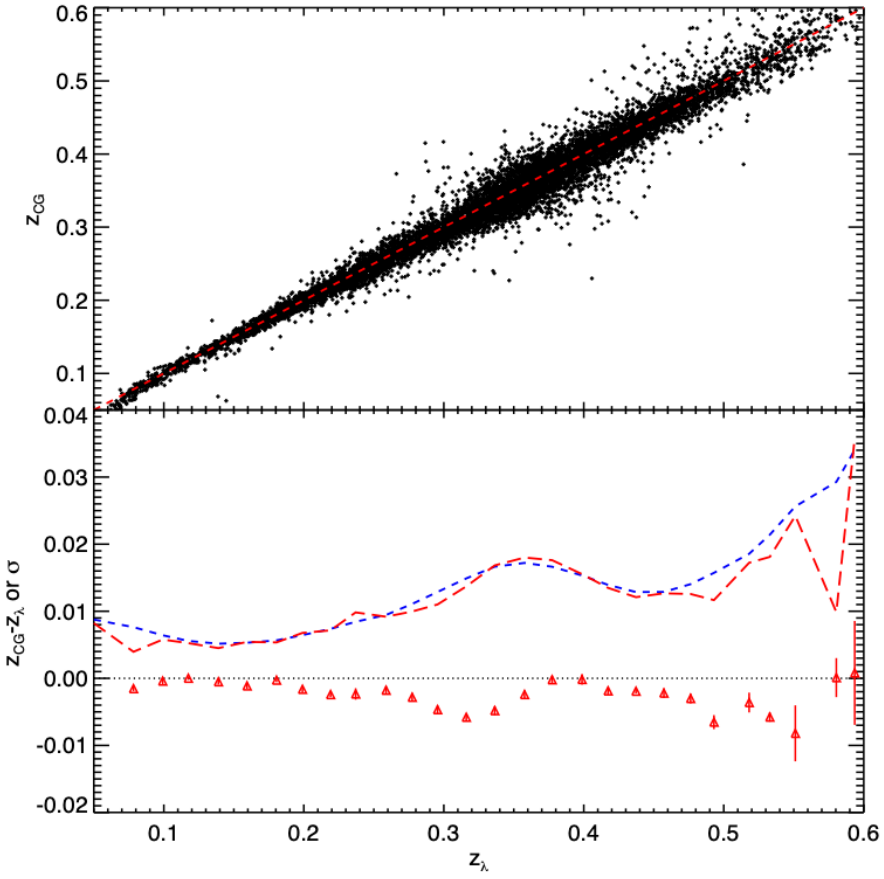


Figure 2.10: Top panel: Figure from Rykoff et al. (2014). RM redshift $z_\lambda$ vs. spectroscopic redshift of the assigned cluster central galaxy (CG) for RM-SDSS clusters with $\lambda > 20$. Bottom panel: Red triangles show the mean offset ($z_\lambda$ - $z_{CG}$) in various redshift bins. The blue short-dashed line shows the average redshift error on $z_\lambda$, while the red long-dashed line shows the measured rms of the redshift offset distribution. The majority of outliers are due to errors in cluster centering, which increases the value of the $z_\lambda$ - $z_{CG}$ offset not because $z_\lambda$ is incorrect, but rather because the chosen central galaxy is not actually a cluster member. See Chapter 4 for a more detailed explanation of this effect.

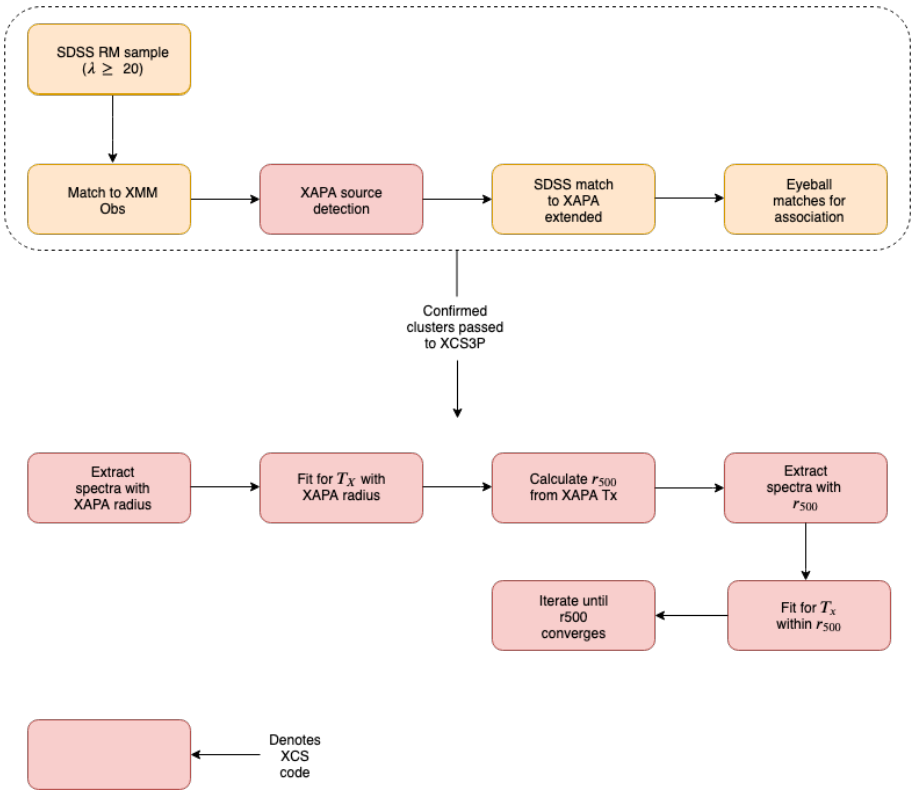


Figure 2.11: Flowchart outlining the key steps involved in the crossmatch process between RM clusters and *XMM* observations. Figure from Giles et al. (in prep).

An additional step which is performed on the X-ray observations, outside of the standard XAPA routine, is the calculation of the location of the X-ray emission peak based on the RM position. This is a key property used to assess the fidelity of matches to RM clusters. The peak position is determined by applying a Gaussian smoothing kernal of width, $\sigma = 50$ kpc $h^{-1}$ to each merged XMM observation. The width of the kernal is determined based on the RM redshift. All extended sources except the closest to the RM targeted cluster are masked or 'drilled out' during this process (see Figure 4.3). After masking, the X-ray peak position is computed within a radius of $1.5R_\lambda$ around the RM position. This method is discussed extensively in Chapter 4, Section 4.2.1 in order to model the centering performance of RM.

## 2.5 Visual inspection

Once each RM cluster has a list of associated *XMM* cluster matches, the clusters are all visually inspected to confirm the physical association between the extended X-ray emission and the RM galaxies.

In Figure 2.12, we show an example of a clear, unambiguous match between a RM

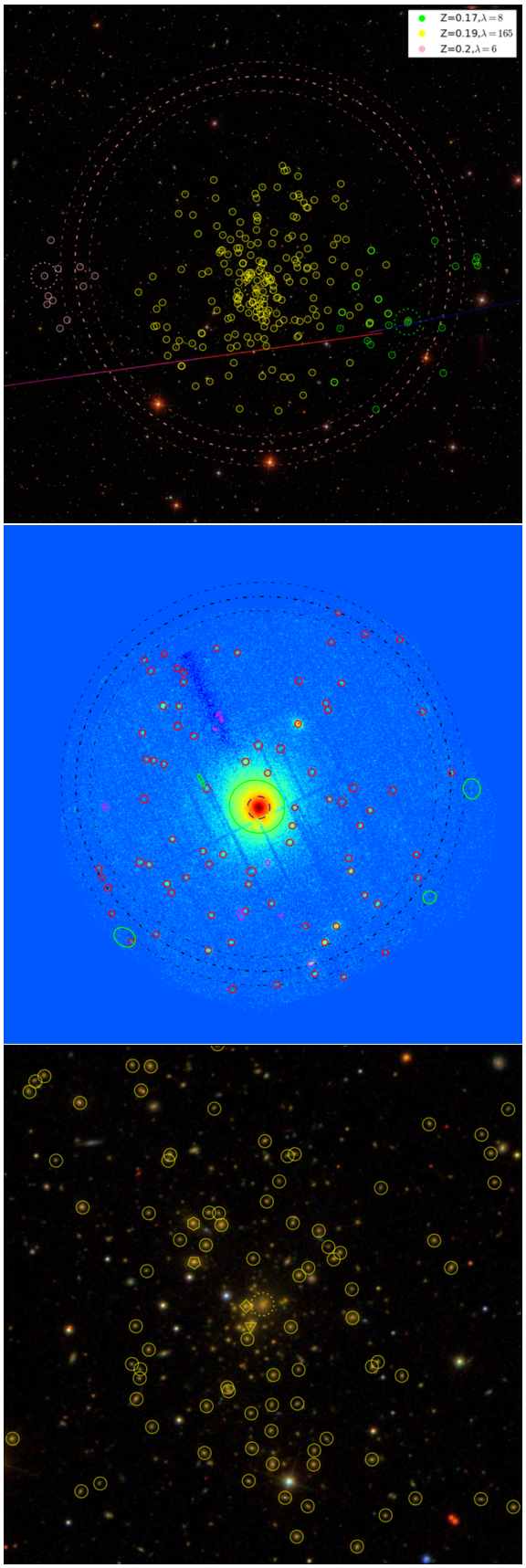


Figure 2.12: An unambiguous physical match between *XMM* cluster XMMXCS J131129.8-012024.5, in ObsID 0093030101, with associated RM ID 3, $\lambda = 165$ and $z = 0.19$. Top: SDSS postage stamp centered on the RM cluster, in which the colour-coded circles define the redshifts of all identified galaxies in the image. The prominent distribution of yellow circles in the image highlight the concentration of red sequence galaxies at the same redshift, indicating a genuine cluster detection. Middle: X-ray FOV image with all detected sources marked. Bottom: $6'$ by $6'$ SDSS image with RM assigned galaxies circled in yellow.

cluster and an X-ray extended source. One of the main criteria determining whether there is a physical association between the optical and X-ray observation is the presence of a single redshift distribution of the cluster member galaxies. This ensures that the X-ray gas is not associated with a nearby RM cluster in projection.

However, there are cases where the match between X-ray source and RM cluster is more ambiguous. The most prominent reason for this is due to a failure in the RM percolation process, known as mispercolations (see Figure 2.13). Mispercolations occur predominantly in massive cluster halos with a nearby lower mass sub-halo. During the percolation process, RM incorrectly assigns a high richness to the low mass system and a low richness to the higher mass cluster. In order to correct clusters affected by mispercolation, we followed the method outlined in Hollowood et al. (2019). The richness of the initial main halo is thus manually assigned to the sub-halo and vice-versa for the sub-halo (assigning it the richness of the main halo). Unlike in Hollowood et al. (2019), we do not remove these sub-halos from the cluster sample upon reassignment (unless the richness is below the $\lambda \leq 20$ threshold).

Other ambiguous matches between X-ray and optical counterparts may be the result of projection effects in the X-ray image (see Figure 2.14) or the associated X-ray source not being a cluster at all (see Figure 2.15). In these instances, the X-ray counterpart is not assumed to be physically associated to the RM cluster, and such matches are subsequently removed from the final sample.

## 2.6 XCS Post Processing Pipeline

All X-ray extended sources which are confirmed to be genuine, physical matches to RM clusters are then passed to the XCS Post Processing Pipeline (hereafter XCS3P). At this stage, it is possible to measure X-ray properties, namely $L_{\rm X}$ and $T_{\rm X}$. In specific cases where the spectral quality is sufficiently high, it is also possible to measure the average metal content of the cluster plasma (described in Chapter 3).

### 2.6.1 X-ray temperature

The X-ray spectra of the clusters are extracted and fit using the spectral fitting package XSPEC (Arnaud, 1996) within a $R_{500}$ aperture. The $R_{500}$ aperture defines a radius in which the mean density $\rho$ is taken to be 500 times the critical value $\rho_c$, as calculated at the redshift of the cluster (See Section 1.4.1 for details). The spectral binning of each cluster is such that there is a minimum of five photon counts per spectral bin. The

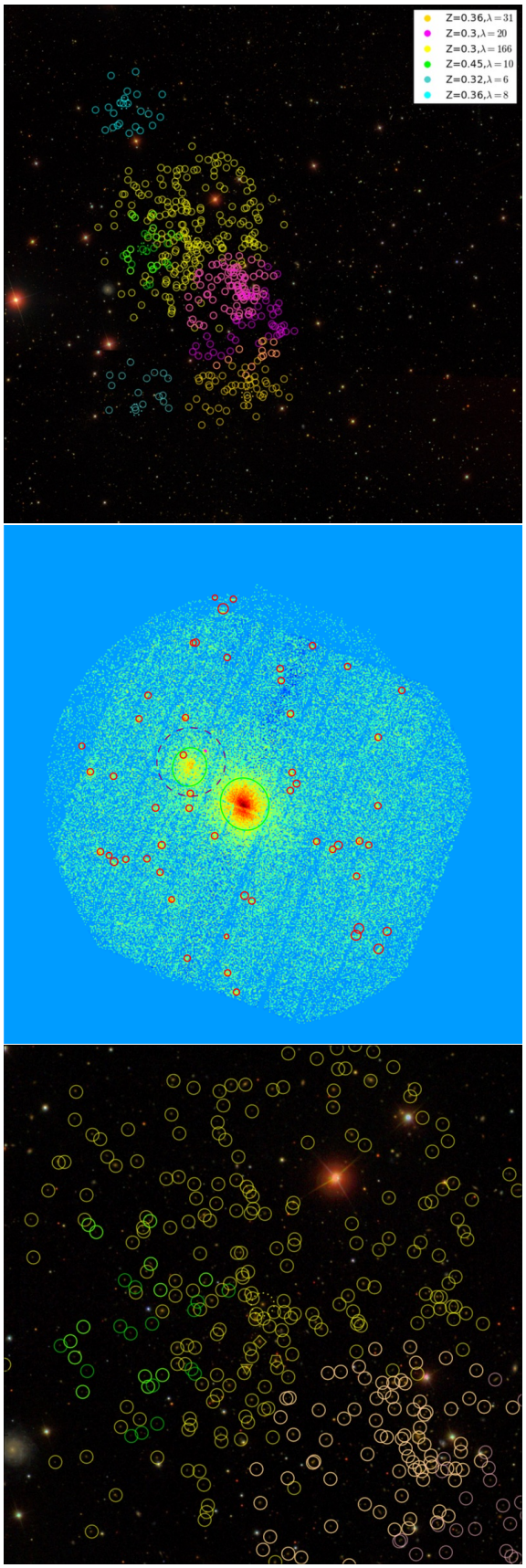


Figure 2.13: An example of a mispercolated cluster, in which RM has incorrectly split the same physical system into two distinct clusters, while incorrectly assigning a higher richness to the subdominant structure, and a lower richness to the larger structure. Top: SDSS image scaled to *XMM* FOV. Middle: X-ray FOV image. Bottom: SDSS $12'$ by $12'$ image showing the smaller structure (yellow circles), and larger structure (coral circles). The most likely central galaxy has been assigned to the smaller group of cluster member galaxies, while the X-ray emission traces the larger structure.

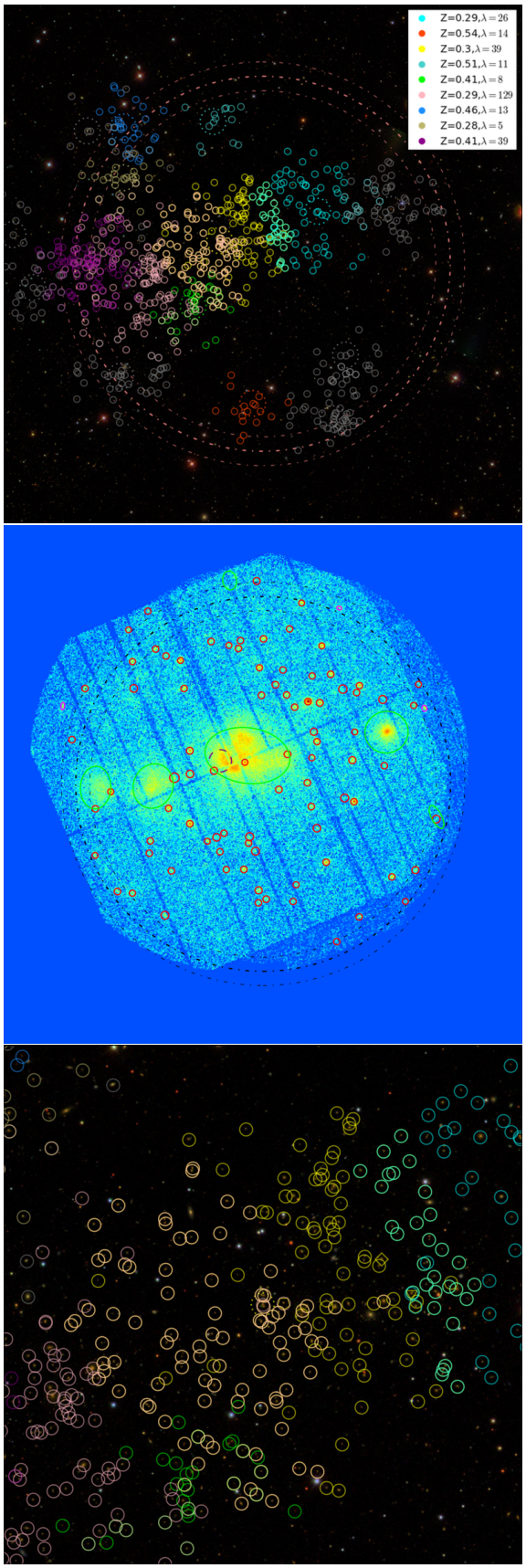


Figure 2.14: An example of an ambiguous match due to projection effects in the X-ray observation, resulting in insufficient information to assign a physical X-ray counterpart to the RM cluster. In this case, there are three distinct clusters at different redshifts.

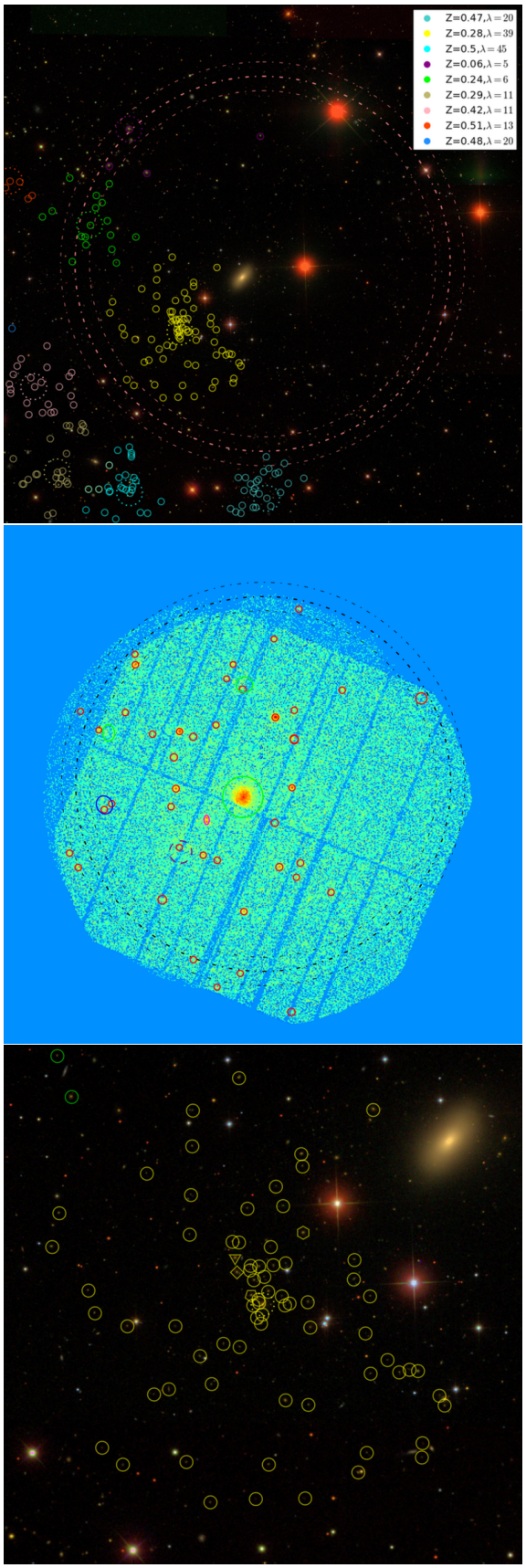


Figure 2.15: An example of a poor match between X-ray source and RM cluster. Although this meets all of the criteria for a match, it is clear from visual inspection that the X-ray source, while extended, is not a cluster but rather a foreground galaxy. This example would not pass the visual inspection check.

fits were performed in the $0.3 - 7.9$ keV band with a `wabs` $\times$ `apec` model using the `cstat` statistic. The `wabs` component accounts for photoelectric absorption by neutral hydrogen along the line of sight to the cluster, using cross-sections defined in Morrison and McCammon (1983). We note that more up-to-date photoelectric cross-sections are available in the `tbabs` model (Wilms et al., 2000). The `apec` component accounts for the emission spectrum from collisionally-ionized diffuse gas calculated from the AtomDB atomic database (Foster et al., 2012), enriched with various elements (Smith et al., 2001). Relative abundances of these elements are defined by their ratios to solar abundances ($Z_{\odot}$) taken from Anders and Grevesse (1989). While running xcs3p, the abundance is fixed at $0.3Z_{\odot}$, the value typical for X-ray clusters (Kravtsov and Borgani, 2012). The choice of a fixed average abundance is supported by recent studies investigating the overall metal content of the ICM. There is typically a weak, negative evolution in the metallicity as a function of cluster temperature (Yates et al., 2017), and no evolution in redshift across entire core-excluded cluster samples (Ettori et al., 2015a). The final temperature is estimated using an iterative process, using the $R_{500} - T_{\rm X}$ scaling relation from Arnaud et al. (2005),

$$E(z)R_{500} = \frac{1.104}{1\ \mathrm{Mpc}} \left( \frac{T_{\rm X}}{5\ \mathrm{keV}} \right)^{0.57} \tag{2.2}$$

The iterations are conducted until $R_{500}$ converges (the ratio of the new to old $R_{500}$ defined to be $> 0.9$ and $< 1.1$). To account for the background in the spectral analysis, we make use of a local background annulus centred on the cluster. For the background annulus, we use an inner and outer radius of $1.05r_{500}$ and $1.5r_{500}$ respectively (see dashed-red outer annulus in Figure 2.16). During each iteration, a calculation of coefficient of variation (Koopmans et al., 1964) of the $T_{\rm X}$ is performed. This coefficient is defined as the ratio of the standard deviation ($\sigma$) to the mean ($\mu$), given by $C_v = \sigma(T_{\rm X})/\mu(T_{\rm X})$. Throughout this thesis, we adopt a value of $C_v \leq 0.25$ as an indicator of a reliable measurement. It is also possible to extract spectra in a smaller $R_{2500}$ radius via the same method as detailed above, with two main differences. First, $R_{2500}$ values were estimated using the corresponding relation found in Arnaud et al. (2005),

$$E(z)R_{2500} = \frac{0.491}{1\ \mathrm{Mpc}} \left( \frac{T_{\rm X}}{5\ \mathrm{keV}} \right)^{0.56} \tag{2.3}$$

Second, the background is taken into account using an annulus centered on the cluster with an inner and outer radius of $2R_{2500}$ and $3R_{2500}$ respectively. Point sources are masked prior to fitting by drilling out the flux from all xapa detected sources around the source of interest (see green circles in Figure 2.16). More details on the xcs3p methodology are

available in Giles et al. (in prep) and Lloyd-Davies et al. (2011), whilst we discuss only the aspects relevant to this thesis.

Most recently, while undertaking the XCS3P analysis for the cluster sample used in Chapter 3, another issue was discovered. The current quality control for assessing whether a X-ray temperature measurement is reliable is $\Delta T_{\rm X}/T_{\rm X} < 0.25$. However, it was found that during the visual inspection of the spectra which pass this check, there were examples of poor model fits to the continuum. Examples of these are shown in Appendix B.2. Typically, these fits were shown to be poor at lower energies (between 0.3 - 1 keV). We estimate these fitting outliers comprise a small fraction of all the XCS cluster samples (less than 5%), nevertheless it is important to filter out cases where 'reliable' temperature estimates might be generated despite poor fits to the data. This could possibly be done by doing a fractional binning test across the spectrum, imposing an upper limit on residuals across the entire (0.3-7.9 keV) energy range. Therefore, if the fit to the cluster spectrum at low energies is poor compared to higher ones, these clusters are filtered out from the final sample, as these are likely to be affected by poorly subtracted background emission or instrumental artefacts. The visual inspection and removal of such outliers has improved the quality of XCS3P.

### 2.6.2 Signal-to-noise ratios

The calculation of the signal-to-noise ratio (SNR) can be determined using either the cluster spectrum or on images generated in the 0.5 – 2.0 keV band. Using the image, we calculate the SNR within a comoving radius of 500 kpc $h^{-1}$ (calculated based upon the RM estimated redshift), with the background determined within an annulus spanning 700 – 1000 kpc $h^{-1}$. The regions are centered on the measured peak position (described in Section 2.4), rather than the XAPA determined cluster position. Due to the fact that the offset between the peak and XAPA position is very small for the cluster sample, this does not significantly affect the calculation of the SNR (see example in Figure 4.2). The SNR is calculated using the following,

$$SNR = \frac{C_s - \frac{A_s}{A_b} \times C_b}{\sqrt{C_s + \left(\frac{A_s}{A_b}\right)^2 \times C_b}} \tag{2.4}$$

where $C_s$ and $C_b$ are the source and background counts, and $A_s$ and $A_b$ are the source and background area.

A separate but related quantity can be determined from the cluster spectrum, by effectively computing a ratio of source counts to background counts for each spectrum,

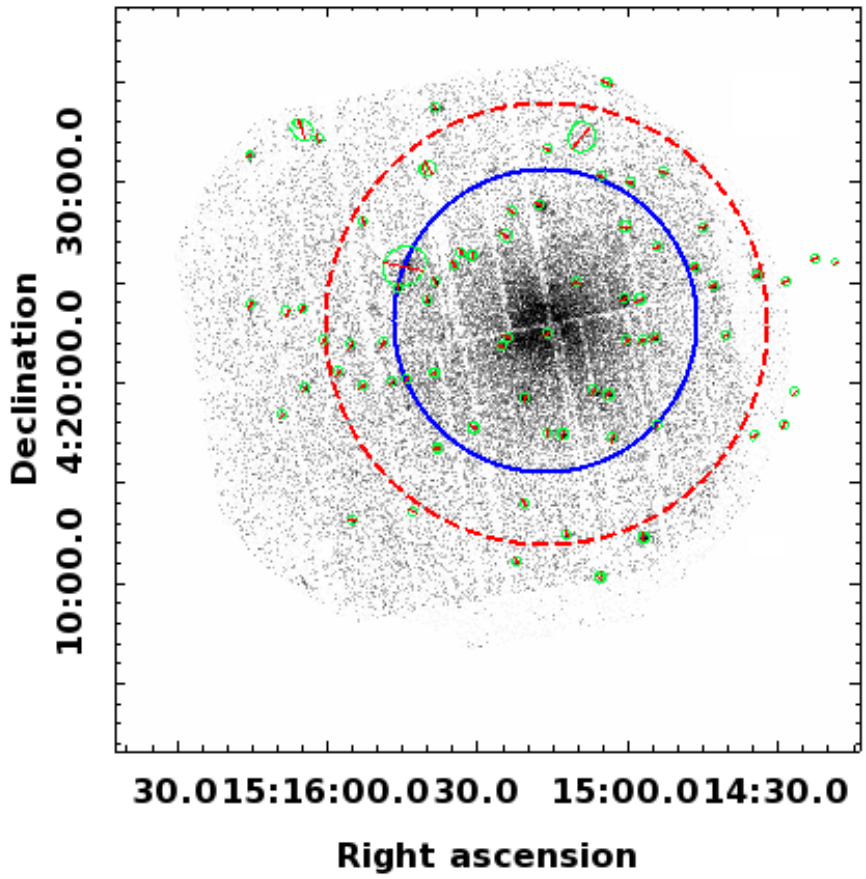


Figure 2.16: Reduced XIP image of ObsID 0760230301 in the 0.5-2.0 keV band. The source region, enclosing X-ray cluster XMMXCSJ151516.1-042253.5, is defined by the blue circle. The dashed red circle defines the background region. Point sources are circled in green and excluded from the spectrum.

in which the background is defined inside an annulus spanning $1.05R_{500}$ to $1.5R_{500}$, and rescaled using the XSPEC `BACKSCAL` keyword.

### 2.6.3 X-ray luminosity

The X-ray luminosity, similar to the temperature, is computed after extracting a spectrum in a chosen radius. The XSPEC `lumin` command is used to measure the luminosity in a chosen energy band. The bolometric luminosity is measured over the full energy range (0.01 - 50.0 keV), while the soft-band luminosity is measured in the range 0.5 - 2 keV (cluster rest-frame).

While developing the latest version of XCS3P, it was found that the luminosity errors in Lloyd-Davies et al. (2011) and Mehrtens et al. (2012) were calculated incorrectly. When estimating the luminosity in XSPEC, the absorption component ($n_H$) must be set to zero in order to represent conditions at the cluster. However, the luminosity errors will be in error if determined while $n_H$ is set to zero (since the errors are determined from the spectral fit to the absorbed data), as was previously done in LD11. This was corrected in the current version of XCS3P using the following method. First, the errors are determined using an initial luminosity ($L_{ini}$) calculation before $n_H$ has been set to zero. Then, $n_H$ is set to zero and the luminosity is determined ($L_0$). The errors are then scaled by the ratio of $L_0$ to $L_{ini}$ (i.e. $L_{err} \times L_0/L_{ini}$).

Another development to XCS3P in terms of luminosity measurements is the improvement in masking nearby extended sources. In the previous version used in Lloyd-Davies et al. (2011), the routine used to exclude nearby extended sources was found to overestimate the masking area around the source in question. This was because the size of the mask was calculated based on the number of counts of the contaminating source. In Figure 2.17, the left image highlights the region used to exclude a nearby bright extended source based upon the previous version (red hashed ellipse). The excluded region overlaps with the source extraction region (green circle), removing a fraction of the source flux. While this example will not have a significant effect, in some cases the excluded region of the nearby source removed a sufficient amount of the source region, making the spectral fit unreliable. Therefore, the scaling factor was removed for the current analysis, improving the fit for clusters affected.

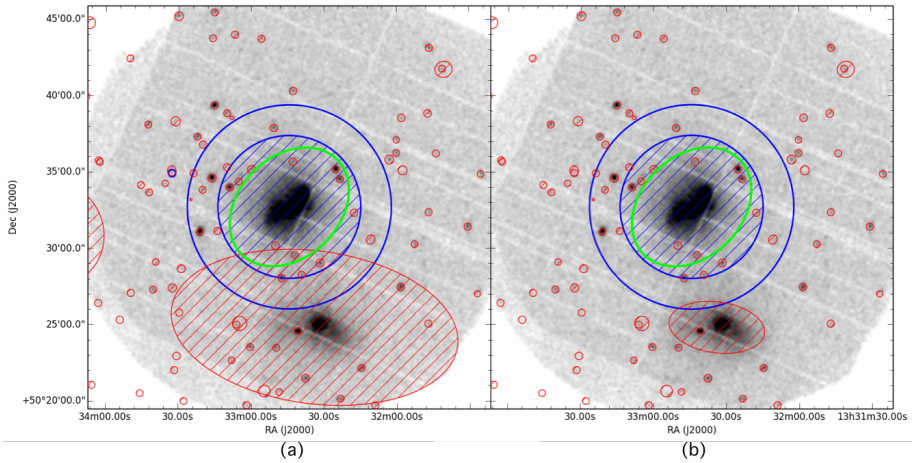


Figure 2.17: Comparison of masking method in previous (a) and current (b) versions of XCS3P, showing the change in mask size between the old and new methodology.

## 2.7 Other catalogues

The methodology described in this chapter to produce the XCS-SDSS sample were repeated to produce two more samples which are used in this thesis. While only the XCS-SDSS sample is used for the main science application of this thesis in Chapter 3, two additional samples, developed using the Year 1 and Year 3 releases of DES data, are used extensively in Chapter 4. The DES data samples are distinct from SDSS in both the choice of photometry used to generate the initial galaxy catalogues, as well as their location (see Figure 2.18). Hence, both Y1 and Y3 samples are largely independent from SDSS (except an overlap in the Stripe-82 region). The redshift range of Y1 and Y3 sample are also larger, however, given the applications of these samples are principally for cosmological studies, both Y1 and Y3 catalogues are volume-limited.

### 2.7.1 XCS-DESY1 sample

The XCS-DESY1 sample was generated using a similar methodology to that which is described above for the SDSS sample. In this case, we begin with a catalogue of RM clusters in the DES Y1 footprint, identifying all the *XMM* observations which fall on the location of RM clusters. The RM sample is taken from the redMaPPer DES Y1-6.4.17 volume-limited catalogue, which is based on the DES Y1 gold catalogue (Drlica-Wagner et al., 2018). The sample contains only clusters with a $\lambda > 20$, totaling 7066 clusters (McClintock et al., 2018). The final sample, crossmatched with XCS, contains 110 clusters. The redshift range of the catalogue is $z \in [0.1, 0.7]$.

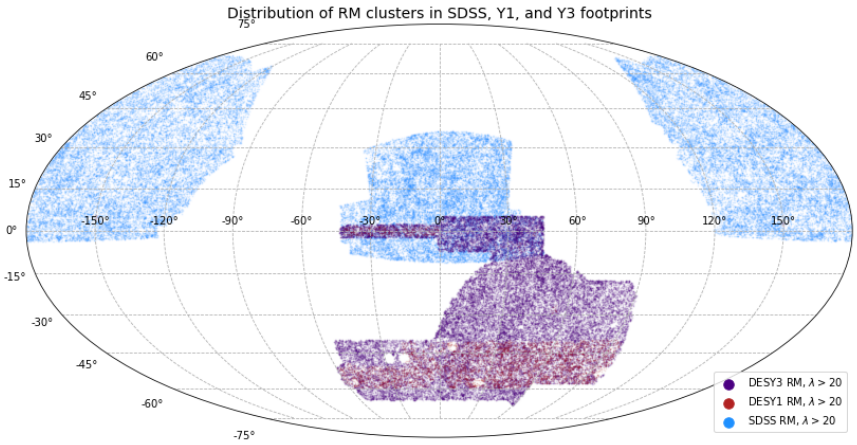


Figure 2.18: 2D sky projection showing the spatial distribution of RM detected clusters in the SDSS, DESY1 and DESY3 footprints. The SDSS sky coverage is shown in blue, while DESY1 and Y3 are shown in red and purple, respectively. All samples in the sky projection show the presence of clusters with a $\lambda > 20$.

### 2.7.2 XCS-DESY3 sample

The XCS-DESY3 sample uses the redMaPPer DES Y3-6.4.22 volume limited catalogue. Currently, the DES Y3 gold catalogue from which this sample is generated is not publicly available. This sample contains a larger number of clusters compared to Y1, largely due to increased survey depth, area and improved photometry using both the single object fitting (SOF) and multi-object fitting (MOF) to measure galaxy colours. For more detail on the input photometry of the XCS-DESY3 sample, the reader is referred to the relevant summary in Klein et al. (2019). The sample contains only clusters with a $\lambda > 20$, totaling 53610 clusters. The final sample, crossmatched with XCS, contains 280 clusters. The redshift range of the catalogue is $z \in [0.1, 0.8]$.

The XCS-SDSS, XCS-DESY1 and XCS-DESY3 samples introduced in this Chapter are each applied within the thesis. In Chapter 3, the scientific analysis principally requires a high-fidelity X-ray cluster sample with associated spectral information. As such it is comparatively low-redshift and insensitive to the choice of photometric calibration used. As a result, the XCS-SDSS sample is used exclusively in this Chapter, where the RM-SDSS catalogue is used to provide optical confirmation and associated redshifts for the clusters used. In Chapter 4, the study is focused on calibrating the centering performance

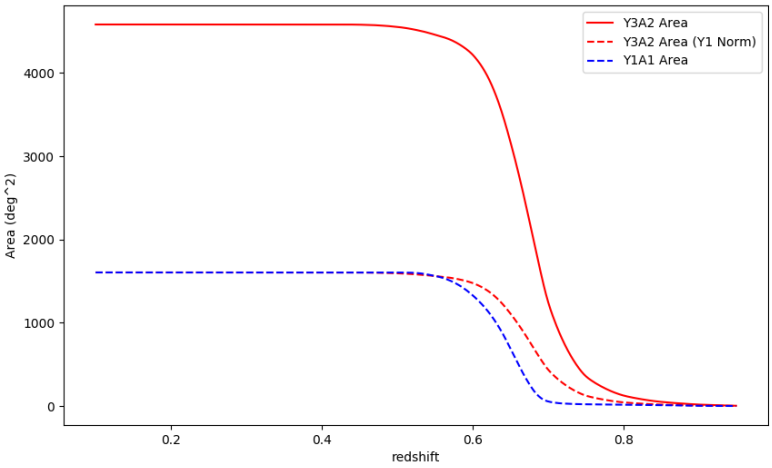


Figure 2.19: Comparison of survey depth between Y1 and Y3 volume limited cluster catalogues. The Y3 area is shown in red, the rescaled Y3 area according to the total area is shown by the red dashed line, and the Y1 is the blue dashed line. The depth improvement is noticeable but not gigantically so, in part due to Y2 covering a different part of the footprint (increasing the area) and poor weather conditions during the Y3 observing season. Plot by E. Rykoff (priv. comm).

of the redMaPPer cluster finder. Such a study is sensitive to both redshift and richness measurements, and therefore requires a comparison between RM samples in both different redshift ranges and photometric calibrations. Hence, in Chapter 4, all three samples are used to compare the impact of miscentering, and subsequently to characterise the extent to which such biases are able to offset galaxy cluster mass estimates.

# Chapter 3

# New evidence that the 3.5 keV feature in clusters is inconsistent with a dark matter origin

The methodology and results discussed in this Chapter are new to the literature and currently being prepared for publication. Section 3.1 is a specialised review of the field and current findings. We have improved upon previous studies which have reported a detection of a claimed X-ray line of dark matter origin in various astrophysical systems. This is done using the largest sample of X-ray and optically confirmed clusters for such a study (118 confirmed clusters compared to 73 from previous analyses). We have computed among the most competitive constraints on the flux and origin of the putative '3.5 keV line,' finding evidence against a dark matter interpretation, contrary to seminal findings in previous cluster searches from Bulbul et al. (2014).

## 3.1 Introduction

There are a plethora of methods to search for dark matter signatures in our cosmos. Among the most well-known of these searches began with observations of the Bullet Cluster (Clowe et al., 2006). Located approximately 3.8 billion light years from Earth, this cluster consists of two clusters of galaxies formed via collision. During the merging process, hot gas in the ICM was significantly displaced from the cluster's centre of mass. X-ray observations of the gas, combined with gravitational lensing studies of the underlying mass distribution concluded that the observed degree of offset between the gas and overall mass could not be explained by simply assuming all gravitating matter in the Bullet cluster is baryonic.

This was deemed 'empirical proof' of the existence of dark matter.

Many different dark matter candidates have been postulated, from relativistic (hot) to non-relativistic (cold), and those in between (warm). In order to be credible, a dark matter candidate must be stable on cosmological timescales, agree with the observed density of dark matter today, describe structure formation, and interact weakly or not at all with observable matter. While non-relativistic weakly interactive massive particles (WIMPs) have been at the forefront of dark matter searches (Roszkowski et al., 2018), their lack of discovery means other candidates remain plausible, with the additional benefit of potentially resolving issues associated with cold dark matter. Known inconsistencies between cold dark matter models and observations include the 'missing satellites problem' (Klypin et al., 1999), which states the predicted number of satellites around a Milky Way-type galaxy from simulations is inconsistent with the number of observed dwarf galaxies. Another is the 'too big to fail' problem, which states that massive CDM halos are predicted to be too dense to form luminous satellite galaxies, in contrast to the observed satellite population around the Milky Way (Boylan-Kolchin et al., 2011). However, counter arguments have been presented, suggesting that baryonic feedback can decrease the central density of these halos, making them consistent with observations. Alternatively, studies by e.g. Lovell et al. (2012) have suggested that no such discrepancy exists if halos are composed of warm, rather than cold dark matter. Warm dark matter halos are expected to be less concentrated on account of their later epoch of formation (see Figure 3.1).

Searches for non-CDM candidates have been invigorated by the claimed detection of a GeV gamma ray excess in the Galactic Centre, which could potentially originate from self-annihilating WIMP dark matter (Ackermann et al., 2017). The existence of constant density profiles near the centre of dark matter halo might also suggest the existence of self-interacting dark matter (e.g. Rocha et al., 2013; Harvey et al., 2019). Such searches have largely been motivated by the conclusive lack of detection of any dark matter candidate so far.

In Chapter 1, we discussed various galaxy cluster observables, particularly those in the X-ray range, typically for the purposes of providing robust cosmological constraints. Reports of a detection of a previously uncatalogued X-ray emission line with an energy between $3.55 - 3.57$ keV (hereafter referred to as 'the 3.5 keV line' based on Bulbul et al., 2014; Boyarsky et al., 2014), in galaxy clusters as well as other astrophysical systems, have invigorated a new use of X-ray cluster observations - as probes for dark matter. There is a suggested dark matter origin for the observed 3.5 keV line. Specifically, a 'sterile'

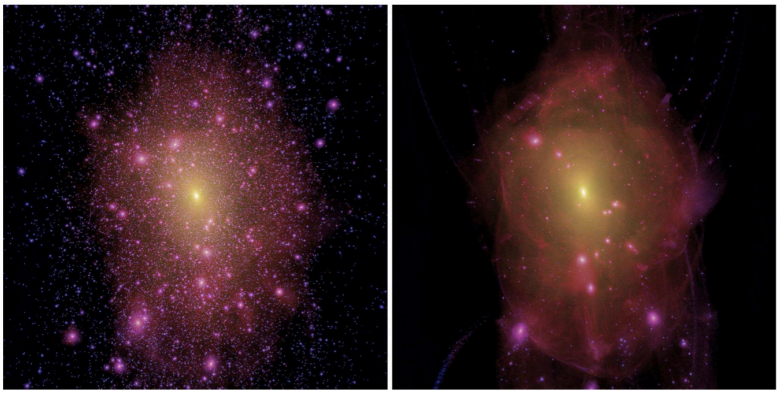

Figure 3.1: Figure and caption from Lovell et al. (2012). Images of the CDM (left) and WDM (right) high-resolution haloes at z = 0 from the Aquarius N-body haloes (Aq-A) simulation. Intensity indicates the line-of-sight projected square of the density, and hue the projected density-weighted velocity dispersion, ranging from blue (low velocity dispersion) to yellow (high velocity dispersion). Each box is 1.5 Mpc on a side. Note the sharp caustics visible at large radii in the WDM image, several of which are also present, although less well defined, in the CDM case.

neutrino with mass $m_s \simeq 7.1$ keV, would have an associated decay mode which results in the two-body state of an active neutrino and a photon with an energy $E = m_s/2$ (Pal and Wolfenstein, 1982).

The range of masses predicted for sterile neutrino dark matter are set by cosmological production mechanisms and its expected phase-space density. Based on the Tremaine-Gunn bound (Tremaine and Gunn, 1979), sterile neutrino dark matter is expected to be in the keV mass range, with $m_s \geq 400$ eV (Boyarsky et al., 2009). The lifetime $\tau_s$ of the sterile neutrino is given by

$$\tau_s \simeq 7.2 \times 10^{29} \text{ sec} \left( \frac{10^{-8}}{\sin^2 2\theta} \right) \left( \frac{1\text{keV}}{m_s} \right)^5 \tag{3.1}$$

where $\theta$ refers to the mixing angle between a sterile and active neutrino:

$$\theta^2 \leq 1.8 \times 10^{-5} \left( \frac{1\text{keV}}{m_s} \right)^5 . \tag{3.2}$$

Solving Equation 3.1 using the lower mixing angle bound results in an approximate lifetime of $\tau_s \geq 10^{24}$ sec (Boyarsky et al., 2009), making sterile neutrino dark matter a stable candidate on cosmological timescales. Moreover, the radiative decay from the sterile neutrino is expected to produce an emission line that would be observable in the $\gamma$/X-ray energy range. Motivated by the constraints displayed in Figure 3.2, the allowed

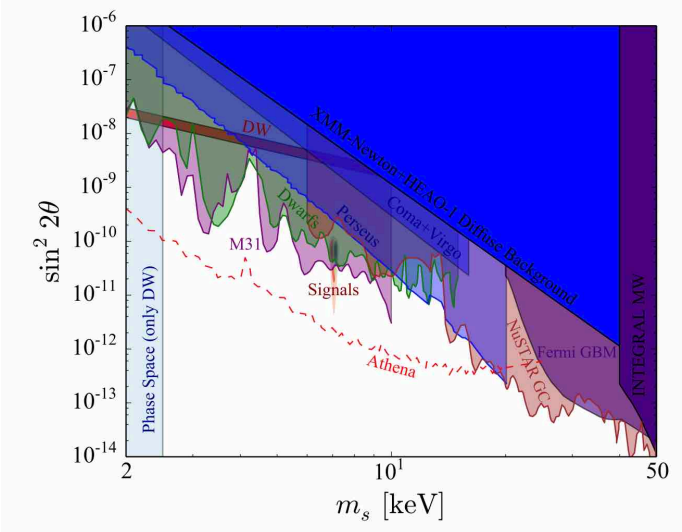


Figure 3.2: Figure and caption from Abazajian (2017) showing the full parameter space for sterile neutrino dark matter, when it comprises all of the dark matter. Among the most stringent constraints at low energies and masses are constraints from X-ray observations (M31), as well as stacked dwarfs. Also shown are constraints from the diffuse X-ray background, and individual clusters such as Coma + Virgo. The vertical mass constraint only directly applies to the Dodelson-Widrow model being all of the dark matter, labeled DW, which is now excluded as all of the dark matter. The Dodelson-Widrow model could still produce sterile neutrinos as a fraction of the dark matter. It also shows forecast sensitivity of the planned Athena X-ray Telescope

.

parameter space for sterile neutrino dark matter is compatible with $\gamma$/X-ray excesses in astrophysical systems. Moreover, sterile neutrino dark matter presents testable scenarios for its existence - through cluster, individual galaxy and satellite searches.

The first reported detection of the 3.5 keV emission line (Bulbul et al., 2014) resulted from the analysis of stacked spectra from 73 galaxy clusters between $0.01 < z < 0.35$ using *XMM-Newton* data. A subsequent independent analysis looking for the line in stacked *Suzaku* observations of 47 clusters between $0.01 < z < 0.45$ found weaker ($2\sigma$) evidence of a line (Bulbul et al., 2016). In addition, there have been several studies exploring the existence of the 3.5 keV line in the spectra of individual galaxy clusters. Bulbul et al. (2014) conducted a search for the line in Perseus, finding a detection but with an anomalously high flux, likely due to contamination from a nearby Ar XVII dielectionic recombination line at 3.62 keV. Urban et al. (2015) also found evidence of a 3.5 keV line in the core of the Perseus cluster, and, to a weaker extent, in the outskirts. Urban et al.

(2015) concluded that the flux ratio between the core and the outskirts is not compatible with a dark matter interpretation: the flux in the Perseus core is ∼14 times too high to be consistent with dark matter predictions. Furthermore, the constraint from the line flux in the core of Perseus is in tension with the flux derived from the *Suzaku* sample (without Perseus). Subsequent observations of the Perseus cluster by the *Hitomi* satellite failed to find evidence for a 3.5 keV line (Aharonian et al., 2017), although some authors have made counter arguments. Specifically, results from hydrodynamical simulations have stated that the non-detection of the line in Perseus is consistent with a dark matter interpretation, in part due to the exposure time in the *Hitomi* observation not being long enough to detect the likely flux of a dark matter decay line (e.g. Conlon et al., 2017; Lovell et al., 2019). Finally, an analysis of three X-ray bright clusters such as Coma, Virgo and Ophiuchus by Urban et al. (2015) also found no evidence of an excess at 3.5 keV.

There have been searches for the 3.5 keV line in X-ray observations besides those of clusters. For example, Boyarsky et al. (2014) claimed to have detected the 3.5 keV line in the X-ray spectrum of the Andromeda galaxy (M31), although a later study found a best fit X-ray spectrum for Andromeda to be consistent with no excess at 3.5 keV (Jeltema and Profumo, 2015). An unpublished paper by Boyarsky et al. (2018) claimed another detection using observations of the Galactic Centre (GC), although this detection had previously been deemed compatible with known plasma emission lines in the region of interest (Jeltema and Profumo, 2015). No line was conclusively detected in the GC using publicly available *Chandra* data (Riemer-Sørensen, 2016). Observations of the Galactic Bulge found $\sim 1.5\sigma$ evidence of a line albeit with a measured flux that is in tension with earlier detections (Hofmann and Wegg, 2019). A study analysing 10 Ms of data from the *Chandra* deep fields found marginal evidence of excess flux around 3.51 keV in the spectrum of the cosmic X-ray background at a significance between $2.5 - 3\sigma$ depending on the choice of statistics used (Cappelluti et al., 2018).

Notable non-detections of the 3.5 keV line in non-cluster X-ray observations include a stacked analysis of individual galaxies (Anderson et al., 2015), an analysis of stacked dwarf spheroidals (dSphs) from Malyshev et al. (2014), a deep observation of the Draco dSph (Jeltema and Profumo, 2016), and an analysis of 30 Ms of blank-sky *XMM-Newton* observations (Dessert et al., 2018). The deepest observations which have yielded non-detections appear to be inconsistent with a dark matter interpretation due to the tension with previously detected fluxes in clusters and the GC. Explanations that place the origin of the 3.5 keV line within the ICM suggest that it is a detection of a known elemental

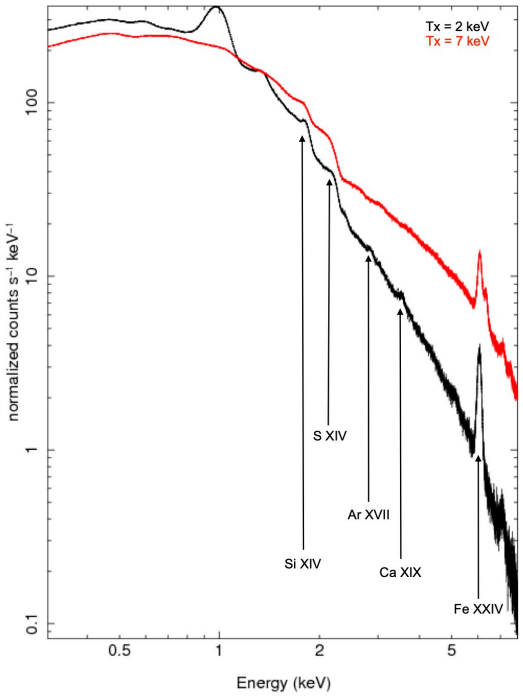


Figure 3.3: Simulated fake spectrum of a 2 keV (7 keV) cluster given by the black (red) line, using data generated by the fiducial plasma model described in Section 3.2. We demonstrate the weakening of known plasma transitions with temperature. The simulated cluster spectrum for both temperatures assumes a fixed abundance of $0.3Z_{\odot}$ and $z = 0.1$.

transition whose precise energy is not resolvable by current X-ray telescopes (Jeltema and Profumo, 2015), or charge exchange processes due to sulphur ions (e.g. Gu et al., 2015; Shah et al., 2016).

In this Chapter, we revisit the pioneering work in Bulbul et al. (2014) - hereafter B14 - by searching for the 3.5 keV line in *XMM-Newton* cluster spectra. Our cluster sample is larger than its precursor, 118 clusters, compared to 73 studied in B14, allowing us to examine the detectability of a 3.5 keV line as a function of X-ray temperature ($T_{\rm X}$), and hence, dark matter halo mass. If a 3.5 keV line is detected, and its flux increases with $T_{\rm X}$, then that would lend weight to a dark matter interpretation. However, if the flux weakens with $T_{\rm X}$, then an astrophysical origin would be more likely, since prominent emission lines in the $3-4$ keV region, e.g. K XVII, Ar XVII, K XIX, weaken with plasma temperature (see Figure 3.3 above, and Figure 4 and Figure 8 in B14 and Urban et al. (2015) respectively).

This Chapter is organised as follows. In Section 3.2 we describe the sample selection. In Section 3.3 we present the method used to test for the presence of a 3.5 keV line. Section

3.4 shows our results. Validation checks and implications of our results are detailed in Section 3.5. Conclusions are made in Section 3.6. In this Chapter, the parameters $R_{500}$ and $M_{500}$ are calculated with respect to the critical density ($\rho_c$) at the measured cluster redshift. We assume a flat ΛCDM cosmology with $H_0 = 70$ km s$^{-1}$ Mpc$^{-1}$, $\Omega_M = 0.3$ and $\Omega_\Lambda = 0.7$. Unless otherwise stated, we use the 68% ($1\sigma$) confidence level for all quoted errors in this analysis.

## 3.2 Sample selection

For this study, we used a subset of clusters drawn from a new sample of 482 clusters introduced in Chapter 2, which is to be published in Giles et al. (in prep, G20 hereafter). The G20 sample was developed by crossmatching the RM SDSS DR8 cluster catalogue (SDSSRM, Rykoff et al., 2014) with the public *XMM-Newton* data archive, where the X-ray data were processed as part of the *XMM* Cluster Survey (XCS, Romer et al., 2001).

Of the 482 clusters in the G20 sample consisting of genuine, physical matches between RM clusters and X-ray extended sources, 346 have reliable X-ray temperature measurements (i.e. $\Delta T_{\rm X}/T_{\rm X} < 0.25$) in the redshift range $0.1 < z < 0.6$ (lower redshift clusters are excluded because they extend over too much of the *XMM-Newton* FOV to allow in-field background subtraction). The X-ray temperatures were measured according to the method outlined in Section 2.6, however, we reiterate the salient points below. Temperatures are measured from spectra extracted in the $0.3 - 7.9$ keV energy band using circular source apertures with a radius of $R_{500}$, and annular background apertures spanning $1.05R_{500}$ to $1.5R_{500}$ (see Figure 3.4 for an example). The $R_{500}$ values are estimated following an iterative method using the $R_{500} - T_{\rm X}$ scaling relation from Arnaud et al. (2005). During the spectral fitting, three of the five parameters are frozen: the redshift at the value given in the SDSSRM catalogue (a photometric estimate based upon the RM analysis), the metal abundance at $Z_\odot = 0.3$ (a value typical for X-ray clusters, see Kravtsov and Borgani, 2012), and hydrogen column density, $n_{\rm H}$, at the value obtained from the HI4PI survey (Ben Bekhti et al., 2016). The remaining two parameters, $T_{\rm X}$ and normalisation, are fitted. The crossmatching process, X-ray spectral analysis and quality control methods for this sample are described extensively in Chapter 2.

For the purposes of the current study, we required high fidelity X-ray spectra. Therefore, rather than using all 346 clusters, we applied additional quality controls, detailed as follows. First, we re-derived $T_{\rm X}$ and $\Delta T_{\rm X}$ values using only data from the PN camera, and calculated associated $0.3 - 7.9$ keV signal-to-noise ratios. For reference, there are three

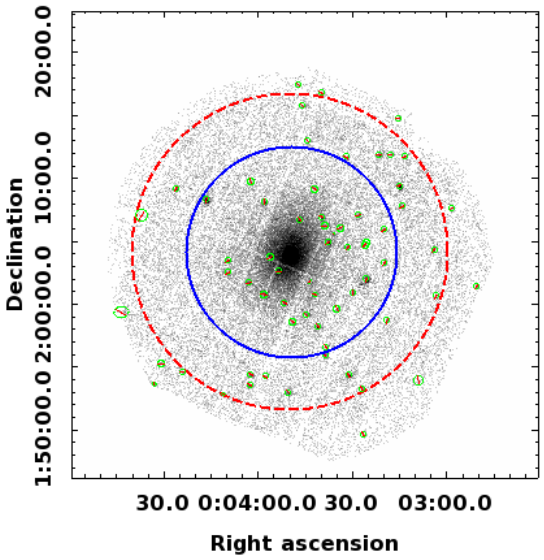


Figure 3.4: The PN+MOS1+MOS2 merged *XMM-Newton* image of XCS J0003.3+0204 in the 0.5–2.0 keV band. The source region is defined by the blue circle. The red dashed-circle defines the background region. Point sources are circled in green and excluded from the spectrum. This cluster is located at $z = 0.11$ in ObsID 0201900101. This cluster has a clear noticeable 3.5 keV excess. Its spectrum is shown in Figure 3.13

cameras in total on board *XMM* – PN, MOS1 and MOS2. The standard G20 spectral analysis uses all available data from the three instruments. After applying an upper limit of $\Delta T_{\rm X}/T_{\rm X}|^{\rm PN} = 0.1$, and a lower limit ratio of source to background counts (denoted by SNR) of $= 25$, 222 (of the original 346) clusters were excluded. The remaining spectra were then visually inspected to check for fitting anomalies. Six such anomalies were identified and the corresponding clusters were excluded from the analysis (these can be found in Appendix B.2 and diagnosed as an issue in Section 2.6). Following these quality controls, we were left with a sample of 118 clusters (see Table B.1). Figure 3.5 shows the distribution of X-ray temperature and RM determined redshift for the 118 clusters, and the boundaries of the four temperature bins as detailed above.

## 3.3 Methodology

### 3.3.1 Blueshifting to the rest frame

Before carrying out spectral fits (described in Sect. 3.3.2), the spectra are blueshifted (i.e. so that $z_{\rm effective} = 0$). This is not strictly necessary when examining individual clusters, but is required when performing joint fits. For joint fits, the blueshifting process has the

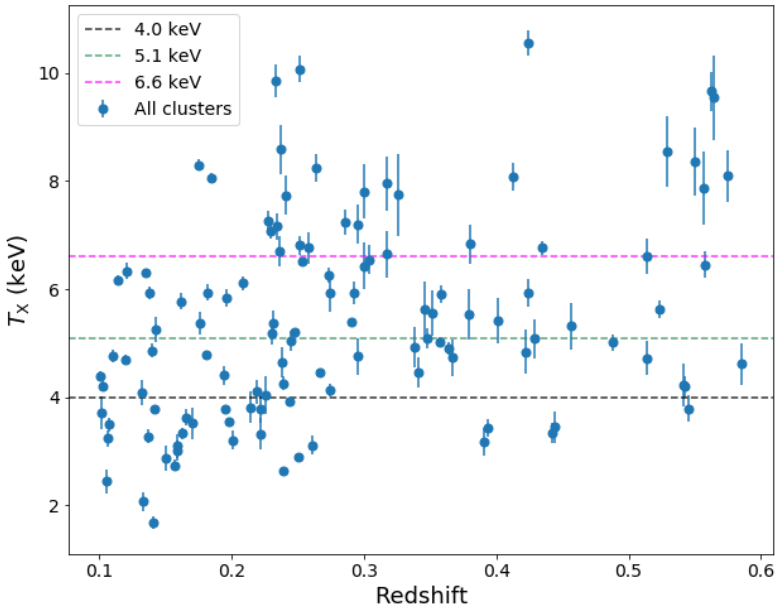


Figure 3.5: Temperature and redshift distributions of the 118 galaxy clusters in the analysis. The dashed lines indicate the boundaries used to define each of the four temperature bins. The median redshift of the cluster sample is $z = 0.25$.

| Bin number | $T_X$ bin (keV) | No. of clusters | $T_X$ average (keV) | $M_{DM}^{proj}$ average ($10^{14}$ $M_\odot$) | Fitted abundance $Z_\odot$ | SNR average | |
|---|---|---|---|---|---|---|---|
| | | | | | | 0.3 – 7.9 keV | 3.0 – 4.0 keV |
| 1 | $\leq 4$ | 30 | 3.24 | 1.88 | 0.24 | 89.6 | 14.7 |
| 2 | $4 - 5.1$ | 29 | 4.60 | 3.26 | 0.34 | 118.9 | 22.8 |
| 3 | $5.1 - 6.6$ | 28 | 5.82 | 4.92 | 0.20 | 179.0 | 37.1 |
| 4 | $\geq 6.6$ | 31 | 7.89 | 8.07 | 0.29 | 163.8 | 36.5 |

Table 3.1: Properties of the cluster sample according to binned X-ray temperature.

**Notes**. Column (1): Bin number; Column (2): temperature range of the bin; Column (3): number of clusters in bin; Column (4): average temperature of bin; Column (5) average projected dark matter mass ($M_{DM}^{proj}$); Column (6): fitted abundance; Column (7): average SNR in the 0.4 – 7.9 keV band; Column (8): average SNR in the 3.0 – 4.0 keV band.

additional advantage of 'smearing out' any redshift-independent instrumental artefacts that could be mistaken for astrophysical emission lines.

The format of a source spectrum measured by the detector is a list of photon counts as a function of channel number. The associated cluster response matrix file (`RMF`) and ancillary response file (`ARF`) contain the energy ranges corresponding to the source spectrum channels. Each cluster spectrum is blueshifted by rescaling the upper and lower energy bounds for each photon channel by a factor of $1 + z$. This shifts the number of photons associated with each energy according to the observed redshift of the cluster. Because the source and background spectra both rely on the `ARF` and `RMF`, modifications to both spectra are required to ensure consistency. We present a validation check of the blueshifting technique in Section 3.5.2. We note that our approach to blueshifting is the same as that used in B14.

### 3.3.2 Spectral fitting

We carry out three separate but related tests on the cluster spectra: the first is on the 118 clusters separately (Sect. 3.4.1) to determine any outliers with excess flux at $\simeq 3.5$ keV. The second is a joint fit to clusters binned into four different temperature bins (Sect. 3.4.2, with and without outliers). The third is a joint fit to the whole sample (minus the outliers, see Sect. 3.4.3). Each test is progressively more sensitive to the existence of a dark matter decay spectral feature. The second test also allows us to search for a potential mass dependence of a $\simeq 3.5$ keV feature, because $T_{\rm X}$ is a robust tracer of the underlying dark matter mass. Hence, evidence of an increase in a $\simeq 3.5$ keV flux excess with $T_{\rm X}$ would give firm support to the dark matter interpretation (and vice versa). For each test, we carry out a fit to a fiducial model ('model A': `tbabs` $\times$ `apec`) and then compare the goodness of fit to a model that includes an addition emission line component ('model B': `tbabs` $\times$ `(apec + weight` $\times$ `Gaussian)`) to mimic a dark matter decay feature. The fitting is performed using XSPEC version 12.10.1F (Arnaud, 1996), APEC version 3.0.9, and solar abundances based on Anders and Grevesse (1989). The XSPEC `cstat` command is used to define the goodness of fit to each model.

There are five parameters in model A. Three are frozen during the fit: the $n_{\rm H}$ value, the X-ray temperature (at the $T_{\rm X}^{\rm PN}$ value, see Sect. 3.2), and the redshift (at $z_{\rm effective} = 0$). Two are left free: the `apec` normalisation, and the metal abundance. During joint fits, the abundance is 'tied' across all the spectra being examined. This results in an average abundance per fit (see column 5 in Table 3.1). For both individual and joint fits, the

normalisation of the electron plasma density is fitted separately to each cluster.

There are nine parameters in model B. Five of these are shared with model A and treated in the same way during the fit. The remaining four parameters are associated with the Gaussian component: the central energy, line width, normalisation, and a constant weighting factor ($0 <$ `weight` $< 1$). The central energy is frozen at a value iterated between $3-5$ keV in intervals of 25 eV, i.e. 80 separate fits to model B are run for a given analysis. The line width is fixed at zero to mimic the narrowest possible line emission allowed by the energy resolution of the detector, which is in turn defined by the `ARF` matrix associated with the respective cluster spectrum. The normalisation is a free parameter but, like the metal abundance, is fitted jointly or 'tied,' generating an average fitted value per bin. The weighting factor is an input to the model, and frozen during the fit. Each cluster has a different assigned weight (described below).

We define the parameter $\Delta C$ to quantify the change in the goodness of fit between the two models at a given energy $E$, where $3 < E < 5$ keV (see above). $\Delta C$ is the difference between the value of the Cash statistic (Cash, 1979) after fitting for model A and the value after fitting for model B (see Section 3.3.4). A positive value of $\Delta C$ indicates that the fit is better for model B. The estimate for the $3\sigma$ threshold (i.e. the value of $\Delta C$ above which is considered a significantly better fit), is calculated based on the probability of exceeding 99.7% significance for model B compared to model A, taking into account the fact that model B has one additional degree of freedom.

### Differences to the B14 method

Our analysis differs from B14 in several ways. Firstly, we implement the `apec` plasma model using the standard approach, i.e. relying on predefined emissivities taken from AtomDB (Foster et al., 2012) to account for emission lines. B14 alternatively define a line-free `apec` plasma model with 28 Gaussian models added to account for emission lines (though some are later removed to improve convergence of their fits). Next, with respect to photoelectric absorption, we use the `tbabs` cross-sections, whereas B14 adopt the `wabs` values (see Sect. 3.5.2). Our methods also differ in the approach to background subtraction. We use an infield background subtraction method (see Sect. 3.2). B14 use a composite background model that accounts for contributions from the quiescent particle background, the cosmic X-ray background, solar wind charge exchange, as well as residual contamination from soft protons. Furthermore, we use the $\Delta C$ parameter to assess the change in the goodness of fit between model A and B (following a similar analysis

undertaken by Urban et al., 2015), whereas B14 uses a $\chi^2$ approach.

Whilst we fit each spectrum in parallel when performing joint fits, B14 stack their data into a composite spectrum first. The advantage of our method is that it allows us to explore the influence of individual spectra on the joint fit (see Sect. 3.3.2). Moreover, in our study, we have focused on *XMM*-PN data, whereas B14 also fitted to *XMM*-MOS, as well as analysing the *Chandra*-ACIS spectra of Virgo and Perseus.

Finally, when searching for evidence of a 3.5 keV feature, the energy values in our analysis are frozen in intervals of 25 eV (e.g. 3.5, 3.525, 3.55, 3.575, 3.6 etc.) whereas B14 nominally compute a best fitted value for their energy of an unidentified line in their stacked spectrum. However, we note that out of the 14 fits in their study, best fitted values are only computed for the full *XMM* PN and MOS samples. Stacked spectra consisting of fewer clusters subsequently assume a fixed energy at 3.57 keV. Similarly, for the *Chandra* ACIS spectra, a best fitted energy is computed for Perseus, and subsequently frozen at 3.56 keV in the *Chandra* spectrum of Virgo.

### Dark matter flux and weighting

If a flux excess (over the fiducial model A) originates from dark matter decay, then for a given cluster, we would expect the flux to increase with the projected dark matter mass in the *XMM* FOV, $M_{\rm DM}^{\rm proj}$, but to decrease with cluster redshift, $z$. To account for this, $M_{\rm DM}^{\rm proj}$ and $z$ dependent weights are applied during the joint spectral fits. The $M_{\rm DM}^{\rm proj}$ values are defined within a radius $R_{\rm ext} = R_{500}$, i.e. the same extraction aperture as the PN spectrum (stated in Sect. 3.2). The total masses for the clusters are estimated by applying the $M_{500} - T_{\rm X}$ scaling relation described in Arnaud et al. (2005). These are then corrected for the fact that the dark matter accounts for only 85% of the total mass, such that

$$M_{\rm DM}(R_{\rm ext}) = M_{\rm tot}(R_{\rm ext}) - M_{\rm gas}(R_{\rm ext}) - M_{*}(R_{\rm ext}). \tag{3.3}$$

where we assume that the total contribution of gas and stellar mass to the overall cluster mass is approximately $0.15 M_{\rm tot}$, which is a suitable approximation for radii $\geq R_{500}$.

Going from the spherical dark matter mass, the projected dark matter mass within a $R_{500}$ cylinder is larger than that within a sphere (see Figure 3.6). The projected mass is computed assuming an NFW halo profile, following the method in Łokas and Mamon (2001),

$$M_{\rm i,DM}^{\rm proj} = \frac{1}{\ln(1+c) - \frac{1}{1+c}} M_{\rm i,500} \frac{\cos^{-1}(1/c)}{|c^2-1|^{1/2}} + \ln\left(\frac{c}{2}\right). \tag{3.4}$$

The chosen concentration parameter for clusters is $c_{500} = 3$ based on the average concentration for each bin, according to the $c_{500} - M_{500}$ scaling relation described in Vikhlinin et al. (2006). We justify the use of a constant concentration value due to the limited sensitivity to the overall flux from the concentration, particularly when the mass range within each bin is small. We therefore assume self-similarity in the density profiles of clusters, and a constant value for the mean concentration.

The projected dark matter mass for each individual cluster is stated in column 4 in Table B.1. The average projected dark matter mass for each temperature bin is stated in column 4 of Table 3.1.

For the joint fits, to account for a different dark matter contribution from each cluster, we apply a weighting to each cluster during the fits to model B. We calculate the weighting $w_i$ from each cluster $i$ in a given temperature bin according to

$$w_{\rm i,DM} = \frac{M^{\rm proj}_{\rm i,DM}(< R_{\rm ext})(1+z_i)}{4\pi d^2_{i,L}}, \tag{3.5}$$

where $d_{i,L}$ is the luminosity distance at $z_i$. Before the fitting to model B takes place, the individual cluster weights $w_{\rm i,DM}$ are normalised by the largest value in the chosen bin, i.e. one cluster per bin has a `weight = 1`, while remaining clusters have $0 <$ `weight` $< 1$. During the fits to individual clusters, the weighting is assigned to unity.

### 3.3.3 Estimation of sterile neutrino mixing angles

If a measured flux excess is due to dark matter decay, we can estimate a sterile neutrino mixing angle using the Gaussian line normalisation taken from the fit to model B. For this we use the B14 relation between decaying dark matter flux, $F_{DM}$ and projected dark matter mass,

$$\sin^2 2\theta = \frac{F_{\rm DM}}{12.76{\rm cm}^{-2}{\rm s}^{-1}} \left(\frac{10^{14} M\odot}{M^{\rm proj}_{\rm DM}}\right) \left(\frac{d_L}{100\,{\rm Mpc}}\right)^2 \left(\frac{1}{1+z}\right) \left(\frac{\rm keV}{m_s}\right)^4. \tag{3.6}$$

### 3.3.4 Use of Cash statistics

This study uses Cash statistics (Cash, 1979) instead of a $\chi^2$ distribution to estimate the best-fit values of the model and corresponding fit improvements. Cash statistics are chosen because the spectral data consists of detected counts, which follow a Poisson distribution. Furthermore, each cluster spectrum in the sample is grouped to have a minimum of five counts per bin. Given that in order to use a $\chi^2$ distribution to assess the goodness of fit of a chosen model, one requires Gaussian statistics and an approximate minimum of 20 counts per bin (a threshold beneath which Gaussian approximations are considerably worse, the

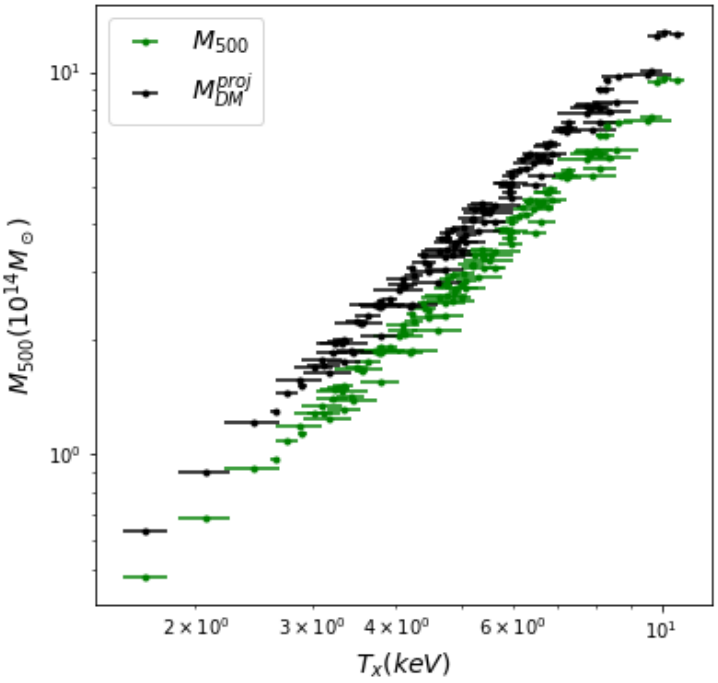


Figure 3.6: The distribution of calculated $M_{\rm DM}$ values for the sample (in green) and the projected $M_{\rm DM}^{\rm proj}$ (in black). The difference in normalisation for both masses is due to the projected mass constituting an integrated dark matter distribution along the line of sight, leading to an increased value for a given $T_{\rm X}$.

Cash statistic is an appropriate choice for this analysis (Kaastra, 2017; Bonamente, 2019). Interestingly, it has been stated that even in the regime of high spectral counts per bin, use of a $\chi^2$ distribution to model Poissonian data can produce systematic biases in parameter estimates (Humphrey et al., 2009). For previous 3.5 keV studies which have utilised the Cash statistic, see Aharonian et al. (2018), Urban et al. (2015), and Cappelluti et al. (2018). Details on the implementation of the Cash statistic within XSPEC can be found in the manual[1], which is based on Arnaud (1996).

The maximum likelihood-based statistic for Poisson data, e.g. source counts within an X-ray spectrum follows from Cash (1979). However, since each source spectrum has its background spectrum subtracted prior to fitting, a modification to the Cash statistic is required. This is because the difference of two Poisson variables (the source and background counts) is not a Poisson variable. In this case, a combined likelihood can be written for both the source and background observation. A profile-likelihood, $W$, can be written for a case in which there is a source and background observation, without a specified model for the background (Equation 3.7). The $W$ statistic is a suitable proxy for a Cash statistic in the case of background-subtracted Poisson-distributed data. In practice, the $W$ statistic is successful provided every bin contains at least one count. Given that our spectral grouping requires a range of 1 to 5 counts per bin in both the source and background spectra, this is a suitable assumption. In the limit of large numbers of counts per bin, the $W$ statistic, similar to the Cash statistic, behaves identically to a $\chi^2$ distribution.

$$W = 2\sum_{i=1} t_s m_i + (t_s + t_b) f_i - S_i \ln(t_s m_i + t_s f_i) - B_i \ln(t_b f_i) - S_i(1 - \ln S_i) - B_i(1 - \ln B_i) \tag{3.7}$$

The $W$ likelihood is a function of several parameters. This includes the data counts of the source and background spectrum, $S_i$ and $B_i$, and corresponding exposure times, $t_s$ and $t_b$. The parameter $m_i$ describes the predicted count rate based on the current model and instrumental response. Finally, $f_i$ encompasses information about the background model when there is no appropriate model provided. The likelihood yields valid solutions in the limit of zero source and background counts, while in the limit of large counts per spectral bin, can be Taylor expanded to second order to replicate a $\chi^2$ distribution.

[1] https://heasarc.gsfc.nasa.gov/xanadu/xspec/manual/

## 3.4 Results

### 3.4.1 Fits to individual clusters

To look for evidence of a $\simeq$ 3.5 keV feature in individual cluster observations, as has previously been reported from Perseus (e.g. B14, Urban et al., 2015; Franse et al., 2016), we perform a $\Delta C$ analysis on each of the 118 clusters in our sample, using the methodology described in Section 3.3.2. We find evidence for a $> 3\sigma$ fit improvement at $\simeq$ 3.5 keV in three cases: XMMXCS J000349.3+020404.8 (hereafter XCS J0003.3+0204), XMMXCS J141627.7+231523.5 (hereafter XCS J1416.7+2315) and XMMXCS J222353.0-013714.4 (hereafter XCS J2223.0-0137). The results are shown in Figure 3.7. For each cluster, the top panel shows $\Delta C$ as a function of energy, and the bottom panel shows the corresponding normalisation of the Gaussian line component in units of photons cm$^{-2}$s$^{-1}$. The horizontal blue shaded area in the top panels represents the $< 3\sigma$ region. The vertical green bars in both top and bottom panels span $3.50 - 3.60$ keV, which indicates the expected energy range in which a $\simeq$ 3.5 keV line would be detected assuming the appropriate spectral resolution for the instrument. All prior detections of the 3.5 keV feature have quoted a best fit energy firmly within this range, hereafter known as 'the region of interest.'

For XCS J0003.3+0204 (XCS J1416.7+2315), the largest fit improvement occurs at 3.55 (3.6) keV, characterised by $\Delta C = 13.4$ (9.17) and a corresponding Gaussian line flux of $1.12^{+0.31}_{-0.31} \times 10^{-5}$ ($6.14^{+2.02}_{-1.99} \times 10^{-6}$) photons cm$^{-2}$ s$^{-1}$. For XCS J2223.0-0137, the maximum value of $\Delta C$ falls below the region of interest, although still exceeds $3\sigma$ therein. Further discussion of XCS J1416.7+2315, XCS J0003.3+0204, and XCS J2223.0-0137 can be found in Sections 3.5.1, 3.5.1, and 3.5.1, respectively.

The sterile neutrino mixing angle estimates for XCS J0003.3+0204 and XCS J1416.7+2315 are given in Table 3.2. We do not provide this information for XCS J2223.0-0137 because, from Figure 3.5.1, the shape of the flux excess found in this cluster is unlikely to indicate the presence of a discrete emission feature (see Sect. 3.5.1). We note that the estimated $\sin^2\theta$ values (of order $\times 10^{-9}$) are significantly larger than those measured by B14, based on the PN-only result for their full sample as well as individual clusters, i.e $4.3^{+1.2}_{-1.0} 10^{-11} < \sin^2\theta < 1.9 \times 10^{-10}$ (as quoted in Table 5 of B14).

### 3.4.2 Joint fits to sub-samples binned by temperature

To test for a potential temperature dependence of the strength of a $\simeq$ 3.5 keV flux excess, the 118 clusters in the sample were subdivided into four temperature bins: $\leq$4 keV,

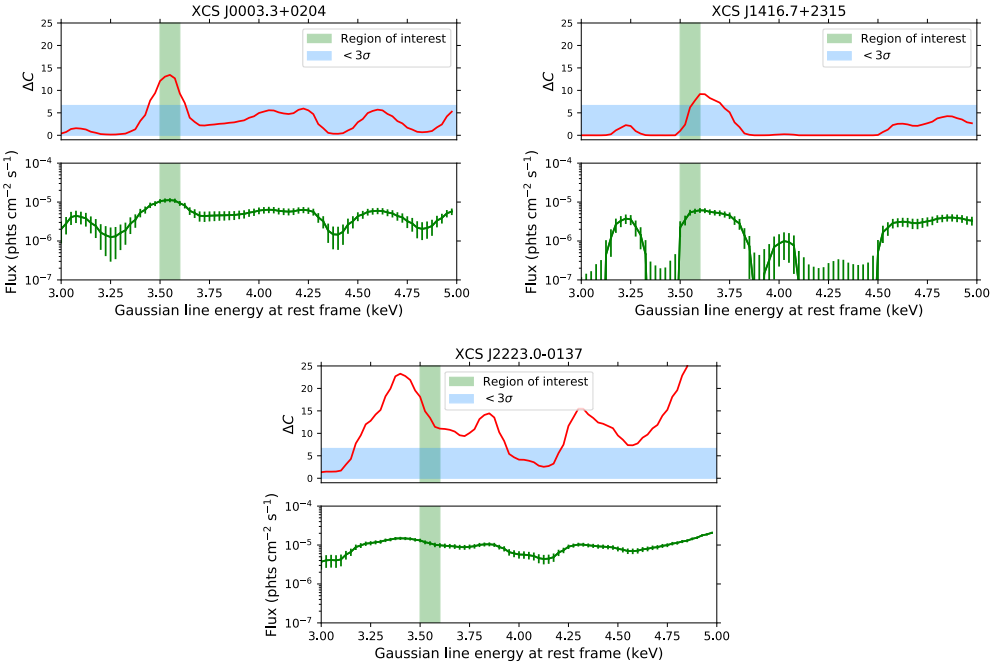


Figure 3.7: Top panels (red line): The change in fit statistic ($\Delta C$) between model A and model B (see Sect 3.3.2) as a function of energy in the range $3-5$ keV. Bottom panels (green line): Fitted normalisation of the Gaussian line and corresponding errors. The value of $\Delta C$ determines the extent to which model B is a better fit to the data than model A. In each plot, the green shaded region encloses the 3.5 – 3.6 kev range (where a potential DM signal is expected), defined as the 'region of interest.' The light blue shaded region determines a $<3\sigma$ detection (see Sect. 3.4 for definition). The top left, top right and bottom plots refer to the clusters XCS J0003.3+0204, XCS J1416.7+2315, and XCS J2223.0-0137 respectively.

| Sample | Line energy (E) (keV) | $\Delta C$ | Flux ($10^{-6}$ photons cm$^{-2}$ s$^{-1}$) | $M_{DM}^{proj}/d_L^2$ ($10^{10}$ $M_\odot$ Mpc$^{-2}$) | Mixing angle ($\sin^2 2\theta$) |
|---|---|---|---|---|---|
| XCS J0003.3+0204 | 3.55 | 13.4 | $11.2^{+0.31}_{-0.31}$ | 0.14 | $2.36^{+0.65}_{-0.65} \times 10^{-9}$ |
| XCS J1416.7+2315 | 3.6 | 9.17 | $6.14^{+1.99}_{-2.02}$ | 0.05 | $3.78^{+1.24}_{-1.23} \times 10^{-9}$ |
| Bin 2 (29 clusters) | 3.5 | 11.8 | $4.17^{+1.22}_{-1.22}$ | 0.65 | $1.97^{+0.58}_{-0.58} \times 10^{-10}$ |
| 115 clusters | None | None | 2.39 | 1.65 | $4.3 \times 10^{-11}$ |

Table 3.2: Measured properties of the 3.5 keV line for all reported detections.

$4-5.1$ keV, $5.1-6.6$ keV, $\geq$6.6 keV, containing 30, 29, 28 and 31 clusters respectively. For simplicity, hereafter we refer to these temperature bins as bin 1 ($\leq$4 keV), bin 2 ($4-5.1$ keV), bin 3 ($5.1-6.6$ keV) and bin 4 ($\geq$6.6 keV). Properties of the bins, averaged according to the number of clusters, can be found in Table 3.1. In Figure 3.8 we present the results of the $\Delta C$ analysis of each the four temperature bins, after removing the three cases shown in Figure 3.7.

No significant fit improvement is found in any bin in the region of interest, i.e. the range defined by the vertical green bar. We note that within the four bins, there are other ranges of $\Delta C$ values that exceed a $3\sigma$ improvement of model B over model A. These regions correspond to energies where there are known astrophysical lines (e.g. Ar XVII complex with the strongest line at 3.32 keV, Ca XIX at 3.86 keV & 3.90 keV, Ca XX at 4.1 keV, and Ca XIX at 4.58 keV). Two prominent instrumental lines are also present; the Ti K$\alpha$ at 4.51 keV, and Ti K$\beta$ at 4.93 keV (see Jeltema and Profumo, 2016). Even though the aforementioned plasma lines are included in the latest version of the APEC model, APEC does not always correctly predict their relative fluxes as a function of plasma temperature and metal abundance (see e.g. Aharonian et al., 2018), hence fit improvements at the location of known emission lines are not unexpected. Analysis of the Perseus core in Urban et al. (2015) has suggested underestimates of the abundances of elements including Ca XIX and Ti XXII (unresolved lines at 4.97 keV and 4.98 keV), the latter of which is responsible for a high $\Delta C$ value at $\simeq 4.9$ keV in each bin (Fig. 3.8).

For completeness, we repeated the joint analysis of bins 1 and 2 with the clusters featured in Figure 3.7 included (see Fig. 3.9). In Figure 3.9 (b), when XCS J2223.0-0137 and XCS J0003.3+0204 are included in bin 2, there is now a $> 3\sigma$ fit improvement within the region of interest. The maximal fit improvement is found when the central line energy is frozen at $E = 3.50$ keV, characterised by a $\Delta C = 11.8$ and corresponding Gaussian line flux of $4.17^{+1.22}_{-1.22} \times 10^{-6}$ photons cm$^{-2}$ s$^{-1}$, corresponding to a mixing angle of $1.97^{+0.58}_{-0.58} \times 10^{-10}$ (see Table 3.2).

To further investigate the influence of individual clusters on the joint fit in each bin, a jackknifing resampling procedure was performed: for a temperature bin containing $N$ clusters, we perform $N$ fittings in each bin containing $N-1$ clusters at 5 equally spaced values of the central Gaussian line energy ($3.5 < E < 3.6$ keV). The subsequent increase or decrease in the value of $\Delta C$ from each of these re-runs quantifies the dominance of $\simeq 3.5$ keV photons in each individual spectrum. We find that the jackknifed iterations in bins 1, 3 and 4 do not result in a significance change in the $\Delta C$ values in the region of interest.

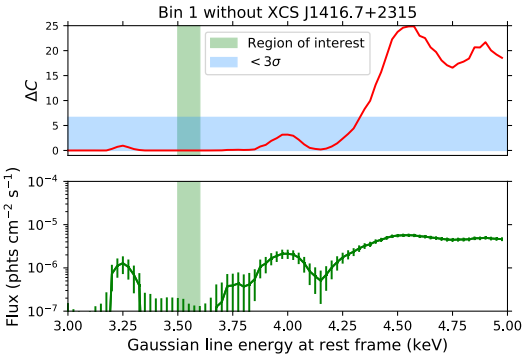


(a)

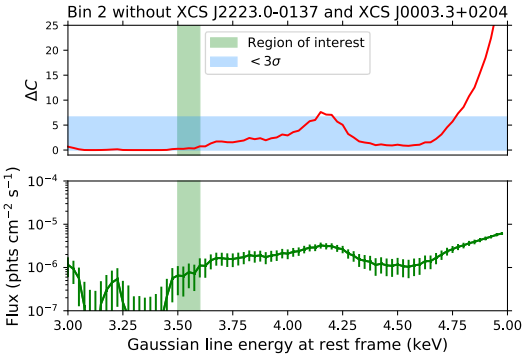


(b)

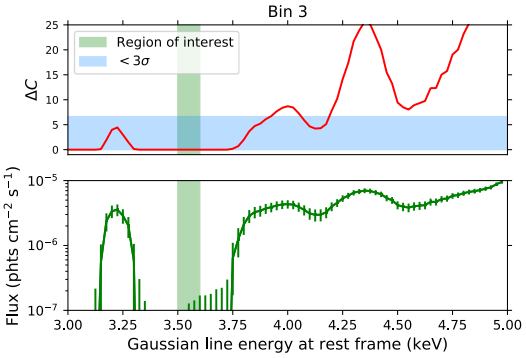


(c)

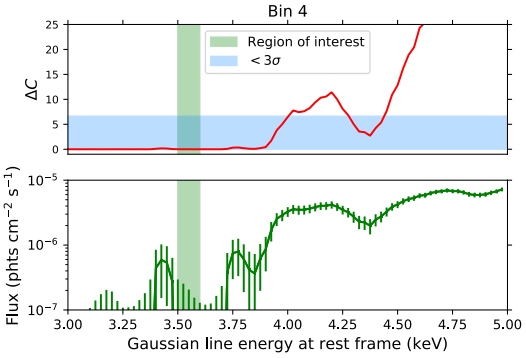


(d)

Figure 3.8: Similar to Figure 3.7. Results from the binned subsets (see Table 3.1) of clusters excluding those with detected excess at ≃3.5 keV. (a): 29 clusters from bin 1 (i.e. excluding XCS J1416.7+2315). (b): 27 clusters from bin 2 (i.e. excluding XCS J0003.3+0204 and XCS J2223.0-0137). (c) 28 clusters from bin 3. (d) 31 clusters from bin 4.

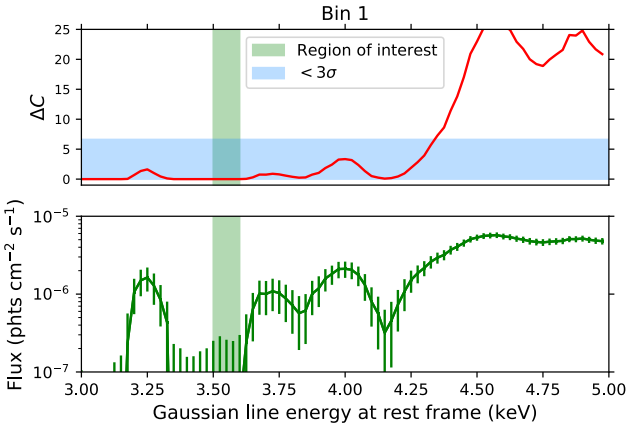


(a)

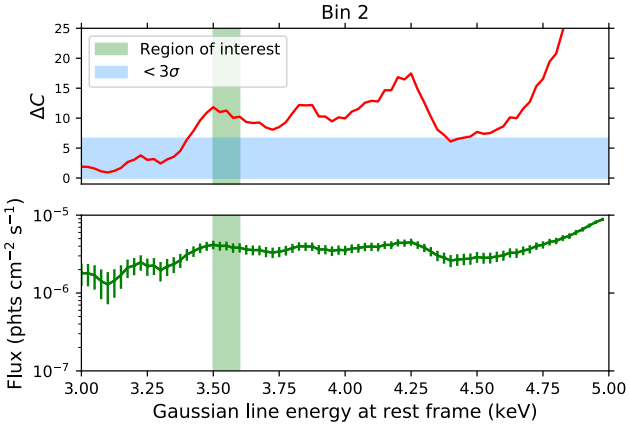


(b)

Figure 3.9: Similar to Figure 3.8, but showing the results from the binned subsets of clusters whilst including those with detected excess at ≃3.5 keV (see Table 3.1). (a): All 30 clusters in bin 1 (i.e. including XCS J1416.7+2315). (b): All 29 clusters in bin 2 (i.e. including XCS J0003.3+0204 and XCS J2223.0-0137).

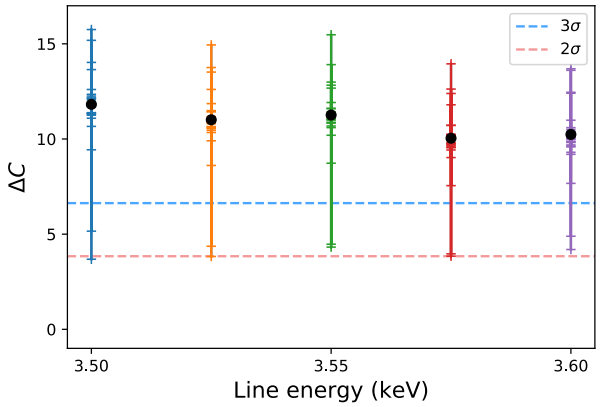


Figure 3.10: Variation of $\Delta C$ during a jackknife analysis performed at five energy intervals between 3.5 and 3.6 keV in bin 2 (all 29 clusters included). The black data points refer to the value of $\Delta C$ with all clusters included (i.e. the fitted value in Fig. 3.9(b)). Each tick-mark refers to the value of $\Delta C$ when a cluster is removed.

However, in bin 2, where there is evidence for a $\simeq 3.5$ keV excess in the joint fit when all 29 clusters are included, we find a significant variation in $\Delta C$ during the jackknifing (Fig. 3.10). This strongly implies that the detection of a $\simeq 3.5$ keV excess in Figure 3.9(b) is being driven by a subset of the clusters in the bin and is not a global feature.

### 3.4.3 Joint fits to the full sample

To obtain the highest possible sensitivity to a spectral feature arising from dark matter, we have carried out joint analysis using all 115 clusters without an individual $\simeq 3.5$ keV excess. In this case, flux errors were only calculated in the region of interest due to the excessive computation required. The results are presented in Figure 3.11. No significant improvement in the fit is found in the region of interest. To demonstrate that this lack of evidence is not a reflection of a lack of sensitivity, we have included on the lower panel of Figure 3.11 an estimate of the $3\sigma$ upper limit on the flux (dashed purple line) of $F_{\rm DM} = 2.39 \times 10^{-6}$ photons cm$^{-2}$ s$^{-1}$. The $3\sigma$ upper limit corresponds to the measured flux where the fit improvement (red line) is equivalent to the $3\sigma$ threshold for a detection (blue band). We assume negligible impact from the `ARF` on the flux limit across the specified energy range.

The 115 clusters in the joint fit have a weighted mass per distance squared of $1.65 \times 10^{10} M_{\odot}$ Mpc$^{-2}$, which corresponds to a maximum mixing angle, $\sin^2 2\theta = 4.3 \times 10^{-11}$. This is the most stringent mixing angle constraint obtained from our analysis - it is well below

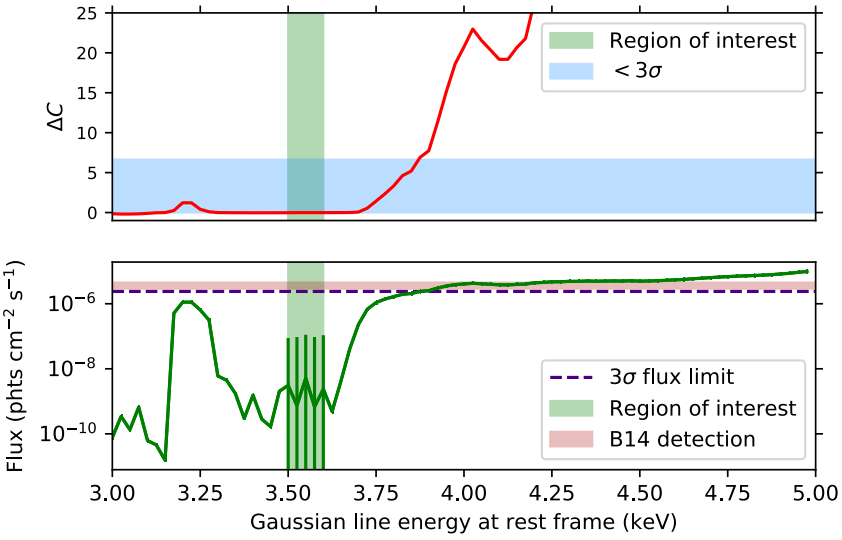


Figure 3.11: Similar to Figure 3.8 showing the trend in $\Delta C$ using 115 clusters in the sample, minus the three clusters with known flux excess at $\simeq 3.5$ keV – XCS J0003.3+0204, XCS J1416.7+2315 and XCS J2223.0-0137. In the bottom panel, the pink horizontal shaded region shows the constraints from B14 for 73 clusters (using PN data only). The dashed purple line corresponds to the $3\sigma$ flux limit defined for the sample. The green bars represent errors computed within the region of interest. The fitted abundance for this analysis was $Z = 0.24 Z_{\odot}$.

the values in Table 3.2 for individual clusters and bin 2 (with all 29 clusters included). Comparisons with the B14 analysis are indicated in the bottom panel of Figure 3.11, where the the red shaded region highlights the flux estimate obtained on the $\simeq 3.5$ keV line using the stacked PN spectrum of 73 clusters. As can be seen in the plot, the upper limit of the flux as a function of energy (given by the dashed purple line) is $2\sigma$ below the preferred B14 value for the line using *XMM*-PN data of 73 clusters ($\sin^2(2\theta) = 6.7^{+2.7}_{-1.7} \times 10^{-11}$).

### 3.4.4 False-positive rate

The methodology presented in Section 3.3 requires a statistically significant excess to display a $3\sigma$ deviation from the baseline model. However, the impact of false positive detections within the region of interest must also be considered. As stated above, the model is iterated over 80 energy intervals between 3.5 – 3.6 keV. Assuming each of these intervals are independent, we measure a total of 9440 ($118 \times 80$) intervals across the entire analysis. Therefore, we expect a $3\sigma$ excess at approximately 28 ($0.003 \times 9440$) energy intervals across the entire sample simply as a result of random noise in the cluster spectra. However, due

to the spectral uncertainty in the resolution of the *XMM* instrument, these energy bins are not strictly independent from one another. We estimate that approximately 20 (80 intervals at a resolution of 25 eV, hence 20 intervals at a resolution of 100 eV) bins are fully independent, yielding a $3\sigma$ excess in approximately 7 ($0.003 \times (118 \times 20)$) energy bins in total across the region of interest. This is below the observed number of energy intervals that exceed $3\sigma$, as demonstrated in each of the three individual clusters. Therefore we conclude that the presence of an excess in these clusters is not a purely statistical artefact, but rather a physical feature (whose potential origin is described in Section 3.5) which persists specifically in the spectrum of XCS J0003.3+0204, XCS J1416.7+2315 and XCS J2223.0-0137.

## 3.5 Discussion

It is clear from Figures 3.8, 3.9, 3.10, and 3.11 that a $\simeq 3.5$ keV flux excess is not a ubiquitous feature in cluster spectra. As Figure 3.9(b) shows, where a flux excess exists, its strength does not increase with cluster temperature (and hence halo mass). Therefore, it seems unlikely that these and previously reported '3.5 keV line' detections have a dark matter origin. In this section we investigate possible reasons why three clusters show an excess of emission at $\simeq 3.5$ keV (Section 3.5.1), and test the robustness of our analysis methods, to ensure that these are not somehow artificially masking a feature related to dark matter decay (Section 3.5.2).

### 3.5.1 Individual clusters with excess emission at $\simeq 3.5$ keV

#### XCS J0003.3+0204

The cluster XCS J0003.3+0204 (better known as Abell 2700, Abell, 1958b), and first identified in X-rays by ROSAT (Ebeling et al., 2000b) has a RM ID = 2789, a RM redshift of $z_{\rm phot}^{\rm RM} = 0.11$ and a RM richness of $\lambda = 38.9$. This well-studied cluster is not reported as having AGN activity or any distinct morphological or galaxy properties (e.g. Ettori et al., 2015b; Lovisari and Reiprich, 2018; Böhringer et al., 2007, 2010; Holland et al., 2015). The best fit temperature and metallicity (following method A, see Sect. 3.2) are $T_{\rm X}^{\rm PN} = 4.78^{+0.12}_{-0.12}$ keV and $Z = 0.4^{+0.04}_{-0.04} Z_{\odot}$ respectively. The fit values quoted here are based on *XMM*-PN observation ObsID `0201900101` (Figure 3.4). This observation was made on 2004-06-24, and has a flare corrected exposure time of 19 ks. We note that the rate of flaring in the raw events file is less than 2% for this observation. There

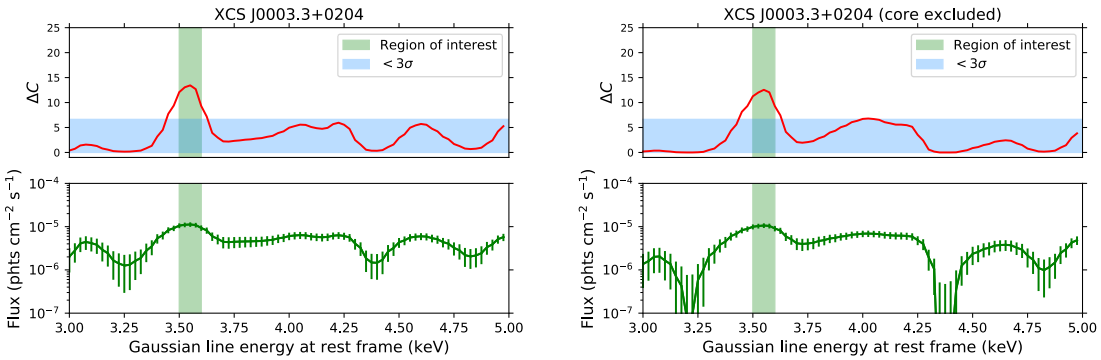


Figure 3.12: Plots showing the trend in $\Delta C$ (see Fig. 3.8 for full description) for the cluster XCS J0003.3+0204. The left plot displays the analysis using a spectrum with the core-included (i.e. our standard analysis) and the right plot shows the trend using a spectrum with the core region excluded (see Sect. 3.5.1).

are no other *XMM*-PN observations available for this cluster, so we cannot investigate any possible variability in the $\simeq$ 3.5 keV excess for this cluster. A comparison of the $\Delta C$ analysis between the original spectrum and one where the core region $r < 0.15R_{500}$ is excluded, is shown in Figure 3.12. We find that the shape of the $\simeq$ 3.5 keV excess is largely insensitive to the removal of the $r < 0.15R_{500}$ region. Finally, we check all available MOS data for XCS J0003.3+0204 for evidence for a 3.5 keV feature. Given the MOS camera is approximately half as sensitive as the PN, we do not expect to detect a feature at the same significance. The comparison of PN and MOS data for this cluster is shown in Figure 3.16(a). We observe a feature of similar shape in the MOS2 data at a slightly higher energy ($\simeq$ 3.6 keV), however, there is no clear evidence of a feature within the region of interest.

From the existing analysis/data, it is not possible to unambiguously explain the flux enhancement at $\simeq$ 3.5 keV in XCS J0003.3+0204. It is unlikely that the enhancement is related to background flare contamination, since ObsID `0201900101` is one the cleanest of the sample (of 118). The symmetrical shape of the $\Delta C$ feature, and the fact that an enhancement is visible in the spectrum (Fig. 3.13), supports the interpretation that this is a genuine astrophysical emission feature, either from the cluster itself, or from a system along the line of sight. Despite this feature being stronger than would be expected from dark matter decay, it is not obvious that the excess is the result of a plasma transition or charge exchange process, since such a feature would also be present in other systems. One interpretation for this excess could lie in the treatment of point sources in the spectrum of XCS J0003.3+0204. As shown in Figure 3.4, all point sources have been masked from the

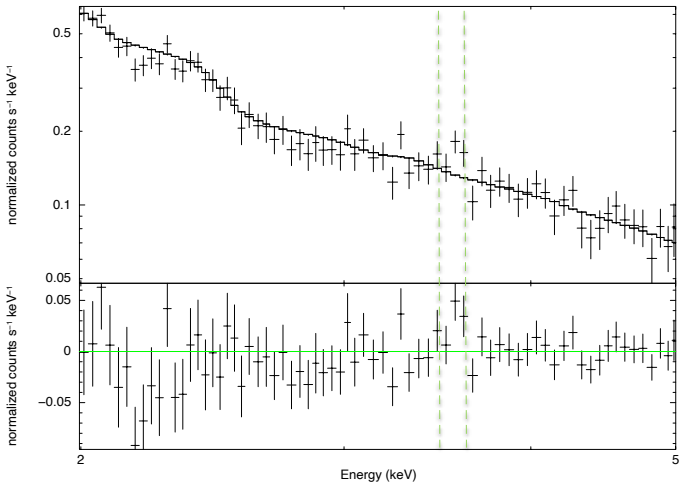


Figure 3.13: Spectrum of the cluster XCS J0003.3+0204 (located in ObsID `0201900101`) fitted using model A outlined in Section 3.3.2. The top panel shows the spectrum and fitted model across the $2-5$ keV energy range. The bottom panel shows the the residuals i.e. the difference between the model and the spectrum. For visual purposes, the spectrum has been grouped such that each bin has a SNR $\geq 15$. The dashed green lines enclose the $3.5-3.6$ keV region of interest.

cluster observation. However, it is possible that some excess point source emission is persisting within the source region, which is responsible for the anomalously high (compared to dark matter) flux in this cluster at $\simeq 3.5$ keV. To examine whether the 3.5 keV feature originates from point source emission, the spectrum of each point source in the vicinity of XCS J0003.3+0204 would need to be extracted and studied for such an excess.

This cluster is the only one of the 118 that displays a conclusive 3.5 keV feature at the $> 3\sigma$ level, so it is rare. Specifically, the detection of a 3.5 keV feature in XCS J0003.3+0204 constitutes only the second ever detection of a line in a single cluster (the first being Perseus). To examine just how rare, we plan to apply our $\Delta C$ technique to the other 228 (346-118) clusters with measured $T_{\rm X}$ values in the G20 sample.

### XCS J1416.7+2315

The cluster XCS J1416.7+2315 (first detected in X-rays by ROSAT, e.g. Ebeling et al., 2000b), and also known as RX J1416.4+2315 (Romer et al., 2000) has a RM ID=5527, a RM redshift of $z^{\rm RM}_{\rm phot} = 0.137$ and a RM richness of $\lambda = 31.7$. Based upon the best fit parameters to the *XMM*-PN spectrum using model A, described in Section 3.2, the cluster has a measured temperature and metallicity of $T^{\rm PN}_{\rm X} = 3.28^{+0.12}_{-0.12}$ keV and $Z = 0.17^{+0.05}_{-0.05} Z\odot$

respectively. It is noteworthy that this system has a comparatively low metal abundance compared to the average obtained in bin 1 (see column 5 of Table 3.1). The $\simeq 3.5$ keV excess, i.e. the region where the $\Delta C$ value is $> 3\sigma$ is significantly wider than the spectral energy resolution of the *XMM*-PN detector ($\Delta E = 88$ eV).

The analysis presented in Section 3.4.1, and the best fit temperature and abundance quoted above, are based on the *XMM* observation with ObsID `0722140401`. This observation was taken on 2014-01-31, and has a cleaned exposure time of 18 ks. However, this cluster has been the target of another *XMM* observation (`0722140101`). This observation was made on 2014-01-03, and has a flare corrected exposure time of 4 ks. The availability of two observations of the same cluster, made roughly a month apart, give us the opportunity to look for time variability in the excess flux at $\simeq 3.5$ keV. A comparison of the analysis between the two observations (using PN data only) is shown in Figure 3.14 (top vs middle). The shorter observation (middle panel) shows a noticeably different shape of the $\Delta C$ excess at $\simeq 3.5$ keV, and a drop in the maximum value of $\Delta C$ in the region of interest to below $3\sigma$. There are several possible causes for these differences. For example, they could be due to poor photon statistics in the shorter observation. Alternatively, they could be due to the differing effects of background flaring, which rises from 35% of the raw events list for ObsID `0722140401` to 90% for ObsID `0722140101`. Assuming the measurement of a shape and flux change is robust, then the most likely astrophysical interpretation for a time-dependent signal would be AGN variability: XCS J1416.7+2315 is described in the literature as a fossil cluster with known variable AGN activity, e.g. Miraghaei et al. (2015).

We have also investigated whether the presence of an excess at $\simeq 3.5$ keV in XCS J1416.7+2315 might be associated with a cool-core. A comparison of the $\Delta C$ analysis between the original spectrum and one where the inner $0.15R_{500}$ is excluded is shown in Figure 3.14 (top vs bottom). The removal of photons from the cluster core does not significantly change the shape of the $\Delta C$ excess at $\simeq 3.5$ keV. The significance of the enhancement is lower after core removal, but remains in excess of $3\sigma$ in the region of interest.

We repeat our analysis on this cluster using available MOS data, shown in Figure 3.16(b). Yet again, owing to the differing sensitivities of the PN and MOS cameras, we do not expect to recover a significant feature in the MOS data. Interestingly, we note two narrower features in the MOS data which align broadly with the energy of the $\simeq 3.5$ keV excess in the PN spectrum of XCS J1416.7+2315.

Finally, this cluster has an associated *Chandra* observation with a cleaned exposure time of 77 ks. so we fit its corresponding cluster spectrum, extracted within an $R_{500}$ radius. Given it is a single cluster, we do not require the blueshifting step and hence search for the 3.5 keV line at the its corresponding energy in the observer frame (see Figure 3.15). We observe a fit improvement at 3.3 keV, however this is outside the region of interest. Although it is a considerably weaker detection, is plausible that the 3.3 keV feature in the *Chandra* observation corresponds to a 3.5 keV line in the rest frame given the spectral energy resolution is $\approx 0.2$ keV in that range. More clusters with both *XMM-Newton* and *Chandra* observations are required to determine whether the 3.5 keV line in individual clusters is result of an *XMM-Newton* detector artefact. If this is the case, it would be in contention with the one arguably significant 3.5 keV detection using *Chandra* data (Cappelluti et al., 2018).

Hence, from the existing analysis/data it is not possible to unambiguously explain the flux enhancement at $\simeq$ 3.5 keV in XCS J1416.7+2315. However, its broad and asymmetrical shape is not consistent with a discrete emission line origin. An additional *XMM* observation would be needed to explore the hint of time dependence seen in Figure 3.14 (top vs middle). If confirmed, then AGN activity would be the most likely cause of the variability (and potentially of the $\simeq$ 3.5 keV flux excess). In that case, follow-up with *Chandra* would assist with resolving the central point source. Both of the *XMM* observations of this cluster (`0722140401` and `0722140101`) were taken during times of enhanced background flaring (especially `0722140101`). It would be possible to explore the impact of background flaring on the goodness of fit of model A and model B at $\simeq$ 3.5 keV, by relaxing/tightening the criteria used to reject time periods affected by flares in these two observations. The spectrum of this cluster is displayed in the top panel of Figure 3.18.

### XCS J2223.0-0137

The cluster XCS J2223.0-0137 (better known as Abell 2440, Abell, 1958b), and first identified in X-rays by HEAO-1 (Nulsen et al., 1979) has a RM ID = 48, a RM redshift of $z^{\rm RM}_{\rm phot} = 0.101$ and a RM richness of $\lambda = 90.7$. The best fit temperature and metallicity (following method A, see Sect. 3.2) are $T^{\rm PN}_{\rm X} = 4.39^{+0.08}_{-0.10}$ keV and $Z = 0.4^{+0.04}_{-0.04} Z\odot$ respectively. The fit values quoted here are based on *XMM*-PN observation ObsID `0401920101`. This observation was made on 2006-11-18, and has a cleaned exposure time of 23 ks, and a background flaring rate of 35%. Due to the fact that this cluster only has one available *XMM* observation, a variability analysis cannot be performed. Furthermore, we forgo

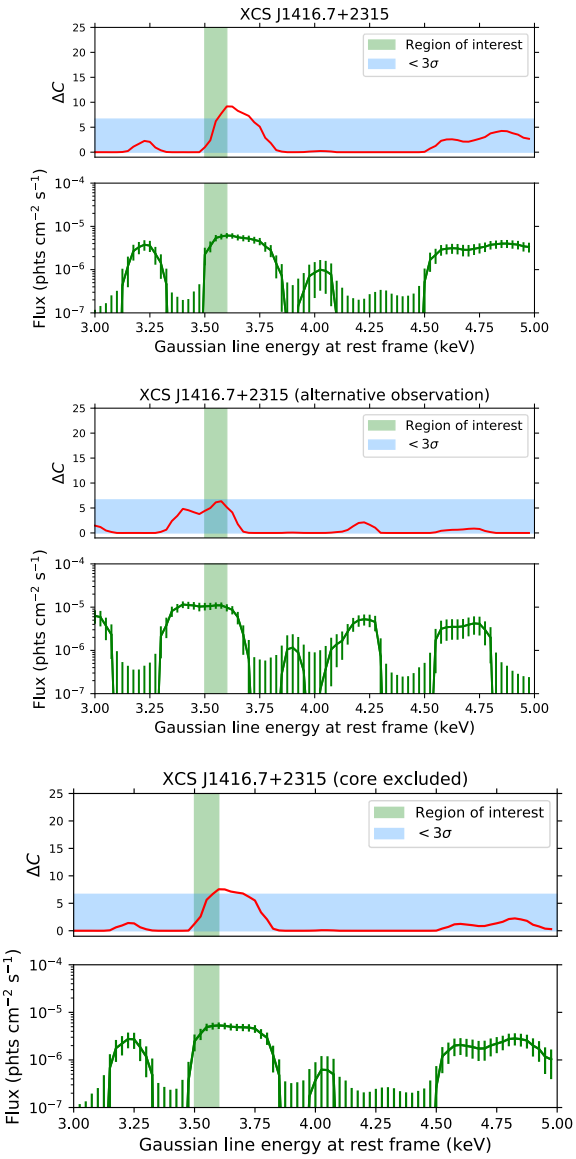


Figure 3.14: Plots showing the trend in $\Delta C$ (see Fig. 3.7 for full description) for the cluster XCS J1416.7+2315. The top plot shows the analysis using the *XMM* ObsID 0722140401 (i.e. our standard analysis), the middle plot shows the analysis performed using the *XMM* ObsID 0722140101 (see Sect. 3.5.1) and the bottom plot shows the analysis performed using ObsID 0722140401 with the core region excluded (see Sect. 3.5.1).

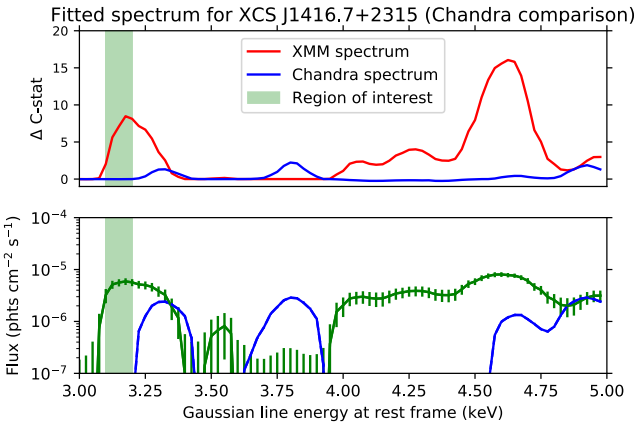


Figure 3.15: Comparison between *Chandra* and *XMM-Newton* observation for cluster XCS J1416.7+2315 , fitted in blue and red, respectively, in the observer frame ($z = 0.137$).

an analysis excluding the central regions of the cluster because XCS J2223.0-0137 is a complex merging system (see e.g. Mohr et al., 1996; Maurogordato et al., 2011) with two distinct peaks in the X-ray emission, making the exclusion of the cluster core problematic. We do, however, study the available MOS data for this cluster (Fig. 3.16(c)), finding no clear evidence of an excess at $\simeq 3.5$ keV.

We argue that the broad ($3.25 < E < 3.85$ keV) and multi-peaked shape of the $> 3\sigma$ flux excess shown in Figure 3.7 (bottom) is not consistent with being associated with a discrete emission line. Due to the complex cluster morphology, we forgo further discussion into the nature of the behaviour of the $\Delta C$ of XCS J2223.0-0137 in the range $3.25 < E < 3.85$ keV. The spectrum of this cluster is displayed in the bottom panel of Figure 3.18.

### 3.5.2 Methodology validation

In this section, we investigate the influence of various aspects of our methodology on the results presented herein: the blueshifting technique (Sect. 3.5.2), alternative weighting methods (Sect. 3.5.2), solar abundance tables (Sect. 3.5.2), photoelectric absorption models (Sect. 3.5.2), the use of photometric redshifts (Sect. 3.5.2), and the choice of plasma code (Sect. 3.5.2).

#### Blueshifting

We tested our blueshifting technique using cluster XCS J0003.3+0204 (see Fig. 3.19). For this, we repeated the fit to model B without carrying out the blueshifting step. As

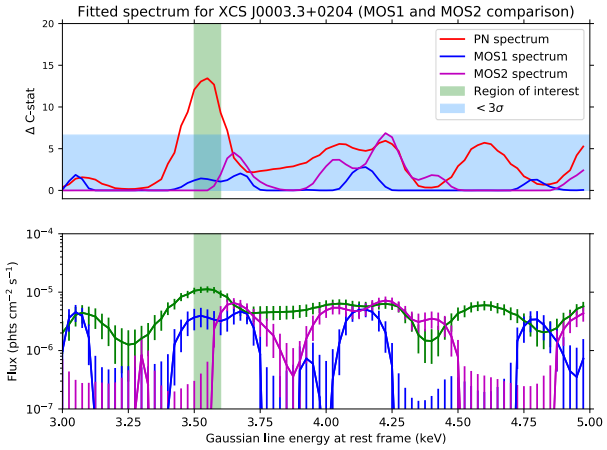


(a)

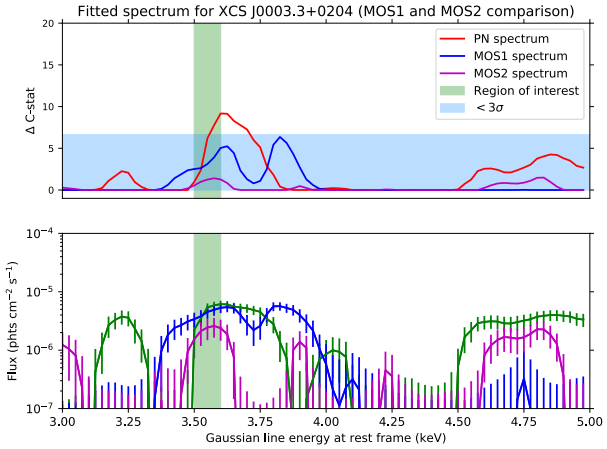


(b)

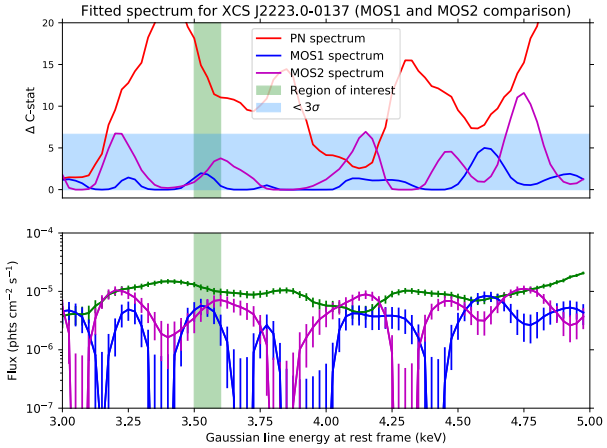


(c)

Figure 3.16: Comparisons in the trend of $\Delta C$ for (a) XCS J0003.3+0204, (b) XCSJ1416.7+2315 and (c) XCS J2223.0-0137 using the highest quality PN and MOS observation for each cluster (described in Section 3.5.1). In the top panels, the $\Delta C$ trend is displayed for the PN (red), MOS1 (blue) and MOS2 (magenta) spectra. In the bottom panels, the corresponding Gaussian normalisation and associated errorbars are shown.

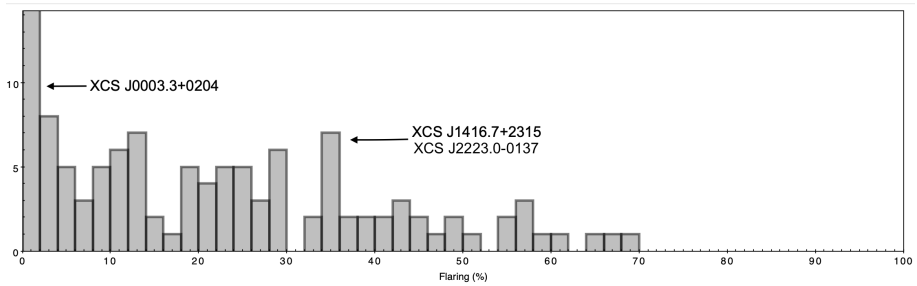


Figure 3.17: The percentage of flaring in all the 118 cluster observations used in the study. The flaring percentage is calculated by dividing the cleaned exposure time by the total exposure time.

expected, we found that the flux excess at $\simeq 3.5$ keV now appears at the observed rather than rest frame energy, i.e. at the expected value ($\sim 3.2$ keV) for a $z_{\rm phot}^{\rm RM} = 0.11$ system (see blue dashed line in Fig. 3.19).

### Flux weighting

The weighting technique described in Section 3.3.2 includes the implicit assumption that any excess flux at $\simeq 3.5$ keV is due to dark matter decay. However, if the flux at that energy was instead a result of emission from the ICM, then the use of a mass-dependent weighting would be inappropriate. Therefore, we test an alternative method of weighting based only on the cluster redshift,

$$w_i' = \frac{1 + z_i}{4\pi d_{i,L}^2}, \tag{3.8}$$

and rerun the joint fits in each temperature bin, finding almost identical results to Figure 3.8 (i.e. no $> 3\sigma$ detection of a flux excess in any of the bins).

### Solar abundance tables

Our default method uses the Asplund et al. (2009) solar abundance table. We have also run the joint fits in each temperature bin, using the Lodders et al. (2009) and Grevesse and Sauval (1998) abundance tables, finding almost identical results to Figure 3.8, (i.e. no $> 3\sigma$ detection of a flux excess in any of the bins). Although we note that the best fit metal abundance for the bin does change slightly compared to the values in column 6 of Table 3.1.

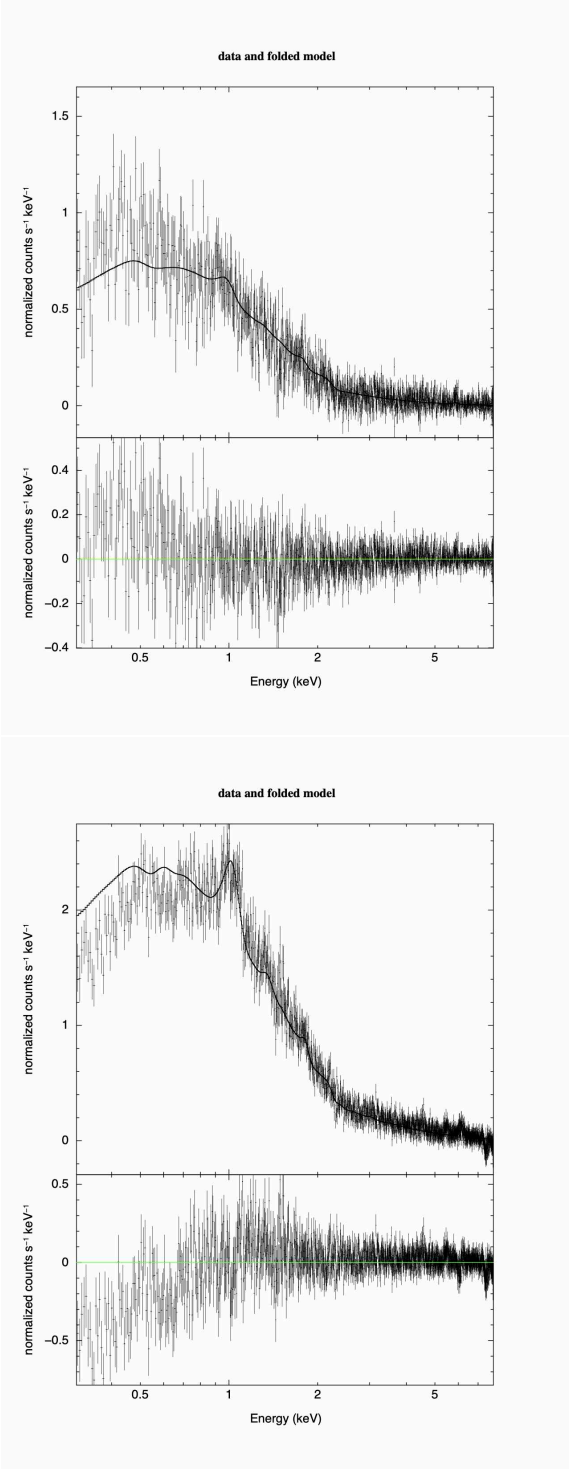


Figure 3.18: Spectra of clusters XCSJ1416.7+2315 (top) and XCS J2223.0-0137 (bottom), across the 0.3 - 7.9 keV energy range.

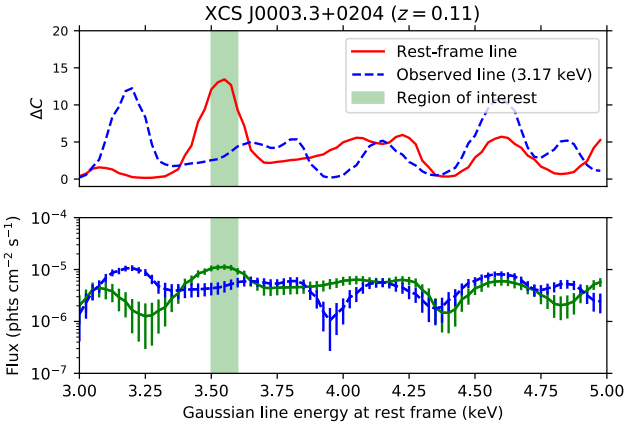


Figure 3.19: Plot of the change in fit statistic, $\Delta C$ (as in Figure 3.8) for the cluster XCS J0003.3+0204. Our standard analysis is given by the red solid line and the blue dashed line shows the change in $\Delta C$ with the analysis perform in the observed frame, i.e. without the blueshifting step (see Sect. 3.5.2).

### Photoelectric absorption

Our default method uses the `tbabs` implementation of photoelectric absorption in XSPEC, because the `wabs` model is now considered to be outdated (Wilms et al., 2010). However, the `wabs` model was implemented in other previous studies of the $\simeq 3.5$ keV flux excess, including B14, so we have also run the joint fits in each temperature bin using `wabs` for comparison. Once again, we find almost identical results to Figure 3.8, (i.e. no $> 3\sigma$ detection of a flux excess in any of the bins).

### Use of photometric redshift measurements

The ensemble behaviour of the $z^{\rm RM}_{\rm phot}$ is well understood. According to Rykoff et al. (2014) the scatter in the photometric redshift measurements is $\sigma_z \approx 0.006$ at $z \approx 0.1$, increasing to $\sigma_z \approx 0.020$ at $z \approx 0.5$. The median value for $|\Delta z|/(1+z)$ for the full sample is 0.006, where $\Delta z = z_{\rm phot} - z_{\rm spec}$. Therefore, the $1\sigma$ error in energy in blueshifting a 3.55 keV line to the local frame ranges from 20 eV for a cluster at $z \approx 0.1$ to 30 eV at $z \approx 0.5$, which is well below the spectral energy resolution of the PN detector ($\Delta E = 88$ eV). Therefore, it is unlikely that the use of $z^{\rm RM}_{\rm phot}$ values is the reason for a non detection of a $> 3\sigma$ detection of a $\simeq 3.5$ keV flux excess in our binned analyses shown in Figures 3.8 and 3.11. For our joint fits, we conclude that the ensemble scatter in $z$ is applicable.

However, errors in estimates of $z^{\rm RM}_{\rm phot}$ for individual clusters may influence the results discussed in Section 3.4.1, if they exceed the ensemble average. For the three indi-

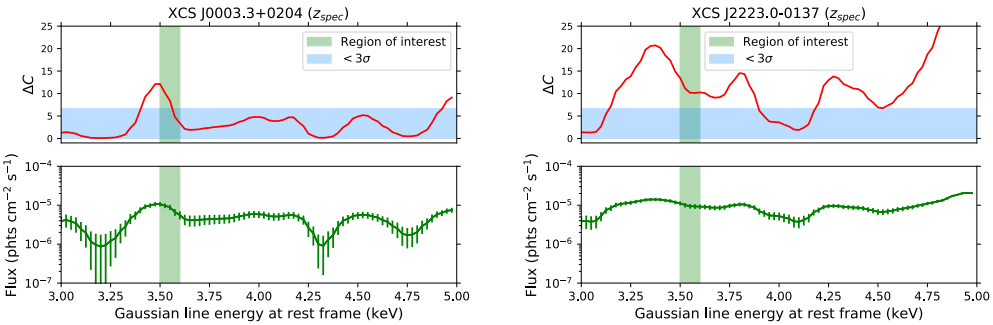


Figure 3.20: Comparisons in the trend of $\Delta C$ for XCS J0003.3+0204 (left) and XCS J2223.0-0137 (right) when replacing the RM photometric estimated redshift with available spectroscopic redshifts (see Sect. 3.5.2.)

vidual clusters described in Section 3.5.1, the spectroscopic redshift for XCS J1416.7+2315 (Romer et al., 2001) is almost exactly the same as the RM value, $z^{\rm RM}_{\rm phot} = 0.137$. However, according to Struble and Rood (1987), XCS J0003.3+0204 (or Abell 2700) has $z_{\rm spec} = 0.0924$ based on 9 cluster members, and XCS J2223.0-0137 (or Abell 2440) has $z_{\rm spec} = 0.0906$ based on 48 cluster members (compared to $z^{\rm RM}_{\rm phot} = 0.11$ and $= 0.101$ respectively). Therefore, we have refitted the spectrum of XCS J0003.3+0204 and XCS J2223.0-0137 using the spectroscopic values. The results are shown in Figure 3.20. We conclude that there is negligible impact from using spectroscopic redshifts, since the $\simeq 3.5$ keV excess in both clusters remains within the region of interest.

### Choice of plasma code

Searches for new emission lines are sensitive to both the temperature and metal abundance. Therefore it is important that these properties are measured precisely to prevent erroneous detections (or non-detections) of excess flux at $\simeq 3.5$ keV. As shown in detail in Mernier et al. (2019) the two codes used most in the field of X-ray cluster spectroscopy, AtomDB and Spexact, do not produce consistent results for metal abundance for low temperatures plasmas. For $T_{\rm X} \leq 2$ keV, the discrepancies can be up to 20% in the Fe abundance. The Spexact code is not implemented inside xspec[2], so it is not possible for to do a direct comparison here. However, only 7 clusters in our sample have measured $T_{\rm X}$ values below 2 keV (and all in bin 1). Even if this issue impacts the results in plot (a) of Figure 3.8, it will not impact the results shown in other three plots.

[2]Spexact is implemented in the SPEX fitting package, `www.sron.nl/astrophysics-spex`.

## 3.6 Summary and Conclusions

In this work, we have used a similar technique to the seminal paper (Bulbul et al., 2014, B14) to explore the evidence for an $\simeq$ 3.5 keV flux excess in the spectra of clusters of galaxies. We used individual and joint fits to *XMM*-PN spectra of 118 SDSS redMaPPer galaxy clusters ($0.1 < z < 0.6$, $1.7 < T_{\rm X} < 10.6$ keV). This is the largest study of its kind to date. By comparison, the B14 study used a sample of 73 clusters.

The analysis of the individual spectra identified three systems with an excess of flux at $\simeq$ 3.5 keV. This refers to an excess over the fiducial plasma model, taking into account one additional degree of freedom. None of these individual clusters are the most dark-matter dominated or nearest systems in our study (see Table B.1). In two of the three cases (XCS J1416.7+2315 and XCS J2223.0-0137), the flux excess, as a function of energy, is not consistent with a discrete emission feature due to the feature's broad, asymmetrical shape in both cases.

In the remaining case (XCS J0003.3+0204), the excess may result from a discrete emission line with a central energy of $E = 3.55$ keV. This feature, however, is unlikely to have a dark matter origin for two reasons. First, this is the only cluster in the sample to show such a feature, and yet there are many other observations of similar or better sensitivity in the sample. Second, the estimated flux ($11.2^{+0.31}_{-0.31} \times 10^{-6}$ photons cm$^{-2}$ s$^{-1}$) results in significantly higher mixing angle constraints ($\sin^2(2\theta) = 2.36^{+0.65}_{-0.65} \times 10^{-9}$) than the ones presented from the stacked analysis of 73 *XMM*-PN spectra in B14. The line strength for XCS J0003.3+0204 is most comparable to the *XMM*-MOS detection for the Perseus cluster (core-included) in B14. Nevertheless, there exists an order of magnitude of difference in the derived mixing angles ($\sin^2(2\theta) \simeq 6 \times 10^{-10}$, B14).

We note that this is only the second time that a significant detection of a $\simeq$ 3.5 keV line-like excess has been measured in an individual cluster (the other being in Perseus). Furthermore, unlike Perseus, the strength of the 3.5 keV excess in XCS J0003.3+0204 shows almost no dependence on the removal of the core region from the spectrum. Flaring is also unlikely to be causing such an excess as we report a very low flare rate (less than 2%) for this observation.

The primary motivation for our study was a search for evidence of an increase in the $\simeq$ 3.5 keV flux excess with $T_{\rm X}$. Such evidence would firmly support the dark matter interpretation (and vice versa if the excess weakens with $T_{\rm X}$) because $T_{\rm X}$ is a reliable tracer of the underlying halo mass. A temperature-dependent search would additionally eliminate the possibility of a plasma line masking an emission line of dark matter origin

as the relevant plasma lines in the region of interest weaken with temperature (contrary to dark matter).

We therefore grouped the remaining 115 clusters into 4 roughly equally sized $T_{\rm X}$ bins, and performed joint fits in each bin. We did not find evidence of a significant excess in flux at $\simeq 3.5$ keV in any of the bins. Therefore, from our study, we cannot comment on whether (if it exists at all) the $\simeq 3.5$ keV flux excess gets stronger or weaker with mass. Repeating the joint fits in each bin with the inclusion of the three clusters with excess emission resulted in a significant joint detection in one bin (bin 2). However, after performing a jackknife analysis on the clusters in this bin, it is found that the joint detection is dependent on the $\simeq 3.5$ keV flux excess in two individual clusters (XCS J0003.3+0204 and XCS J2223.0-0137).

We maximised sensitivity to a potential weak dark matter decay feature at $\simeq 3.5$ keV, by performing a joint fit across all 115 clusters. Again, no significant excess was found at $\simeq 3.5$ keV. From this fit, we estimated a $3\sigma$ upper limit of an undetected emission line at $\simeq 3.5$ keV to be $F_{\rm DM} = 2.39 \times 10^{-6}$ photons cm$^{-2}$ s$^{-1}$. The resulting maximum mixing angle from our 115 clusters is then $\sin^2(2\theta) = 4.3 \times 10^{-11}$, lower than the previous estimates for favoured mixing angles from cluster studies. These include the *XMM*-PN value for 73 clusters in B14 ($\sin^2(2\theta) \simeq 7 \times 10^{-11}$) and Bulbul et al. (2016) study of *Suzaku* observations for 47 clusters ($\sin^2(2\theta) \simeq 6 \times 10^{-11}$). Moreover, our result is comparable to among the most stringent constraints on the non-detection of a dark matter decay feature using *XMM* observations of Draco ($\sin^2(2\theta) \simeq 2 \times 10^{-11}$, Jeltema and Profumo, 2016) and *XMM* blank sky observations (Dessert et al., 2018).

We conclude that although there is a measurable flux excess at $\simeq 3.5$ keV in some cluster spectra (e.g. XCS J0003.3+0204), this is not a ubiquitous feature, and hence unlikely to originate from sterile neutrino dark matter decay. We have carried out a series of checks to demonstrate that our methodology is not artificially masking the existence of a weak dark matter decay feature. We perform tests on our blueshifting technique to ensure the purported 3.5 keV feature appears at the correct rest-frame energy, in addition to alternative weighting methods, abundance and photoelectric absorption models, and comparisons with spectroscopic data. We have found our methodology to be robust to these tests and have negligible impact on our presented results.

Future work on the constraining the origin of the purported 3.5 keV feature will be informed most directly by the launch of the *XRISM* satellite (the successor to the short-lived *Hitomi* mission). With significantly improved spectral resolution, it will be possible

to determine the precise energies of elemental and unknown lines, to clarify whether a $\simeq$ 3.5 keV flux excess is indeed originating from a discrete emission line (such as in the case of XCS J0003.3+0204). Moreover, deeper observations of single clusters with claimed $\simeq$ 3.5 keV emission such as Perseus will be able to confirm whether such a line exists, and if so, to what extent it is resolvable from the nearby K and Ar transition lines.

We further aim to revisit previous analyses such as B14, in which the cluster sample is produced using publicly available *XMM* observations. Given the complications associated with stacking methods and the fact that individual systems can contribute significantly to the appearance of a line in joint cluster searches, we will repeat the analysis in B14 simply by jointly fitting all available clusters in parallel, in addition to fitting each cluster individually. The aim of this would be to see if a $\simeq$ 3.5 keV excess is detected in any individual clusters in the B14 analysis, which could suggest these clusters are responsible for an overall so-called dark matter decay feature (or masking one).

Given that two of the three clusters in this study with a measured flux excess at $\simeq$ 3.5 keV also display high rates of flaring, investigating the rate of flaring across all clusters which might contain such flux excesses would be a useful diagnostic to examine whether the origin of the line is instrumental. Deeper, repeated observations of individual clusters are also needed to further test the possibility of a variable $\simeq$ 3.5 keV feature (e.g. there is a hint of variability in the feature observed in XCS J1416.7+2315), which could lend support to the interpretation that $\simeq$ 3.5 keV emission arises from AGN variability (or the interaction between AGN and ALPs in a more exotic dark matter scenario).

Finally, further work to conclusively determine the existence and properties of the intriguing 3.5 keV feature will require even larger jointly fitted cluster samples. Hence, future work on this topic will involve a repeat of this analysis on a larger sample of redMaPPer selected clusters in the Dark Energy Survey Year 3 footprint with associated archival X-ray data.

# Chapter 4

# Calibration of cluster miscentering in the redMaPPer catalogues

The majority of the results discussed in this Chapter have been published in Zhang et al. (2019). In the sections below, we describe the sample selection, methodology and results which were used in the Zhang et al. (2019) analysis, followed by ongoing and new work to characterise the centering performance of RM for the XCS-DESY3 sample. For the reprisal of the centering analysis using the XCS-DESY3 sample, the calibration of X-ray to optical scaling relations ($T_X - \lambda$, $L_X - \lambda$) is combined with the miscentering measurements. The modelling was performed using an adapted version of Y. Zhang's centre modelling code, which is publicly available.[1]

## 4.1 Introduction

As discussed in Chapter 1, the abundance of galaxy clusters is highly sensitive to various cosmological scenarios. However, such uses require a reliable measurement of the total cluster mass. In Section 1.3, we outlined three key methods used in cluster mass determinations. Nevertheless, each of these techniques suffer from biases, which result in overestimated/underestimated values of the true cluster mass.

When using optical datasets for cluster cosmology, (e.g. Rozo et al., 2009; Costanzi et al., 2019; Abbott et al., 2020), it is typical to calculate stacked weak lensing masses for a chosen cluster sample. For low mass systems, the lensing signal is simply too weak to be measured individually. At increased survey volumes, massive systems are preferentially detected, however, the lensing signal decreases as the lens approaches the source redshift

[1] https://github.com/yyzhang/center_modeling_y1

(as shown in Equation 1.40). An advantage of stacked lensing is that by stacking shapes of background galaxies, one enhances signal-to-noise ratio of the measured lensing signal (Murata et al., 2019).

Examples of stacked cluster masses can be found in Melchior et al. (2017) and McClintock et al. (2018). This requires an understanding of various systematic effects, such as correlated structures along the line of sight leading to projection effects, uncertainties in the modelling of mass profiles and contamination of non-cluster member galaxies to lensing measurements ('boost factors,' see Section 1.3.3). In order of contribution to the amplitude of the mass-richness relation, the various sources of error are as follows: shear measurement (4%), photometric redshifts (3%), modelling systematics (1%), cluster triaxiality (1%), line-of-sight projections (1%) and membership dilution and miscentering ($\sim$ 1%). These all result in slight biases to the measured amplitude of the stacked lensing signal, $\Delta\Sigma$, which can be related to the cluster mass via some fitted value of logarithmic slope, such as $M_{200} \propto \Delta\Sigma^{4/3}$ (see Melchior et al., 2017).

As described in Section 1.2, clusters are observable through their baryonic components, e.g. the brightest cluster galaxy (hereafter BCG) in optical observations; the peak of the ICM emission in X-ray observations. As a result, the measured centres of a cluster based on these observables do not necessarily trace the centre of the cluster's underlying dark matter halo (the largest mass component of the cluster). The centre of the underlying dark matter halo in clusters is usually determined using a model based on some definition of the cluster centre, either described theoretically (e.g. a spherical cluster potential) or based on halo catalogues determined from N-body simulations. In the latter case, the N-body simulation is run and dark matter halos are found within lightcones using a halo finder such as ROCKSTAR (Behroozi et al., 2013). Halos are defined according to some number of particles in a spherical volume within a given lightcone, with masses (and centres) typically corresponding to $M_{vir}$ strict spherical overdensity (SO) masses (Bryan and Norman, 1998; DeRose et al., 2019).

Optical cluster finders often attempt to identify a central galaxy based on some criteria such as brightness or the density of neighbouring galaxies (see Section 2.3.2). While a BCG might look dominant in optical observations of clusters, misidentifications, due to a variety of reasons, are common. For example, massive halos experience growth through merger scenarios. Therefore, in larger clusters, it is possible that the central galaxy is displaced from the local gravitational potential minimum (e.g. Martel et al., 2014). An additional effect is when the second most likely galaxy in the cluster is chosen to be the centre

in the event the central galaxy is experiencing recent star formation (McDonald et al., 2016). Such galaxies do not appear sufficiently quenched and therefore may not fall on the red sequence (a problem particular to red-sequence based cluster finders such as RM). Furthermore, a misidentification might occur in the instance of a merging event of two progenitor halos with nearly identical central galaxies, such as in the case of the Coma cluster and others (Vikhlinin et al., 2001; Kim et al., 2019). Finally, misidentifications might refer to the selection of a central galaxy which is not physically associated with the cluster halo but aligned with the cluster in projection (e.g. Costanzi et al., 2018).

The impact of miscentering has been studied by e.g. Johnston et al. (2007), Simet et al. (2016), Baxter et al. (2017) and various others. In testing the centering performance of optical cluster finders, the X-ray gas comprising the ICM is considered a reliable tracer of the cluster potential (and 'true' centre) since it is the dominant baryonic mass component (galaxies, by comparison, are a much smaller proportion), see e.g. Buote and Tsai (1995). The cluster's X-ray centroid or surface brightness peak is therefore a useful way to calibrate optically-selected centres (Lin and Mohr, 2004). SZ cluster centres can also be used as a alternative tracer (e.g. Bleem et al., 2020).

Miscentering can be modelled as a correction to the weak lensing signal from background galaxies around clusters. The recovered weak lensing signal ($\Delta\Sigma$), which is derived from the tangential shear, is thus effectively a weighted sum of two independent contributions - a contribution from well-centred clusters, $\Delta\Sigma(R)$, and a contribution from miscentered clusters, $\Delta\Sigma_{mis}$, such that

$$\Delta\Sigma_{model} = (1 - f_{mis})\Delta\Sigma(R) + f_{mis}\Delta\Sigma_{mis}(R). \tag{4.1}$$

Depending on the choice of parameterisation used to quantify miscentering (discussed in Section 4.3), the miscentering model can be specified entirely by two or three parameters.

The resulting measured shear profile of a cluster halo can therefore be 'diluted' as a result of miscentering (shown in Figure 4.1). This can affect the resulting mass estimates. Moreover, miscentering has an impact on the richness estimation from RM (discussed in Section 4.5), which can lead to biased cosmological analyses (discussed in Section 4.6).

## 4.2 Sample selection

In this Chapter, we characterise the centering performance of the RM cluster finder using data from the *XMM-Newton* public archive. Two samples were used for this study - XCS-SDSS and XCS-DESY1. The RM catalogues are the same as those described in Chapter

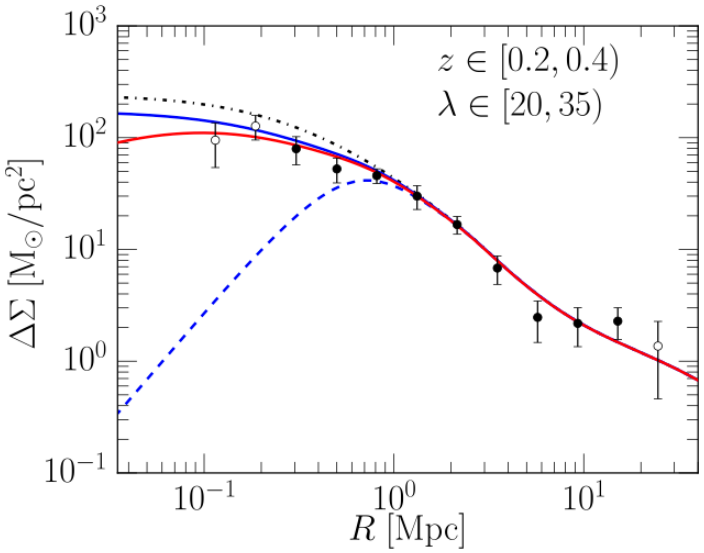


Figure 4.1: Figure from Melchior et al. (2017), showing a fitted model to a perfectly centred lensing signal (given by the dash-dotted black curve). The solid blue curve includes the effect of miscentering on the lensing profile. The solid red curve takes into account the effects of both miscentering and cluster member contamination (this is the model which is fitted to the observed profile). Finally, the dashed blue line is the miscentered profile ($\Delta\Sigma_{mis}$). No data below R $<$ 200 kpc is included as the lensing profiles are strongly affected by crowded field photometry and large boost factor corrections in the cluster core.

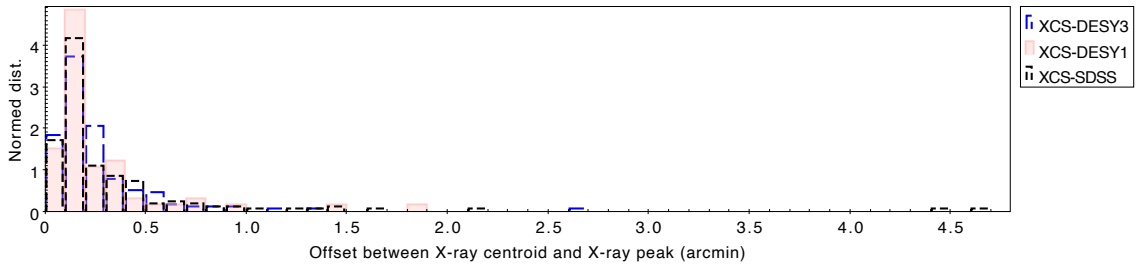


Figure 4.2: Measured offset between the XAPA determined centroid position and X-ray peak position across the three samples in this study: XCS-SDSS (black, dashed), XCS-DESY1 (pink, filled) and XCS-DESY3 (blue, dashed).

2 (i.e. redMaPPer DES-Y1-6.4.17 and redMaPPer SDSS 6.3.1, with input photometry from SDSS DR8). For this study, both catalogues needed to be volume limited, to ensure the optical centering performance is not biased due to sample incompleteness. Hence, the DESY1 catalogue is volume limited spanning a redshift $z \in [0.2, 0.7]$, while the SDSS catalogue is limited to clusters spanning $z \in [0.1, 0.35]$.

The crossmatching procedure used to construct the XCS-SDSS and XCS-DESY1 samples for the centering analysis follows the methodology described in Section 2.4. However we note, as described above, that both RM catalogues cover a smaller redshift range than the complete RM catalogues, and hence contain fewer clusters. After crossmatching between XAPA detected sources and RM clusters, the XCS-SDSS (XCS-DESY1) samples comprised 356 (282) clusters. Subsequently, a robust definition of the X-ray centre was required for the centering comparison. Indeed, an X-ray centroid is calculated by XAPA for each X-ray extended source. X-ray centroid positions are used for centering comparisons if one assumes that they resemble the centroid of the cluster gravitational potential (Stott et al., 2012). Alternative methods use the X-ray emission peak assuming it follows the peaks of the cluster matter distribution (such as in Lin and Mohr, 2004). For this study, we use the X-ray peak position to measure offsets to the RM centres. Nevertheless, we show in Figure 4.2 that the choice of using the X-ray peak or centroid will likely have little impact on the measurement of the centering performance of RM since they exhibit strong agreement (showing a characteristic offset of $\simeq 0.5$ arcminutes) across all samples in this analysis.

### 4.2.1 X-ray peak analysis

For the two samples, we determine the position of the X-ray peak starting from the reduced, exposure-corrected, and point source subtracted XIP images. Note that all extended sources other than the one closest to the RM target are also removed (although this

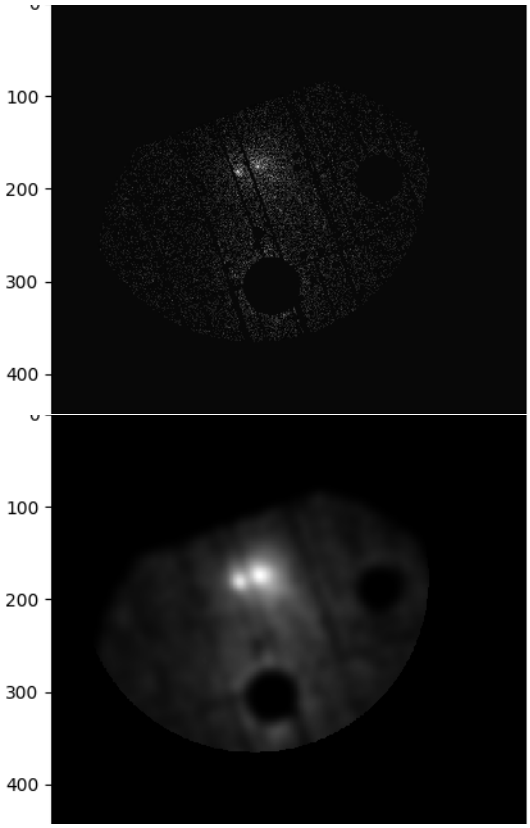


Figure 4.3: An example of a reduced XIP image corresponding to ObsID 0652460201, showing an X-ray confirmed cluster (top). The same cluster featured in a Gaussian smoothed image is shown in the bottom image. Black circular masks are applied to both images to blot out nearby point and extended sources. The smoothed image makes it easier to locate the X-ray emission peak of the cluster.

assumption is corrected in the event of mispercolations, described below). Next, these images are smoothed by applying a Gaussian smoothing kernel with $\sigma = 50$ kpc $h^{-1}$ width, based on the RM redshift. The X-ray peak position is then found within a radius $1.5\times R_\lambda$ around the RM position. The value, $R_\lambda = (\lambda/100.0)^{0.2}h^{-1}$ Mpc comes from the optimised radius in which to measure the RM richness, based on minimising the scatter in the mass-richness relation (refer back to Section 2.3.2 for more details). The peak is defined to be the brightest pixel in this smoothed image (see an example in Figure 4.3). All peaks are then visually inspected.

Once the peak has been found in the smoothed image, it is possible to overlay all relevant centres onto both an optical and *X*MM postage stamp, to assess whether the optical and X-ray centres are in agreement. We show an example of good agreement between X-ray and optical centre in Figure 4.4. The good agreement is determined based on the RM central galaxy (highlighted by the yellow circle in the top and middle images)

overlapping almost entirely on the location of the centre determined using the X-ray emission peak (highlighted by the pink circle in the top and middle images). The cyan circle in the top and middle images represents the XAPA determined centroid for the cluster, which additionally almost entirely overlaps with the location of the other defined centres. This implies that not only are the optical galaxies aligned with the X-ray gas distribution of this cluster, but both the cluster matter distribution and underlying gravitational potential are in agreement.

In a subset of cases, the X-ray peak location is incorrect or unreliable. In the event of such 'failure modes,' the clusters are flagged and either reanalysed or removed from the sample. We outline the key failure modes below.

- **X-ray detector artefacts** Clusters falling on or near a detector chip gap or edge in the X-ray observation such that the position of the X- ray peak could not be reliably determined (see Figure 4.5). A related failure is caused by unreliable peak measurements due to clusters detected near the edge of the *XMM* FOV being too faint to extract a peak value. These clusters are removed.

- **Point source emission** Occasionally relic point source emission can bias the peak determination. This is resolved by recalculating the peak position after accounting for excess point source emission, most commonly by increasing the mask size (see Figure 4.6).

- **Bad association** In a few cases the identified X-ray cluster is clearly not the RM cluster (e.g. a bright foreground or background cluster in the same observation). These clusters are likewise removed (see Figure 4.7).

Moreover, there are some particular RM miscentering cases, known as 'mispercolations,' because these cases are related to the "percolation" step in the RM cluster failing (see Section 2.3.2 for a description and Figure 2.13 for an example). In these cases there is a spatially close pair of clusters with similar redshifts, and the one with a less luminous X-ray detection is assigned a greater richness. In these cases, we manually re-associated the richer RM candidate with the more luminous X-ray detection and remove the less rich system from the resulting XCS-SDSS and XCS-DESY1 samples.

Following the visual inspection of all X-ray peak locations, the XCS-SDSS (XCS-DESY1) samples consisted of 248 (109) clusters. A SNR cut was applied to both samples, wherein the SNR was determined within a $500h^{-1}$ kpc aperture using 0.5 – 2.0 keV *XMM*

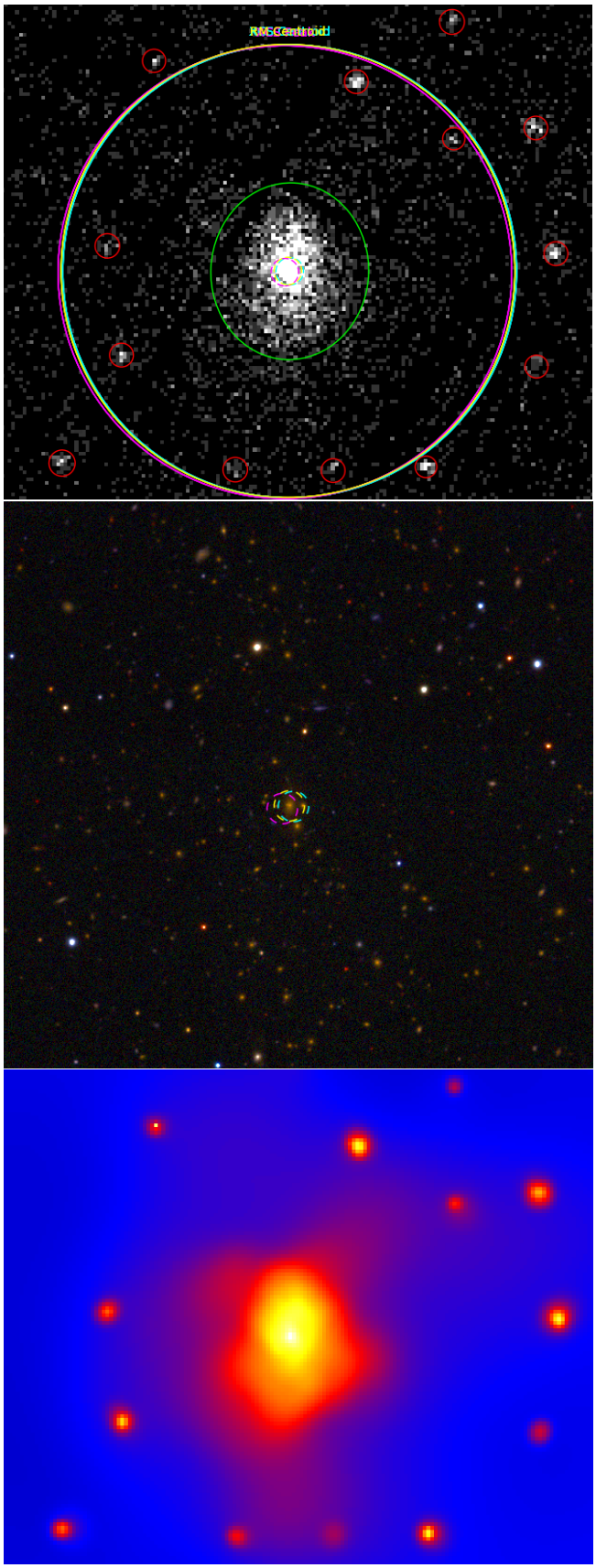

Figure 4.4: 6′ by 6′ postage stamps for cluster XMMXCSJ233227.2-535828.2 (RM ID: 156) in ObsID 0604010101 showing a reduced *XMM* image (left), DES image (middle) and smoothed X-ray image using `CIAO` tools (right). The cyan circle represents the X-ray peak, magenta circle corresponds to the XAPA centroid and the yellow circle denotes the RM selected centre.

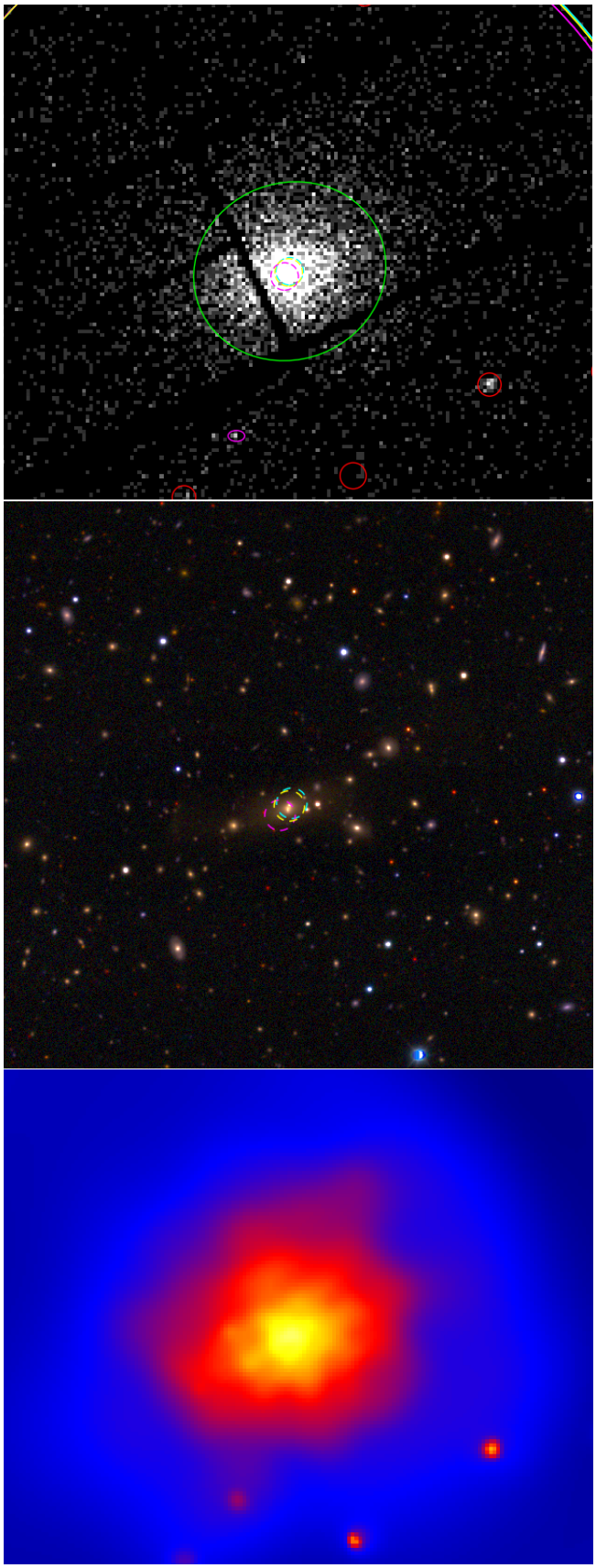

Figure 4.5: Similar to Figure 4.4, 6′ by 6′ postage stamps for cluster XMMXCSJ052548.9-471507.3 (RM ID: 109) in ObsID 0692932801. This cluster was removed from the sample due to a chip gap failure mode.

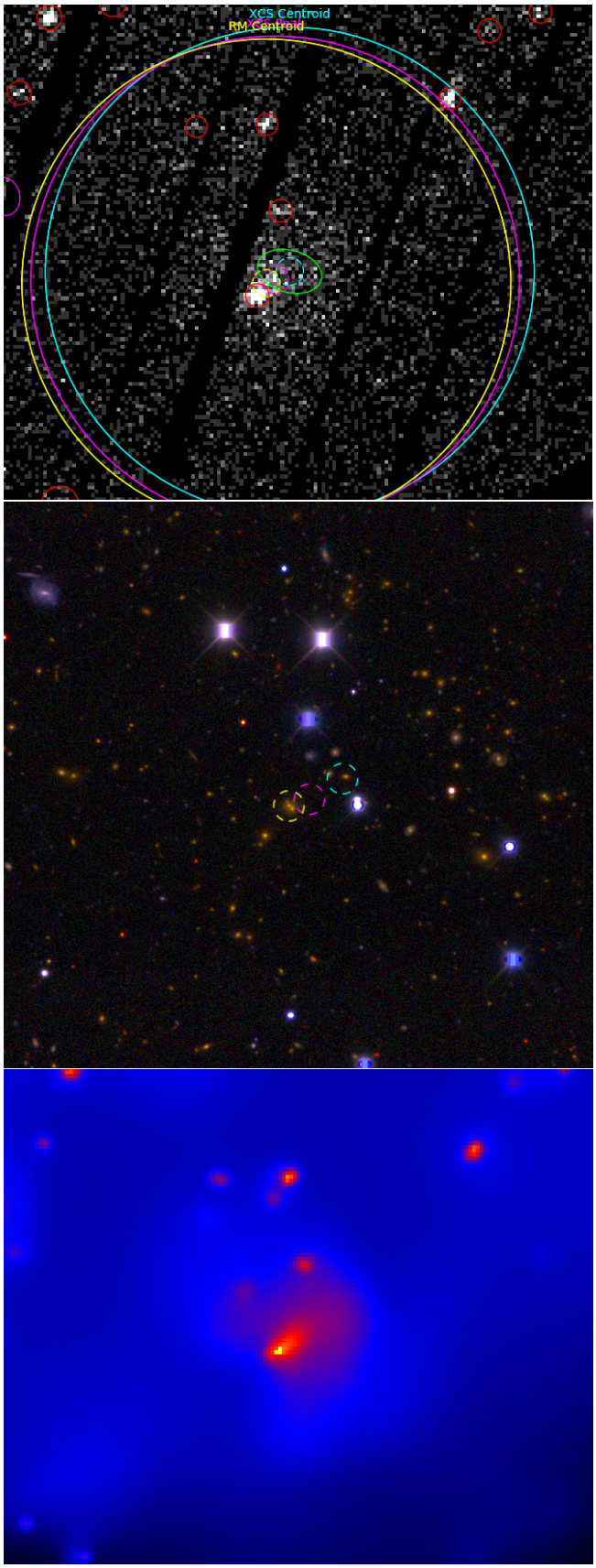


Figure 4.6: Similar to Figure 4.4, 6′ by 6′ postage stamps for cluster XMMXCSJ034005.2-285024.4 (RM ID: 569) in ObsID 0653770101. This cluster was flagged from the sample due to a point source contamination failure mode, and a peak position was remeasured after manually increasing the size of the mask around the point source (shown in red).

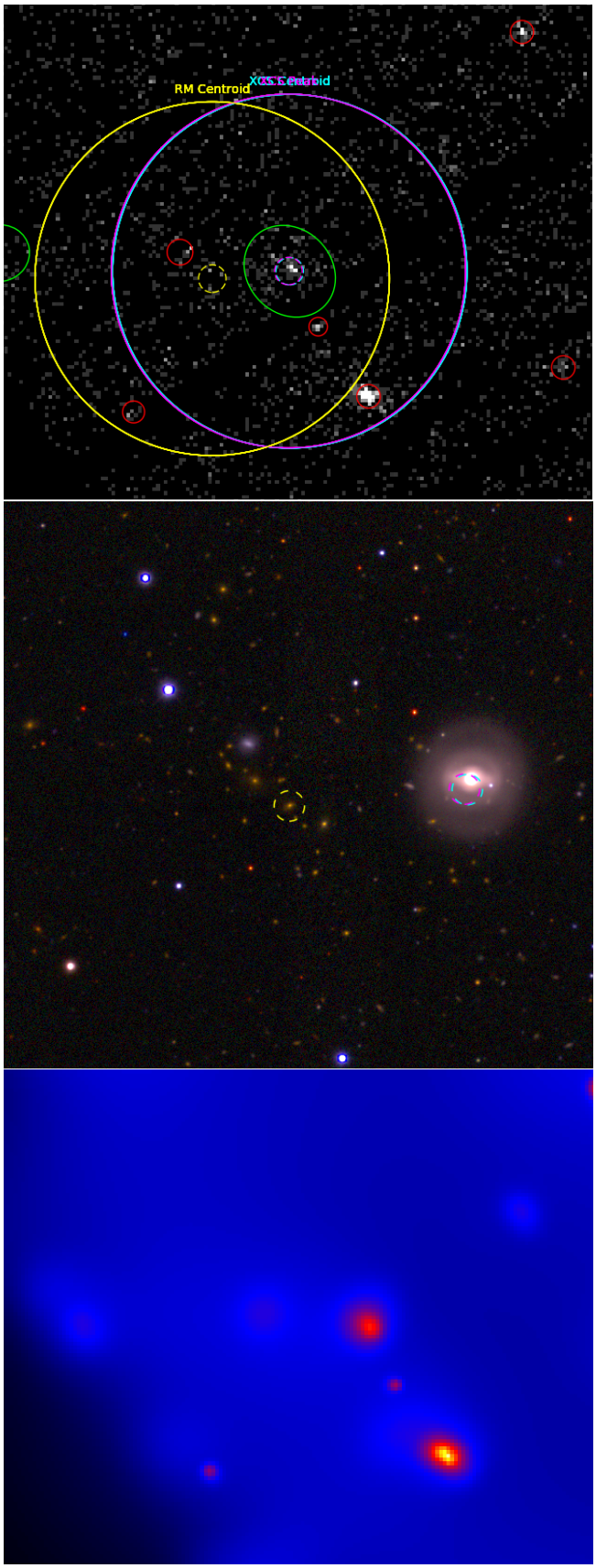


Figure 4.7: Similar to Figure 4.4, 6′ by 6′ postage stamps for cluster XMMXCSJ005042.0-521316.8 (RM ID: 10157) in ObsID 0125320701. This cluster was removed from the sample due to a bad association failure mode, where it is clear from the optical image (middle), the X-ray source matched to the RM cluster is a spiral galaxy, not a cluster.

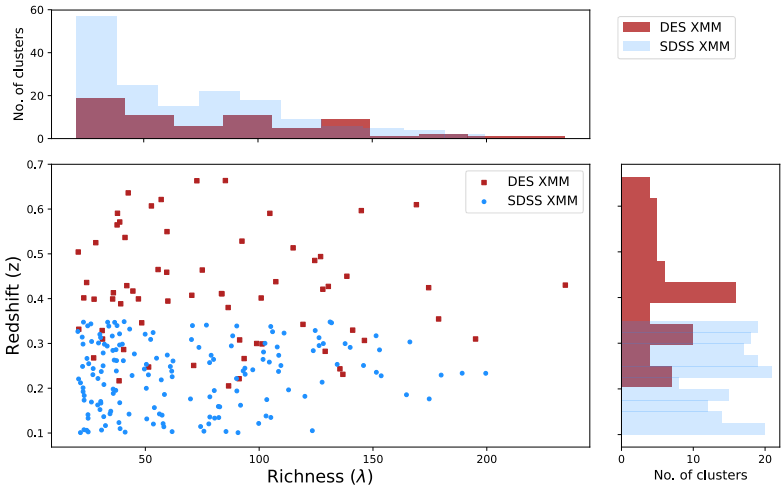


Figure 4.8: Redshift and richness distributions of the 163 SDSS (blue) and 66 DESY1 (red) RM clusters matched to archival *XMM* observations comprising the centering samples.

images. For both samples, the SNR was required to be $\geq 6.5$, to match the SNR cuts from the corresponding *Chandra* centering analysis (Section 4.3.4).

A FOV cut was also applied to both datasets. For the XCS-SDSS sample, the RM centre was required to be within $8.5'$ of the aimpoint (or $6.5'$ away from the FOV edge assuming a $15'$ FOV radius). For the XCS-DESY1 sample, the RM centre was required to be within $10.5'$ of the aimpoint. These FOV cuts were applied to ensure that the RM centers are at least 500 kpc $h^{-1}$ away from the FOV edge. This is so that the corresponding X-ray peak search radius ($1.5R_\lambda$) for the nearest clusters – $z = 0.1$ ($z = 0.2$) in the SDSS (DES) samples are contained within the FOV and therefore measurable. It also ensures the peak finding is reliable given the sensitivity of the *XMM* detector falls off sharply at the FOV edges (described in Section 2.3.1). After applying the FOV and SNR cuts, the XCS-SDSS (XCS-DESY1) samples consisted of 163 (66) clusters. The redshift and richness distributions of both samples are shown in Figure 4.8.

## 4.3 Modelling the X-ray-RM offset

The aforementioned X-ray peaks calculated in Section 4.2.1 are considered to be the cluster's fiducial centre. We therefore model the offsets between X-ray peaks and RM centre to characterize the RM centering distribution. When RM misidentifies which galaxy

lies at the cluster centre, an offset between X-ray peak emission and the RM centre is expected. On the other hand, when the RM centers are correct, the X-ray peaks may still be offset from them because of the different dynamics and relaxation timescales of gas and galaxies (see e.g. Mantz et al., 2015). There are additional uncertainties in accurately identifying the X-ray peaks due to the resolution of X-ray instruments, but these offsets tend to be small (less than tens of kpc). Therefore, we expect the well and miscentered RM clusters to have different offset distributions when compared to the X-ray peaks. We model the X-ray-RM offset as a mixture of well-centred and miscentered components,

$$P(x|\rho,\sigma,\tau) = \rho \times P_{cent}(x|\sigma) + (1-\rho) \times P_{miscent}(x|\tau) \tag{4.2}$$

where $x = r_{\rm offset}/R_\lambda$ is the scaled X-ray-RM offset. The value of $r_{\rm offset}$ is the distance between the X-ray peak and RM centre, determined in units of $h^{-1}$ Mpc at the RM redshift. Given its dependence on $R_\lambda$, $x$ scales the offset with a mild dependence on RM richness. The remaining three parameters ($\sigma, \tau$ and $\rho$) in the model are fitted. We can decompose the dependencies from both the well-centred and miscentered distributions in the following way:

$$P_{cent}(x|\sigma) = \frac{1}{\sigma}\exp(-\frac{x}{\sigma}) \tag{4.3}$$

$$P_{miscent}(x|\tau) = \frac{x}{\tau^2}\exp(-\frac{x}{\tau}) \tag{4.4}$$

The parameter $\sigma$, characterised by an exponential function, describes the X-ray offset distribution for the well-centred clusters (Equation 4.3). The miscentered component is modelled using a Gamma distribution, described by the scale parameter $\tau$ (Equation 4.4). This model is used to fit to data with an extended distribution of large offsets, and optimised for the X-ray-RM offsets measured from the *Chandra* data. The comparison of fitting *XMM* and *Chandra* offsets using a Gamma distribution is discussed in Section 4.3.4. Finally, the fraction of well-centered clusters in the entire sample is modeled by the $\rho$ parameter. Following the measurement of $x$, given a prior distribution of $\rho$, $\sigma$ and $\tau$ (stated in Table 4.1), the posterior distributions can be sampled using a Markov Chain Monte Carlo (MCMC) method (via the Python EMCEE module).

### 4.3.1 XCS-SDSS constraints

For the 163 clusters in the XCS-SDSS sample, the measured scaled offset distribution is displayed in Figure 4.9.

The posterior constraints of the model parameters including the correctly-centered fraction $\rho$, miscentering characteristic offset $\tau$, and the X-ray-RM characteristic offset, $\sigma$

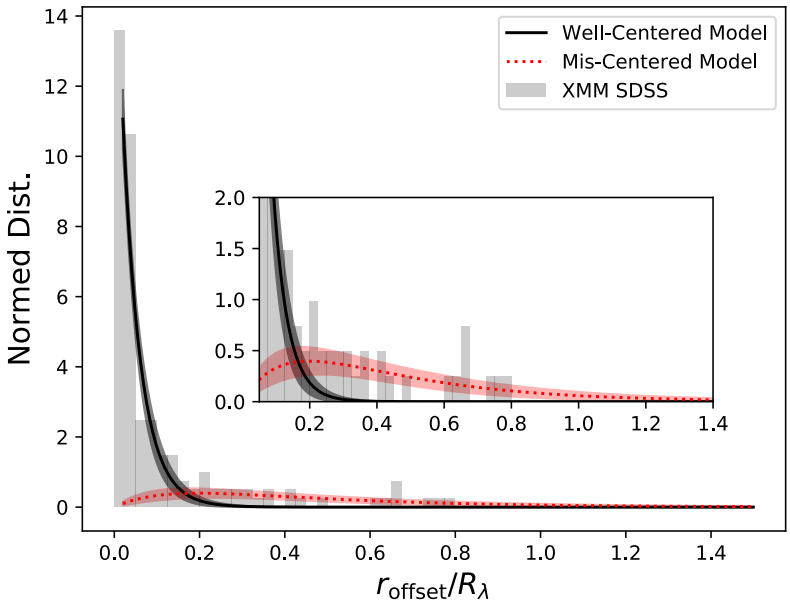


Figure 4.9: The scaled offset distribution between the RM centers and the X-ray peaks for the XCS-SDSS sample from the *XMM* archival observations, with the inset zooming on the miscentered component, starting at $R_{Offset}/R_\lambda = 0.05$. The distribution can be fitted with two components, a concentrated component that represents the well centered clusters, and an extended component that represents the miscentered clusters. The best fit SDSS offset model is shown by the solid lines (black: well-centred model, red: miscentered model), with the shaded regions representing the uncertainties.

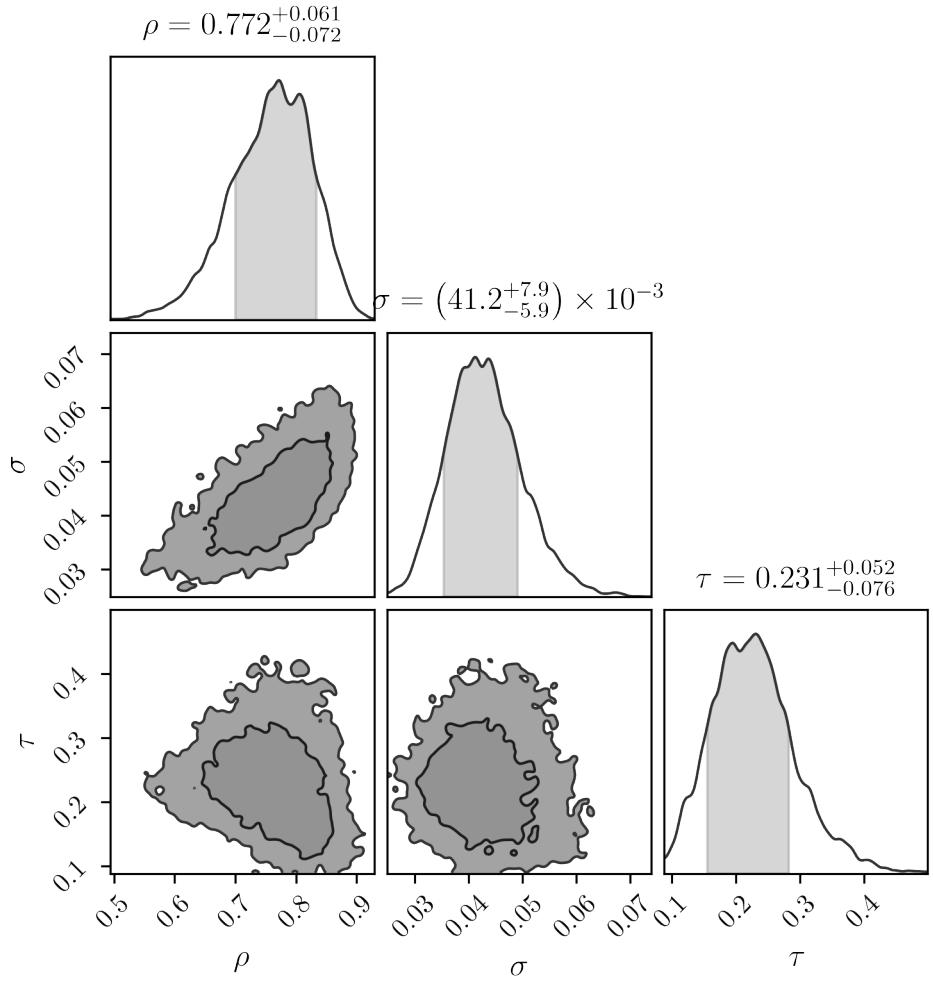


Figure 4.10: Centering offset parameter constraints (Equation 4.2) for the XCS-SDSS sample. About 77% XCS-SDSS clusters appear to be well-centred (indicated by the $\rho$ parameter). For the miscentered clusters, the miscentering offsets are characterized by a Gamma distribution with a characteristic offset (the $\tau$ parameter) around $0.23R_\lambda$. The contours represent $1\sigma$ (68%) and $2\sigma$ (95%) confidence intervals.

are displayed in Figure 4.10. The XCS-SDSS sample contains approximately 77% well-centred clusters. The light and dark grey regions in the posterior panels refer to $1\sigma$ and $2\sigma$ confidence intervals. Best-fit values of the model parameters for the XCS-SDSS sample can be found in row 1 of Table 4.1.

### 4.3.2 XCS-DESY1 constraints

We then model the offset for the 66 clusters comprising the XCS-DESY1 sample. The measured scaled offset distribution is displayed in Figure 4.11.

The corresponding best fit values for the centering parameters are as displayed in

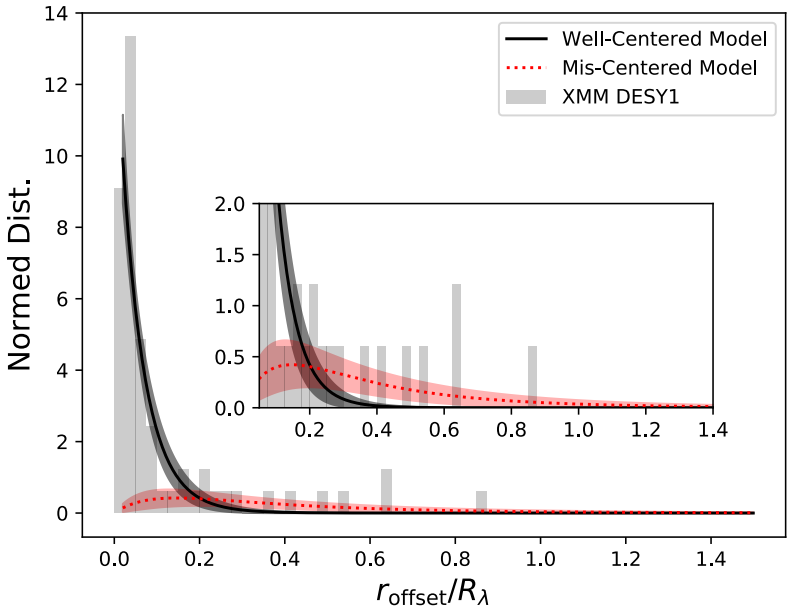


Figure 4.11: Similar to Figure 4.9, the scaled offset distribution for the XCS-DESY1 sample

.

Figure 4.12 and in row 2 of Table 4.1. The well-centred fraction $\rho$ is reported to be approximately 84% for this sample, however, the errorbars on this value are larger than those for the XCS-SDSS sample. We discuss the comparison between the XCS-SDSS and XCS-DESY1 datasets in Section 4.3.3 below.

### 4.3.3 Comparison of X-ray offsets between SDSS and DESY1

The X-ray-RM offset model described in Section 4.3 is constrained separately for the *XMM* SDSS and DES RM samples. Figure 4.13 shows the posterior constraints of the model parameters for both the SDSS and DES samples. The SDSS sample yields higher precision because of the larger sample size. The fraction of well-centered clusters $\rho$ and the miscentering offset $\tau$ for the miscentered clusters are mildly different from the DES sample which displays a hint of having a higher fraction of well-centered clusters. For the well-centred clusters, the characteristic X-ray-RM offset, $\sigma$, of the DES sample is larger than the respective parameter of the SDSS sample. This reflects the limited angular resolution of X-ray peak identification. Specifically, the higher redshift range results in the lower physical separation resolution of the DES X-ray peak identification.

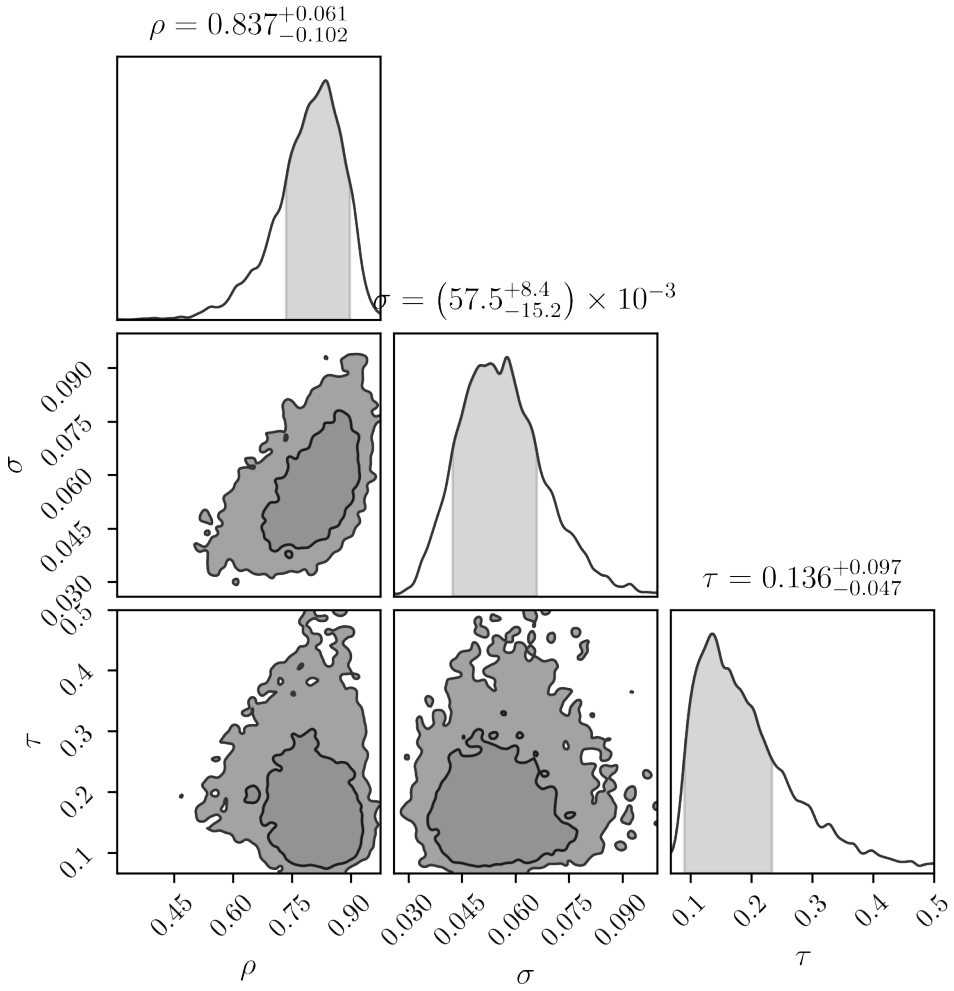


Figure 4.12: Similar to Figure 4.10, the centering offset parameter constraints (Equation 4.2) for the XCS-DESY1 sample are shown here. About 84% of XCS-DESY1 clusters appear to be well-centred (indicated by the $\rho$ parameter). The miscentering offsets are modelled by a Gamma distribution with a characteristic offset (the $\tau$ parameter) around $0.14R_\lambda$

| Prior | $\rho$ | $\sigma$ | $\tau$ |
|---|---|---|---|
| | [0.3,1] | [0.0001.0.1] | [0.04, 0.5] |
| XCS-SDSS | $0.772^{+0.061}_{-0.072}$ | $0.0412^{+0.0079}_{-0.0059}$ | $0.231^{+0.052}_{-0.076}$ |
| XCS-DESY1 | $0.837^{+0.061}_{-0.102}$ | $0.0575^{+0.0084}_{-0.0152}$ | $0.136^{+0.097}_{-0.047}$ |
| XCS-DESY3 | $0.911^{+0.033}_{-0.066}$ | $0.0655^{+0.0099}_{-0.0061}$ | $0.196^{+0.103}_{-0.059}$ |

Table 4.1: Measured centering posterior values for the samples used in this study. Prior ranges for the parameters are listed underneath the parameter names.

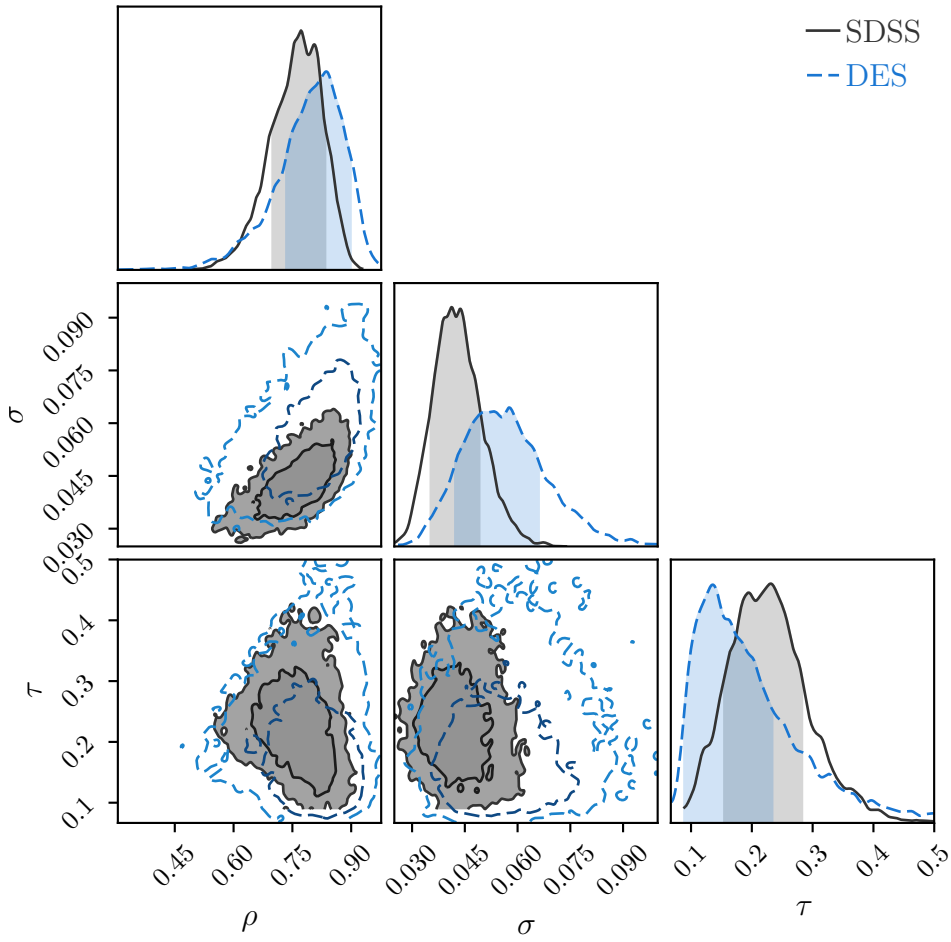


Figure 4.13: The comparison between the centering posteriors for the model parameters for the XCS-SDSS (black solid lines) and XCS-DESY1 (blue dashed lines) samples are displayed, showing the higher well-centred fraction of the DES sample compared to SDSS. The narrower distribution of the SDSS posteriors is due to the larger sample size.

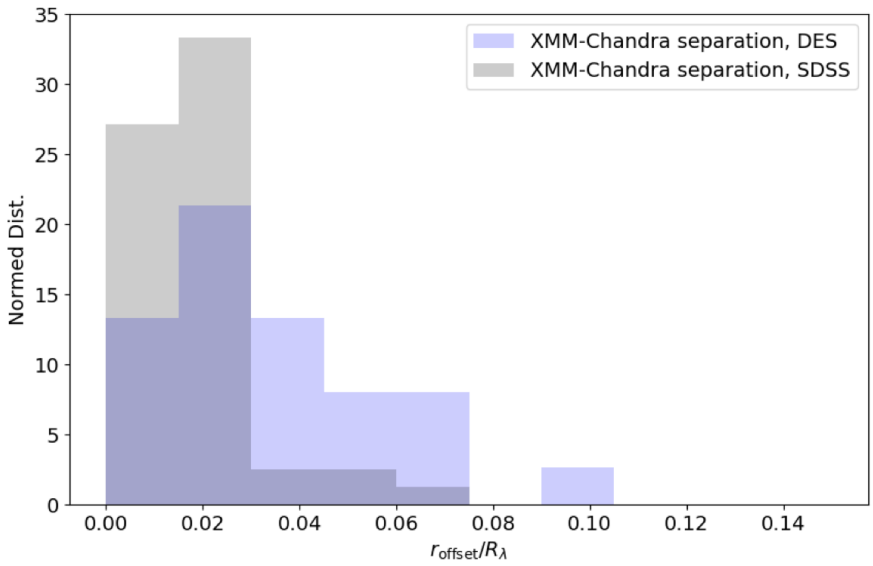


Figure 4.14: The $R_\lambda$ scaled offset distribution between the *Chandra* and *XMM* peak identifications for the same RM clusters.

### 4.3.4 Comparisons between *XMM* and *Chandra*

The offset models described so far have been fitted using *XMM* archival data (i.e. XCS-SDSS and XCS-DESY1). However, the offset model for well-centred clusters (Equation 4.3) is optimised for the *Chandra* PSF (described below). Therefore, we conducted a comparison between both *XMM* and *Chandra* archives to explore the robustness of the fits presented in Figures 4.9 and 4.11. This was done by using a subsample of the RM clusters - 54 in SDSS, and 25 in DES - which were observed by both *XMM* and *Chandra*. In these overlapping cases, we compared the *XMM* peak measurements to those from *Chandra*. Figure 4.14 shows the offset distribution between *XMM* and *Chandra* peak identifications for the same RM clusters, scaled by their $R_\lambda$. The *XMM* and *Chandra* peak identifications are highly consistent: their separations are within $0.05R_\lambda$ for 53/54 of the overlapping SDSS clusters, and 20/25 of the overlapping DES clusters. The separations are noted to have a wider distribution for the DES RM sample, again reflecting its higher redshift range, and hence higher X-ray peak identification uncertainties in terms of physical distances. We also note that Chandra's higher resolution helps at higher redshift, which might further contribute to the increased offset for the DES clusters.

For the full SDSS and DES samples (i.e. containing all and not just overlapping clusters), the *XMM* and *Chandra* best-fitted parameters are shown in Figures 4.15 and 4.16.

The agreement between the $\rho$ and $\tau$ parameters using both *XMM* and *Chandra* SDSS

and DES samples shows that both X-ray telescopes have sufficient resolution to measure the fraction of well-centred clusters ($\rho$) in both RM catalogues. Additionally, the agreement in the miscentering characteristic offset, $\tau$ is also consistent between both X-ray telescopes.

One discrepancy worth examining is the approximately $2\sigma$ deviation in the $\sigma$ parameter measured from the *XMM* and *Chandra* SDSS samples. As described before, the $\sigma$ parameter in the RM centering offset model (Equation 4.2) represents the X-ray peak offset to cluster central galaxy for well-centered clusters, which is further smeared by X-ray peak identification uncertainty and X-ray telescope PSFs. Namely, $\sigma$ is affected by both resolution and positional accuracy. Given the pixel scale for *XMM* ($4.35''$) is larger than Chandra ($0.5''$), peak localising is intrinsically less accurate for *XMM* (especially relevant probing smaller offsets). Given both telescopes also have a resolution which falls off as a function of axis (due to the non-uniform exposure map and shape of the *XMM* PSF), the possibility of a higher fraction of serendipitous vs targeted clusters in either the *XMM* or *Chandra* samples could drive the $\sigma$ differences.

Additionally, since $\sigma$ is in the unit of physical distance, the difference between the *XMM* and *Chandra* samples can be driven by the different angular resolutions of these telescopes at low redshift. Measuring the separation between X-ray peak and RM centre is more precise at lower redshift since the physical distance corresponding to a given angular separation is smaller, hence it is possible to probe the well-centred distribution more accurately. This explains why we note that the $\sigma$ difference is especially larger for the lower redshift SDSS samples.

### 4.3.5 Comparison between XCS-DESY1 and XCS-DESY3

The XCS-DESY3 sample consists of 1093 clusters which fall on an *XMM* observation. Following visual inspection and applying the relevant SNR cuts described in Section 4.2, the sample consists of 180 clusters. Given this sample is approximately 3 times larger than the XCS-DESY1 sample, the centering statistics from the DESY3 sample are expected to deliver more precise constraints on RM's centering performance. The redshift range for the DESY3 sample is the same as the DESY1 sample. Figure 4.18 shows the measured scaled offset distribution of the sample. In Figure 4.19, we show the comparisons in the model parameter constraints between the XCS-DESY1 and XCS-DESY3 samples. The DESY3 sample has a higher fraction of well-centred clusters ($\rho$) - 91% in DESY3 versus 84% in DESY1. This is possibly due to the fact there is a larger proportion of clusters in

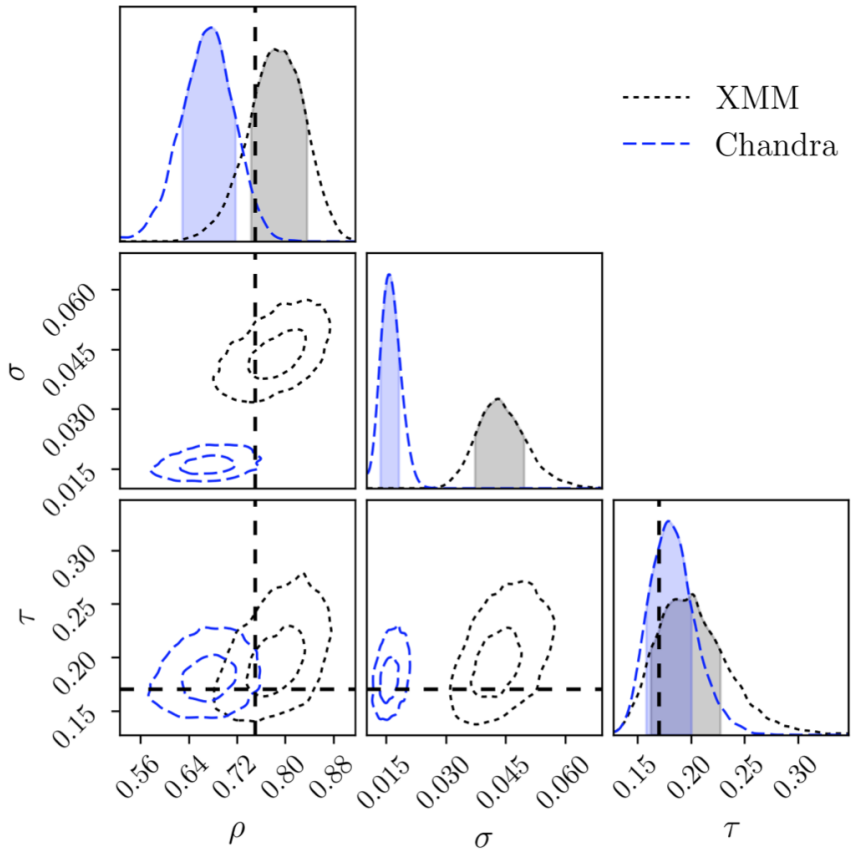


Figure 4.15: Centering model parameter constraints for both the *XMM* and *Chandra* data on the SDSS RM sample.

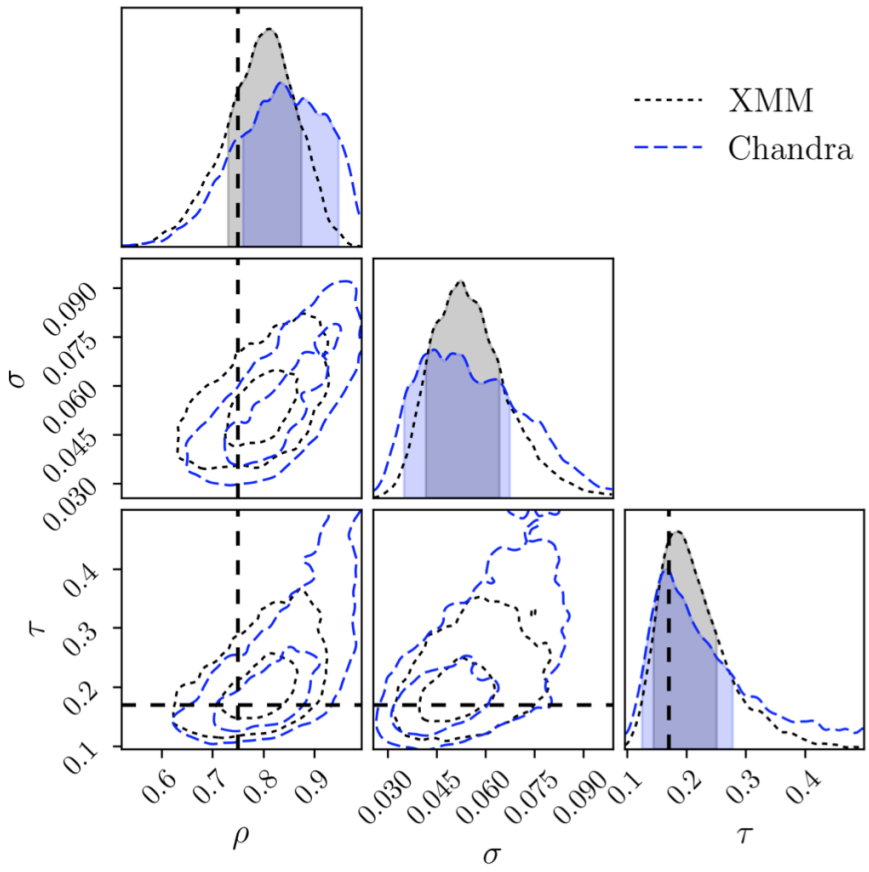


Figure 4.16: Centering model parameter constraints for both the *XMM* and *Chandra* data on the DESY1 RM sample.

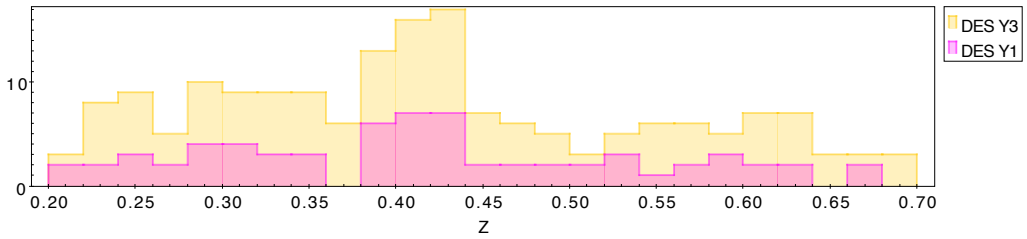


Figure 4.17: Redshift distributions of the XCS-DESY1 (pink) and XCS-DESY3 (yellow). Although the proportion of clusters above the median redshift $z \sim 0.45$ is largely comparable, there are slightly more clusters at higher redshift in XCS-DESY3.

the sample at higher redshift (see Figure 4.17), hence the lower offset resolution may boost the value of $\rho$ compared to the Y1 sample. An improvement in the input photometry used for the DESY3 galaxies might also contribute to a better centering performance. Overall, there is no significant change in the measured values of the $\rho$, $\sigma$ and $\tau$ parameters between the Y1 and Y3 samples, implying the centering statistics determined using the Y1 sample were largely robust.

## 4.4 Impact of miscentering on X-ray properties and selection effects

With a larger set of X-ray observations associated to the DESY3 RM clusters compared to DESY1 (180 compared to 66), it is possible for the first time to examine the centering statistics of RM in different ranges of richness, X-ray temperatures or luminosities, and for serendipitous vs targeted observations. This analysis is new to the literature as previous X-ray samples from *XMM* and *Chandra* were not large enough to produce robust centering statistics as a function of X-ray properties or selection effects. To perform this analysis, we utilise all the XCS-DESY3 clusters with reliable X-ray temperature and luminosity measurements (using the method described in Section 2.6). Out of the 180 clusters, 163 pass the quality checks outlined in Section 2.6.

In lieu of a full correction for selection effects, we separate the XCS-DESY3 cluster sample into targeted and serendipitously detected clusters to investigate the impact of selection effects on the centering performance of RM. We use the simple assumption that clusters falling $>3'$ away from the aimpoint of the observation are serendipitous detections, with clusters $<3'$ to the aimpoint assumed to be targeted observations. We use the XAPA-defined centroid as the centre at which we calculate the off-axis position. Based on this

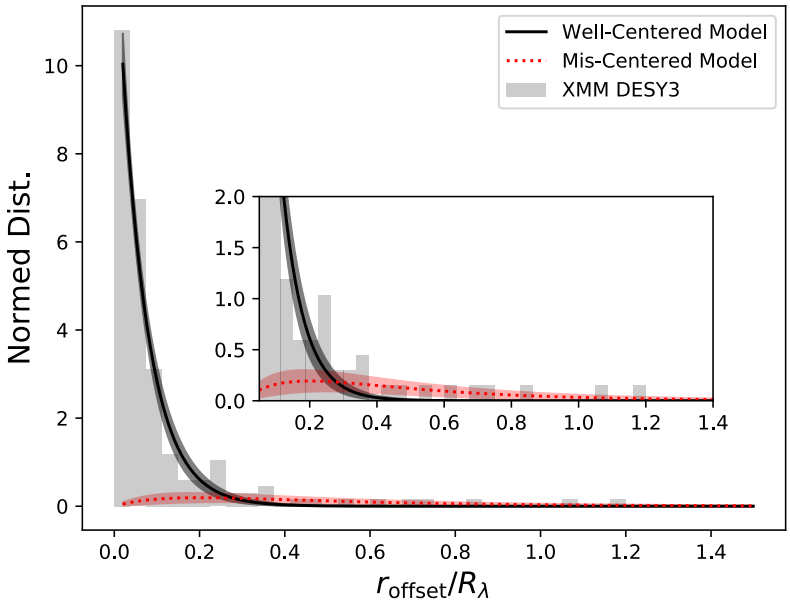


Figure 4.18: Similar to Figure 4.9, the scaled offset distribution for the XCS-DESY3 sample

simple cut, we find 84 clusters are target observations and 79 clusters are serendipitously detected. We display the comparison of the centering parameters for the serendipitous and targeted subsamples in the top-left panel of Figure 4.20.

We find the well-centered fraction is higher for the targeted clusters in the sample compared to the serendipitous clusters ($\rho \simeq 92\%$ and $\rho \simeq 78\%$ respectively), suggesting that miscentering might be more prominent in clusters with large off-axis angles, possibly due to the non-uniform sensitivity of the detector area of *XMM*. This would result in better peak finding at closer distances to the aimpoint. During the initial run, the prior on $\tau$ [0.04 - 0.5] was not wide enough to constrain the offset parameter sufficiently. Therefore, for the serendipitous and targeted subsamples, the chains were rerun with a wider prior [0.04 - 0.8] on $\tau$ to ensure convergence. As expected, the characteristic offset is higher for the serendipitous sample than for the targeted sample, again due to the targeted sample exhibiting very few clusters with significant offsets. Nevertheless, the values of $\tau$ show agreement at the $2\sigma$ level between the serendipitous and targeted clusters, implying that the centering performance is not heavily impacted by this crude estimate of X-ray based selection effects.

We go on to examine the centering dependence on X-ray temperature by coarsely binning the sample into 83 (80) clusters with a $T_{\mathrm{X}}$ less (greater) than 4 keV. This value

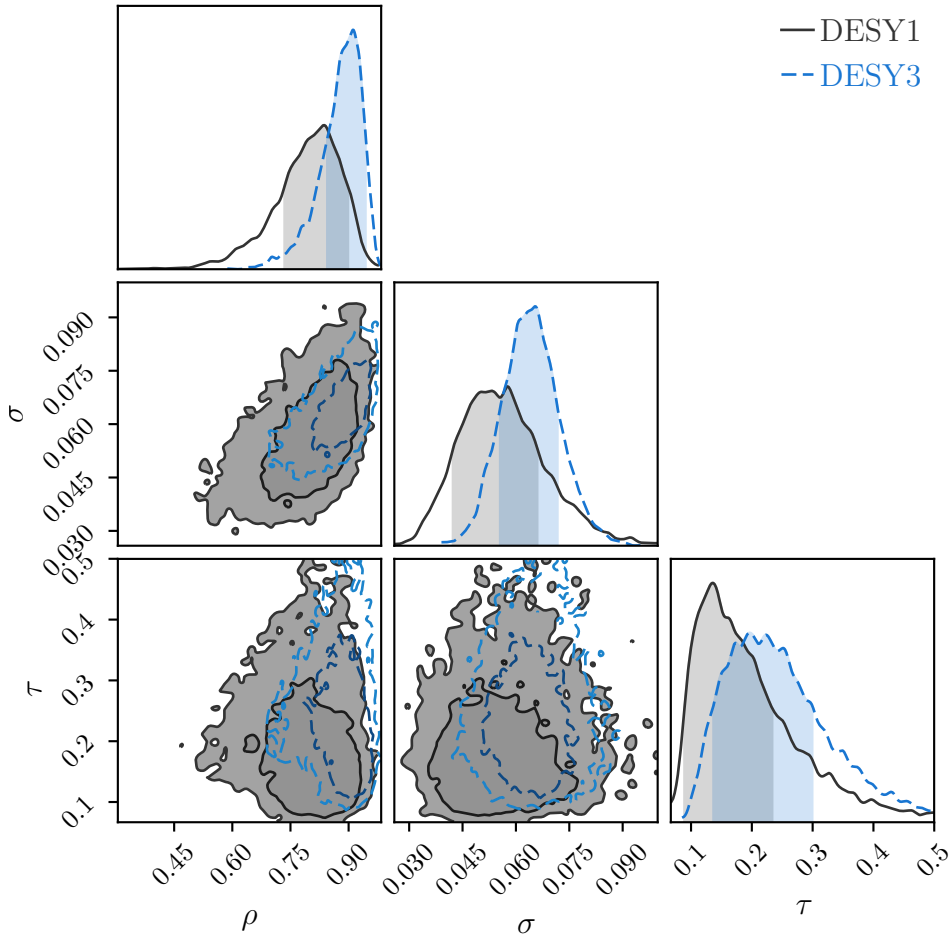


Figure 4.19: Similar to Figure 4.13, a comparison between the posteriors for the model parameters for both the XCS-DESY1 (black solid line) and XCS-DESY3 (blue dashed line) samples are displayed.

was chosen as it closely approximates the median temperature value in the XCS-DESY3 sample. We find the centering performance of RM is largely insensitive to the associated X-ray temperatures of the RM clusters (top right panel of Figure 4.20). The proportion of miscentered clusters in both subsamples is comparable, hence the $\tau$ parameter agrees strongly in both bins. There is marginal evidence that clusters with a $T_{\rm X} > 4$ keV are more well-centered, though this is likely due to higher temperature clusters being defined as targeted clusters in our sample.

Finally, we investigate the centering dependence on photometric redshift and richness by separating our clusters into two redshift bins. We find 84 (79) clusters above (below) $z = 0.4$. Again, this cut is chosen based on the median redshift of the sample. We find almost no difference to the centering parameter values by diving clusters at this redshift (top-left panel of Figure 4.20). It is possible that a trend towards a larger fraction of well-centered clusters might be noticeable at higher redshifts, in part due to the effects described in the comparisons between the SDSS and DESY1 samples, however, better statistics for clusters at high redshift would be required to undertake this comparison. A richness comparison is also performed after splitting the sample into those in the range $20 < \lambda < 50$ (77 clusters) and those greater than 50 (86 clusters). Again, we find the centering parameters to be in good agreement for both the 'high' and 'low' richness clusters, with a hint that $\lambda < 50$ clusters feature a more prominent miscentering offset.

It is important to note that while these tests confirm that the values of $\rho$, $\sigma$ and $\tau$ obtained for the full XCS-DESY3 sample are largely insensitive to the chosen $T_{\rm X}$, $\lambda$ and $z$ distribution of the clusters, the posteriors highlighted in Figure 4.20 are likely to be correlated. For example, it is likely that the higher richness clusters in the sample also have a higher associated $T_{\rm X}$, which would be reflected in the posterior constraints. In order to quantify the full extent of correlation between centering posteriors obtained on the basis of X-ray/optical properties, a calculation of the covariance matrices between the cluster properties would be required.

## 4.5 Impact of miscentering on X-ray-richness scaling relations

It is possible to rerun the RM $\lambda$ algorithm by manually assigning the X-ray peaks as the cluster centres. This procedure is equivalent to the original $\lambda$ estimation with the exception of a "percolation" process, which re-evaluates $\lambda$ upon masking neighbouring RM clusters.

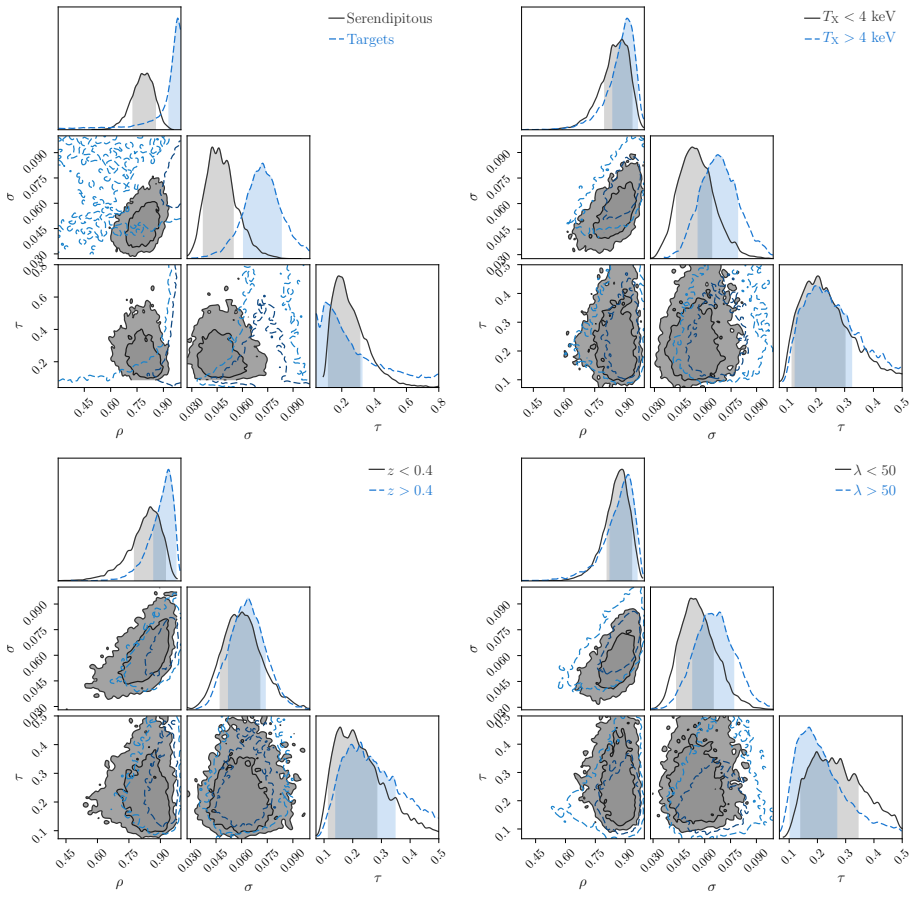


Figure 4.20: Centering posteriors on the XCS-DESY3 sample for serendipitous vs targeted observations (top-left), in different ranges of X-ray temperature (top-right), photometric redshift (bottom-left) and RM richness (bottom-right).

The $\lambda$ estimations on X-ray peaks do not go through the "percolation" process as the run does not consider RM clusters not present in the X-ray sample. To ensure that the percolation process is negligible, we remove clusters whose $\lambda$ changed by 10% in the initial RM percolation process. Once those clusters are removed, it is possible to examine the variation in X-ray centred ($\lambda_{Xray}$) and initial richness ($\lambda$). The distribution of original RM richness versus X-ray centred richness for both the XCS-SDSS and XCS-DESY1 samples are shown in Figure 4.21. In both the XCS-SDSS and XCS-DESY1 samples, the richness measured at the RM and X-ray position display good agreement. In the case of XCS-SDSS, there is increased scatter at the lower richness end ($\lambda \leq 30$) compared to XCS-DESY1. This is likely due to the comparatively low well-centered fraction in the former sample.

Evidence of a richness bias within X-ray selected cluster samples affects the robustness of $T_{\rm X} - \lambda$, $L_{\rm X} - \lambda$ scaling relations. Given that X-ray properties are measured at the location of the relevant X-ray centre, if this is significantly offset from the location of the richness measurement (i.e. in the case of severely miscentered clusters), a bias will be introduced. This bias can be modelled via measurements of the normalisation, slope and intrinsic scatter on $T_{\rm X} - \lambda$, $L_{\rm X} - \lambda$ relation at the original RM centre and subsequent X-ray centre (X. Chen, priv. comm).

### 4.5.1 Outlier analysis

Based on Figure 4.21, it is clear that in the majority of cases, the RM selected and X-ray centred richness are in agreement. However, it is clear that in three cases (2 in SDSS, 1 in DES), there is a significant discrepancy in the two richness values. In all three cases, the X-ray richness is biased considerably higher than the initial richness estimate. All three of these outliers are caused by RM's mispercolation failure mode (see a visual example in Figure 2.13). We outline the details of the specific clusters below. The first outlier is the XCS-SDSS cluster with RM ID 21 in ObsID 0401170101, $\lambda_{RM,orig} = 39$, $\lambda_{RM,xray} = 177$, $z = 0.30$. This is a mispercolated, merging system comprised of three clusters aligned in projection. The optical centre is associated to a lower richness cluster in projection, while the X-ray peak is aligned more with the higher richness cluster. This cluster could not be manually corrected in the analysis due to the two clusters being too close in the *XMM* FOV to be separable, given the angular resolution of the instrument. The second outlier is an XCS-SDSS cluster with RM ID 685 in ObsID 0723161601, $\lambda_{RM,orig} = 39$, $\lambda_{RM,xray} = 116$, $z = 0.32$, which is a mispercolated system where the optical centre is aligned with a lower richness cluster. The third and final outlier is an XCS-DESY1 cluster

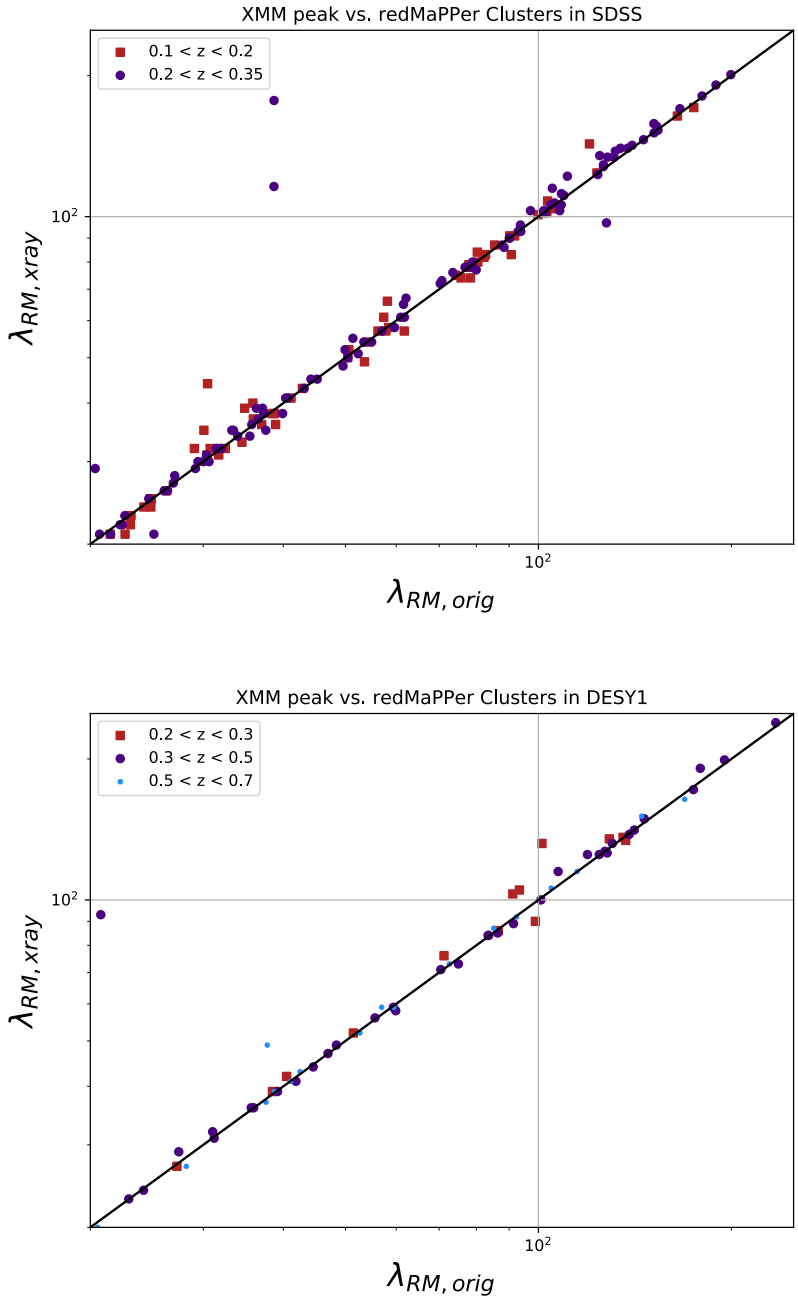


Figure 4.21: Re-estimation of RM-selected cluster richnesses at the X-ray emission peak versus their original RM richness. Top (bottom) panel shows the clusters with a matched X-ray source in the SDSS (DES) RM samples. The black line is a unity line for the reference.

with RM ID 201 in ObsID 0723161601, $\lambda_{RM,orig} = 21$, $\lambda_{RM,xray} = 93$, $z = 0.33$, which has a low SNR ($\simeq 11$), and consists of multiple systems at different redshifts, such that the peak measurement is offset from the optical centre, likely due to the presence of a star in the middle of the cluster.

## 4.6 Impact of miscentering on mass estimates and abundance cosmology

In stacked cluster lensing studies, the measured signal ($\Sigma$), is fitted to an analytic model to determine cluster mass, as per Equation 4.1. For the centering analysis described in this Chapter, the equivalent method to correct for miscentering, as described in McClintock et al. (2018) is,

$$\Sigma(r|M,c) = \rho\Sigma_{cent}(r|M,c) + (1-\rho)\Sigma_{miscent}(r|M,c) \tag{4.5}$$

where $\Sigma(r|M,c)$ is the cluster mass profile model, with mass $M$ and concentration $c$. The mass profile for well-centred clusters is defined by $\Sigma_{cent}(r|M,c)$, while the one for miscentered clusters is given by $\Sigma_{miscent}(r|M,c)$. The miscentered profile is averaged over the angle, $\theta$, and magnitude, $R$, of the radial vector to the correct center, and is described by the parameter $\tau$. Based on the values presented in Zhang et al. (2019), the chosen values for the centering parameters in the weak lensing mass measurements are as follows: $\rho = 0.75 \pm 0.08$ and $\tau = 0.17 \pm 0.04$. By probing the sensitivity of $M$ and $c$ values on different choices of $\rho$ and $\tau$, it is found that cluster mass estimation is robust under inaccurate assumptions of $\rho$, but susceptible to inaccuracy in $\tau$. The concentration parameter, on the contrary, is more susceptible to the inaccuracy of $\rho$ than $\tau$ (Zhang et al., 2019). Uncertainities in $\tau$ at a level of $\pm 0.04$ (comparable to the constraints provided from this Chapter) result in a mass uncertainty of $\pm 0.015$ dex ($\delta \log(M_{200}) = 0.015$).

Miscentered clusters are typically biased low in the richness. This is due to the fact the brightest central galaxy selected by the cluster finder is offset from the remainder of the cluster galaxy population. As a result, all genuine red sequence cluster members are not considered, in addition to impacts from non-cluster member contamination. This $\lambda$ offset introduces bias into the mass-richness scaling relation. To test the extent of this bias, Zhang et al. (2019) uses an N-body simulation in which richnesses are assigned for each of the simulated dark matter halos, using the richness-mass scaling relation from Saro et al. (2015). The richness values are then perturbed using the *Chandra* SDSS offset model and richness bias model. No evidence of a richness bias is found in the corresponding *XMM*

SDSS and DES datasets. The resulting impact from miscentering on the mass-richness scatter, denoted by $\sigma_{ln\lambda}|M$, is 2% (Zhang et al., 2019).

Physically, the bias in the mass-richness relation manifests in the number count for clusters selected by $\lambda$. As stated above, miscentering tends to lower the richness estimation. This means the fraction of clusters above a given richness threshold, when taking into account the effect of miscentering, is smaller. The average mass of the clusters selected by the miscentered richnesses tend to be higher (by $\simeq 0.5\%$).

Although miscentering is a subdominant contribution to the overall systematic uncertainty in cluster lensing studies (Melchior et al., 2017; McClintock et al., 2018), and abundance cosmology (Costanzi et al., 2018), it can nevertheless be explicitly modelled. For larger datasets such as those from DESY3, DESY6 and LSST, the effect of miscentering is likely to be a more substantial contribution than one which is purely statistical.

## 4.7 Summary and future work

In this Chapter, we made use of archival X-ray observations to constrain the centering performance of the RM cluster finding algorithm. We calibrated the well-centred fraction of three datasets - XCS-SDSS, XCS-DESY1 and XCS-DESY3 using *XMM* observations, additionally testing the robustness of the fits from XCS-SDSS and XCS-DESY1 using archival *Chandra* data. We find that for the XCS-SDSS (XCS-DESY1) sample, there are approximately $77^{+6}_{-7}\%$ ($84^{+6}_{-10}\%$) well-centred clusters. For the XCS-DESY3 sample, the well-centred fraction is $91^{+3}_{-6}\%$. The offset distribution of the miscentered clusters is modelled using a Gamma distribution described by the $\tau$ parameter. The cluster mass modelling is demonstrably most sensitive to this parameter, while the choice of concentration appears to be more sensitive to the well-centred fraction.

Proposed future work on this analysis involves modelling the offset distribution of larger RM samples with archival X-ray data, in order to obtain more precise constraints on the $\tau$ and $\rho$ parameters. Access to larger samples will also enable accurate measurements of the scatter in X-ray-richness and mass-richness relations, which will be explored in an upcoming publication.

Additional future work on this analysis is to quantify the occurrence of large offsets due to various reasons. As discussed in Section 4.1, misidentifications of the cluster centre can occur in merging and/or mispercolated systems, due to 'blue' star-forming BCGs and clusters with multiple 'central' galaxies. Flagging and quantifying the dominant reason for miscentering is hence useful for modelling the overall centering performance of RM.

For example, if the largest contribution to miscentering arises from mispercolated systems or blue star-forming BCGs, it is possible to compare these statistics to other non-red sequence based cluster finders such as WazP (Wavelet Adapted z Photometric, Benoist et al. in prep).

A particularly prescient application in understanding the contribution of miscentering is due to the aforementioned effect of cluster richnesses being biased lower as a result. The richness bias is offset dependent, low for clusters with small miscentering offsets, but larger than 50% for severely miscentered clusters. Cluster cosmology studies based on full depth DES data or LSST data should explicitly account for this effect to avoid biased cosmological parameter inferences. The results from Abbott et al. (2020) have invigorated a new, robust examination of systematic effects in optical cluster cosmology. The results of the analysis of DES Y1 RM clusters favour surprisingly low values for cosmological parameters: $S_8 = \sigma_8(\Omega_m/0.3)^{0.5} = 0.65 \pm 0.04$, with $\sigma_8 - \Omega_m$ posteriors in $2.4\sigma$ internal tension with DES galaxy clustering measurements (Abbott et al., 2018), and a $5.6\sigma$ tension with the *Planck* CMB analysis. Though the impact of miscentering across the entire sample, and hence the richness bias, is found to be negligible in this analysis, larger future datasets will need to quantify such effects more robustly.

Given that multiple independent cosmological probes favour significantly higher values of the matter density parameter suggests the presence of systematic errors in the data or incomplete modelling of the relevant physics. Various cross-checks using both X-ray and SZ-selected clusters, which yield independent observable-mass relations, have suggested the issue lies in the weak lensing analysis rather than the cluster abundance. In repeating the analysis using a higher richness threshold for the cluster sample ($\lambda \geq 30$) significantly reduces the tension with other probes, and points to one or more richness-dependent effects not captured by the model. Therefore, investigating the origin of any potential richness bias - potentially through modelling the prominence of miscentering in clusters with $\lambda \leq 30$, will be a key component in understanding what drives the current cosmological tension between galaxy clusters and other probes.

# Chapter 5

# Conclusions

In this thesis, we have explored the use of clusters as both novel and standard probes of dark matter. This has been enabled by the use of archival X-ray data from *XMM-Newton* and optical information from the redMaPPer SDSS and DES catalogues. Given that approximately 85% of the cluster mass is in the form of dark matter, these systems are ideal laboratories to indirectly test for new dark matter candidates, in addition to constraining the overall matter content in the Universe.

In Chapter 2, we constructed three samples drawn from the RM cluster catalogues, derived from SDSS DR8, DES Y1 and DES Y3. These catalogues were then crossmatched with all sufficiently high quality, usable observations in the *XMM* public archive. We outlined the key steps undertaken in ensuring all X-ray and optical counterparts are genuine matches. We then detailed the measurement of X-ray properties from these confirmed clusters, resulting in the creation of the XCS-SDSS, XCS-DESY1 and XCS-DESY3 samples. All clusters in these samples are optically confirmed and also have an associated X-ray temperature, luminosity, optical richness, photometric redshift, and signal-to-noise estimate.

In Chapter 3, we used clusters of galaxies as novel astrophysical probes of dark matter. This was based on the most influential study to date, (Bulbul et al., 2014, B14), in which 73 clusters observed by the *XMM-Newton* satellite were found to have an unexplained excess of X-ray emission at $\simeq$ 3.5 keV. We explored the sterile neutrino dark matter interpretation for this excess with the spectra of clusters of galaxies. We used individual and joint fits to *XMM*-PN spectra of 118 XCS-SDSS clusters. In our analysis of individual spectra, we identified three systems with an excess of flux (over the fiducial plasma model) at $\simeq$ 3.5 keV. In one case (XCS J0003.3+0204) this excess may result from

a discrete emission line. None of these systems are the most dark matter dominated in our sample. We then grouped the remaining 115 clusters into four temperature ($T_{\rm X}$) bins, and performed joint fits to search for evidence of an increase in $\simeq 3.5$ keV flux excess with $T_{\rm X}$. Such a trend would support a dark matter interpretation given that $T_{\rm X}$ is a reliable tracer of the underlying halo mass. However, we do not find evidence of a significant excess in flux at $\simeq 3.5$ keV in any of the bins. Finally, to maximise sensitivity to a potentially weak dark matter decay line at $\simeq 3.5$ keV, we performed a joint fit across the 115 clusters. Again, no significant excess is found at $\simeq 3.5$ keV. We estimate the upper limit of an undetected emission line at $\simeq 3.5$ keV to be $2.39 \times 10^{-6}$ photons cm$^{-2}$ s$^{-1}$, which corresponds to a mixing angle $\sin^2(2\theta) = 4.3 \times 10^{-11}$. This is lower than previous estimates from cluster studies (e.g. $\sin^2(2\theta) \simeq 7 \times 10^{-11}$, B14). We conclude that although there is a measurable flux excess at $\simeq 3.5$ keV in some individual cluster spectra (e.g. XCS J0003.3+0204), this is not a ubiquitous feature, and hence unlikely to originate from sterile neutrino dark matter decay. Following the arrival of future X-ray instruments such as *XRISM* in 2022, with its heightened spectral resolution, in addition to updates to the necessary plasma and atomic models for the cluster ICM, it should be possible to finally reveal the origin of the heavily speculated 3.5 keV line in both individual and joint cluster searches.

In Chapter 4, we measured the offset between cluster centre assigned by the RM cluster finding algorithm against the 'true' halo centre, defined by X-ray emission peak. Such offsets impact both richness measurements and the weak lensing shear profile around clusters. We modelled the centering performance of the RM cluster finding algorithm using the XCS-SDSS, XCS-DESY1 and XCS-DESY3 samples. By analysing the offset of the X-ray emission peaks to the RM centers, we found that $\sim 77 \pm 8\%$ of the RM clusters are well centred and the miscentered offset can be sufficiently described using a Gamma distribution as a function of scaled comoving distance. These miscentering offsets cause a systematic underestimation of cluster richness relative to the well-centered clusters, however it is only significant in severely miscentered clusters. Outliers are established to be the result of mispercolated clusters. Our results have enabled the DES Y1 cluster cosmology analysis by characterising the necessary corrections to both the weak lensing and richness abundance functions of the DES Y1 RM cluster catalogue. The XCS-DESY3 results will be used in future DES Y3 RM cosmology analysis.

In general, cosmological analyses have greatly benefited from the addition of constraints

provided by galaxy clusters. The unique $\Omega_M$-$\sigma_8$ parameter space spanned by clusters can successfully break degeneracies from other probes such as type-Ia supernovae and CMB anisotropies. However, cluster studies thus far have been limited in the use of multi-wavelength confirmed datasets, generation of statistically complete samples, as well as efforts to mitigate dominant sources of uncertainty. Many of these sources of uncertainty are specific to the wavelength in question, e.g. X-ray surveys are typically less susceptible to projection effects but suffer in sensitivity at higher redshifts. Optical cluster finders such as RM can accurately confirm cluster membership based on photometric properties but can over/underestimate cluster members based on correlated structures along the line of sight or mispercolated systems. On the other hand, SZ surveys have recently emerged as a powerful contender in the generation of cosmological estimates from cluster samples, due to the redshift-independent nature of the SZ signal and low scatter in SZ mass proxies (Bocquet et al., 2019).

In general, the main uncertainty for cluster cosmology lies in the understanding of the chosen mass-observable relation (Planck Collaboration et al., 2018). Hence, a crucial step for ensuring an accurate cosmological inference is in the measurement of cluster masses. Given that recent optical datasets have alluded to mass biases caused by underestimating the impact of baryonic 'gastrophysics,' deeper observations of clusters at the group scale and/or with lower richness (e.g. $\lambda < 30$), will also help to quantify the extent of such biases. Subsequent cluster analyses will therefore need to utilise the advantages of multiwavelength data to confirm clusters in a wide range of both masses and redshifts. Future catalogues such as the ACT catalogue (Hilton et al., 2020) and upcoming surveys such as LSST, Euclid, and eROSITA will yield even larger numbers of clusters in cosmological volumes. With the measurement of low scatter mass proxies and reconstruction techniques, one can obtain a robust mass calibration to derive the most precise estimates from galaxy clusters so far.

# Bibliography

Abazajian, K., Adelman-McCarthy, J. K., Ageros, M. A., Allam, S. S., Anderson, S. F., Annis, J., Bahcall, N. A., Baldry, I. K., Bastian, S., Berlind, A., and et al. (2003). The first data release of the sloan digital sky survey. *The Astronomical Journal*, 126(4):20812086. 38

Abazajian, K. N. (2017). Sterile neutrinos in cosmology. *Physics Reports*, 711-712:128. xviii, 67

Abbott, T., Abdalla, F., Alarcon, A., Aleksi, J., Allam, S., Allen, S., Amara, A., Annis, J., Asorey, J., Avila, S., and et al. (2018). Dark energy survey year 1 results: Cosmological constraints from galaxy clustering and weak lensing. *Physical Review D*, 98(4). 41, 132

Abbott, T., Aguena, M., Alarcon, A., Allam, S., Allen, S., Annis, J., Avila, S., Bacon, D., Bechtol, K., Bermeo, A., and et al. (2020). Dark energy survey year 1 results: Cosmological constraints from cluster abundances and weak lensing. *Physical Review D*, 102(2). 41, 101, 132

Abbott, T. M. C., Allam, S., Andersen, P., Angus, C., Asorey, J., Avelino, A., Avila, S., Bassett, B. A., Bechtol, K., Bernstein, G. M., and et al. (2019). First cosmology results using type ia supernovae from the dark energy survey: Constraints on cosmological parameters. *The Astrophysical Journal*, 872(2):L30. 41

Abell, G. O. (1958a). The Distribution of Rich Clusters of Galaxies. , 3:211. 8

Abell, G. O. (1958b). The Distribution of Rich Clusters of Galaxies. , 3:211. 86, 90

Abell, G. O., Corwin, Harold G., J., and Olowin, R. P. (1989). A Catalog of Rich Clusters of Galaxies. , 70:1. 8

Ackermann, M., Ajello, M., Albert, A., Atwood, W. B., Baldini, L., Ballet, J., Barbiellini, G., Bastieri, D., Bellazzini, R., Bissaldi, E., and et al. (2017). Thefermigalactic center gev excess and implications for dark matter. *The Astrophysical Journal*, 840(1):43. 65

Ade, P. A. R., Aghanim, N., Arnaud, M., Ashdown, M., Aumont, J., Baccigalupi, C., Banday, A. J., Barreiro, R. B., Barrena, R., and et al. (2016). Planck2015 results. *Astronomy Astrophysics*, 594:A27. 9

Aharonian, Hitomi Collaboration, F., Akamatsu, H., Akimoto, F., Allen, S. W., Angelini, L., Audard, M., Awaki, H., Axelsson, M., Bamba, A., Bautz, M. W., and et al. (2018). Atomic data and spectral modeling constraints from high-resolution x-ray observations of the perseus cluster with hitomi*. *Publications of the Astronomical Society of Japan*, 70(2). 38, 78, 81

Aharonian, F. A., Akamatsu, H., Akimoto, F., Allen, S. W., Angelini, L., Arnaud, K. A., Audard, M., Awaki, H., Axelsson, M., Bamba, A., Bautz, M. W., Blandford, R. D., Bulbul, E., Brenneman, L. W., Brown, G. V., Cackett, E. M., Chernyakova, M., Chiao, M. P., Coppi, P., Costantini, E., de Plaa, J., den Herder, J. W., Done, C., Dotani, T., Ebisawa, K., Eckart, M. E., Enoto, T., Ezoe, Y., Fabian, A. C., Ferrigno, C., Foster, A. R., Fujimoto, R., Fukazawa, Y., Furuzawa, A., Galeazzi, M., Gallo, L. C., Gandhi, P., Giustini, M., Goldwurm, A., Gu, L., Guainazzi, M., Haba, Y., Hagino, K., Hamaguchi, K., Harrus, I., Hatsukade, I., Hayashi, K., Hayashi, T., Hayashida, K., Hiraga, J., Hornschemeier, A. E., Hoshino, A., Hughes, J. P., Ichinohe, Y., Iizuka, R., Inoue, H., Inoue, S., Inoue, Y., Ishibashi, K., Ishida, M., Ishikawa, K., Ishisaki, Y., Itoh, M., Iwai, M., Iyomoto, N., Kaastra, J. S., Kallman, T., Kamae, T., Kara, E., Kataoka, J., Katsuda, S., Katsuta, J., Kawaharada, M., Kawai, N., Kelley, R. L., Khangulyan, D., Kilbourne, C. A., King, A. L., Kitaguchi, T., Kitamoto, S., Kitayama, T., Kohmura, T., Kokubun, M., Koyama, S., Koyama, K., Kretschmar, P., Krimm, H. A., Kubota, A., Kunieda, H., Laurent, P., Lebrun, F., Lee, S. H., Leutenegger, M. A., Limousin, O., Loewenstein, M., Long, K. S., Lumb, D. H., Madejski, G. M., Maeda, Y., Maier, D., Makishima, K., Markevitch, M., Matsumoto, H., Matsushita, K., McCammon, D., McNamara, B. R., Mehdipour, M., Miller, E. D., Miller, J. M., Mineshige, S., Mitsuda, K., Mitsuishi, I., Miyazawa, T., Mizuno, T., Mori, H., Mori, K., Moseley, H., Mukai, K., Murakami, H., Murakami, T., Mushotzky, R. F., Nakagawa, T., Nakajima, H., Nakamori, T., Nakano, T., Nakashima, S., Nakazawa, K., Nobukawa, K., Nobukawa, M., Noda, H., Nomachi, M., O' Dell, S. L., Odaka, H., Ohashi, T., Ohno, M., Okajima, T., Ota, N., Ozaki, M., Paerels, F., Paltani, S., Parmar, A., Petre, R., Pinto, C., Pohl, M., Porter, F. S., Pottschmidt, K., Ramsey, B. D., Reynolds, C. S., Russell, H. R., Safi-Harb, S., Saito, S., Sakai, K., Sameshima, H., Sasaki, T., Sato, G., Sato, K., Sato, R., Sawada, M., Schartel, N., Serlemitsos, P. J., Seta, H., Shidatsu, M., Simionescu,

A., Smith, R. K., Soong, Y., Stawarz, Ł., Sugawara, Y., Sugita, S., Szymkowiak, A. E., Tajima, H., Takahashi, H., Takahashi, T., Takeda, S., Takei, Y., Tamagawa, T., Tamura, K., Tamura, T., Tanaka, T., Tanaka, Y., Tanaka, Y., Tashiro, M., Tawara, Y., Terada, Y., Terashima, Y., Tombesi, F., Tomida, H., Tsuboi, Y., Tsujimoto, M., Tsunemi, H., Tsuru, T., Uchida, H., Uchiyama, H., Uchiyama, Y., Ueda, S., Ueda, Y., Ueno, S., Uno, S., Urry, C. M., Ursino, E., de Vries, C. P., Watanabe, S., Werner, N., Wik, D. R., Wilkins, D. R., Williams, B. J., Yamada, S., Yamaguchi, H., Yamaoka, K., Yamasaki, N. Y., Yamauchi, M., Yamauchi, S., Yaqoob, T., Yatsu, Y., Yonetoku, D., Yoshida, A., Zhuravleva, I., Zoghbi, A., and Hitomi Collaboration (2017). Hitomi Constraints on the 3.5 keV Line in the Perseus Galaxy Cluster. , 837(1):L15. 68

Ahumada, R., Prieto, C. A., Almeida, A., Anders, F., Anderson, S. F., Andrews, B. H., Anguiano, B., Arcodia, R., Armengaud, E., Aubert, M., Avila, S., Avila-Reese, V., Badenes, C., Balland, C., Barger, K., Barrera-Ballesteros, J. K., Basu, S., Bautista, J., Beaton, R. L., Beers, T. C., Benavides, B. I. T., Bender, C. F., Bernardi, M., Bershady, M., Beutler, F., Bidin, C. M., Bird, J., Bizyaev, D., Blanc, G. A., Blanton, M. R., Boquien, M., Borissova, J., Bovy, J., Brandt, W. N., Brinkmann, J., Brownstein, J. R., Bundy, K., Bureau, M., Burgasser, A., Burtin, E., Cano-Diaz, M., Capasso, R., Cappellari, M., Carrera, R., Chabanier, S., Chaplin, W., Chapman, M., Cherinka, B., Chiappini, C., Choi, P. D., Chojnowski, S. D., Chung, H., Clerc, N., Coffey, D., Comerford, J. M., Comparat, J., da Costa, L., Cousinou, M.-C., Covey, K., Crane, J. D., Cunha, K., da Silva Ilha, G., Dai, Y. S., Damsted, S. B., Darling, J., Darrington, D. H., Jr., J. W. D., Davies, R., Dawson, K., De, N., de la Macorra, A., Lee, N. D., de Andrade Queiroz, A. B., Machado, A. D., de la Torre, S., Dell'Agli, F., du Mas des Bourboux, H., Diamond-Stanic, A. M., Dillon, S., Donor, J., Drory, N., Duckworth, C., Dwelly, T., Ebelke, G., Eftekharzadeh, S., Eigenbrot, A. D., Elsworth, Y. P., Eracleous, M., Erfanianfar, G., Escoffier, S., Fan, X., Farr, E., Fernandez-Trincado, J. G., Feuillet, D., Finoguenov, A., Fofie, P., Fraser-McKelvie, A., Frinchaboy, P. M., Fromenteau, S., Fu, H., Galbany, L., Garcia, R. A., Garcia-Hernandez, D. A., Oehmichen, L. A. G., Ge, J., Maia, M. A. G., Geisler, D., Gelfand, J., Goddy, J., Goff, J.-M. L., Gonzalez-Perez, V., Grabowski, K., Green, P., Grier, C. J., Guo, H., Guy, J., Harding, P., Hasselquist, S., Hawken, A. J., Hayes, C. R., Hearty, F., Hekker, S., Hogg, D. W., Holtzman, J., Hou, J., Hsieh, B.-C., Huber, D., Hunt, J. A. S., Chitham, J. I., Imig, J., Jaber, M., Angel, C. E. J., Johnson, J. A., Jones, A. M., Jonsson, H., Jullo, E., Kim, Y., Kinemuchi, K., IV, C. C. K., Kite, G. W., Klaene, M., Kneib, J.-P., Kollmeier,

J. A., Kong, H., Kounkel, M., Krishnarao, D., Lacerna, I., Lan, T.-W., Lane, R. R., Law, D. R., Leung, H. W., Lewis, H., Li, C., Lian, J., Lin, L., Long, D., Longa-Pena, P., Lundgren, B., Lyke, B. W., Mackereth, J. T., MacLeod, C. L., Majewski, S. R., Manchado, A., Maraston, C., Martini, P., Masseron, T., Masters, K. L., Mathur, S., McDermid, R. M., Merloni, A., Merrifield, M., Meszaros, S., Miglio, A., Minniti, D., Minsley, R., Miyaji, T., Mohammad, F. G., Mosser, B., Mueller, E.-M., Muna, D., Munoz-Gutierrez, A., Myers, A. D., Nadathur, S., Nair, P., do Nascimento, J. C., Nevin, R. J., Newman, J. A., Nidever, D. L., Nitschelm, C., Noterdaeme, P., O'Connell, J. E., Olmstead, M. D., Oravetz, D., Oravetz, A., Osorio, Y., Pace, Z. J., Padilla, N., Palanque-Delabrouille, N., Palicio, P. A., Pan, H.-A., Pan, K., Parker, J., Paviot, R., Peirani, S., Ramrez, K. P., Penny, S., Percival, W. J., Perez-Fournon, I., Perez-Rafols, I., Petitjean, P., Pieri, M. M., Pinsonneault, M., Poovelil, V. J., Povick, J. T., Prakash, A., Price-Whelan, A. M., Raddick, M. J., Raichoor, A., Ray, A., Rembold, S. B., Rezaie, M., Riffel, R. A., Riffel, R., Rix, H.-W., Robin, A. C., Roman-Lopes, A., Roman-Zuniga, C., Rose, B., Ross, A. J., Rossi, G., Rowlands, K., Rubin, K. H. R., Salvato, M., Sanchez, A. G., Sanchez-Menguiano, L., Sanchez-Gallego, J. R., Sayres, C., Schaefer, A., Schiavon, R. P., Schimoia, J. S., Schlafly, E., Schlegel, D., Schneider, D. P., Schultheis, M., Schwope, A., Seo, H.-J., Serenelli, A., Shafieloo, A., Shamsi, S. J., Shao, Z., Shen, S., Shetrone, M., Shirley, R., Aguirre, V. S., Simon, J. D., Skrutskie, M. F., Slosar, A., Smethurst, R., Sobeck, J., Sodi, B. C., Souto, D., Stark, D. V., Stassun, K. G., Steinmetz, M., Stello, D., Stermer, J., Storchi-Bergmann, T., Streblyanska, A., Stringfellow, G. S., Stutz, A., Suarez, G., Sun, J., Taghizadeh-Popp, M., Talbot, M. S., Tayar, J., Thakar, A. R., Theriault, R., Thomas, D., Thomas, Z. C., Tinker, J., Tojeiro, R., Toledo, H. H., Tremonti, C. A., Troup, N. W., Tuttle, S., Unda-Sanzana, E., Valentini, M., Vargas-Gonzalez, J., Vargas-Magana, M., Vazquez-Mata, J. A., Vivek, M., Wake, D., Wang, Y., Weaver, B. A., Weijmans, A.-M., Wild, V., Wilson, J. C., Wilson, R. F., Wolthuis, N., Wood-Vasey, W. M., Yan, R., Yang, M., Yeche, C., Zamora, O., Zarrouk, P., Zasowski, G., Zhang, K., Zhao, C., Zhao, G., Zheng, Z., Zheng, Z., Zhu, G., and Zou, H. (2019). The sixteenth data release of the sloan digital sky surveys: First release from the apogee-2 southern survey and full release of eboss spectra. 38

Aihara, H., Allende Prieto, C., An, D., Anderson, S. F., Aubourg, ., Balbinot, E., Beers, T. C., Berlind, A. A., Bickerton, S. J., Bizyaev, D., and et al. (2011). The eighth data release of the sloan digital sky survey: First data from sdss-iii. *The Astrophysical*

*Journal Supplement Series*, 193(2):29. xiv, 38, 39, 48

Aihara, H., Arimoto, N., Armstrong, R., Arnouts, S., Bahcall, N. A., Bickerton, S., Bosch, J., Bundy, K., Capak, P. L., Chan, J. H. H., Chiba, M., Coupon, J., Egami, E., Enoki, M., Finet, F., Fujimori, H., Fujimoto, S., Furusawa, H., Furusawa, J., Goto, T., Goulding, A., Greco, J. P., Greene, J. E., Gunn, J. E., Hamana, T., Harikane, Y., Hashimoto, Y., Hattori, T., Hayashi, M., Hayashi, Y., Hełminiak, K. G., Higuchi, R., Hikage, C., Ho, P. T. P., Hsieh, B.-C., Huang, K., Huang, S., Ikeda, H., Imanishi, M., Inoue, A. K., Iwasawa, K., Iwata, I., Jaelani, A. T., Jian, H.-Y., Kamata, Y., Karoji, H., Kashikawa, N., Katayama, N., Kawanomoto, S., Kayo, I., Koda, J., Koike, M., Kojima, T., Komiyama, Y., Konno, A., Koshida, S., Koyama, Y., Kusakabe, H., Leauthaud, A., Lee, C.-H., Lin, L., Lin, Y.-T., Lupton, R. H., Mand elbaum, R., Matsuoka, Y., Medezinski, E., Mineo, S., Miyama, S., Miyatake, H., Miyazaki, S., Momose, R., More, A., More, S., Moritani, Y., Moriya, T. J., Morokuma, T., Mukae, S., Murata, R., Murayama, H., Nagao, T., Nakata, F., Niida, M., Niikura, H., Nishizawa, A. J., Obuchi, Y., Oguri, M., Oishi, Y., Okabe, N., Okamoto, S., Okura, Y., Ono, Y., Onodera, M., Onoue, M., Osato, K., Ouchi, M., Price, P. A., Pyo, T.-S., Sako, M., Sawicki, M., Shibuya, T., Shimasaku, K., Shimono, A., Shirasaki, M., Silverman, J. D., Simet, M., Speagle, J., Spergel, D. N., Strauss, M. A., Sugahara, Y., Sugiyama, N., Suto, Y., Suyu, S. H., Suzuki, N., Tait, P. J., Takada, M., Takata, T., Tamura, N., Tanaka, M. M., Tanaka, M., Tanaka, M., Tanaka, Y., Terai, T., Terashima, Y., Toba, Y., Tominaga, N., Toshikawa, J., Turner, E. L., Uchida, T., Uchiyama, H., Umetsu, K., Uraguchi, F., Urata, Y., Usuda, T., Utsumi, Y., Wang, S.-Y., Wang, W.-H., Wong, K. C., Yabe, K., Yamada, Y., Yamanoi, H., Yasuda, N., Yeh, S., Yonehara, A., and Yuma, S. (2018). The Hyper Suprime-Cam SSP Survey: Overview and survey design. , 70:S4. 41

Allen, S. W., Evrard, A. E., and Mantz, A. B. (2011). Cosmological parameters from observations of galaxy clusters. *Annual Review of Astronomy and Astrophysics*, 49(1):409470. xii, 7

Allen, S. W., Rapetti, D. A., Schmidt, R. W., Ebeling, H., Morris, R. G., and Fabian, A. C. (2008). Improved constraints on dark energy from Chandra X-ray observations of the largest relaxed galaxy clusters. , 383(3):879–896. xiii, 28, 29

Allen, S. W., Schmidt, R. W., and Fabian, A. C. (2002). Cosmological constraints from the X-ray gas mass fraction in relaxed lensing clusters observed with Chandra. , 334(2):L11–L15. 28

Anders, E. and Grevesse, N. (1989). Abundances of the elements - Meteoritic and solar. , 53:197–214. 57, 73

Anderson, M. E., Churazov, E., and Bregman, J. N. (2015). Non-detection of X-ray emission from sterile neutrinos in stacked galaxy spectra. , 452(4):3905–3923. 68

Andreon, S. (2008). The history of mass assembly of faint red galaxies in 28 galaxy clusters since z = 1.3. *Monthly Notices of the Royal Astronomical Society*, 386(2):10451052. 9

Applegate, D. E., von der Linden, A., Kelly, P. L., Allen, M. T., Allen, S. W., Burchat, P. R., Burke, D. L., Ebeling, H., Mantz, A., and Morris, R. G. (2014). Weighing the giants iii. methods and measurements of accurate galaxy cluster weak-lensing masses. *Monthly Notices of the Royal Astronomical Society*, 439(1):4872. 19

Arnaud, K. A. (1996). XSPEC: The First Ten Years. In Jacoby, G. H. and Barnes, J., editors, *Astronomical Data Analysis Software and Systems V*, volume 101 of *Astronomical Society of the Pacific Conference Series*, page 17. 53, 73, 78

Arnaud, M. and Evrard, A. E. (1999). The lx–t relation and intracluster gas fractions of x-ray clusters. *Monthly Notices of the Royal Astronomical Society*, 305(3):631640. 25

Arnaud, M., Pointecouteau, E., and Pratt, G. W. (2005). The structural and scaling properties of nearby galaxy clusters. II. The M-T relation. , 441:893–903. xiii, 22, 23, 57, 70, 75

Arnaud, M., Pointecouteau, E., and Pratt, G. W. (2007). Calibration of the galaxy cluster m500$y_x$ relation with xmm-newton. *Astronomy Astrophysics*, 474(3):L37L40. 25

Asplund, M., Grevesse, N., Sauval, A. J., and Scott, P. (2009). The Chemical Composition of the Sun. , 47:481–522. 94

Bacon, D. J., Refregier, A. R., and Ellis, R. S. (2000). Detection of weak gravitational lensing by large-scale structure. *Monthly Notices of the Royal Astronomical Society*, 318(2):625640. 17

Bahcall, J. N. and Sarazin, C. L. (1978). X-ray line spectroscopy for clusters of galaxies. I. , 219:781–794. 11

Bahcall, N. A. (1977). X-ray clusters of galaxies: correlations with optical morphology and galaxy density. , 217:L77–L82. 15

Bahcall, N. A. (1999). The cosmic triangle: Revealing the state of the universe. *Science*, 284(5419):14811488. 1

Baxter, E., Chang, C., Jain, B., Adhikari, S., Dalal, N., Kravtsov, A., More, S., Rozo, E., Rykoff, E., and Sheth, R. K. (2017). The halo boundary of galaxy clusters in the sdss. *The Astrophysical Journal*, 841(1):18. 103

Becker, M. R. and Kravtsov, A. V. (2011). On the accuracy of weak-lensing cluster mass reconstructions. *The Astrophysical Journal*, 740(1):25. 19

Behroozi, P. S., Wechsler, R. H., and Wu, H.-Y. (2013). The ROCKSTAR Phase-space Temporal Halo Finder and the Velocity Offsets of Cluster Cores. , 762(2):109. 102

Ben Bekhti, N., Fler, L., Keller, R., Kerp, J., Lenz, D., Winkel, B., Bailin, J., Calabretta, M. R., Dedes, L., and et al. (2016). Hi4pi: a full-sky hi survey based on ebhis and gass. *Astronomy Astrophysics*, 594:A116. 70

Birkinshaw, M. (1999). The Sunyaev-Zel'dovich effect. , 310(2-3):97–195. 9

Bleem, L. E., Bocquet, S., Stalder, B., Gladders, M. D., Ade, P. A. R., Allen, S. W., Anderson, A. J., Annis, J., Ashby, M. L. N., Austermann, J. E., and et al. (2020). The sptpol extended cluster survey. *The Astrophysical Journal Supplement Series*, 247(1):25. 103

Bocquet, S., Dietrich, J. P., Schrabback, T., Bleem, L. E., Klein, M., Allen, S. W., Applegate, D. E., Ashby, M. L. N., Bautz, M., Bayliss, M., Benson, B. A., Brodwin, M., Bulbul, E., Canning, R. E. A., Capasso, R., Carlstrom, J. E., Chang, C. L., Chiu, I., Cho, H. M., Clocchiatti, A., Crawford, T. M., Crites, A. T., de Haan, T., Desai, S., Dobbs, M. A., Foley, R. J., Forman, W. R., Garmire, G. P., George, E. M., Gladders, M. D., Gonzalez, A. H., Grandis, S., Gupta, N., Halverson, N. W., Hlavacek-Larrondo, J., Hoekstra, H., Holder, G. P., Holzapfel, W. L., Hou, Z., Hrubes, J. D., Huang, N., Jones, C., Khullar, G., Knox, L., Kraft, R., Lee, A. T., von der Linden, A., Luong-Van, D., Mantz, A., Marrone, D. P., McDonald, M., McMahon, J. J., Meyer, S. S., Mocanu, L. M., Mohr, J. J., Morris, R. G., Padin, S., Patil, S., Pryke, C., Rapetti, D., Reichardt, C. L., Rest, A., Ruhl, J. E., Saliwanchik, B. R., Saro, A., Sayre, J. T., Schaffer, K. K., Shirokoff, E., Stalder, B., Stanford, S. A., Staniszewski, Z., Stark, A. A., Story, K. T., Strazzullo, V., Stubbs, C. W., Vanderlinde, K., Vieira, J. D., Vikhlinin, A., Williamson, R., and Zenteno, A. (2019). Cluster Cosmology Constraints from the 2500 deg$^2$ SPT-SZ

Survey: Inclusion of Weak Gravitational Lensing Data from Magellan and the Hubble Space Telescope. , 878(1):55. 135

Böhringer, H., Pratt, G. W., Arnaud, M., Borgani, S., Croston, J. H., Ponman, T. J., Ameglio, S., Temple, R. F., and Dolag, K. (2010). Substructure of the galaxy clusters in the rexcess sample: observed statistics and comparison to numerical simulations. *Astronomy and Astrophysics*, 514:A32. 86

Böhringer, H., Schuecker, P., Guzzo, L., Collins, C. A., Voges, W., Cruddace, R. G., Ortiz-Gil, A., Chincarini, G., De Grandi, S., Edge, A. C., MacGillivray, H. T., Neumann, D. M., Schindler, S., and Shaver, P. (2004). The ROSAT-ESO Flux Limited X-ray (REFLEX) Galaxy cluster survey. V. The cluster catalogue. , 425:367–383. 37

Böhringer, H., Schuecker, P., Pratt, G. W., Arnaud, M., Ponman, T. J., Croston, J. H., Borgani, S., Bower, R. G., Briel, U. G., Collins, C. A., and et al. (2007). The representative xmm-newton cluster structure survey (rexcess) of an x-ray luminosity selected galaxy cluster sample. *Astronomy Astrophysics*, 469(1):363. 86

Böhringer, H. and Werner, N. (2010). X-ray spectroscopy of galaxy clusters: studying astrophysical processes in the largest celestial laboratories. *The Astronomy and Astrophysics Review*, 18(1):127–196. 11

Bonamente, M. (2019). Distribution of the c statistic with applications to the sample mean of poisson data. 78

Borgani, S. and Guzzo, L. (2001). X-ray clusters of galaxies as tracers of structure in the universe. *Nature*, 409(6816):3945. xiii, 30

Bower, R. G., Lucey, J. R., and Ellis, R. S. (1992). Precision photometry of early-type galaxies in the Coma and Virgo clusters : a test of the universality of the colour-magnitude relation - I. The data. , 254:589–600. 8

Boyarsky, A., Iakubovskyi, D., Ruchayskiy, O., and Savchenko, D. (2018). Surface brightness profile of the 3.5 keV line in the Milky Way halo. *arXiv e-prints*, page arXiv:1812.10488. 68

Boyarsky, A., Ruchayskiy, O., Iakubovskyi, D., and Franse, J. (2014). Unidentified line in x-ray spectra of the andromeda galaxy and perseus galaxy cluster. *Phys. Rev. Lett.*, 113:251301. 65, 68

Boyarsky, A., Ruchayskiy, O., and Shaposhnikov, M. (2009). The Role of Sterile Neutrinos in Cosmology and Astrophysics. *Annual Review of Nuclear and Particle Science*, 59(1):191–214. 66

Boylan-Kolchin, M., Bullock, J. S., and Kaplinghat, M. (2011). Too big to fail? The puzzling darkness of massive Milky Way subhaloes. , 415(1):L40–L44. 65

Bryan, G. L. and Norman, M. L. (1998). Statistical Properties of X-Ray Clusters: Analytic and Numerical Comparisons. , 495(1):80–99. 102

Bulbul, E., Markevitch, M., Foster, A., Miller, E., Bautz, M., Loewenstein, M., Randall, S. W., and Smith, R. K. (2016). Searching for the 3.5 kev line in the stackedsuzakuobservations of galaxy clusters. *The Astrophysical Journal*, 831(1):55. 67, 99

Bulbul, E., Markevitch, M., Foster, A., Smith, R. K., Loewenstein, M., and Randall, S. W. (2014). Detection of an Unidentified Emission Line in the Stacked X-Ray Spectrum of Galaxy Clusters. , 789:13. 64, 65, 67, 69, 98, 133

Bundy, K., Bershady, M. A., Law, D. R., Yan, R., Drory, N., MacDonald, N., Wake, D. A., Cherinka, B., Snchez-Gallego, J. R., Weijmans, A.-M., and et al. (2014). Overview of the sdss-iv manga survey: Mapping nearby galaxies at apache point observatory. *The Astrophysical Journal*, 798(1):7. 40

Buote, D. A. and Tsai, J. C. (1995). The reliability of x-ray constraints of intrinsic cluster shapes. *The Astrophysical Journal*, 439:29. 103

Burenin, R. A., Vikhlinin, A., Hornstrup, A., Ebeling, H., Quintana, H., and Mescheryakov, A. (2007). The 400 square degree rosat pspc galaxy cluster survey: Catalog and statistical calibration. *The Astrophysical Journal Supplement Series*, 172(2):561582. 37

Cappelluti, N., Bulbul, E., Foster, A., Natarajan, P., Urry, M. C., Bautz, M. W., Civano, F., Miller, E., and Smith, R. K. (2018). Searching for the 3.5 keV Line in the Deep Fields with Chandra: The 10 Ms Observations. , 854(2):179. 68, 78, 90

Cash, W. (1979). Parameter estimation in astronomy through application of the likelihood ratio. , 228:939–947. 74, 76, 78

Cavaliere, A. and Fusco-Femiano, R. (1976). Reprint of 1976A&A....49..137C. X-rays from hot plasma in clusters of galaxies. , 500:95–102. 12

Chiu, I.-N., Umetsu, K., Murata, R., Medezinski, E., and Oguri, M. (2019). The richness-to-mass relation of camira galaxy clusters from weak-lensing magnification in the subaru hyper suprime-cam survey. 25

Clerc, N., Merloni, A., Zhang, Y.-Y., Finoguenov, A., Dwelly, T., Nandra, K., Collins, C., Dawson, K., Kneib, J.-P., Rozo, E., and et al. (2016). Spiders: the spectroscopic follow-up of x-ray-selected clusters of galaxies in sdss-iv. *Monthly Notices of the Royal Astronomical Society*, 463(4):44904515. 37, 40

Clerc, N., Sadibekova, T., Pierre, M., Pacaud, F., Le Fvre, J.-P., Adami, C., Altieri, B., and Valtchanov, I. (2012). The cosmological analysis of x-ray cluster surveys - ii. application of the cr-hr method to the xmm archive. *Monthly Notices of the Royal Astronomical Society*, 423(4):35613583. 36

Clowe, D., Brada, M., Gonzalez, A. H., Markevitch, M., Randall, S. W., Jones, C., and Zaritsky, D. (2006). A direct empirical proof of the existence of dark matter. *The Astrophysical Journal*, 648(2):L109L113. 64

Conlon, J. P., Day, F., Jennings, N., Krippendorf, S., and Rummel, M. (2017). Consistency of hitomi, xmm-newton, and chandra 3.5 kev data from perseus. *Phys. Rev. D*, 96:123009. 68

Costanzi, M., Rozo, E., Rykoff, E. S., Farahi, A., Jeltema, T., Evrard, A. E., Mantz, A., Gruen, D., Mandelbaum, R., DeRose, J., and et al. (2018). Modelling projection effects in optically selected cluster catalogues. *Monthly Notices of the Royal Astronomical Society*, 482(1):490505. 103, 131

Costanzi, M., Rozo, E., Simet, M., Zhang, Y., Evrard, A. E., Mantz, A., Rykoff, E. S., Jeltema, T., Gruen, D., Allen, S., and et al. (2019). Methods for cluster cosmology and application to the sdss in preparation for des year 1 release. *Monthly Notices of the Royal Astronomical Society*, 488(4):47794800. 101

Dark Energy Survey Collaboration, Abbott, T., Abdalla, F. B., Aleksić, J., Allam, S., Amara, A., Bacon, D., Balbinot, E., Banerji, M., Bechtol, K., Benoit-Lévy, A., Bernstein, G. M., Bertin, E., Blazek, J., Bonnett, C., Bridle, S., Brooks, D., Brunner, R. J., Buckley-Geer, E., Burke, D. L., Caminha, G. B., Capozzi, D., Carlsen, J., Carnero-Rosell, A., Carollo, M., Carrasco-Kind, M., Carretero, J., Castander, F. J., Clerkin, L., Collett, T., Conselice, C., Crocce, M., Cunha, C. E., D'Andrea, C. B., da Costa, L. N.,

Davis, T. M., Desai, S., Diehl, H. T., Dietrich, J. P., Dodelson, S., Doel, P., Drlica-Wagner, A., Estrada, J., Etherington, J., Evrard, A. E., Fabbri, J., Finley, D. A., Flaugher, B., Foley, R. J., Fosalba, P., Frieman, J., García-Bellido, J., Gaztanaga, E., Gerdes, D. W., Giannantonio, T., Goldstein, D. A., Gruen, D., Gruendl, R. A., Guarnieri, P., Gutierrez, G., Hartley, W., Honscheid, K., Jain, B., James, D. J., Jeltema, T., Jouvel, S., Kessler, R., King, A., Kirk, D., Kron, R., Kuehn, K., Kuropatkin, N., Lahav, O., Li, T. S., Lima, M., Lin, H., Maia, M. A. G., Makler, M., Manera, M., Maraston, C., Marshall, J. L., Martini, P., McMahon, R. G., Melchior, P., Merson, A., Miller, C. J., Miquel, R., Mohr, J. J., Morice-Atkinson, X., Naidoo, K., Neilsen, E., Nichol, R. C., Nord, B., Ogando, R., Ostrovski, F., Palmese, A., Papadopoulos, A., Peiris, H. V., Peoples, J., Percival, W. J., Plazas, A. A., Reed, S. L., Refregier, A., Romer, A. K., Roodman, A., Ross, A., Rozo, E., Rykoff, E. S., Sadeh, I., Sako, M., Sánchez, C., Sanchez, E., Santiago, B., Scarpine, V., Schubnell, M., Sevilla-Noarbe, I., Sheldon, E., Smith, M., Smith, R. C., Soares-Santos, M., Sobreira, F., Soumagnac, M., Suchyta, E., Sullivan, M., Swanson, M., Tarle, G., Thaler, J., Thomas, D., Thomas, R. C., Tucker, D., Vieira, J. D., Vikram, V., Walker, A. R., Wechsler, R. H., Weller, J., Wester, W., Whiteway, L., Wilcox, H., Yanny, B., Zhang, Y., and Zuntz, J. (2016). The Dark Energy Survey: more than dark energy - an overview. , 460(2):1270–1299. xv, 41, 42

Dawson, K. S., Schlegel, D. J., Ahn, C. P., Anderson, S. F., Aubourg, ., Bailey, S., Barkhouser, R. H., Bautista, J. E., Beifiori, A., Berlind, A. A., and et al. (2012). The baryon oscillation spectroscopic survey of sdss-iii. *The Astronomical Journal*, 145(1):10. 40

de Jong, J. T. A., Kuijken, K., Applegate, D., Begeman, K., Belikov, A., Blake, C., Bout, J., Boxhoorn, D., Buddelmeijer, H., Buddendiek, A., Cacciato, M., Capaccioli, M., Choi, A., Cordes, O., Covone, G., Dall'Ora, M., Edge, A., Erben, T., Franse, J., Getman, F., Grado, A., Harnois-Deraps, J., Helmich, E., Herbonnet, R., Heymans, C., Hildebrand t, H., Hoekstra, H., Huang, Z., Irisarri, N., Joachimi, B., Köhlinger, F., Kitching, T., La Barbera, F., Lacerda, P., McFarland, J., Miller, L., Nakajima, R., Napolitano, N. R., Paolillo, M., Peacock, J., Pila-Diez, B., Puddu, E., Radovich, M., Rifatto, A., Schneider, P., Schrabback, T., Sifon, C., Sikkema, G., Simon, P., Sutherland, W., Tudorica, A., Valentijn, E., van der Burg, R., van Uitert, E., van Waerbeke, L., Veland er, M., Verdoes Kleijn, G., Viola, M., and Vriend, W. J. (2013). The Kilo-Degree Survey. *The Messenger*, 154:44–46. 41

De Lucia, G. and Blaizot, J. (2007). The hierarchical formation of the brightest cluster galaxies. , 375(1):2–14. 8

DeRose, J., Wechsler, R. H., Becker, M. R., Busha, M. T., Rykoff, E. S., MacCrann, N., Erickson, B., Evrard, A. E., Kravtsov, A., Gruen, D., Allam, S., Avila, S., Bridle, S., Brooks, D., Buckley-Geer, E., Rosell, A. C., Kind, M. C., Carretero, J., Castander, F. J., Cawthon, R., Crocce, M., da Costa, L. N., Davis, C., Vicente, J. D., Dietrich, J. P., Doel, P., Drlica-Wagner, A., Fosalba, P., Frieman, J., Garcia-Bellido, J., Gutierrez, G., Hartley, W. G., Hollowood, D. L., Hoyle, B., James, D. J., Krause, E., Kuehn, K., Kuropatkin, N., Lima, M., Maia, M. A. G., Menanteau, F., Miller, C. J., Miquel, R., Ogando, R. L. C., Malagn, A. P., Romer, A. K., Sanchez, E., Schindler, R., Serrano, S., Sevilla-Noarbe, I., Smith, M., Suchyta, E., Swanson, M. E. C., Tarle, G., and Vikram, V. (2019). The buzzard flock: Dark energy survey synthetic sky catalogs. 102

Dessert, C., Rodd, N. L., and Safdi, B. R. (2018). Evidence against the decaying dark matter interpretation of the 3.5 keV line from blank sky observations. *arXiv e-prints*, page arXiv:1812.06976. 68, 99

Diaferio, A. (2009). Measuring the mass profile of galaxy clusters beyond their virial radius. 14

Dressler, A. (1980). A catalog of morphological types in 55 rich clusters of galaxies. , 42:565–609. 8

Drlica-Wagner, A., Sevilla-Noarbe, I., Rykoff, E. S., Gruendl, R. A., Yanny, B., Tucker, D. L., Hoyle, B., Rosell, A. C., Bernstein, G. M., Bechtol, K., and et al. (2018). Dark energy survey year 1 results: The photometric data set for cosmology. *The Astrophysical Journal Supplement Series*, 235(2):33. 61

Dutton, A. A. and Macci, A. V. (2014). Cold dark matter haloes in the planck era: evolution of structural parameters for einasto and nfw profiles. *Monthly Notices of the Royal Astronomical Society*, 441(4):33593374. 14

Ebeling, H., Edge, A., and Henry, J. P. (2000a). MACS: The Evolution & Properties of Massive CLusters of Galaxies. In Plionis, M. and Georgantopoulos, I., editors, *Large Scale Structure in the X-ray Universe*, page 39. 37

Ebeling, H., Edge, A. C., Allen, S. W., Crawford, C. S., Fabian, A. C., and Huchra, J. P. (2000b). The ROSAT Brightest Cluster Sample - IV. The extended sample. , 318(2):333–340. 86, 88

Ebeling, H., Edge, A. C., Fabian, A. C., Allen, S. W., Crawford, C. S., and Bhringer, H. (1997). The [ital]rosat[/ital] brightest cluster sample (bcs): The cluster x-ray luminosity function within [clc][ital]z[/ital][/clc] = 0.3. *The Astrophysical Journal*, 479(2):L101L104. 37

Edge, A. C. and Stewart, G. C. (1991). EXOSAT observations of clusters of galaxies - I. The X-ray data. , 252:414. 25

Einasto, J. (1965). On the Construction of a Composite Model for the Galaxy and on the Determination of the System of Galactic Parameters. *Trudy Astrofizicheskogo Instituta Alma-Ata*, 5:87–100. 14

Eke, V. R., Cole, S., Frenk, C. S., and Patrick Henry, J. (1998). Measuring Omega_0 using cluster evolution. , 298(4):1145–1158. 29

Ettori, S. (2003). Are we missing baryons in galaxy clusters? *Monthly Notices of the Royal Astronomical Society*, 344(2):L13L16. 29

Ettori, S., Baldi, A., Balestra, I., Gastaldello, F., Molendi, S., and Tozzi, P. (2015a). The evolution of the spatially resolved metal abundance in galaxy clusters up to z = 1.4. , 578:A46. 57

Ettori, S., Baldi, A., Balestra, I., Gastaldello, F., Molendi, S., and Tozzi, P. (2015b). The evolution of the spatially resolved metal abundance in galaxy clusters up to z = 1.4. , 578:A46. 86

Ettori, S., Donnarumma, A., Pointecouteau, E., Reiprich, T. H., Giodini, S., Lovisari, L., and Schmidt, R. W. (2013). Mass profiles of galaxy clusters from x-ray analysis. *Space Science Reviews*, 177(1-4):119154. xii, 16

Ettori, S., Ghirardini, V., Eckert, D., Pointecouteau, E., Gastaldello, F., Sereno, M., Gaspari, M., Ghizzardi, S., Roncarelli, M., and Rossetti, M. (2019). Hydrostatic mass profiles in x-cop galaxy clusters. *Astronomy Astrophysics*, 621:A39. 19

Fabian, A. C. (1994). Cooling Flows in Clusters of Galaxies. , 32:277–318. 26

Farahi, A., Chen, X., Evrard, A. E., Hollowood, D. L., Wilkinson, R., Bhargava, S., Giles, P., Romer, A. K., Jeltema, T., Hilton, M., Bermeo, A., Mayers, J., Vergara Cervantes, C., Rozo, E., Rykoff, E. S., Collins, C., Costanzi, M., Everett, S., Liddle, A. R., Mann, R. G., Mantz, A., Rooney, P., Sahlen, M., Stott, J., Viana, P. T. P.,

Zhang, Y., Annis, J., Avila, S., Brooks, D., Buckley-Geer, E., Burke, D. L., Carnero Rosell, A., Carrasco Kind, M., Carretero, J., Castander, F. J., da Costa, L. N., De Vicente, J., Desai, S., Diehl, H. T., Dietrich, J. P., Doel, P., Flaugher, B., Fosalba, P., Frieman, J., García-Bellido, J., Gaztanaga, E., Gerdes, D. W., Gruen, D., Gruendl, R. A., Gschwend, J., Gutierrez, G., Honscheid, K., James, D. J., Krause, E., Kuehn, K., Kuropatkin, N., Lima, M., Maia, M. A. G., Marshall, J. L., Melchior, P., Menanteau, F., Miquel, R., Ogando, R. L. C., Plazas, A. A., Sanchez, E., Scarpine, V., Schubnell, M., Serrano, S., Sevilla-Noarbe, I., Smith, M., Sobreira, F., Suchyta, E., Swanson, M. E. C., Tarle, G., Thomas, D., Tucker, D. L., Vikram, V., Walker, A. R., Weller, J., and DES Collaboration (2019). Mass variance from archival X-ray properties of Dark Energy Survey Year-1 galaxy clusters. , 490(3):3341–3354. 26, 171

Felten, J. E., Gould, R. J., Stein, W. A., and Woolf, N. J. (1966). X-Rays from the Coma Cluster of Galaxies. , 146:955–958. 10

Finoguenov, A., Guzzo, L., Hasinger, G., Scoville, N. Z., Aussel, H., Bohringer, H., Brusa, M., Capak, P., Cappelluti, N., Comastri, A., and et al. (2007). The xmmnewton wide-field survey in the cosmos field: Statistical properties of clusters of galaxies. *The Astrophysical Journal Supplement Series*, 172(1):182195. 36

Foster, A. R., Ji, L., Smith, R. K., and Brickhouse, N. S. (2012). Updated Atomic Data and Calculations for X-Ray Spectroscopy. , 756(2):128. 57, 74

Fournier, B. (2019). *The impact of active galactic nuclei and cooling mechanisms on the intra-cluster properties in the L-Galaxies semi-analytical model*. PhD thesis, University of Sussex. 171

Franse, J., Bulbul, E., Foster, A., Boyarsky, A., Markevitch, M., Bautz, M., Iakubovskyi, D., Loewenstein, M., McDonald, M., Miller, E., Randall, S. W., Ruchayskiy, O., and Smith, R. K. (2016). Radial Profile of the 3.5 keV Line Out to R200 in the Perseus Cluster. , 829(2):124. 79

Freeman, P. E., Kashyap, V., Rosner, R., and Lamb, D. Q. (2002). A waveletbased algorithm for the spatial analysis of poisson data. *The Astrophysical Journal Supplement Series*, 138(1):185218. 45

Geller, M. J., Diaferio, A., Rines, K. J., and Serra, A. L. (2013). Measuring the mass distribution in galaxy clusters. *The Astrophysical Journal*, 764(1):58. 20

Gifford, D., Kern, N., and Miller, C. J. (2017). Stacking caustic masses from galaxy clusters. *The Astrophysical Journal*, 834(2):204. 20

Gioia, I. M., Henry, J. P., Maccacaro, T., Morris, S. L., Stocke, J. T., and Wolter, A. (1990). The Extended Medium-Sensitivity Survey Distant Cluster Sample: X-Ray Cosmological Evolution. , 356:L35. 37

Girardi, M., Biviano, A., Giuricin, G., Mardirossian, F., and Mezzetti, M. (1993). Velocity Dispersions in Galaxy Clusters. , 404:38. 8

Gladders, M. D. and Yee, H. K. C. (2000). A new method for galaxy cluster detection. i. the algorithm. *The Astronomical Journal*, 120(4):21482162. 8

Grainge, K., Borgani, S., Colafrancesco, S., Ferrari, C., Scaife, A., Marchegiani, P., Emritte, S., and Weller, J. (2014). Galaxy cluster science with the sunyaev-zel'dovich effect. 9

Grevesse, N. and Sauval, A. J. (1998). Standard Solar Composition. , 85:161–174. 94

Gu, L., Kaastra, J., Raassen, A. J. J., Mullen, P. D., Cumbee, R. S., Lyons, D., and Stancil, P. C. (2015). A novel scenario for the possible X-ray line feature at ~3.5 keV. Charge exchange with bare sulfur ions. , 584:L11. 69

Haehnelt, M. G. and Tegmark, M. (1996). Using the kinematic sunyaev-zeldovich effect to determine the peculiar velocities of clusters of galaxies. *Monthly Notices of the Royal Astronomical Society*, 279(2):545556. 9

Harvey, D., Robertson, A., Massey, R., and McCarthy, I. G. (2019). Observable tests of self-interacting dark matter in galaxy clusters: Bcg wobbles in a constant density core. *Monthly Notices of the Royal Astronomical Society*, 488(2):15721579. 65

Henriques, B. M. B., White, S. D. M., Thomas, P. A., Angulo, R., Guo, Q., Lemson, G., Springel, V., and Overzier, R. (2015). Galaxy formation in the planck cosmology i. matching the observed evolution of star formation rates, colours and stellar masses. *Monthly Notices of the Royal Astronomical Society*, 451(3):26632680. 171

Hilton, M., Hasselfield, M., Sifn, C., Battaglia, N., Aiola, S., Bharadwaj, V., Bond, J. R., Choi, S. K., Crichton, D., Datta, R., and et al. (2018). The atacama cosmology telescope: The two-season actpol sunyaevzeldovich effect selected cluster catalog. *The Astrophysical Journal Supplement Series*, 235(1):20. 9

Hilton, M., Romer, A. K., Kay, S. T., Mehrtens, N., Lloyd-Davies, E. J., Thomas, P. A., Short, C. J., Mayers, J. A., Rooney, P. J., Stott, J. P., Collins, C. A., Harrison, C. D., Hoyle, B., Liddle, A. R., Mann, R. G., Miller, C. J., Sahlén, M., Viana, P. T. P., Davidson, M., Hosmer, M., Nichol, R. C., Sabirli, K., Stanford, S. A., and West, M. J. (2012). The XMM Cluster Survey: evidence for energy injection at high redshift from evolution of the X-ray luminosity-temperature relation. , 424(3):2086–2096. 25

Hilton, M., Sifón, C., Naess, S., Madhavacheril, M., Oguri, M., Rozo, E., Rykoff, E., Abbott, T. M. C., Adhikari, S., Aguena, M., Aiola, S., Allam, S., Amodeo, S., Amon, A., Annis, J., Ansarinejad, B., Aros-Bunster, C., Austermann, J. E., Avila, S., Bacon, D., Battaglia, N., Beall, J. A., Becker, D. T., Bernstein, G. M., Bertin, E., Bhand arkar, T., Bhargava, S., Bond, J. R., Brooks, D., Burke, D. L., Calabrese, E., Carretero, J., Choi, S. K., Choi, A., Conselice, C., da Costa, L. N., Costanzi, M., Crichton, D., Crowley, K. T., Dünner, R., Denison, E. V., Devlin, M. J., Dicker, S. R., Diehl, H. T., Dietrich, J. P., Doel, P., Duff, S. M., Duivenvoorden, A. J., Dunkley, J., Everett, S., Ferraro, S., Ferrero, I., Ferté, A., Flaugher, B., Frieman, J., Gallardo, P. A., García-Bellido, J., Gaztanaga, E., Gerdes, D. W., Giles, P., Golec, J. E., Gralla, M. B., Grandis, S., Gruen, D., Gruendl, R. A., Gschwend, J., Gutierrez, G., Han, D., Hartley, W. G., Hasselfield, M., Hill, J. C., Hilton, G. C., Hincks, A. D., Hinton, S. R., Ho, S.-P. P., Honscheid, K., Hoyle, B., Hubmayr, J., Huffenberger, K. M., Hughes, J. P., Jaelani, A. T., Jain, B., James, D. J., Jeltema, T., Kent, S., Carrasco Kind, M., Knowles, K., Koopman, B. J., Kuehn, K., Lahav, O., Lima, M., Lin, Y.-T., Lokken, M., Loubser, S. I., MacCrann, N., Maia, M. A. G., Marriage, T. A., Martin, J., McMahon, J., Melchior, P., Menanteau, F., Miquel, R., Miyatake, H., Moodley, K., Morgan, R., Mroczkowski, T., Nati, F., Newburgh, L. B., Niemack, M. D., Nishizawa, A. J., Ogando, R. L. C., Orlowski-Scherer, J., Page, L. A., Palmese, A., Partridge, B., Paz-Chinchón, F., Phakathi, P., Plazas, A. A., Robertson, N. C., Romer, A. K., Carnero Rosell, A., Salatino, M., Sanchez, E., Schaan, E., Schillaci, A., Sehgal, N., Serrano, S., Shin, T., Simon, S. M., Smith, M., Soares-Santos, M., Spergel, D. N., Staggs, S. T., Storer, E. R., Suchyta, E., Swanson, M. E. C., Tarle, G., Thomas, D., To, C., Trac, H., Ullom, J. N., Vale, L. R., Van Lanen, J., Vavagiakis, E. M., De Vicente, J., Wilkinson, R. D., Wollack, E. J., Xu, Z., and Zhang, Y. (2020). The Atacama Cosmology Telescope: A Catalog of ¿ 4000 Sunyaev-Zel'dovich Galaxy Clusters. *arXiv e-prints*, page arXiv:2009.11043. 135

Hoekstra, H. (2003). How well can we determine cluster mass profiles from weak lensing? , 339(4):1155–1162. 19

Hoekstra, H. (2007). A comparison of weak-lensing masses and X-ray properties of galaxy clusters. , 379(1):317–330. 19

Hofmann, F. and Wegg, C. (2019). 7.1 kev sterile neutrino dark matter constraints from a deep chandra x-ray observation of the galactic bulge limiting window. *Astronomy Astrophysics*, 625:L7. 68

Holland, J. G., Böhringer, H., Chon, G., and Pierini, D. (2015). Optical and X-ray profiles in the REXCESS sample of galaxy clusters*. , 448(3):2644. 86

Hollowood, D. L., Jeltema, T., Chen, X., Farahi, A., Evrard, A., Everett, S., Rozo, E., Rykoff, E., Bernstein, R., Bermeo-Hernandez, A., and et al. (2019). Chandra follow-up of the sdss dr8 redmapper catalog using the matcha pipeline. *The Astrophysical Journal Supplement Series*, 244(2):22. 26, 53

Honscheid, K. and DePoy, D. L. (2008). The Dark Energy Camera (DECam). *arXiv e-prints*, page arXiv:0810.3600. 40

Hudson, D. S., Mittal, R., Reiprich, T. H., Nulsen, P. E. J., Andernach, H., and Sarazin, C. L. (2010). What is a cool-core cluster? a detailed analysis ofthecores ofthex-ray flux-limitedhiflugcscluster sample. *Astronomy and Astrophysics*, 513:A37. xiii, 27

Humphrey, P. J., Liu, W., and Buote, D. A. (2009). 2and poissonian data: Biases even in the high-count regime and how to avoid them. *The Astrophysical Journal*, 693(1):822. 78

Jeltema, T. and Profumo, S. (2015). Discovery of a 3.5 keV line in the Galactic Centre and a critical look at the origin of the line across astronomical targets. , 450(2):2143–2152. 68, 69

Jeltema, T. and Profumo, S. (2016). Deep XMM observations of Draco rule out at the 99 per cent confidence level a dark matter decay origin for the 3.5 keV line. , 458(4):3592–3596. 68, 81, 99

Jeltema, T. E., Hallman, E. J., Burns, J. O., and Motl, P. M. (2008). Cluster structure in cosmological simulations. i. correlation to observables, mass estimates, and evolution. *The Astrophysical Journal*, 681(1):167186. 15

Johnston, D. E., Sheldon, E. S., Wechsler, R. H., Rozo, E., Koester, B. P., Frieman, J. A., McKay, T. A., Evrard, A. E., Becker, M. R., and Annis, J. (2007). Cross-correlation

weak lensing of sdss galaxy clusters ii: Cluster density profiles and the mass–richness relation. 103

Johnstone, R. M., Fabian, A. C., and Nulsen, P. E. J. (1987). The optical spectra of central galaxies in southern clusters : evidence for star formation. , 224:75–91. 26

Kaastra, J. S. (2017). On the use of c-stat in testing models for x-ray spectra. *Astronomy Astrophysics*, 605:A51. 78

Kaiser, N. (1986). Evolution and clustering of rich clusters. , 222:323–345. 21

Kettula, K., Giodini, S., van Uitert, E., Hoekstra, H., Finoguenov, A., Lerchster, M., Erben, T., Heymans, C., Hildebrandt, H., Kitching, T. D., Mahdavi, A., Mellier, Y., Miller, L., Mirkazemi, M., Van Waerbeke, L., Coupon, J., Egami, E., Fu, L., Hudson, M. J., Kneib, J. P., Kuijken, K., McCracken, H. J., Pereira, M. J., Rowe, B., Schrabback, T., Tanaka, M., and Velander, M. (2015). CFHTLenS: weak lensing calibrated scaling relations for low-mass clusters of galaxies. , 451(2):1460–1481. 19

Kim, M., Jee, M. J., Finner, K., Golovich, N., Wittman, D. M., Weeren, R. J. v., and Dawson, W. A. (2019). Multiwavelength analysis of the merging galaxy cluster a115. *The Astrophysical Journal*, 874(2):143. 103

King, I. R. (1972). Density Data and Emission Measure for a Model of the Coma Cluster. , 174:L123. 12

Klein, M., Grandis, S., Mohr, J. J., Paulus, M., Abbott, T. M. C., Annis, J., Avila, S., Bertin, E., Brooks, D., Buckley-Geer, E., and et al. (2019). A new rass galaxy cluster catalogue with low contamination extending to z  1 in the des overlap region. *Monthly Notices of the Royal Astronomical Society*, 488(1):739769. 37, 62

Klypin, A., Kravtsov, A. V., Valenzuela, O., and Prada, F. (1999). Where are the missing galactic satellites? *The Astrophysical Journal*, 522(1):8292. 65

Koopmans, A. L. H., Owen, D. B., and Rosenblatt, J. I. (1964). Confidence Intervals for the Coefficient of Variation for the Normal and Log Normal Distributions. *Biometrika*, 51(1):25–32. 57

Kravtsov, A. V. and Borgani, S. (2012). Formation of Galaxy Clusters. , 50:353–409. 57, 70

Kravtsov, A. V., Vikhlinin, A., and Nagai, D. (2006). A New Robust Low-Scatter X-Ray Mass Indicator for Clusters of Galaxies. , 650(1):128–136. 25

Lau, E. T., Nagai, D., and Nelson, K. (2013). Weighing galaxy clusters with gas. i. on the methods of computing hydrostatic mass bias. *The Astrophysical Journal*, 777(2):151. 15

Lieu, M., Smith, G. P., Giles, P. A., Ziparo, F., Maughan, B. J., Dmocls, J., Pacaud, F., Pierre, M., Adami, C., Bah, Y. M., and et al. (2016). The xxl survey. *Astronomy Astrophysics*, 592:A4. xiii, 22, 23

Lin, Y. and Mohr, J. J. (2004). Kband properties of galaxy clusters and groups: Brightest cluster galaxies and intracluster light. *The Astrophysical Journal*, 617(2):879895. 103, 105

Lloyd-Davies, E. J., Romer, A. K., Mehrtens, N., Hosmer, M., Davidson, M., Sabirli, K., Mann, R. G., Hilton, M., Liddle, A. R., Viana, P. T. P., Campbell, H. C., Collins, C. A., Dubois, E. N., Freeman, P., Harrison, C. D., Hoyle, B., Kay, S. T., Kuwertz, E., Miller, C. J., Nichol, R. C., Sahlén, M., Stanford, S. A., and Stott, J. P. (2011). The XMM Cluster Survey: X-ray analysis methodology. , 418:14–53. 34, 43, 58, 60

Lodders, K., Palme, H., and Gail, H.-P. (2009). Abundances of the Elements in the Solar System. *Landolt Börnstein*, page 712. 94

Łokas, E. L. and Mamon, G. A. (2001). Properties of spherical galaxies and clusters with an NFW density profile. , 321(1):155–166. 75

Lovell, M. R., Barnes, D., Bah, Y., Schaye, J., Schaller, M., Theuns, T., Bose, S., Crain, R. A., dallaVecchia, C., Frenk, C. S., Hellwing, W., Kay, S. T., Ludlow, A. D., and Bower, R. G. (2019). The signal of decaying dark matter with hydrodynamical simulations. *Monthly Notices of the Royal Astronomical Society*, 485(3):4071–4089. 68

Lovell, M. R., Eke, V., Frenk, C. S., Gao, L., Jenkins, A., Theuns, T., Wang, J., White, S. D. M., Boyarsky, A., and Ruchayskiy, O. (2012). The haloes of bright satellite galaxies in a warm dark matter universe. , 420(3):2318–2324. xvii, 65, 66

Lovisari, L. and Reiprich, T. H. (2018). The non-uniformity of galaxy cluster metallicity profiles. *Monthly Notices of the Royal Astronomical Society*, 483(1):540. 86

Lovisari, L., Reiprich, T. H., and Schellenberger, G. (2015). Scaling properties of a complete x-ray selected galaxy group sample. *Astronomy  Astrophysics*, 573:A118. 24

Mahdavi, A., Hoekstra, H., Babul, A., Bildfell, C., Jeltema, T., and Henry, J. P. (2013). Joint analysis of cluster observations. ii.chandra/xmm-newtonx-ray and weak lensing scaling relations for a sample of 50 rich clusters of galaxies. *The Astrophysical Journal*, 767(2):116. 16

Malyshev, D., Neronov, A., and Eckert, D. (2014). Constraints on 3.55 keV line emission from stacked observations of dwarf spheroidal galaxies. , 90(10):103506. 68

Mantz, A., Allen, S. W., Ebeling, H., Rapetti, D., and Drlica-Wagner, A. (2010). The observed growth of massive galaxy clusters - ii. x-ray scaling relations. *Monthly Notices of the Royal Astronomical Society*, page nono. xiv, 33

Mantz, A. B., Allen, S. W., Morris, R. G., Schmidt, R. W., von der Linden, A., and Urban, O. (2015). Cosmology and astrophysics from relaxed galaxy clusters i. sample selection. *Monthly Notices of the Royal Astronomical Society*, 449(1):199219. 113

Mantz, A. B., Allen, S. W., Morris, R. G., and von der Linden, A. (2018). Centre-excised X-ray luminosity as an efficient mass proxy for future galaxy cluster surveys. , 473(3):3072–3079. 24

Martel, H., Robichaud, F., and Barai, P. (2014). Major cluster mergers and the location of the brightest cluster galaxy. *The Astrophysical Journal*, 786(2):79. 102

Mathews, W. G. (1978). The enormous mass of the elliptical galaxy M87: a model for the extended X-ray source. , 219:413–423. 15

Maughan, B. J. (2007). Thelxyxrelation: Using galaxy cluster xray luminosity as a robust, lowscatter mass proxy. *The Astrophysical Journal*, 668(2):772780. xiii, 24

Maughan, B. J., Giles, P. A., Rines, K. J., Diaferio, A., Geller, M. J., Van Der Pyl, N., and Bonamente, M. (2016). Hydrostatic and caustic mass profiles of galaxy clusters. *Monthly Notices of the Royal Astronomical Society*, 461(4):41824191. 20

Maughan, B. J., Jones, L. R., Ebeling, H., and Scharf, C. (2006). The evolution of the cluster X-ray scaling relations in the Wide Angle ROSAT Pointed Survey sample at 0.6 < z < 1.0. , 365(2):509–529. 24, 25

Maurogordato, S., Sauvageot, J. L., Bourdin, H., Cappi, A., Benoist, C., Ferrari, C., Mars, G., and Houairi, K. (2011). Merging history of three bimodal clusters. , 525:A79. 92

McClintock, T., Varga, T., Gruen, D., Rozo, E., Rykoff, E., Shin, T., Melchior, P., DeRose, J., Seitz, S., Dietrich, J., and et al. (2018). Dark energy survey year 1 results: weak lensing mass calibration of redmapper galaxy clusters. *Monthly Notices of the Royal Astronomical Society*, 482(1):13521378. 61, 102, 130, 131

McDonald, M., Allen, S. W., Bayliss, M., Benson, B. A., Bleem, L. E., Brodwin, M., Bulbul, E., Carlstrom, J. E., Forman, W. R., Hlavacek-Larrondo, J., and et al. (2017). The remarkable similarity of massive galaxy clusters fromz 0 toz 1.9. *The Astrophysical Journal*, 843(1):28. 26

McDonald, M., Stalder, B., Bayliss, M., Allen, S. W., Applegate, D. E., Ashby, M. L. N., Bautz, M., Benson, B. A., Bleem, L. E., Brodwin, M., and et al. (2016). Star-forming brightest cluster galaxies at 0.25 ¡z¡ 1.25: A transitioning fuel supply. *The Astrophysical Journal*, 817(2):86. 103

Mehrtens, N., Romer, A. K., Hilton, M., Lloyd-Davies, E. J., Miller, C. J., Stanford, S. A., Hosmer, M., Hoyle, B., Collins, C. A., Liddle, A. R., and et al. (2012). The xmm cluster survey: optical analysis methodology and the first data release. *Monthly Notices of the Royal Astronomical Society*, 423(2):10241052. 43, 60

Melchior, P., Gruen, D., McClintock, T., Varga, T. N., Sheldon, E., Rozo, E., Amara, A., Becker, M. R., Benson, B. A., Bermeo, A., and et al. (2017). Weak-lensing mass calibration of redmapper galaxy clusters in dark energy survey science verification data. *Monthly Notices of the Royal Astronomical Society*, 469(4):48994920. xxi, 102, 104, 131

Meneghetti, M., Rasia, E., Merten, J., Bellagamba, F., Ettori, S., Mazzotta, P., Dolag, K., and Marri, S. (2010). Weighing simulated galaxy clusters using lensing and X-ray. , 514:A93. 17

Mernier, F., Werner, N., Lakhchaura, K., de Plaa, J., Gu, L., Kaastra, J. S., Mao, J., Simionescu, A., and Urdampilleta, I. (2019). How do atomic code uncertainties affect abundance measurements in the intracluster medium? 97

Miraghaei, H., Khosroshahi, H. G., Sengupta, C., Raychaudhury, S., Jetha, N. N., and Abbassi, S. (2015). Agn activity and igm heating in the fossil cluster rx j1416.4+2315. *The Astronomical Journal*, 150(6):196. 89

Mitchell, R. J., Culhane, J. L., Davison, P. J. N., and Ives, J. C. (1976). Ariel 5 observations of the X-ray spectrum of the Perseus cluster. , 175:29P–34P. 11

Mohr, J. J., Geller, M. J., and Wegner, G. (1996). A Dynamical Analysis of the Poor Galaxy Clusters Abell 2626 and Abell 2440. , 112:1816. 92

Morrison, R. and McCammon, D. (1983). Interstellar photoelectric absorption cross sections, 0.03-10 keV. *The Astrophysical Journal*, 270:119. 57

Murata, R., Oguri, M., Nishimichi, T., Takada, M., Mandelbaum, R., More, S., Shirasaki, M., Nishizawa, A. J., and Osato, K. (2019). The massrichness relation of optically selected clusters from weak gravitational lensing and abundance with subaru hsc first-year data. *Publications of the Astronomical Society of Japan*, 71(5). 102

Navarro, J. F., Frenk, C. S., and White, S. D. M. (1996). The Structure of Cold Dark Matter Halos. , 462:563. 14

Neumann, D. M. and Arnaud, M. (1999). Regularity in the x-ray surface brightness profiles of galaxy clusters and the m-t relation. 13

Newman, A. B., Treu, T., Ellis, R. S., and Sand , D. J. (2011). The Dark Matter Distribution in A383: Evidence for a Shallow Density Cusp from Improved Lensing, Stellar Kinematic, and X-ray Data. , 728(2):L39. 17

Nulsen, P. E. J., Fabian, A. C., Mushotzky, R. F., Boldt, E. A., Holt, S. S., Marshall, F. J., and Serlemitsos, P. J. (1979). Large-scale structure of X-ray clusters of galaxies. , 189:183–188. 90

Okabe, N., Takada, M., Umetsu, K., Futamase, T., and Smith, G. P. (2010). Locuss: Subaru weak lensing study of 30 galaxy clusters. *Publications of the Astronomical Society of Japan*, 62(3):811870. 19

Osterbrock, D. E. (1974). *Astrophysics of gaseous nebulae*. 11

Oukbir, J. and Blanchard, A. (1992). X-ray clusters in open universes. , 262:L21–L24. 29

Oukbir, J. and Blanchard, A. (1997). X-ray clusters: towards a new determination of the density parameter of the universe. , 317:1–13. 29

Pal, P. B. and Wolfenstein, L. (1982). Radiative decays of massive neutrinos. , 25(3):766–773. 66

Palmese, A., Annis, J., Burgad, J., Farahi, A., Soares-Santos, M., Welch, B., da SilvaPereira, M., Lin, H., Bhargava, S., Hollowood, D. L., and et al. (2020). Stellar

mass as a galaxy cluster mass proxy: application to the dark energy survey redmapper clusters. *Monthly Notices of the Royal Astronomical Society*, 493(4):45914606. 25

Peebles, P. J. E. (1993). *Principles of Physical Cosmology*. 29

Perlmutter, S., Aldering, G., Goldhaber, G., Knop, R. A., Nugent, P., Castro, P. G., Deustua, S., Fabbro, S., Goobar, A., Groom, D. E., and et al. (1999). Measurements of and from 42 highredshift supernovae. *The Astrophysical Journal*, 517(2):565586. 2

Peterson, J. R., Kahn, S. M., Paerels, F. B. S., Kaastra, J. S., Tamura, T., Bleeker, J. A. M., Ferrigno, C., and Jernigan, J. G. (2003). Highresolution xray spectroscopic constraints on coolingflow models for clusters of galaxies. *The Astrophysical Journal*, 590(1):207224. 26

Pierre, M., Pacaud, F., Adami, C., Alis, S., Altieri, B., Baran, N., Benoist, C., Birkinshaw, M., Bongiorno, A., Bremer, M. N., Brusa, M., Butler, A., Ciliegi, P., Chiappetti, L., Clerc, N., Corasaniti, P. S., Coupon, J., De Breuck, C., Democles, J., Desai, S., Delhaize, J., Devriendt, J., Dubois, Y., Eckert, D., Elyiv, A., Ettori, S., Evrard, A., Faccioli, L., Farahi, A., Ferrari, C., Finet, F., Fotopoulou, S., Fourmanoit, N., Gandhi, P., Gastaldello, F., Gastaud, R., Georgantopoulos, I., Giles, P., Guennou, L., Guglielmo, V., Horellou, C., Husband, K., Huynh, M., Iovino, A., Kilbinger, M., Koulouridis, E., Lavoie, S., Le Brun, A. M. C., Le Fevre, J. P., Lidman, C., Lieu, M., Lin, C. A., Mantz, A., Maughan, B. J., Maurogordato, S., McCarthy, I. G., McGee, S., Melin, J. B., Melnyk, O., Menanteau, F., Novak, M., Paltani, S., Plionis, M., Poggianti, B. M., Pomarede, D., Pompei, E., Ponman, T. J., Ramos-Ceja, M. E., Ranalli, P., Rapetti, D., Raychaudury, S., Reiprich, T. H., Rottgering, H., Rozo, E., Rykoff, E., Sadibekova, T., Santos, J., Sauvageot, J. L., Schimd, C., Sereno, M., Smith, G. P., Smolčić, V., Snowden, S., Spergel, D., Stanford, S., Surdej, J., Valageas, P., Valotti, A., Valtchanov, I., Vignali, C., Willis, J., and Ziparo, F. (2016). The XXL Survey. I. Scientific motivations - XMM-Newton observing plan - Follow-up observations and simulation programme. , 592:A1. 36

Pierre, M., Valtchanov, I., Altieri, B., Andreon, S., Bolzonella, M., Bremer, M., Disseau, L., Santos, S. D., Gandhi, P., Jean, C., and et al. (2004). The xmm-lss survey. survey design and first results. *Journal of Cosmology and Astroparticle Physics*, 2004(09):011011. 36

Planck Collaboration, Aghanim, N., Akrami, Y., Ashdown, M., Aumont, J., Baccigalupi,

C., Ballardini, M., Banday, A. J., Barreiro, R. B., Bartolo, N., Basak, S., Battye, R., Benabed, K., Bernard, J. P., Bersanelli, M., Bielewicz, P., Bock, J. J., Bond, J. R., Borrill, J., Bouchet, F. R., Boulanger, F., Bucher, M., Burigana, C., Butler, R. C., Calabrese, E., Cardoso, J. F., Carron, J., Challinor, A., Chiang, H. C., Chluba, J., Colombo, L. P. L., Combet, C., Contreras, D., Crill, B. P., Cuttaia, F., de Bernardis, P., de Zotti, G., Delabrouille, J., Delouis, J. M., Di Valentino, E., Diego, J. M., Doré, O., Douspis, M., Ducout, A., Dupac, X., Dusini, S., Efstathiou, G., Elsner, F., Enßlin, T. A., Eriksen, H. K., Fantaye, Y., Farhang, M., Fergusson, J., Fernandez-Cobos, R., Finelli, F., Forastieri, F., Frailis, M., Fraisse, A. A., Franceschi, E., Frolov, A., Galeotta, S., Galli, S., Ganga, K., Génova-Santos, R. T., Gerbino, M., Ghosh, T., González-Nuevo, J., Górski, K. M., Gratton, S., Gruppuso, A., Gudmundsson, J. E., Hamann, J., Handley, W., Hansen, F. K., Herranz, D., Hildebrandt, S. R., Hivon, E., Huang, Z., Jaffe, A. H., Jones, W. C., Karakci, A., Keihänen, E., Keskitalo, R., Kiiveri, K., Kim, J., Kisner, T. S., Knox, L., Krachmalnicoff, N., Kunz, M., Kurki-Suonio, H., Lagache, G., Lamarre, J. M., Lasenby, A., Lattanzi, M., Lawrence, C. R., Le Jeune, M., Lemos, P., Lesgourgues, J., Levrier, F., Lewis, A., Liguori, M., Lilje, P. B., Lilley, M., Lindholm, V., López-Caniego, M., Lubin, P. M., Ma, Y. Z., Macías-Pérez, J. F., Maggio, G., Maino, D., Mandolesi, N., Mangilli, A., Marcos-Caballero, A., Maris, M., Martin, P. G., Martinelli, M., Martínez-González, E., Matarrese, S., Mauri, N., McEwen, J. D., Meinhold, P. R., Melchiorri, A., Mennella, A., Migliaccio, M., Millea, M., Mitra, S., Miville-Deschênes, M. A., Molinari, D., Montier, L., Morgante, G., Moss, A., Natoli, P., Nørgaard-Nielsen, H. U., Pagano, L., Paoletti, D., Partridge, B., Patanchon, G., Peiris, H. V., Perrotta, F., Pettorino, V., Piacentini, F., Polastri, L., Polenta, G., Puget, J. L., Rachen, J. P., Reinecke, M., Remazeilles, M., Renzi, A., Rocha, G., Rosset, C., Roudier, G., Rubiño-Martín, J. A., Ruiz-Granados, B., Salvati, L., Sandri, M., Savelainen, M., Scott, D., Shellard, E. P. S., Sirignano, C., Sirri, G., Spencer, L. D., Sunyaev, R., Suur-Uski, A. S., Tauber, J. A., Tavagnacco, D., Tenti, M., Toffolatti, L., Tomasi, M., Trombetti, T., Valenziano, L., Valiviita, J., Van Tent, B., Vibert, L., Vielva, P., Villa, F., Vittorio, N., Wand elt, B. D., Wehus, I. K., White, M., White, S. D. M., Zacchei, A., and Zonca, A. (2018). Planck 2018 results. VI. Cosmological parameters. *arXiv e-prints*, page arXiv:1807.06209. 2, 4, 135

Pratt, G. W., Croston, J. H., Arnaud, M., and Bhringer, H. (2009). Galaxy cluster x-ray luminosity scaling relations from a representative local sample (rexcess). *Astronomy Astrophysics*, 498(2):361378. 11, 25

Press, W. H. and Schechter, P. (1974). Formation of Galaxies and Clusters of Galaxies by Self-Similar Gravitational Condensation. , 187:425–438. 1, 29

Prieto, C. A., Majewski, S., Schiavon, R., Cunha, K., Frinchaboy, P., Holtzman, J., Johnston, K., Shetrone, M., Skrutskie, M., Smith, V., and et al. (2008). Apogee: The apache point observatory galactic evolution experiment. *Astronomische Nachrichten*, 329(9-10):10181021. 40

Rasia, E., Ettori, S., Moscardini, L., Mazzotta, P., Borgani, S., Dolag, K., Tormen, G., Cheng, L. M., and Diaferio, A. (2006). Systematics in the x-ray cluster mass estimators. *Monthly Notices of the Royal Astronomical Society*, 369(4):20132024. 15

Reiprich, T. H. and Böhringer, H. (2002). The Mass Function of an X-Ray Flux-limited Sample of Galaxy Clusters. , 567(2):716–740. 24, 31

Riemer-Sørensen, S. (2016). Constraints on the presence of a 3.5 kev dark matter emission line fromchandraobservations of the galactic centre. *Astronomy Astrophysics*, 590:A71. 68

Riess, A. G., Filippenko, A. V., Challis, P., Clocchiatti, A., Diercks, A., Garnavich, P. M., Gilliland, R. L., Hogan, C. J., Jha, S., Kirshner, R. P., Leibundgut, B., Phillips, M. M., Reiss, D., Schmidt, B. P., Schommer, R. A., Smith, R. C., Spyromilio, J., Stubbs, C., Suntzeff, N. B., and Tonry, J. (1998). Observational Evidence from Supernovae for an Accelerating Universe and a Cosmological Constant. , 116(3):1009–1038. 2

Rocha, M., Peter, A. H. G., Bullock, J. S., Kaplinghat, M., Garrison-Kimmel, S., Oorbe, J., and Moustakas, L. A. (2013). Cosmological simulations with self-interacting dark matter i. constant-density cores and substructure. *Monthly Notices of the Royal Astronomical Society*, 430(1):81104. 65

Romer, A. K., Nichol, R. C., Holden, B. P., Ulmer, M. P., Pildis, R. A., Merrelli, A. J., Adami, C., Burke, D. J., Collins, C. A., Metevier, A. J., and et al. (2000). The bright sharc survey: The cluster catalog. *The Astrophysical Journal Supplement Series*, 126(2):209269. 37

Romer, A. K., Nichol, R. C., Holden, B. P., Ulmer, M. P., Pildis, R. A., Merrelli, A. J., Adami, C., Burke, D. J., Collins, C. A., Metevier, A. J., Kron, R. G., and Commons, K. (2000). The Bright SHARC Survey: The Cluster Catalog. , 126(2):209–269. 88

Romer, A. K., Viana, P. T. P., Liddle, A. R., and Mann, R. G. (2001). A serendipitous galaxy cluster survey with xmm: Expected catalog properties and scientific applications. *The Astrophysical Journal*, 547(2):594–608. 43, 70, 97

Rosati, P., Borgani, S., and Norman, C. (2002). The Evolution of X-ray Clusters of Galaxies. , 40:539–577. 7

Rossetti, M. and Molendi, S. (2010). Cool core remnants in galaxy clusters. *Astronomy and Astrophysics*, 510:A83. 26

Roszkowski, L., Sessolo, E. M., and Trojanowski, S. (2018). Wimp dark matter candidates and searchescurrent status and future prospects. *Reports on Progress in Physics*, 81(6):066201. 65

Rozo, E. and Rykoff, E. S. (2014). redMaPPer II: X-Ray and SZ Performance Benchmarks for the SDSS Catalog. , 783(2):80. 25

Rozo, E., Rykoff, E. S., Becker, M., Reddick, R. M., and Wechsler, R. H. (2015). redmapper iv. photometric membership identification of red cluster galaxies with 1percent precision. *Monthly Notices of the Royal Astronomical Society*, 453(1):3852. 48

Rozo, E., Wechsler, R. H., Rykoff, E. S., Annis, J. T., Becker, M. R., Evrard, A. E., Frieman, J. A., Hansen, S. M., Hao, J., Johnston, D. E., and et al. (2009). Cosmological constraints from the sloan digital sky survey maxbcg cluster catalog. *The Astrophysical Journal*, 708(1):645660. 101

Rykoff, E. S., Koester, B. P., Rozo, E., Annis, J., Evrard, A. E., Hansen, S. M., Hao, J., Johnston, D. E., McKay, T. A., and Wechsler, R. H. (2012). Robust Optical Richness Estimation with Reduced Scatter. , 746(2):178. 25

Rykoff, E. S., Rozo, E., Busha, M. T., Cunha, C. E., Finoguenov, A., Evrard, A., Hao, J., Koester, B. P., Leauthaud, A., Nord, B., Pierre, M., Reddick, R., Sadibekova, T., Sheldon, E. S., and Wechsler, R. H. (2014). redMaPPer. I. Algorithm and SDSS DR8 Catalog. , 785:104. xvi, 8, 34, 46, 48, 50, 70, 96

Sadat, R. (1997). Clusters of galaxies and mass estimates. 13

Sarazin, C. L. (1986). X-ray emission from clusters of galaxies. *Rev. Mod. Phys.*, 58:1–115. 11

Saro, A., Bocquet, S., Rozo, E., Benson, B. A., Mohr, J., Rykoff, E. S., Soares-Santos, M., Bleem, L., Dodelson, S., Melchior, P., and et al. (2015). Constraints on the richness-mass relation and the optical-sze positional offset distribution for sze-selected clusters. *Monthly Notices of the Royal Astronomical Society*, 454(3):23052319. 130

Schrabback, T., Applegate, D., Dietrich, J. P., Hoekstra, H., Bocquet, S., Gonzalez, A. H., von der Linden, A., McDonald, M., Morrison, C. B., Raihan, S. F., and et al. (2017). Cluster mass calibration at high redshift: Hst weak lensing analysis of 13 distant galaxy clusters from the south pole telescope sunyaevzeldovich survey. *Monthly Notices of the Royal Astronomical Society*, 474(2):26352678. 19

Schuster, H. E. (1980). Mapping the Southern Sky with the ESO 1-METER Schmidt Telescope. *The Messenger*, 22:7. 8

Shah, C., Dobrodey, S., Bernitt, S., Steinbrügge, R., Crespo López-Urrutia, J. R., Gu, L., and Kaastra, J. (2016). Laboratory Measurements Compellingly Support a Charge-exchange Mechanism for the 'Dark Matter' ~3.5 keV X-Ray Line. , 833(1):52. 69

Shapiro, P. R., Iliev, I. T., Martel, H., Ahn, K., and Alvarez, M. A. (2004). The equilibrium structure of cdm halos. 14

Simet, M., McClintock, T., Mandelbaum, R., Rozo, E., Rykoff, E., Sheldon, E., and Wechsler, R. H. (2016). Weak lensing measurement of the massrichness relation of sdss redmapper clusters. *Monthly Notices of the Royal Astronomical Society*, 466(3):31033118. 25, 103

Smith, G. P., Mazzotta, P., Okabe, N., Ziparo, F., Mulroy, S. L., Babul, A., Finoguenov, A., McCarthy, I. G., Lieu, M., Bah, Y. M., and et al. (2015). Locuss: Testing hydrostatic equilibrium in galaxy clusters. *Monthly Notices of the Royal Astronomical Society: Letters*, 456(1):L74L78. 19

Smith, R. K., Brickhouse, N. S., Liedahl, D. A., and Raymond, J. C. (2001). Collisional Plasma Models with APEC/APED: Emission-Line Diagnostics of Hydrogen-like and Helium-like Ions. , 556:L91–L95. 57

Stanek, R., Evrard, A. E., Bohringer, H., Schuecker, P., and Nord, B. (2006). The xray luminositymass relation for local clusters of galaxies. *The Astrophysical Journal*, 648(2):956. 24

Stott, J. P., Hickox, R. C., Edge, A. C., Collins, C. A., Hilton, M., Harrison, C. D., Romer, A. K., Rooney, P. J., Kay, S. T., Miller, C. J., and et al. (2012). The xmm cluster survey: the interplay between the brightest cluster galaxy and the intracluster medium via agn feedback. *Monthly Notices of the Royal Astronomical Society*, 422(3):22132229. 105

Stott, J. P., Pimbblet, K. A., Edge, A. C., Smith, G. P., and Wardlow, J. L. (2009). The evolution of the red sequence slope in massive galaxy clusters. *Monthly Notices of the Royal Astronomical Society*, 394(4):20982108. 8

Struble, M. F. and Rood, H. J. (1987). A Compilation of Redshifts and Velocity Dispersions for Abell Clusters. , 63:543. 97

Strüder, L., Briel, U., Dennerl, K., Hartmann, R., Kendziorra, E., Meidinger, N., Pfeffermann, E., Reppin, C., Aschenbach, B., Bornemann, W., Bräuninger, H., Burkert, W., Elender, M., Freyberg, M., Haberl, F., Hartner, G., Heuschmann, F., Hippmann, H., Kastelic, E., Kemmer, S., Kettenring, G., Kink, W., Krause, N., Müller, S., Oppitz, A., Pietsch, W., Popp, M., Predehl, P., Read, A., Stephan, K. H., Stötter, D., Trümper, J., Holl, P., Kemmer, J., Soltau, H., Stötter, R., Weber, U., Weichert, U., von Zanthier, C., Carathanassis, D., Lutz, G., Richter, R. H., Solc, P., Böttcher, H., Kuster, M., Staubert, R., Abbey, A., Holland, A., Turner, M., Balasini, M., Bignami, G. F., La Palombara, N., Villa, G., Buttler, W., Gianini, F., Lainé, R., Lumb, D., and Dhez, P. (2001). The European Photon Imaging Camera on XMM-Newton: The pn-CCD camera. , 365:L18–L26. 35

Sunyaev, R. A. and Zeldovich, Y. B. (1970). The Spectrum of Primordial Radiation, its Distortions and their Significance. *Comments on Astrophysics and Space Physics*, 2:66. 9

Takahashi, T., Kokubun, M., Mitsuda, K., Kelley, R. L., Ohashi, T., Aharonian, F., Akamatsu, H., Akimoto, F., Allen, S. W., Anabuki, N., Angelini, L., Arnaud, K., Asai, M., Audard, M., Awaki, H., Axelsson, M., Azzarello, P., Baluta, C., Bamba, A., Bando, N., Bautz, M. W., Bialas, T., Blandford, R., Boyce, K., Brenneman, L. W., Brown, G. V., Bulbul, E., Cackett, E. M., Canavan, E., Chernyakova, M., Chiao, M. P., Coppi, P. S., Costantini, E., O'Dell, S., DiPirro, M., Done, C., Dotani, T., Doty, J., Ebisawa, K., Eckart, M. E., Enoto, T., Ezoe, Y., Fabian, A. C., Ferrigno, C., Foster, A. R., Fujimoto, R., Fukazawa, Y., Funk, S., Furuzawa, A., Galeazzi, M., Gallo, L. C., Gandhi, P., Gilmore, K., Giustini, M., Goldwurm, A., Gu, L., Guainazzi, M., Haas, D., Haba, Y., Hagino, K., Hamaguchi, K., Harrus, I. M., Hatsukade, I., Hayashi, T.,

Hayashi, K., Hayashida, K., den Herder, J.-W., Hiraga, J. S., Hirose, K., Hornschemeier, A., Hoshino, A., Hughes, J. P., Ichinohe, Y., Iizuka, R., Inoue, H., Inoue, Y., Ishibashi, K., Ishida, M., Ishikawa, K., Ishimura, K., Ishisaki, Y., Itoh, M., Iwai, M., Iwata, N., Iyomoto, N., Jewell, C., Kaastra, J., Kallman, T., Kamae, T., Kara, E., Kataoka, J., Katsuda, S., Katsuta, J., Kawaharada, M., Kawai, N., Kawano, T., Kawasaki, S., Khangulyan, D., Kilbourne, C. A., Kimball, M., King, A., Kitaguchi, T., Kitamoto, S., Kitayama, T., Kohmura, T., Konami, S., Kosaka, T., Koujelev, A., Koyama, K., Koyama, S., Kretschmar, P., Krimm, H. A., Kubota, A., Kunieda, H., Laurent, P., Lee, S.-H., Leutenegger, M. A., Limousin, O., Loewenstein, M., Long, K. S., Lumb, D., Madejski, G., Maeda, Y., Maier, D., Makishima, K., Markevitch, M., Masters, C., Matsumoto, H., Matsushita, K., McCammon, D., Mcguinness, D., McNamara, B. R., Mehdipour, M., Miko, J., Miller, E. D., Miller, J. M., Mineshige, S., Minesugi, K., Mitsuishi, I., Miyazawa, T., Mizuno, T., Mori, H., Mori, K., Moroso, F., Moseley, H., Muench, T., Mukai, K., Murakami, H., Murakami, T., Mushotzky, R. F., Nagano, H., Nagino, R., Nakagawa, T., Nakajima, H., Nakamori, T., Nakano, T., Nakashima, S., Nakazawa, K., Namba, Y., Natsukari, C., Nishioka, Y., Nobukawa, K. K., Nobukawa, M., Noda, H., Nomachi, M., Odaka, H., Ogawa, H., Ogawa, M., Ogi, K., Ohno, M., Ohta, M., Okajima, T., Okamoto, A., Okazaki, T., Ota, N., Ozaki, M., Paerels, F., Paltani, S., Parmar, A., Petre, R., Pinto, C., de Plaa, J., Pohl, M., Pontius, J., Porter, F. S., Pottschmidt, K., Ramsey, B., Reynolds, C., Russell, H., Safi-Harb, S., Saito, S., Sakai, K., Sakai, S.-i., Sameshima, H., Sasaki, T., Sato, G., Sato, K., Sato, R., Sato, Y., Sawada, M., Schartel, N., Serlemitsos, P. J., Seta, H., Shibano, Y., Shida, M., Shidatsu, M., Shimada, T., Shinozaki, K., Shirron, P., Simionescu, A., Simmons, C., Smith, R. K., Sneiderman, G., Soong, Y., Stawarz, Ł., Sugawara, Y., Sugita, S., Sugita, H., Szymkowiak, A., Tajima, H., Takahashi, H., Takeda, S., Takei, Y., Tamagawa, T., Tamura, T., Tamura, K., Tanaka, T., Tanaka, Y., Tanaka, Y. T., Tashiro, M. S., Tawara, Y., Terada, Y., Terashima, Y., Tombesi, F., Tomida, H., Tsuboi, Y., Tsujimoto, M., Tsunemi, H., Tsuru, T. G., Uchida, H., Uchiyama, H., Uchiyama, Y., Ueda, S., Ueda, Y., Ueno, S., Uno, S., Urry, C. M., Ursino, E., de Vries, C. P., Wada, A., Watanabe, S., Watanabe, T., Werner, N., Wik, D. R., Wilkins, D. R., Williams, B. J., Yamada, S., Yamada, T., Yamaguchi, H., Yamaoka, K., Yamasaki, N. Y., Yamauchi, M., Yamauchi, S., Yaqoob, T., Yatsu, Y., Yonetoku, D., Yoshida, A., Yuasa, T., Zhuravleva, I., and Zoghbi, A. (2018). Hitomi (ASTRO-H) X-ray Astronomy Satellite. *Journal of Astronomical Telescopes, Instruments, and Systems*, 4:021402. 37

Takey, A., Schwope, A., and Lamer, G. (2011). The 2xmmi/sdss galaxy cluster survey. *Astronomy Astrophysics*, 534:A120. 36

Tremaine, S. and Gunn, J. E. (1979). Dynamical role of light neutral leptons in cosmology. *Phys. Rev. Lett.*, 42:407–410. 66

Troxel, M., MacCrann, N., Zuntz, J., Eifler, T., Krause, E., Dodelson, S., Gruen, D., Blazek, J., Friedrich, O., Samuroff, S., and et al. (2018). Dark energy survey year 1 results: Cosmological constraints from cosmic shear. *Physical Review D*, 98(4). 41

Turner, M. J. L., Abbey, A., Arnaud, M., Balasini, M., Barbera, M., Belsole, E., Bennie, P. J., Bernard, J. P., Bignami, G. F., Boer, M., Briel, U., Butler, I., Cara, C., Chabaud, C., Cole, R., Collura, A., Conte, M., Cros, A., Denby, M., Dhez, P., Di Coco, G., Dowson, J., Ferrando, P., Ghizzardi, S., Gianotti, F., Goodall, C. V., Gretton, L., Griffiths, R. G., Hainaut, O., Hochedez, J. F., Holland, A. D., Jourdain, E., Kendziorra, E., Lagostina, A., Laine, R., La Palombara, N., Lortholary, M., Lumb, D., Marty, P., Molendi, S., Pigot, C., Poindron, E., Pounds, K. A., Reeves, J. N., Reppin, C., Rothenflug, R., Salvetat, P., Sauvageot, J. L., Schmitt, D., Sembay, S., Short, A. D. T., Spragg, J., Stephen, J., Strüder, L., Tiengo, A., Trifoglio, M., Trümper, J., Vercellone, S., Vigroux, L., Villa, G., Ward, M. J., Whitehead, S., and Zonca, E. (2001). The European Photon Imaging Camera on XMM-Newton: The MOS cameras. , 365:L27–L35. 35

Umetsu, K., Medezinski, E., Nonino, M., Merten, J., Postman, M., Meneghetti, M., Donahue, M., Czakon, N., Molino, A., Seitz, S., and et al. (2014). Clash: Weak-lensing shear-and-magnification analysis of 20 galaxy clusters. *The Astrophysical Journal*, 795(2):163. 19

Urban, O., Werner, N., Allen, S. W., Simionescu, A., Kaastra, J. S., and Strigari, L. E. (2015). A Suzaku search for dark matter emission lines in the X-ray brightest galaxy clusters. *Monthly Notices of the Royal Astronomical Society*, 451(3):2447–2461. 67, 68, 69, 75, 78, 79, 81

Vanderlinde, K., Crawford, T. M., de Haan, T., Dudley, J. P., Shaw, L., Ade, P. A. R., Aird, K. A., Benson, B. A., Bleem, L. E., Brodwin, M., and et al. (2010). Galaxy clusters selected with the sunyaev-zeldovich effect from 2008 south pole telescope observations. *The Astrophysical Journal*, 722(2):11801196. 9

Vikhlinin, A., Kravtsov, A., Forman, W., Jones, C., Markevitch, M., Murray, S. S., and Van Speybroeck, L. (2006). Chandra Sample of Nearby Relaxed Galaxy Clusters: Mass, Gas Fraction, and Mass-Temperature Relation. , 640(2):691–709. 76

Vikhlinin, A., Kravtsov, A. V., Burenin, R. A., Ebeling, H., Forman, W. R., Hornstrup, A., Jones, C., Murray, S. S., Nagai, D., Quintana, H., and Voevodkin, A. (2009). Chandra Cluster Cosmology Project III: Cosmological Parameter Constraints. , 692:1060–1074. xiv, 31, 32, 36

Vikhlinin, A., Markevitch, M., Forman, W., and Jones, C. (2001). Zooming in on the coma cluster with [ital]chandra[/ital]: Compressed warm gas in the brightest cluster galaxies. *The Astrophysical Journal*, 555(2):L87L90. 103

Vikhlinin, A., Markevitch, M., Murray, S. S., Jones, C., Forman, W., and Van Speybroeck, L. (2005). Chandratemperature profiles for a sample of nearby relaxed galaxy clusters. *The Astrophysical Journal*, 628(2):655672. 12

White, S. D. M., Navarro, J. F., Evrard, A. E., and Frenk, C. S. (1993). The baryon content of galaxy clusters: a challenge to cosmological orthodoxy. , 366(6454):429–433. 27

Wilms, J., Allen, A., and McCray, R. (2000). On the Absorption of X-Rays in the Interstellar Medium. , 542:914–924. 57

Wilms, J., Lee, J. C., Nowak, M. A., Schulz, N. S., Xiang, J., and Juett, A. (2010). Don't Use Wabs - Improved Absorption Models for the ISM. In *AAS/High Energy Astrophysics Division #11*, volume 42 of *Bulletin of the American Astronomical Society*, page 674. 96

Yates, R. M., Thomas, P. A., and Henriques, B. M. B. (2017). Iron in galaxy groups and clusters: confronting galaxy evolution models with a newly homogenized data set. , 464:3169–3193. 57

York, D. G., Adelman, J., Anderson, John E., J., Anderson, S. F., Annis, J., Bahcall, N. A., Bakken, J. A., Barkhouser, R., Bastian, S., Berman, E., Boroski, W. N., Bracker, S., Briegel, C., Briggs, J. W., Brinkmann, J., Brunner, R., Burles, S., Carey, L., Carr, M. A., Castander, F. J., Chen, B., Colestock, P. L., Connolly, A. J., Crocker, J. H., Csabai, I., Czarapata, P. C., Davis, J. E., Doi, M., Dombeck, T., Eisenstein, D., Ellman, N., Elms, B. R., Evans, M. L., Fan, X., Federwitz, G. R., Fiscelli, L., Friedman, S.,

Frieman, J. A., Fukugita, M., Gillespie, B., Gunn, J. E., Gurbani, V. K., de Haas, E., Haldeman, M., Harris, F. H., Hayes, J., Heckman, T. M., Hennessy, G. S., Hindsley, R. B., Holm, S., Holmgren, D. J., Huang, C.-h., Hull, C., Husby, D., Ichikawa, S.-I., Ichikawa, T., Ivezić, Ž., Kent, S., Kim, R. S. J., Kinney, E., Klaene, M., Kleinman, A. N., Kleinman, S., Knapp, G. R., Korienek, J., Kron, R. G., Kunszt, P. Z., Lamb, D. Q., Lee, B., Leger, R. F., Limmongkol, S., Lindenmeyer, C., Long, D. C., Loomis, C., Loveday, J., Lucinio, R., Lupton, R. H., MacKinnon, B., Mannery, E. J., Mantsch, P. M., Margon, B., McGehee, P., McKay, T. A., Meiksin, A., Merelli, A., Monet, D. G., Munn, J. A., Narayanan, V. K., Nash, T., Neilsen, E., Neswold, R., Newberg, H. J., Nichol, R. C., Nicinski, T., Nonino, M., Okada, N., Okamura, S., Ostriker, J. P., Owen, R., Pauls, A. G., Peoples, J., Peterson, R. L., Petravick, D., Pier, J. R., Pope, A., Pordes, R., Prosapio, A., Rechenmacher, R., Quinn, T. R., Richards, G. T., Richmond, M. W., Rivetta, C. H., Rockosi, C. M., Ruthmansdorfer, K., Sand ford, D., Schlegel, D. J., Schneider, D. P., Sekiguchi, M., Sergey, G., Shimasaku, K., Siegmund, W. A., Smee, S., Smith, J. A., Snedden, S., Stone, R., Stoughton, C., Strauss, M. A., Stubbs, C., SubbaRao, M., Szalay, A. S., Szapudi, I., Szokoly, G. P., Thakar, A. R., Tremonti, C., Tucker, D. L., Uomoto, A., Vanden Berk, D., Vogeley, M. S., Waddell, P., Wang, S.-i., Watanabe, M., Weinberg, D. H., Yanny, B., Yasuda, N., and SDSS Collaboration (2000). The Sloan Digital Sky Survey: Technical Summary. , 120(3):1579–1587. 38

Zhang, Y., Jeltema, T., Hollowood, D. L., Everett, S., Rozo, E., Farahi, A., Bermeo, A., Bhargava, S., Giles, P., Romer, A. K., Wilkinson, R., Rykoff, E. S., Mantz, A., Diehl, H. T., Evrard, A. E., Stern, C., Gruen, D., von der Linden, A., Splettstoesser, M., Chen, X., Costanzi, M., Allen, S., Collins, C., Hilton, M., Klein, M., Mann, R. G., Manolopoulou, M., Morris, G., Mayers, J., Sahlen, M., Stott, J., Vergara Cervantes, C., Viana, P. T. P., Wechsler, R. H., Allam, S., Avila, S., Bechtol, K., Bertin, E., Brooks, D., Burke, D. L., Carnero Rosell, A., Carrasco Kind, M., Carretero, J., Castander, F. J., da Costa, L. N., De Vicente, J., Desai, S., Dietrich, J. P., Doel, P., Flaugher, B., Fosalba, P., Frieman, J., García-Bellido, J., Gaztanaga, E., Gruendl, R. A., Gschwend, J., Gutierrez, G., Hartley, W. G., Honscheid, K., Hoyle, B., Krause, E., Kuehn, K., Kuropatkin, N., Lima, M., Maia, M. A. G., Marshall, J. L., Melchior, P., Menanteau, F., Miller, C. J., Miquel, R., Ogando, R. L. C., Plazas, A. A., Sanchez, E., Scarpine, V., Schindler, R., Serrano, S., Sevilla-Noarbe, I., Smith, M., Soares-Santos, M., Suchyta, E., Swanson, M. E. C., Tarle, G., Thomas, D., Tucker, D. L., Vikram, V., Wester, W., and DES Collaboration (2019). Dark Energy Survey Year 1 results: calibration of cluster

mis-centring in the redMaPPer catalogues. , 487(2):2578–2593. 101, 130, 131

Zhang, Y., Miller, C. J., Rooney, P., Bermeo, A., Romer, A. K., Vergara Cervantes, C., Rykoff, E. S., Hennig, C., Das, R., Mckay, T., Song, J., Wilcox, H., Bacon, D., Bridle, S. L., Collins, C., Conselice, C., Hilton, M., Hoyle, B., Kay, S., Liddle, A. R., Mann, R. G., Mehrtens, N., Mayers, J., Nichol, R. C., Sahlen, M., Stott, J., Viana, P. T. P., Wechsler, R. H., Abbott, T., Abdalla, F. B., Allam, S., Benoit-Levy, A., Brooks, D., Buckley-Geer, E., Burke, D. L., Carnero Rosell, A., Carrasco Kind, M., Carretero, J., Castander, F. J., Crocce, M., Cunha, C. E., Dandrea, C. B., Da costa, L. N., Diehl, H. T., Dietrich, J. P., Eifler, T. F., Flaugher, B., Fosalba, P., Garcia-Bellido, J., Gaztanaga, E., Gerdes, D. W., Gruen, D., Gruendl, R. A., Gschwend, J., Gutierrez, G., Honscheid, K., James, D. J., Jeltema, T., Kuehn, K., Kuropatkin, N., Lima, M., Lin, H., Maia, M. A. G., March, M., Marshall, J. L., Melchior, P., Menanteau, F., Miquel, R., Ogando, R. L. C., Plazas, A. A., Sanchez, E., Schubnell, M., Sevilla-Noarbe, I., Smith, M., Soares-Santos, M., Sobreira, F., Suchyta, E., Swanson, M. E. C., Tarle, G., and Walker, A. R. (2017). Galaxies in X-ray Selected Clusters and Groups in Dark Energy Survey Data II: Hierarchical Bayesian Modeling of the Red-Sequence Galaxy Luminosity Function. *arXiv e-prints*, page arXiv:1710.05908. 8

Ziparo, F., Smith, G. P., Mulroy, S. L., Lieu, M., Willis, J. P., Hudelot, P., McGee, S. L., Fotopoulou, S., Lidman, C., Lavoie, S., and et al. (2016). The xxl survey. *Astronomy Astrophysics*, 592:A9. 25

Zwicky, F. (1933). Die Rotverschiebung von extragalaktischen Nebeln. *Helvetica Physica Acta*, 6:110–127. 13

Zwicky, F., Herzog, E., Wild, P., Karpowicz, M., and Kowal, C. T. (1961). *Catalogue of galaxies and of clusters of galaxies, Vol. I.* 8

# Appendix A

# Contributions to other publications

Much of the work presented in Chapters 2 and 4 has been utilised in various publications. In the sections below, we describe some of these key publications and their connection to the work in this thesis.

## A.1 Stellar mass as a galaxy cluster mass proxy: application to the Dark Energy Survey redMaPPer clusters

This paper introduces a galaxy cluster mass observable, $\mu_*$, based on the stellar masses of cluster members, and also present results for the DES-Y1 observations. Stellar masses are computed using a Bayesian Model Averaging method, and are validated for DES data using simulations and COSMOS data. We show that $\mu_*$ works as a promising mass proxy by comparing our predictions to Xray measurements. We measure the Xray temperature$\mu_*$ relation for a total of 150 clusters matched between the widefield DES-Y1 redMaPPer catalogue and *Chandra* and *XMM* archival observations, spanning the redshift range $0.1 < z < 0.7$. For a scaling relation which is linear in logarithmic space, we find a slope of $\alpha = 0.488 \pm 0.043$ and a scatter in the Xray temperature at fixed $\mu_*$ for the joint sample. By using the halo mass scaling relations of the Xray temperature from the Weighing the Giants program, we further derive the $\mu_*$conditioned scatter in mass, finding $\sigma_{\ln M|\mu_*} = 0.26^{+0.15}_{-0.10}$. These results are competitive with wellestablished cluster mass proxies used for cosmological analyses, showing that $\mu$ can be used as a reliable and physically motivated mass proxy to derive cosmological constraints.

## A.2 Galaxy populations and dynamical states of 289 SPT clusters in DES Year 3 footprint

We use imaging from the first three years of the Dark Energy Survey to characterize the dynamical state of 288 galaxy clusters at $0.1 < z < 0.9$ detected in the South Pole Telescope (SPT) Sunyaev-Zeldovich (SZ) effect survey (SPT-SZ). We examine spatial offsets between the position of the brightest cluster galaxy (BCG) and the center of the gas distribution as traced by the SPT-SZ centroid and by the X-ray centroid/peak position from *Chandra* and *XMM* data. We show that the radial distribution of offsets provides no evidence that SPT-SZ-selected cluster samples include a higher fraction of mergers than X-ray-selected cluster samples. We use the offsets to classify the dynamical state of the clusters, selecting the 43 most disturbed clusters, with half of those at $z \geq 0.5$, a region seldom explored previously. We find that Schechter function fits to the galaxy population in disturbed clusters and relaxed clusters differ at $z > 0.55$ but not at lower redshifts. Disturbed clusters at $z > 0.55$ have steeper faint-end slopes and brighter characteristic magnitudes. Within the same redshift range, we find that the BCGs in relaxed clusters tend to be brighter than the BCGs in disturbed samples, while in agreement in the lower redshift bin. Possible explanations includes a higher merger rate, and a more efficient dynamical friction at high redshift. The red-sequence population is less affected by the cluster dynamical state than the general galaxy population.

## A.3 Dark Energy Survey Year 1 Results: Weak Lensing Mass Calibration of redMaPPer Galaxy Clusters

We constrain the mass-richness scaling relation of redMaPPer galaxy clusters identified in the Dark Energy Survey Year 1 data using weak gravitational lensing. We split clusters into 43 bins of richness $\lambda$ and redshift $z$ for $\lambda \geq 20$ and $0.2 \geq z \leq 0.65$ and measure the mean masses of these bins using their stacked weak lensing signal. By modeling the scaling relation as $\langle M_{200m}|\lambda, z\rangle = M_0(\lambda/40)^F((1+z)/1.35)^G$, we constrain the normalization of the scaling relation at the 5% level, constituting the tightest measurements of the normalization and richness scaling index made to date. We use a semi-analytic covariance matrix to characterize the statistical errors in the recovered weak lensing profiles. Our analysis accounts for the following sources of systematic error: shear and photometric redshift errors, cluster miscentering, cluster member dilution of the source sample, systematic uncertainties in the modeling of the halo–mass correlation function, halo triaxiality,

and projection effects. We discuss prospects for reducing this systematic error budget, which dominates the uncertainty on $M_0$. Our result is in excellent agreement with, but has significantly smaller uncertainties than, previous measurements in the literature, and augurs well for the power of the DES cluster survey as a tool for precision cosmology and upcoming galaxy surveys such as LSST, Euclid and WFIRST.

## A.4 Mass Variance from Archival X-ray Properties of Dark Energy Survey Year-1 Galaxy Clusters

Using archival X-ray observations and a log-normal population model, Farahi et al. (2019) estimate constraints on the intrinsic scatter in halo mass at fixed optical richness for a galaxy cluster sample identified in Dark Energy Survey Year-One (DES-Y1) data with the redMaPPer algorithm. The scaling behaviour for clusters with X-ray temperatures, $T_{\rm X}$, and optical richness, $\Lambda_{RM}$, was examined in the redshift range $0.2 < z < 0.7$. X-ray temperatures are obtained from Chandra and XMM observations for 58 and 110 redMaPPer systems, respectively.

## A.5 The Impact of Active Galactic Nuclei and Cooling Mechanisms on the Intra-cluster Properties in the L-Galaxies Semi-analytical Model

A separate sample of XCS clusters located within the SDSS DR13 footprint (not discussed in this thesis) were used to compare simulated abundances from the L-GALAXIES semi-analytical model (Henriques et al., 2015), and those measured using an `apec` model with thawed abundance. The model and data show good agreement at low redshift ($0.1 < z < 0.3$), while at higher redshifts ($0.3 < z < 0.6$), the model seems to underproduce metals in the ICM relative to the data. Additionally, the observations suggest a weak negative slope between average metal abundance and temperature as the temperature increases while the model distribution of metals remains flat. This work is explained in detail in Chapter 5 of Fournier (2019).

# Appendix B

# Properties of the cluster sample used in Chapter 3

## B.1 The cluster catalogue

The catalogue of clusters used in Chapter 3 is provided below. All 118 clusters have their X-ray properties and associated projected dark matter masses listed.

## B.2 Exclusion of bad spectra

For the work conducted in Chapter 3, during the visual inspection, six clusters were excluded from the final sample due to fitting anomalies. The *XMM* FOV images and associated spectra for each cluster are highlighted in Figures B.1, B.2, B.3 and B.4 below. In the images, the source region is defined by the blue circle. The red dashed-circle defines the background region. All XAPA detected sources are circled in green and excluded from the spectrum. In the spectrum, the top panel shows the background subtracted source spectrum and model across the energy range ($0.3-7.9$ keV). The bottom panel shows the the residuals i.e. the difference between the model and the spectrum.

Table B.1: Properties of the cluster sample. XCSIDS with an * denote clusters which were part of the B14 analysis.

| XCSID | $z$ | $T_{\rm X}$ (keV) | $M_{DM}^{proj}$ ($10^{14}M_{\odot}$) | ObsID | $n_{\rm H}$ ($\rm cm^{-2}$) |
|---|---|---|---|---|---|
| XMMXCSJ000312.1-060530.5 | 0.251 | $6.81^{+0.22}_{-0.13}$ | 6.52 | 0652010401 | 0.012 |
| XMMXCSJ000349.3+020404.8 | 0.11 | $4.78^{+0.12}_{-0.12}$ | 3.8 | 0201900101 | 0.01 |
| XMMXCSJ001053.4+290939.6 | 0.338 | $4.93^{+0.38}_{-0.37}$ | 3.59 | 0650380101 | 0.024 |
| XMMXCSJ001737.5-005234.2 | 0.219 | $4.1^{+0.22}_{-0.22}$ | 2.78 | 0403760701 | 0.022 |
| XMMXCSJ001833.2+162609.9 | 0.562 | $9.66^{+0.37}_{-0.36}$ | 10.03 | 0111000101 | 0.021 |
| XMMXCSJ001938.0+033635.3 | 0.273 | $6.26^{+0.15}_{-0.15}$ | 5.59 | 0693010301 | 0.035 |
| XMMXCSJ002635.9+170930.7 | 0.394 | $3.43^{+0.19}_{-0.14}$ | 1.87 | 0050140201 | 0.03 |
| XMMXCSJ003456.6+023357.9 | 0.379 | $5.53^{+0.53}_{-0.41}$ | 4.27 | 0650380601 | 0.017 |
| XMMXCSJ003706.4+090925.8 | 0.264 | $8.24^{+0.26}_{-0.26}$ | 8.98 | 0084230201 | 0.049 |
| XMMXCSJ004630.7+202803.6 | 0.105 | $2.44^{+0.23}_{-0.23}$ | 1.21 | 0652460101 | 0.031 |
| XMMXCSJ005138.5+271958.8 | 0.38 | $6.83^{+0.42}_{-0.32}$ | 6.13 | 0650380701 | 0.02 |
| XMMXCSJ005559.1+261949.0 | 0.196 | $5.84^{+0.16}_{-0.16}$ | 5.15 | 0203220101 | 0.028 |
| XMMXCSJ010649.3+010324.7 | 0.25 | $2.89^{+0.04}_{-0.04}$ | 1.51 | 0762870601 | 0.036 |
| XMMXCSJ013724.6-082727.6 | 0.557 | $7.87^{+0.67}_{-0.66}$ | 7.08 | 0700180201 | 0.01 |
| XMMXCSJ014656.7-092940.5 | 0.429 | $5.09^{+0.36}_{-0.35}$ | 3.6 | 0673750101 | 0.029 |
| XMMXCSJ015242.1+010029.4 | 0.231 | $5.38^{+0.31}_{-0.15}$ | 4.4 | 0084230401 | 0.029 |
| XMMXCSJ015334.1-011816.1 | 0.245 | $5.05^{+0.19}_{-0.19}$ | 3.93 | 0762870401 | 0.029 |
| XMMXCSJ015707.7-055233.7 | 0.132 | $4.09^{+0.24}_{-0.23}$ | 2.89 | 0781200101 | 0.032 |
| XMMXCSJ015824.9-014654.3 | 0.157 | $2.74^{+0.11}_{-0.11}$ | 1.44 | 0762870301 | 0.008 |
| XMMXCSJ020143.0-021146.5 | 0.198 | $3.55^{+0.08}_{-0.08}$ | 2.19 | 0605000301 | 0.022 |
| XMMXCSJ021441.2-043313.8 | 0.143 | $5.25^{+0.25}_{-0.22}$ | 4.4 | 0553911401 | 0.02 |
| XMMXCSJ022145.6-034613.7 | 0.422 | $4.84^{+0.41}_{-0.41}$ | 3.33 | 0604280101 | 0.009 |
| XMMXCSJ023142.5-045254.5 | 0.194 | $4.41^{+0.17}_{-0.18}$ | 3.19 | 0762870201 | 0.023 |
| XMMXCSJ023953.0-013441.1 | 0.358 | $5.91^{+0.16}_{-0.16}$ | 4.84 | 0782150101 | 0.043 |
| XMMXCSJ024803.3-033143.4* | 0.195 | $3.78^{+0.06}_{-0.06}$ | 2.45 | 0084230501 | 0.011 |
| XMMXCSJ024811.9-021624.9 | 0.241 | $7.74^{+0.36}_{-0.36}$ | 8.15 | 0721890401 | 0.033 |
| XMMXCSJ025632.9+000558.5 | 0.364 | $4.9^{+0.12}_{-0.12}$ | 3.51 | 0801610101 | 0.016 |
| XMMXCSJ073220.2+313751.1 | 0.182 | $5.94^{+0.16}_{-0.16}$ | 5.34 | 0673850201 | 0.017 |
| XMMXCSJ080056.7+360323.0 | 0.292 | $5.93^{+0.21}_{-0.21}$ | 5.03 | 0781590201 | 0.017 |
| XMMXCSJ082318.4+155758.0 | 0.159 | $3.01^{+0.2}_{-0.19}$ | 1.69 | 0742510401 | 0.029 |
| XMMXCSJ082557.4+041445.6 | 0.238 | $4.65^{+0.28}_{-0.27}$ | 3.42 | 0762950301 | 0.049 |
| XMMXCSJ085026.7+001506.2 | 0.201 | $3.21^{+0.18}_{-0.18}$ | 1.84 | 0761730501 | 0.051 |

| XCSID | $z$ | $T_{\rm X}$ (keV) | $M_{DM}^{proj}$ ($10^{14}M_{\odot}$) | ObsID | $n_{\rm H}$ ($\rm cm^{-2}$) |
|---|---|---|---|---|---|
| XMMXCSJ085612.8+375605.7 | 0.401 | $5.42^{+0.52}_{-0.31}$ | 4.08 | 0302581801 | 0.014 |
| XMMXCSJ090036.8+205340.6 | 0.244 | $3.91^{+0.09}_{-0.09}$ | 2.54 | 0402250701 | 0.03 |
| XMMXCSJ090849.1+143831.6 | 0.442 | $3.34^{+0.21}_{-0.17}$ | 1.74 | 0674370201 | 0.048 |
| XMMXCSJ090851.4+144550.0 | 0.457 | $5.32^{+0.45}_{-0.42}$ | 3.84 | 0674370201 | 0.037 |
| XMMXCSJ090912.4+105831.2 | 0.176 | $5.38^{+0.26}_{-0.16}$ | 4.52 | 0673850901 | 0.017 |
| XMMXCSJ091048.8+385007.5 | 0.564 | $9.55^{+0.78}_{-0.78}$ | 9.81 | 0723780101 | 0.032 |
| XMMXCSJ091110.7+174627.4 | 0.514 | $6.61^{+0.33}_{-0.3}$ | 5.38 | 0693662501 | 0.019 |
| XMMXCSJ091345.5+405626.3 | 0.424 | $5.94^{+0.25}_{-0.25}$ | 4.71 | 0147671001 | 0.02 |
| XMMXCSJ091752.2+514332.6* | 0.228 | $7.25^{+0.2}_{-0.2}$ | 7.35 | 0084230601 | 0.008 |
| XMMXCSJ092018.6+370622.2 | 0.239 | $2.63^{+0.05}_{-0.05}$ | 1.29 | 0149010201 | 0.014 |
| XMMXCSJ094300.0+465937.3 | 0.348 | $5.09^{+0.18}_{-0.18}$ | 3.77 | 0106460101 | 0.045 |
| XMMXCSJ100304.6+325339.3 | 0.391 | $3.17^{+0.26}_{-0.26}$ | 1.64 | 0302581601 | 0.03 |
| XMMXCSJ100742.4+380046.1 | 0.106 | $3.24^{+0.16}_{-0.16}$ | 1.96 | 0653450201 | 0.013 |
| XMMXCSJ101703.4+390250.1 | 0.208 | $6.11^{+0.13}_{-0.13}$ | 5.54 | 0084230701 | 0.023 |
| XMMXCSJ102339.7+041115.3* | 0.291 | $5.4^{+0.03}_{-0.03}$ | 4.3 | 0605540201 | 0.021 |
| XMMXCSJ103801.2+414619.8 | 0.133 | $2.07^{+0.21}_{-0.15}$ | 0.9 | 0206180101 | 0.016 |
| XMMXCSJ104044.2+395711.1* | 0.142 | $3.79^{+0.05}_{-0.05}$ | 2.52 | 0147630101 | 0.019 |
| XMMXCSJ104545.6+042025.4 | 0.15 | $2.87^{+0.25}_{-0.21}$ | 1.57 | 0653450601 | 0.034 |
| XMMXCSJ104724.0+151436.0 | 0.214 | $3.82^{+0.3}_{-0.3}$ | 2.47 | 0721880101 | 0.007 |
| XMMXCSJ111253.4+132640.2* | 0.181 | $4.78^{+0.08}_{-0.08}$ | 3.68 | 0500760101 | 0.035 |
| XMMXCSJ113313.2+500838.5 | 0.367 | $4.73^{+0.33}_{-0.33}$ | 3.29 | 0650382001 | 0.021 |

| XCSID | $z$ | $T_{\rm X}$ (keV) | $M_{DM}^{proj}$ ($10^{14}M_{\odot}$) | ObsID | $n_{\rm H}$ ($\rm cm^{-2}$) |
|---|---|---|---|---|---|
| XMMXCSJ114224.9+583134.7 | 0.326 | $7.75^{+0.75}_{-0.75}$ | 7.82 | 0650382201 | 0.022 |
| XMMXCSJ114935.6+222401.8 | 0.529 | $8.55^{+0.76}_{-0.55}$ | 8.29 | 0693661701 | 0.018 |
| XMMXCSJ115518.2+232424.3 | 0.135 | $6.31^{+0.07}_{-0.07}$ | 6.06 | 0551280201* | 0.024 |
| XMMXCSJ115827.8+262943.4 | 0.141 | $1.68^{+0.2}_{-0.05}$ | 0.63 | 0601260201 | 0.014 |
| XMMXCSJ120022.7+032007.4 | 0.138 | $5.94^{+0.12}_{-0.12}$ | 5.45 | 0827010301 | 0.006 |
| XMMXCSJ121937.0-031840.9 | 0.295 | $4.75^{+0.35}_{-0.35}$ | 3.45 | 0693010401 | 0.015 |
| XMMXCSJ122656.3+334332.8 | 0.514 | $4.73^{+0.33}_{-0.32}$ | 3.04 | 0200340101 | 0.022 |
| XMMXCSJ123355.5+152608.2 | 0.23 | $5.19^{+0.23}_{-0.23}$ | 4.15 | 0404120101 | 0.029 |
| XMMXCSJ123422.8+094718.7 | 0.239 | $4.26^{+0.16}_{-0.1}$ | 2.94 | 0673851101 | 0.024 |
| XMMXCSJ123618.1+285901.9 | 0.222 | $3.33^{+0.35}_{-0.23}$ | 1.94 | 0722660201 | 0.067 |
| XMMXCSJ123658.8+631117.9 | 0.3 | $6.43^{+0.45}_{-0.43}$ | 5.77 | 0402250101 | 0.04 |
| XMMXCSJ124133.3+325023.7 | 0.352 | $5.56^{+0.47}_{-0.39}$ | 4.37 | 0056020901 | 0.034 |
| XMMXCSJ124401.5+165347.3 | 0.542 | $4.2^{+0.22}_{-0.17}$ | 2.44 | 0302581501 | 0.021 |
| XMMXCSJ130357.9+673055.2 | 0.222 | $3.8^{+0.26}_{-0.26}$ | 2.43 | 0136000101 | 0.015 |
| XMMXCSJ130749.5+292549.3 | 0.261 | $3.11^{+0.18}_{-0.18}$ | 1.7 | 0205910101 | 0.048 |
| XMMXCSJ131129.8-012024.5* | 0.185 | $8.06^{+0.08}_{-0.08}$ | 8.99 | 0093030101 | 0.018 |
| XMMXCSJ131145.1+220206.1 | 0.17 | $3.52^{+0.32}_{-0.27}$ | 2.2 | 0402250301 | 0.046 |
| XMMXCSJ132250.7+313911.4 | 0.317 | $6.65^{+0.55}_{-0.32}$ | 6.05 | 0650384601 | 0.012 |
| XMMXCSJ132250.7+313911.4 | 0.317 | $7.96^{+0.51}_{-0.51}$ | 8.22 | 0650384601 | 0.012 |
| XMMXCSJ133048.5-015149.4 | 0.103 | $4.21^{+0.07}_{-0.07}$ | 3.08 | 0112240301 | 0.018 |
| XMMXCSJ133108.4-014338.4 | 0.545 | $3.79^{+0.25}_{-0.25}$ | 2.04 | 0112240301 | 0.024 |
| XMMXCSJ133233.8+502450.2 | 0.274 | $5.94^{+0.35}_{-0.35}$ | 5.1 | 0142860201 | 0.039 |
| XMMXCSJ133244.2+503243.5 | 0.286 | $7.24^{+0.22}_{-0.23}$ | 7.11 | 0142860201* | 0.01 |
| XMMXCSJ133421.5+503058.9 | 0.585 | $4.62^{+0.39}_{-0.38}$ | 2.8 | 0111160101 | 0.026 |
| XMMXCSJ133519.5+410004.9* | 0.234 | $7.16^{+0.25}_{-0.25}$ | 7.16 | 0084230901 | 0.015 |
| XMMXCSJ133648.8+102624.0 | 0.159 | $3.1^{+0.22}_{-0.22}$ | 1.78 | 0761590701 | 0.034 |
| XMMXCSJ140101.9+025238.3* | 0.253 | $6.52^{+0.04}_{-0.04}$ | 6.04 | 0551830201 | 0.036 |
| XMMXCSJ141627.7+231523.5 | 0.137 | $3.28^{+0.12}_{-0.12}$ | 1.98 | 0722140401 | 0.019 |
| XMMXCSJ141956.1+063434.9 | 0.541 | $4.23^{+0.43}_{-0.36}$ | 2.47 | 0303670101 | 0.021 |
| XMMXCSJ142039.8+395505.8 | 0.575 | $8.1^{+0.48}_{-0.48}$ | 7.36 | 0693661001 | 0.018 |
| XMMXCSJ142348.0+240444.1 | 0.523 | $5.63^{+0.16}_{-0.16}$ | 4.08 | 0720700301 | 0.018 |
| XMMXCSJ142521.4+631143.1 | 0.14 | $4.86^{+0.13}_{-0.13}$ | 3.87 | 0765031201 | 0.049 |
| XMMXCSJ142601.0+374937.0* | 0.175 | $8.3^{+0.11}_{-0.11}$ | 9.5 | 0112230201 | 0.018 |

| XCSID | $z$ | $T_{\rm X}$ (keV) | $M_{DM}^{proj}$ ($10^{14}M_{\odot}$) | ObsID | $n_{\rm H}$ ($\rm cm^{-2}$) |
|---|---|---|---|---|---|
| XMMXCSJ143150.0+133159.5 | 0.166 | $3.63^{+0.16}_{-0.16}$ | 2.32 | 0601970101 | 0.033 |
| XMMXCSJ144219.8+221809.9 | 0.107 | $3.49^{+0.11}_{-0.16}$ | 2.23 | 0765010501 | 0.015 |
| XMMXCSJ145715.0+222032.3 | 0.267 | $4.47^{+0.06}_{-0.06}$ | 3.15 | 0108670201 | 0.036 |
| XMMXCSJ150019.6+212214.5 | 0.162 | $5.78^{+0.15}_{-0.15}$ | 5.15 | 0693011001 | 0.023 |
| XMMXCSJ150817.8+575437.8 | 0.55 | $8.36^{+0.72}_{-0.54}$ | 7.88 | 0723780501 | 0.023 |
| XMMXCSJ151012.0+333058.0* | 0.121 | $6.34^{+0.15}_{-0.15}$ | 6.14 | 0149880101 | 0.025 |
| XMMXCSJ151618.5+000532.4 | 0.12 | $4.69^{+0.09}_{-0.09}$ | 3.66 | 0201902001 | 0.021 |
| XMMXCSJ151820.6+292735.3 | 0.558 | $6.45^{+0.25}_{-0.25}$ | 5.04 | 0693661101 | 0.023 |
| XMMXCSJ152642.6+164734.9 | 0.341 | $4.47^{+0.28}_{-0.27}$ | 3.03 | 0650382801 | 0.018 |
| XMMXCSJ152925.0+104144.0 | 0.488 | $5.01^{+0.16}_{-0.16}$ | 3.4 | 0762520201 | 0.019 |
| XMMXCSJ153253.8+302100.5* | 0.357 | $5.03^{+0.08}_{-0.08}$ | 3.67 | 0651240101 | 0.008 |
| XMMXCSJ153941.0+342512.8 | 0.236 | $6.7^{+0.28}_{-0.27}$ | 6.39 | 0673850601 | 0.046 |
| XMMXCSJ163936.8+470310.0 | 0.226 | $4.04^{+0.36}_{-0.33}$ | 2.7 | 0761590401 | 0.032 |
| XMMXCSJ164020.2+464227.1 | 0.233 | $9.86^{+0.3}_{-0.3}$ | 12.39 | 0605000501 | 0.023 |
| XMMXCSJ165943.9+323654.9 | 0.102 | $3.71^{+0.3}_{-0.31}$ | 2.48 | 0083150801 | 0.012 |
| XMMXCSJ172227.0+320758.0 | 0.229 | $7.09^{+0.14}_{-0.14}$ | 7.06 | 0693180901 | 0.019 |
| XMMXCSJ212939.7+000516.9* | 0.248 | $5.2^{+0.06}_{-0.06}$ | 4.12 | 0093030201 | 0.033 |
| XMMXCSJ213516.8+012600.0 | 0.237 | $8.59^{+0.58}_{-0.32}$ | 9.76 | 0692931301 | 0.017 |
| XMMXCSJ215101.0-073633.5 | 0.274 | $4.13^{+0.12}_{-0.12}$ | 2.74 | 0744390301 | 0.021 |
| XMMXCSJ215337.0+174146.9* | 0.251 | $10.08^{+0.25}_{-0.25}$ | 12.75 | 0111270101 | 0.02 |
| XMMXCSJ221145.8-034936.8 | 0.424 | $10.55^{+0.24}_{-0.24}$ | 12.59 | 0693010601 | 0.016 |
| XMMXCSJ222353.0-013714.4 | 0.101 | $4.39^{+0.08}_{-0.1}$ | 3.31 | 0401920101 | 0.016 |
| XMMXCSJ222605.0+172220.2 | 0.114 | $6.17^{+0.08}_{-0.08}$ | 5.88 | 0762470101 | 0.038 |
| XMMXCSJ222831.6+203729.9 | 0.413 | $8.09^{+0.26}_{-0.26}$ | 8.04 | 0147890101 | 0.044 |
| XMMXCSJ224321.4-093550.2 | 0.435 | $6.77^{+0.17}_{-0.09}$ | 5.86 | 0503490201 | 0.015 |
| XMMXCSJ224413.0-093427.9 | 0.444 | $3.45^{+0.33}_{-0.24}$ | 1.84 | 0503490201 | 0.04 |
| XMMXCSJ224523.7+280802.8 | 0.346 | $5.63^{+0.52}_{-0.51}$ | 4.48 | 0650384401 | 0.05 |
| XMMXCSJ230821.8-021127.4 | 0.3 | $7.81^{+0.49}_{-0.49}$ | 8.04 | 0205330501 | 0.021 |
| XMMXCSJ231132.6+033759.9 | 0.304 | $6.55^{+0.27}_{-0.27}$ | 5.93 | 0693010101 | 0.044 |
| XMMXCSJ231825.4+184246.9 | 0.163 | $3.33^{+0.11}_{-0.11}$ | 2.0 | 0762950201 | 0.039 |
| XMMXCSJ233738.6+001614.5 | 0.295 | $7.21^{+0.36}_{-0.36}$ | 7.02 | 0042341301 | 0.02 |
| XMMXCSJ234116.6-090128.8 | 0.258 | $6.77^{+0.35}_{-0.24}$ | 6.43 | 0693010801 | 0.023 |

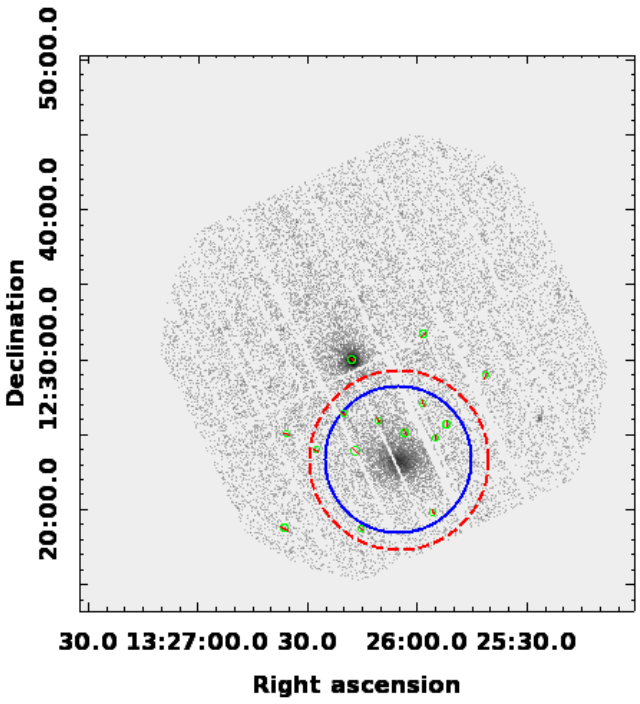


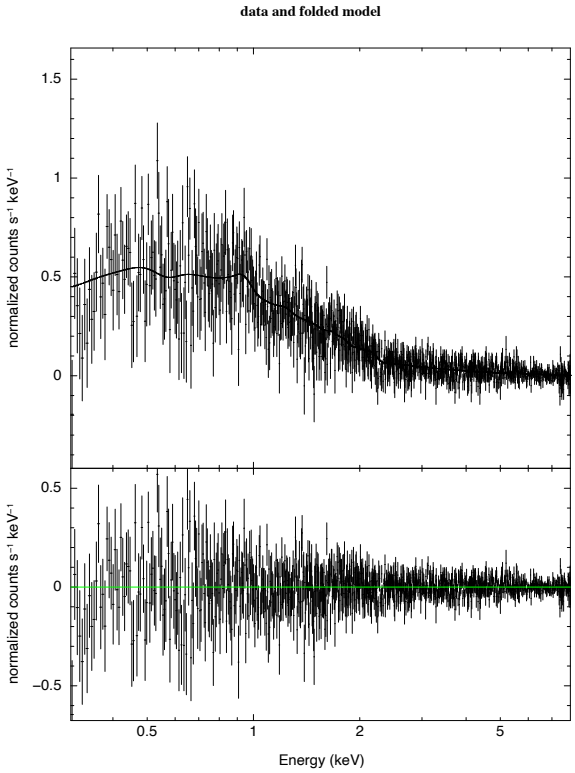


Figure B.1: Top: *XMM-Newton* FOV image for cluster XMMXCS J132604.8+122314.6 located in ObsID 0721890101, which has been contaminated by a bright X-ray source as well as instrumental features contaminating the background. The source region is defined by the blue circle. The red dashed-circle defines the background region. All XAPA detected sources are circled in green and excluded from the spectrum. Bottom: fitted spectrum for the cluster. The top panel shows the spectrum and model across the energy range $(0.3 - 7.9$ keV). The bottom panel shows the the residuals i.e. the difference between the model and the spectrum.

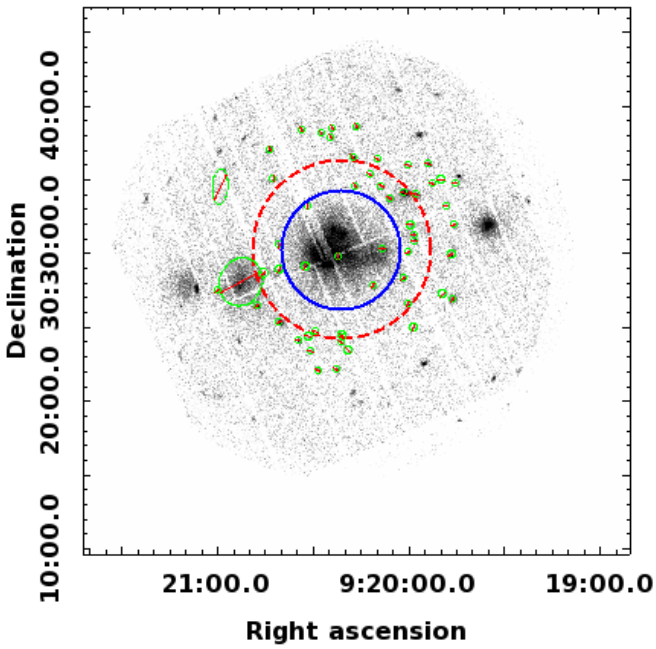


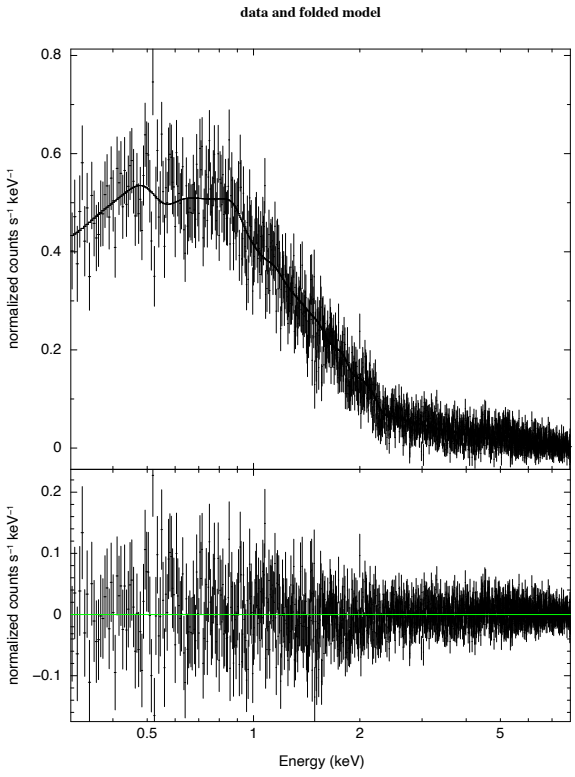


Figure B.2: Top: *XMM-Newton* FOV image of ObsID 0401170101. This is a targeted observation of the merging cluster, Abell 781, which is a composite of three clusters at two different redshifts (0.3 and 0.45), aligned in projection. Bottom: fitted spectrum for the central source (circled in blue).

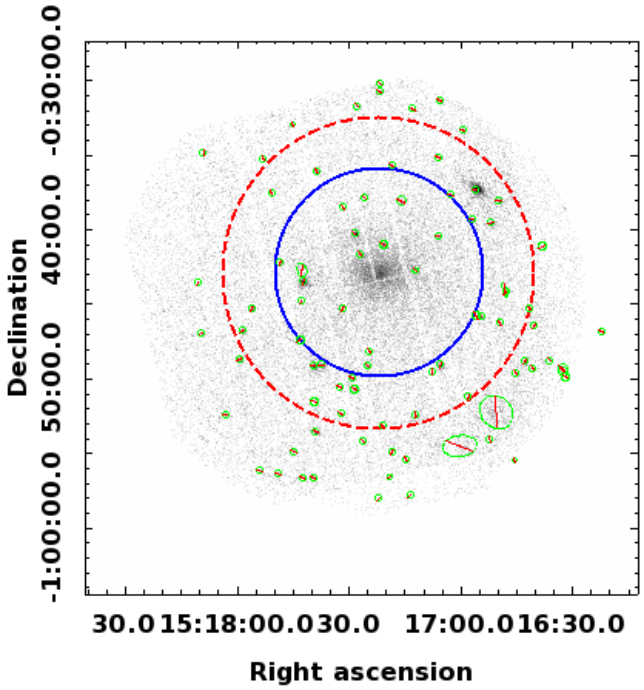


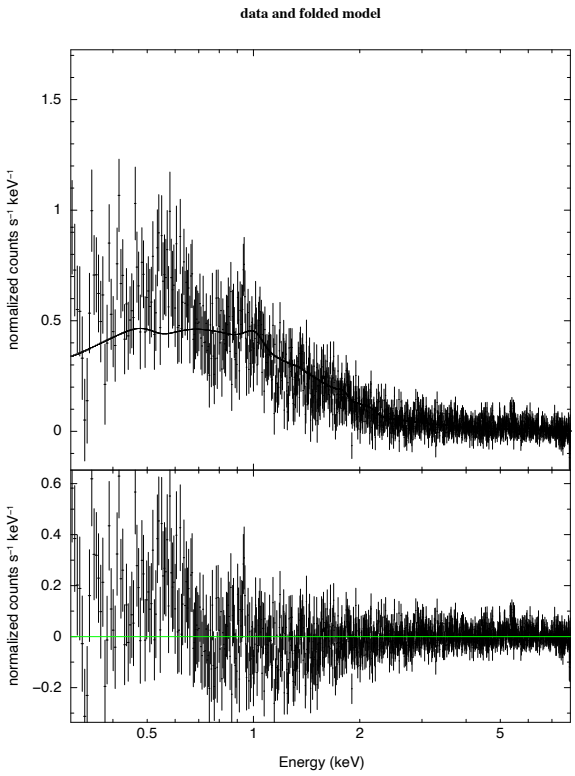


Figure B.3: Top: *XMM-Newton* FOV image of cluster XMMXCS J151721.7-004255.2 located in ObsID 0761590301. Bottom: fitted spectrum for the cluster.

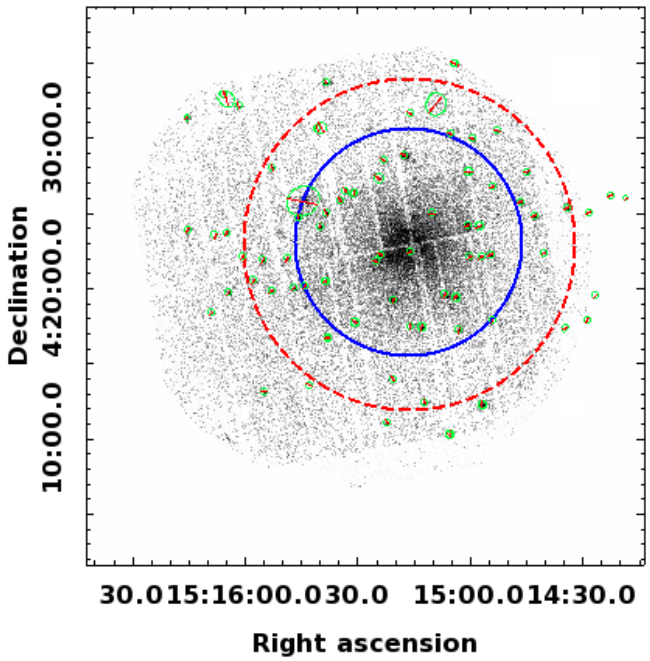


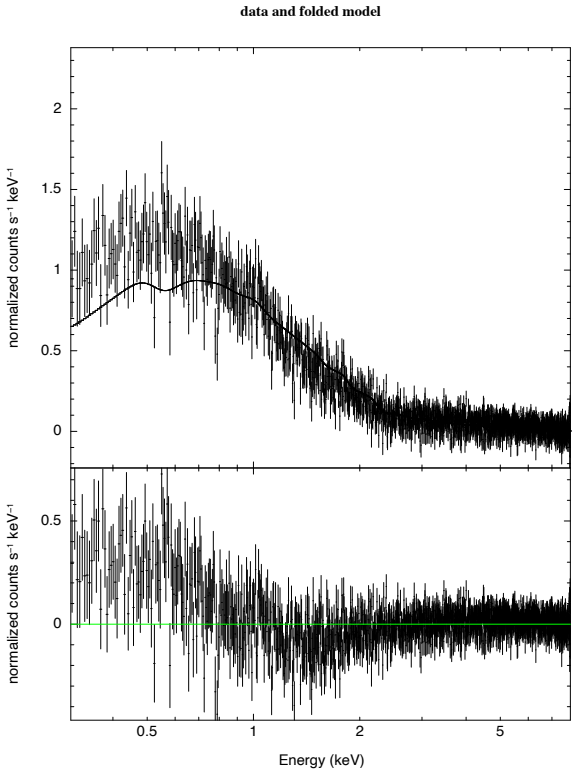


Figure B.4: Top: *XMM-Newton* FOV image of cluster XMMXCS J151516.1+042253.5 located in ObsID 0760230301. Bottom: fitted spectrum for the cluster.